

TWO-STAGE THERMOACOUSTIC ELECTRICITY GENERATOR  
WITH PUSH-PULL LINEAR ALTERNATOR

By

Ahmed Mohammed Hamood

Thesis submitted in accordance with the requirements for the degree of  
Doctor of Philosophy

At the University of Leeds  
School of Mechanical Engineering

September, 2016

## **Work Formed from Jointly Authored Publication**

The candidate has published two papers form work contained in this thesis. These were submitted with help of the supervisors.

- 1- The first paper was presented in the 24th IIR International Congress of Refrigeration, 16-22 Aug 2015. Yokohama, Japan: International Institute of Refrigeration.
  - i. The title of this paper is: (Design of two-stage thermoacoustic Stirling engine coupled with push-pull linear alternator for waste heat recovery).
  - ii. The authors are as follow: Ahmed Hamood, Xiaoan Mao and Artur J Jaworski.
  - iii. The work was done by the student under supervision of professor Jaworski and Dr Mao. Most the parts of the paper were obtained from Chapters 2 and 3.
  
- 2- The second paper was presented in the Proceeding of the World Congress on Engineering, London, UK, 29 June-1 July 2016.
  - i. The title of this paper is: (Two-Stage Thermoacoustic Electricity Generator for Waste Heat Recovery)
  - ii. The authors are as follow: Ahmed Hamood, Xiaoan Mao and Artur J Jaworski.
  - iii. The work was done by the student under supervision of professor Jaworski and Dr Mao. Most the parts of the paper were obtained from Chapters 2, 3, 4, and 5.

The candidate Ahmed Mohammed Hamood confirms that the work submitted is his own and that appropriate credit has been given where reference has been made to the work of others.

This copy has been supplied on the understanding that it is copyright material and that no quotation from the thesis may be published without proper acknowledgement.

*Assertion of moral rights:*

The right of Ahmed Mohammed Hamood to be identified as Author of this work has been asserted by him in accordance with the Copyright, Designs and Patents Act 1988.

## **Acknowledgements**

First and foremost, praise and thanks to the God, the Almighty, for His showers of blessings throughout my research work to complete the research successfully.

Undertaking this PhD has been a truly life-changing experience for me and it would have been impossible without the support and guidance that I received from many people.

Special mention goes to my enthusiastic main supervisor, Professor Artur Jaworski. My PhD has been a valuable experience and I thank Professor Artur Jaworski, not only for his tremendous academic support, but also for giving me so many lessons in life. The joy and enthusiasm he has for his research was contagious and motivational for me, even during tough times in the pursuit of my Ph.D. It has been an honour to be his Ph.D. student.

Similar profound gratitude goes to my second supervisor Dr Xiaoan Mao, who has been a truly dedicated guide through the laboratory work. I have very deep memories of my time there. I also want to thank him for letting my defence be an enjoyable moment, and for his brilliant comments and suggestions.

Special thanks to all the technical staff and my gratitude goes to Mr David Instrell, for his conscientious approach. Building a pilot size rig would have been a very difficult job without his amazing contribution.

I gratefully acknowledge the funding received towards my Ph.D. from the Kurdistan Regional Government, under the Human Capacity Development Program in Higher Education (HCDP) .

Finally, but by no means least, thanks go to my mother (R.I.P.), father and siblings for almost unbelievable support, and to my darling wife, who has been by my side throughout this Ph.D., living every single minute of it, and without whom, I would not have had the courage to embark on this journey in the first place. To my darling children for being a very good hope for the future. They are the most important people in my world and I dedicate this thesis to them.

## Abstract

This study focuses on the design, construction and experimental evaluation of a thermoacoustic electricity generator prototype with a push-pull linear alternator. The push-pull coupling offers a solution to run the looped-tube thermoacoustic engine at high acoustic impedance using one alternator. The novel configuration of the engine consists of two identical half-wavelength stages with an alternator connected between them. A simulation was carried out using the DeltaEC programme. The modelling started by investigating the required acoustic field for the alternator. The engine modelling has been done as half of the engine which is one-stage, because the DeltaEC shooting method showed that it was unable to run two identical stages. The engine is 16.02 m long and run at 55.1 Hz. The simulation showed that it is possible to produce more than 133 W of electricity at a thermal-to-electric efficiency of 23% while using helium pressurized at 28 bar. In practice, the engine failed to self-start. After exciting it to run by an external pulse, an electric power of 48.6 W was generated with a thermal-to-electric efficiency of 2.7%. The high heat leak detected was reduced by installing an insulating gasket between the ambient heat exchanger and regenerator holder, which encouraged the electricity generation to increase. The engine became self-starting when the regenerator thickness was reduced from 73 mm to 71.8 mm. The maximum generated electric power was 73.3 W at 3.33% thermal-to-electric efficiency at a heating power of 2200 W, and a maximum efficiency of 3.6% was achieved at 71.9 W electric power at a heating power of 2000 W. The success of the two-stage engine with a push-pull linear alternator encouraged modelling and design of a four-stage engine with two push-pull linear alternators able to generate up to 269 W of electricity, theoretically.

## Table of Contents

<b>Acknowledgements</b> .....	<b>iii</b>
<b>Abstract</b> .....	<b>iv</b>
<b>Table of Contents</b> .....	<b>v</b>
<b>List of Tables</b> .....	<b>viii</b>
<b>List of Figures</b> .....	<b>ix</b>
<b>List of symbols</b> .....	<b>xxiv</b>
<b>Chapter 1</b> .....	<b>1</b>
1.1 Introduction to Thermoacoustics.....	1
1.2 Motivation for the Study .....	2
1.3 Aim and Objective of the Study.....	3
1.4 Thesis Structure.....	4
<b>Chapter 2</b> .....	<b>7</b>
2.1 Thermoacoustics .....	7
2.2 Key Parameters .....	9
2.3 Thermoacoustic Technology.....	10
2.4 Standing Wave and Travelling Wave Thermoacoustic Engine .....	12
2.4.1 Principles of a standing-wave thermoacoustic engine .....	13
2.4.2 Principles of travelling-wave thermoacoustic engine .....	16
2.5 Linear Thermoacoustic Theory .....	19
2.6 Mass Streaming in Thermoacoustic Devices .....	22
2.6.1 Gedeon streaming.....	24
2.6.2 Rayleigh streaming.....	25
2.6.3 Jet-driven streaming.....	26
2.6.4 Streaming within a regenerator or stack.....	27
2.7 Development Review of Travelling-Wave Thermoacoustics Engines .....	28
2.7.1 Torus thermoacoustic engines.....	29
2.7.2 Looped tube thermoacoustic engines .....	38
2.7.3 Multi-stage thermoacoustic engines.....	49
2.7.4 Concluding remarks .....	55
<b>Chapter 3</b> .....	<b>57</b>
3.1. Conceptual Design .....	57
3.2. DeltaEC Modelling .....	59

3.3. Simulation Results .....	70
3.4 Concluding Remarks .....	73
<b>Chapter 4 .....</b>	<b>74</b>
4.1 Experimental Apparatus .....	74
4.1.1 Thermodynamic section .....	76
4.1.2 Acoustic section .....	81
4.2 Measurements .....	84
4.3 Heating and Cooling Systems .....	87
4.3.1 Heating system .....	87
4.3.2 Cooling system .....	88
4.4 Concluding Remarks .....	89
<b>Chapter 5 .....</b>	<b>90</b>
5.1 Start-up and System Debugging .....	90
5.2 Experimental Results .....	92
5.2.1 The Effect of External Load Resistance .....	97
5.2.2 The Effect Of Mean Pressure .....	103
5.2.3 The Effect of Heating Power .....	109
5.2.4 Mixed Variable Studies .....	117
5.3 Concluding Remarks .....	122
<b>Chapter 6 .....</b>	<b>123</b>
6.1 Optimization Target .....	123
6.2 Heat Leak Reduction: Effect of Installing an Insulating Gasket .....	123
6.3 Increase of Heating Power .....	133
6.4 Self-Start-Up Improvement .....	137
6.5 Efforts Towards Suppressing Streaming .....	142
6.6 Concluding Remarks .....	145
<b>Chapter 7 .....</b>	<b>147</b>
7.1 Four-stage Engine .....	147
<b>Chapter 8 .....</b>	<b>152</b>
8.1 Conclusions .....	152
8.2 Future Work .....	155
8.2.1 Further Simulation .....	155
8.2.2 Experimental improvements .....	156

<b>List of References .....</b>	<b>158</b>
<b>Appendix 1 .....</b>	<b>169</b>
<b>Appendix 2 .....</b>	<b>170</b>
<b>Appendix 3 .....</b>	<b>175</b>
<b>Appendix 4 .....</b>	<b>183</b>
<b>Appendix 5 .....</b>	<b>212</b>
<b>Appendix 6 .....</b>	<b>228</b>
<b>Appendix 7 .....</b>	<b>233</b>
Appendix 7.1 .....	233
Appendix 7.2 .....	234
<b>Appendix 8 .....</b>	<b>236</b>

## **List of Tables**

Table 3.1 Linear alternator specifications (Q-Drive 1S132M) .....	61
Table 4.1 Dimensions and materials summary .....	84
Table 5.1 Summary of the main five selected parameters at various heating power and mean pressure .....	121
Table 6.1 Summary of the main five selected parameters at various heating power and mean pressure, after installing the insulating gasket .....	135
Table 6.2 Performance of the engine at various membrane profile and locations ...	146

## List of Figures

Figure 1-1 Energy balance in different loads (Taymaz, 2006) .....	2
Figure 1-2: Function diagram of the proposed thermoacoustic engine.....	3
Figure 2-1: a) The singing Flame apparatus (Putnam and Dennis, 1956), b) Rijke tube (Feldman, 1968a).....	8
Figure 2-2: Sondhauss tube (Feldman, 1968b). .....	9
Figure 2-3: Work principles of (a) engine and (b) refrigerator. ....	11
Figure 2-4: Wave propagation of a (a) standing wave and (b) travelling wave.....	13
Figure 2-5: a) Acoustic pressure and velocity as a function of the position in a resonator having both sides closed, b) example of a stack Bhansali (2009). .....	14
Figure 2-6: Simplified thermoacoustic effect in a standing wave thermoacoustic engine showing the schematic diagram and the cyclic thermodynamics of the gas parcel inside the stack. ....	15
Figure 2-7: Standing wave engine processes showing a parcel of gas oscillating inside a stack channel: (a) Temperature-position diagram (b) Pressure-volume diagram (Swift, 2002). ....	16
Figure 2-8: Travelling wave engine processes showing a parcel of gas oscillating inside a regenerator channel: (a) Temperature-position diagram (b) Pressure-volume diagram (Swift, 2002).....	17
Figure 2-9: The simplified thermoacoustic effect in a travelling wave thermoacoustic engine showing the schematic diagram and the cyclic thermodynamics of the gas parcel inside the stack. ....	18
Figure 2-10: Sketches of streaming: (a) Rayleigh streaming (b) Jet-driven streaming (c) Gedeon streaming (d) streaming within the regenerator or stack (Swift, 2002) .....	23
Figure 2-11: Desirable mass streaming: (a) flow parallel to the oscillating flow (b) flow perpendicular to the oscillatory flow, (Swift, 2002). ....	24
Figure 2-12: Schematic diagram of a jet pump (Backhaus and Swift, 2000). ....	25
Figure 2-13: The net draft near the wall which causes Rayleigh streaming: (a) near a vertical wall (b) inclined wall, (Swift, 2002). ....	26
Figure 2-14: Oscillatory flow at a small orifice to an open space: (a) ejection (b) suction, (Swift, 2002). ....	27
Figure 2-15: Schematic drawing of an internal streaming flow in a regenerator (So <i>et al</i> , 2006).....	28
Figure 2-16: Scale drawing of the thermoacoustic engine showing all the parts, (Swift, 2000) .....	30
Figure 2-17: A schematic diagram of Ueda et al. (2002) thermoacoustic engine.....	31

Figure 2-18: Engine’s schematic diagrams of: (a) Leo et al. (2005 and 2006); (b) Leo et al. (2008) .....	33
Figure 2-19: Photograph of the solar-powered engine of Wu <i>et al.</i> (2012).....	34
Figure 2-20: PV diagram of the thermoacoustically driven refrigerator (Luo <i>et al.</i> , 2006) .....	35
Figure 2-21: Dissipation distributions at variable load resistance when the heating temperature is 650 C at 2.48 MPa, (Wang <i>et al.</i> , 2015).....	37
Figure 2-22: Schematic of experimental looped tube thermoacoustic engine, Yazaki <i>et al.</i> (1998).....	39
Figure 2-23: Schematic drawing of the combined thermoacoustic device of Sakamoto <i>et al.</i> (2004) .....	40
Figure 2-24: (a) labelled photograph of a thermoacoustic electricity generator (Abdulla <i>et al.</i> , 2013); (b) labelled photograph of a thermoacoustic combined system (Saechan <i>et al.</i> , 2013).....	43
Figure 2-25: (a) photograph of a thermoacoustic electricity generator (b) schematic drawing of the proposed engine, Yu and Jaworski (2012) .....	44
Figure 2-26: (a) photograph and schematic diagram of a thermoacoustic engine (Abduljalil <i>et al.</i> , 2009); (b) general and close-up views of the ceramic regenerator (Abduljalil <i>et al.</i> , 2011).....	46
Figure 2-27: Photographs of regenerator set-ups and close-ups of materials: (a) ceramic catalyst support; (b) steel “scourers”; (c) stainless steel “wool” and (d) wire mesh screens (Abduljalil <i>et al.</i> (2011b).....	46
Figure 2-28: (a) simplified sketch of the two-stage thermoacoustic electricity generator; (b) photograph of propane-burner driven engine; (c) photograph of wood-burner driven engine, (Chen <i>et al.</i> (2012).....	48
Figure 2-29: Schematic of the two-stage thermoacoustic generator prototype, Kang <i>et al.</i> (2015). .....	49
Figure 2-30: Four stage thermoacoustic engine scheme (Blok, 2010).....	51
Figure 2-31: Schematic of the travelling-wave thermoacoustic heat pump (Yang <i>et al.</i> , 2014). .....	53
Figure 2-32: Schematic of a three-stage combined system Xu <i>et al.</i> (2015a) .....	54
Figure 2-33: Schematic drawing of the four-stage combined system (Li <i>et al.</i> 2016). .....	55
Figure 3-1: Conceptual drawing of the proposed two-stage engine. ....	58
Figure 3-2: Linear alternator coupling configurations (a) push-pull (b) compliance housing .....	61
Figure 3-3: Linear alternator behaviour at various acoustic impedances and phase differences at the piston (a) push-pull coupling and (b) compliance housing coupling. ....	63
Figure 3-4: The effect of the cross-sectional area ratio on various parameters. ....	66

Figure 3-5: Block diagram of the segments in the DeltaEC simulation: ambient heat exchanger (AHX), regenerator (Reg), hot heat exchanger (HHX), thermal buffer tube (TBT), secondary cold heat exchanger (2 <sup>nd</sup> AHX), feedback pipe (Feedback), linear alternator (LA).....	66
Figure 3-6: The effect of $\delta k/rh$ through the regenerator on various parameters.....	67
Figure 3-7: The effect of the regenerator length on various parameters.....	68
Figure 3-8: The effect of the regenerator porosity on various parameters.....	68
Figure 3-9: The effect of <i>fin spacing</i> / $\delta k$ through the hot heat exchanger on various parameters. ....	69
Figure 3-10: The effect of the heat exchanger blockage ratio on various parameters. ....	69
Figure 3-11: Effect of the length of the thermal buffer tube on various parameters. ....	69
Figure 3-12: Effect of the feedback loop diameter on various parameters. ....	70
Figure 3-13: Simulation results (a) pressure amplitude, (b) volumetric flow, (c) acoustic impedance, (d) phase difference angle and (e) acoustic power flow, the schematic drawing at the bottom and top of the figure shows a simplified layout of the engine.....	72
Figure 4-1: A photograph of the experimental rig .....	75
Figure 4-2: Cross-section of the thermodynamic section, ambient heat exchanger (AHX), regenerator (Reg), hot heat exchanger (HHX), thermal buffer tube (TBT), secondary cold heat exchanger (2 <sup>nd</sup> AHX). ....	76
Figure 4-3: (a) ambient and secondary ambient heat exchangers; (b) hot heat exchanger; (c) a channel of ambient heat exchanger; (d) a channel of hot heat exchanger.....	78
Figure 4-4: Regenerator stacking stages (a) one screen; (b) half filled; (c) full regenerator. ....	79
Figure 4-5: The acoustic network layout of the experimental rig.....	82
Figure 4-6: (a) linear alternator housing cross-sectional view; (b) the plastic insert.....	83
Figure 4-7: Thermodynamic cross-sectional view showing the thermocouple (TC) locations. ....	85
Figure 4-8: A schematic drawing of the rig showing the locations of the pressure transducers (PT).....	88
Figure 5-1: The preliminary experimental pressure amplitude measurements against the theoretical values along the engine loop, the schematic drawing at the bottom of the figure shows a simplified layout of the engine.....	91
Figure 5-2: The connection arrangement of the control box and other equipment.....	92

Figure 5-3: Pressure waveform of theoretical vs experimental at 28 bar mean pressure, 1800 W heating power and 30.8 $\Omega$ external load, the schematic drawing at the bottom of the figure shows a simplified layout of the engine.....	95
Figure 5-4: Acoustic power distribution of experimental vs theoretical results at 28 bar mean pressure, 1800 W heating power and 30.8 $\Omega$ external load, the schematic drawing at the bottom of the figure shows a simplified layout of the engine.....	95
Figure 5-5: Temperature distribution at the two thermoacoustic cores at 28 bar mean pressure, 1800 W heating power and 30.8 $\Omega$ external load.....	96
Figure 5-6: Pressure phase difference between two identical points on the stage loop at 28 bar mean pressure, 1800 W heating power and 30.8 $\Omega$ external load.....	96
Figure 5-7: The performance of the engine as a function of the load resistance at 28 bar mean pressure and 1800 W heating power .....	98
Figure 5-8: Total efficiency for different load resistances at 28 bar mean pressure and 1800 W heating power .....	98
Figure 5-9: The effect of load resistance on the linear alternator efficiency at 28 bar mean pressure and 1800 W heating power .....	99
Figure 5-10: The relation between load resistance and measured acoustic efficiency at 28 bar mean pressure and 1800 W heating power .....	100
Figure 5-11: The alternator piston displacement versus load resistance at 28 bar mean pressure and 1800 W heating power .....	100
Figure 5-12: Measured drive ratio versus load resistance at 28 bar mean pressure and 1800 W heating power .....	100
Figure 5-13: The effect of load resistance on the measured regenerator temperature difference at 28 bar mean pressure and 1800 W heating power.....	101
Figure 5-14: Core temperature distribution of different load resistance at 28 bar mean pressure and 1800 W heating power .....	101
Figure 5-15: Fraction to Carnot efficiency for various load resistances at 28 bar mean pressure and 1800 W heating power .....	102
Figure 5-16: Experimental and theoretical phase difference versus load resistance at the alternator piston .....	103
Figure 5-17: Theoretical and experimental performance of the engine as a function of the load resistance at 1800 W heating power and 30 $\Omega$ load resistance.....	104
Figure 5-18: The performance of the engine versus mean pressure for various load resistances at 1800 W heating power .....	105
Figure 5-19: Total efficiency versus mean pressure for various load resistances at 1800 W heating power .....	105

Figure 5-20: The relation between mean pressure and acoustic efficiency for various load resistances at 1800 W heating power .....	106
Figure 5-21: Fraction to Carnot efficiency versus mean pressure for various load resistances at 1800 W heating power .....	106
Figure 5-22: The effect of mean pressure on the linear alternator efficiency for various load resistance at 1800 W heating power .....	107
Figure 5-23: Measured drive ratio versus mean pressure for various load resistances at 1800 W heating power .....	107
Figure 5-24: The effect of mean pressure on the piston displacement for various load resistances at 1800 W heating power .....	108
Figure 5-25: The effect of mean pressure on the regenerator temperature difference for various load resistances at 1800 W heating power .....	108
Figure 5-26: Core temperature distribution of different mean pressure at 1800 W heating power and 30.8 $\Omega$ load resistance.....	109
Figure 5-27: Theoretical vs experimental generated electricity at 28 bar mean pressure and 30.8 $\Omega$ external load resistance .....	110
Figure 5-28: The performance of the engine as a function of heating power for various load resistances at 28 bar mean pressure.....	111
Figure 5-29: Total efficiency of different heating power for various load resistances at 28 bar mean pressure .....	111
Figure 5-30: The relation between heating power and acoustic efficiency for various load resistances at 28 bar mean pressure.....	112
Figure 5-31: Fraction to Carnot efficiency versus heating powers for various load resistances at 28 bar mean pressure .....	112
Figure 5-32: The effect of heating power on the alternator efficiency for various load resistances at 28 bar mean pressure.....	112
Figure 5-33: The effect of heating power on the alternator piston displacement for various load resistances at 28 bar mean pressure .....	113
Figure 5-34: The effect of heating power on the temperature difference across the regenerator for various load resistances at 28 bar mean pressure .....	113
Figure 5-35: Core temperature distribution of different heating powers at 28 bar mean pressure.....	114
Figure 5-36: The performance of the engine as a function of mean pressure and heating power at 30.8 $\Omega$ load resistance.....	114
Figure 5-37: Total efficiency of different mean pressure for various heating powers at 30.8 $\Omega$ load resistance.....	115
Figure 5-38: The effect of mean pressure on the acoustic efficiency for various heating powers at 30.8 $\Omega$ load resistance.....	115
Figure 5-39: The effect of mean pressure on the fraction to Carnot efficiency for various heating powers at 30.8 $\Omega$ load resistance .....	116

Figure 5-40: The effect of mean pressure on the alternator efficiency for various heating powers at 30.8Ω load resistance .....	116
Figure 5-41: The effect of mean pressure on the alternator piston displacement for various heating powers at 30Ω load resistance .....	117
Figure 5-42: The effect of mean pressure on the regenerator temperature difference for various heating powers at 30Ω load resistance .....	117
Figure 6-1: A cross section of the thermodynamic section showing (a) metal-to-metal contact between the regenerator holder and the ambient heat exchanger, (b) gasket, in yellow, installed in position.....	124
Figure 6-2: Performance of the engine with and without an insulating gasket at 28 bar mean pressure and 1800 W heating power .....	124
Figure 6-3: Total efficiency for both with and without insulating gasket at 28 bar mean pressure and 1800 W heating power .....	125
Figure 6-4: Regenerator temperature difference with and without an installing insulating gasket at 28 bar mean pressure and 1800 W heating power .....	125
Figure 6-5: A comparison of the engine's acoustic efficiency with and without an insulating gasket at 28 bar mean pressure and 1800 W heating power ....	126
Figure 6-6: Drive ratio before and after installing the insulating gasket at 28 bar mean pressure and 1800 W heating power .....	126
Figure 6-7: The effect of using an insulating gasket on the alternator efficiency at 28 bar mean pressure and 1800 W heating power .....	127
Figure 6-8: Performance of the engine with insulating gasket at different heating power for various load resistance at 28 bar mean pressure.....	128
Figure 6-9: Alternator efficiency of the engine with insulating gasket at different heating power for various load resistance at 28 bar mean pressure .....	128
Figure 6-10: Thermal-to-electric efficiency at different heating power for various load resistances for an engine with an insulating gasket at 28 bar....	129
Figure 6-11: Acoustic efficiency versus heating power for an engine with an insulating gasket for various load resistances at 28 bar .....	129
Figure 6-12: Fraction to Carnot efficiency versus heating power for the engine with an insulating gasket for various load resistances at 28 bar .....	130
Figure 6-13: The effect of heating power on the temperature difference across the regenerator for the engine with an insulating gasket for various load resistances at 28 bar mean pressure .....	130
Figure 6-14: Performance of the engine with an insulating gasket at different mean pressure for various load resistance at 28 bar mean pressure.....	131
Figure 6-15: Drive ratio at different mean pressures for various load resistances with the insulating gasket at 1800 W heating power.....	132
Figure 6-16: Regenerator temperature difference after installing the insulating gasket for various load resistances at 1800 W heating power .....	132

Figure 6-17: Regenerator temperature difference after installing the insulating gasket for various heating powers at 30.8 $\Omega$ load resistance .....	132
Figure 6-18: Performance of the engine with an insulating gasket at extra heating power for various load resistances at 28 bar mean pressure .....	133
Figure 6-19: Alternator efficiency of the engine with an insulating gasket at extra heating power for various load resistances at 28 bar mean pressure ....	135
Figure 6-20: Thermal-to-electric efficiency at extra heating power for various load resistance for engine with insulating gasket at 28 bar mean pressure....	135
Figure 6-21: Acoustic efficiency versus extra heating power for the engine with an insulating gasket for various load resistances at 28 bar mean pressure .....	136
Figure 6-22: Fraction to Carnot efficiency versus extra heating power for the engine with an insulating gasket for various load resistances at 28 bar mean pressure.....	137
Figure 6-23: Drive ratio at extra heating power for various load resistances with the insulating gasket at 28 bar mean pressure.....	137
Figure 6-24: Performance of the engine with an insulating gasket versus regenerator thickness for various load resistances at 1800 W heating power.....	139
Figure 6-25: The effect of regenerator thickness on the temperature difference across the regenerator for the engine with an insulating gasket for various load resistances at 28 bar mean pressure and 1800 W heating power.....	139
Figure 6-26: Performance of the engine with an insulating gasket versus regenerator thickness for various heating powers at 30.8 $\Omega$ load resistance and 28 bar mean pressure .....	140
Figure 6-27: Thermal-to-electric efficiency at different heating powers for the engine with an insulating gasket at 30.8 $\Omega$ load resistance and 28 bar mean pressure.....	140
Figure 6-28: Acoustic efficiency versus regenerator thickness for the engine with an insulating gasket for various heating powers at 30.8 $\Omega$ load resistance and 28 bar mean pressure .....	141
Figure 6-29: Fraction to Carnot efficiency versus regenerator thickness for the engine with an insulating gasket for various load resistance at 30.8 $\Omega$ load resistance and 28 bar mean pressure .....	141
Figure 6-30: Drive ratio at different regenerator thickness for various heating power with the insulating gasket at 30.8 $\Omega$ load resistance and 28 bar mean pressure.....	141
Figure 6-31: (a) Locations of the membrane along the engine loop (b) locations of the membrane on the volumetric flow rate graph .....	143
Figure 6-32: (a) A membrane assembled on a flange, (b) concave membrane, (c) flat membrane, (d) loose membrane. ....	144

Figure 6-33: The effect of the presence of a concave membrane on the temperature profiles in the regenerator at 1400 W heating power and 28 bar mean pressure.....	144
Figure 6-34: pressure amplitude distribution along the engine both with and without a concave membrane at 1400 W heating power and 28 bar mean pressure .....	145
Figure 7-1: Conceptual drawing of the proposed four-stage engine.....	147
Figure 7-2: Block diagram of the segments in the DeltaEC four-stage simulation: ambient heat exchanger (AHX), regenerator (Reg), hot heat exchanger (HHX), thermal buffer tube (TBT), secondary cold heat exchanger (2 <sup>nd</sup> AHX), feedback pipe (Feedback), linear alternator (LA). .....	149
Figure 7-3: A proposed layout of the four-stage engine. ....	151
Figure 7-4: Simulation results (a) pressure amplitude, (b) volumetric velocity, (c) acoustic impedance, (d) phase difference angle and (e) acoustic power flow along the engine.....	151
Figure 8-1: Proposed hot heat exchanger with insulation jacket .....	156
Figure A3-1: Ambient heat exchanger detailed drawing .....	176
Figure A3-2: Simulation of stress of the ambient heat exchanger, done by the SolidWorks .....	177
Figure A3-3: Simulation of factor of safety of the ambient heat exchanger, done by the SolidWorks .....	177
Figure A3-4: Detailed drawing of the proposed gas-to-gas cross flow hot heat exchanger .....	178
Figure A3-5: Detailed drawing of the hot heat exchanger .....	179
Figure A3-6: Simulation of stress of the hot heat exchanger at 400°C, done by the SolidWorks.....	180
Figure A3-7: Simulation of factor of safety of the hot heat exchanger at 400°C, done by the SolidWorks .....	180
Figure A3-8: Detailed drawing of the secondary ambient heat exchanger.....	181
Figure A3-9: Simulation of stress of the secondary ambient heat exchanger, done by the SolidWorks .....	182
Figure A3-10: Simulation of factor of safety of the secondary ambient heat exchanger, done by the SolidWorks .....	182
Figure A4-1: The performance of the engine versus mean pressure for various load resistances at 1600 W heating power .....	184
Figure A4-2: Total efficiency for different load resistances at 28 bar mean pressure and 1600 W heating power .....	184
Figure A4-3: Fraction to Carnot efficiency versus mean pressure for various load resistances at 1600 W heating power .....	184

Figure A4-4: The relation between mean pressure and acoustic efficiency for various load resistances at 1600 W heating power .....	185
Figure A4-5: The effect of mean pressure on the linear alternator efficiency for various load resistance at 1600 W heating power .....	185
Figure A4-6: The effect of mean pressure on the piston displacement for various load resistances at 1600 W heating power .....	185
Figure A4-7: Measured drive ratio versus mean pressure for various load resistances at 1600 W heating power .....	186
Figure A4-8: Core temperature distribution of different mean pressure at 1600 W heating power and 30.8 $\Omega$ load resistance.....	186
Figure A4-9: The effect of mean pressure on the regenerator temperature difference for various load resistances at 1600 W heating power .....	186
Figure A4-10: The performance of the engine versus mean pressure for various load resistances at 1400 W heating power .....	187
Figure A4-11: Total efficiency for different load resistances at 28 bar mean pressure and 1400 W heating power .....	187
Figure A4-12: Fraction to Carnot efficiency versus mean pressure for various load resistances at 1400 W heating power .....	187
Figure A4-13: The relation between mean pressure and acoustic efficiency for various load resistances at 1400 W heating power .....	188
Figure A4-14: The effect of mean pressure on the piston displacement for various load resistances at 1400 W heating power .....	188
Figure A4-15: Measured drive ratio versus mean pressure for various load resistances at 1400 W heating power .....	188
Figure A4-16: The effect of mean pressure on the linear alternator efficiency for various load resistance at 1400 W heating power .....	189
Figure A4-17: Core temperature distribution of different mean pressure at 1400 W heating power and 30.8 $\Omega$ load resistances .....	189
Figure A4-18: The effect of mean pressure on the regenerator temperature difference for various load resistance at 1400 W heating power .....	189
Figure A4-19: The performance of the engine as a function of heating power for various load resistances at 26 bar mean pressure .....	190
Figure A4-20: Total efficiency of different heating power for various load resistances at 26 bar mean pressure .....	190
Figure A4-21: The relation between heating power and acoustic efficiency for various load resistances at 26 bar mean pressure.....	190
Figure A4-22: Fraction to Carnot efficiency versus heating powers for various load resistances at 26 bar mean pressure .....	191
Figure A4-23: The effect of heating power on the alternator piston displacement for various load resistances at 26 bar mean pressure .....	191

Figure A4-24: Measured drive ratio versus heating power for various load resistances at 26 bar mean pressure .....	191
Figure A4-25: The effect of heating power on the alternator efficiency for various load resistances at 26 bar mean pressure.....	192
Figure A4-26: The effect of heating power on the temperature difference across the regenerator for various load resistances at 26 bar mean pressure .....	192
Figure A4-27: Core temperature distribution of different heating powers at 26 bar mean pressure.....	192
Figure A4-28: The performance of the engine as a function of heating power for various load resistances at 24 bar mean pressure .....	193
Figure A4-29: Total efficiency of different heating power for various load resistances at 24 bar mean pressure .....	193
Figure A4-30: The relation between heating power and acoustic efficiency for various load resistances at 24 bar mean pressure.....	193
Figure A4-31: Fraction to Carnot efficiency versus heating powers for various load resistances at 24 bar mean pressure .....	194
Figure A4-32: The effect of heating power on the alternator piston displacement for various load resistances at 24 bar mean pressure.....	194
Figure A4-33: Measured drive ratio versus heating power for various load resistances at 24 bar mean pressure .....	194
Figure A4-34: The effect of heating power on the alternator efficiency for various load resistances at 24 bar mean pressure.....	195
Figure A4-35: The effect of heating power on the temperature difference across the regenerator for various load resistances at 24 bar mean pressure .....	195
Figure A4-36: Core temperature distribution of different heating powers at 24 bar mean pressure.....	195
Figure A4-37: The performance of the engine as a function of heating power for various load resistances at 22 bar mean pressure .....	196
Figure A4-38 Total efficiency of different heating power for various load resistances at 22 bar mean pressure .....	196
Figure A4-39: The relation between heating power and acoustic efficiency for various load resistances at 22 bar mean pressure.....	196
Figure A4-40: Fraction to Carnot efficiency versus heating powers for various load resistances at 22 bar mean pressure .....	197
Figure A4-41: The effect of heating power on the alternator piston displacement for various load resistances at 22 bar mean pressure.....	197
Figure A4-42: Measured drive ratio versus heating power for various load resistances at 22 bar mean pressure .....	197

Figure A4-43: The effect of heating power on the alternator efficiency for various load resistances at 22 bar mean pressure.....	198
Figure A4-44: The effect of heating power on the temperature difference across the regenerator for various load resistances at 22 bar mean pressure .....	198
Figure A4-45: Core temperature distribution of different heating powers at 22 bar mean pressure.....	198
Figure A4-46: The performance of the engine as a function of heating power for various load resistances at 20 bar mean pressure .....	199
Figure A4-47: Total efficiency of different heating power for various load resistances at 20 bar mean pressure .....	199
Figure A4-48: The relation between heating power and acoustic efficiency for various load resistances at 20 bar mean pressure.....	199
Figure A4-49: Fraction to Carnot efficiency versus heating powers for various load resistances at 20 bar mean pressure .....	200
Figure A4-50: The effect of heating power on the alternator piston displacement for various load resistances at 20 bar mean pressure.....	200
Figure A4-51: Measured drive ratio versus heating power for various load resistances at 20 bar mean pressure .....	200
Figure A4-52: The effect of heating power on the alternator efficiency for various load resistances at 20 bar mean pressure.....	201
Figure A4-53: Core temperature distribution of different heating powers at 20 bar mean pressure.....	201
Figure A4-54: The effect of heating power on the temperature difference across the regenerator for various load resistances at 20 bar mean pressure .....	201
Figure A4-55: The performance of the engine as a function of heating power for various load resistances at 18 bar mean pressure .....	202
Figure A4-56: Total efficiency of different heating power for various load resistances at 18 bar mean pressure .....	202
Figure A4-57: The relation between heating power and acoustic efficiency for various load resistances at 18 bar mean pressure.....	202
Figure A4-58: Fraction to Carnot efficiency versus heating powers for various load resistances at 18 bar mean pressure .....	203
Figure A4-59: The effect of heating power on the alternator piston displacement for various load resistances at 18 bar mean pressure.....	203
Figure A4-60: Measured drive ratio versus heating power for various load resistances at 18 bar mean pressure .....	203
Figure A4-61: The effect of heating power on the alternator efficiency for various load resistances at 18 bar pressure .....	204

Figure A4-62: Core temperature distribution of different heating powers at 18 bar mean pressure.....	204
Figure A4-63: The effect of heating power on the temperature difference across the regenerator for various load resistances at 18 bar mean pressure .....	204
Figure A4-64: The performance of the engine as a function of heating power for various load resistances at 16 bar mean pressure .....	205
Figure A4-65: Total efficiency of different heating power for various load resistances at 16 bar mean pressure .....	205
Figure A4-66: The relation between heating power and acoustic efficiency for various load resistances at 16 bar mean pressure.....	205
Figure A4-67: Fraction to Carnot efficiency versus heating powers for various load resistances at 16 bar mean pressure .....	206
Figure A4-68: The effect of heating power on the alternator piston displacement for various load resistances at 16 bar mean pressure.....	206
Figure A4-69: Measured drive ratio versus heating power for various load resistances at 16 bar mean pressure .....	206
Figure A4-70: The effect of heating power on the alternator efficiency for various load resistances at 16 bar mean pressure.....	207
Figure A4-71: Core temperature distribution of different heating powers at 16 bar mean pressure.....	207
Figure A4-72: The effect of heating power on the temperature difference across the regenerator for various load resistances at 16 bar mean pressure .....	207
Figure A4-73: The performance of the engine as a function of heating power for various load resistances at 14 bar mean pressure .....	208
Figure A4-74: Total efficiency of different heating power for various load resistances at 14 bar mean pressure .....	208
Figure A4-75: The relation between heating power and acoustic efficiency for various load resistances at 14 bar mean pressure.....	208
Figure A4-76: Fraction to Carnot efficiency versus heating powers for various load resistances at 14 bar mean pressure .....	209
Figure A4-77: The effect of heating power on the alternator piston displacement for various load resistances at 14 bar mean pressure.....	209
Figure A4-78: Measured drive ratio versus heating power for various load resistances at 14 bar mean pressure .....	209
Figure A4-79: The effect of heating power on the alternator efficiency for various load resistances at 14 bar mean pressure.....	210
Figure A4-80: Core temperature distribution of different heating powers at 14 bar mean pressure.....	210

Figure A4-81: The effect of heating power on the temperature difference across the regenerator for various load resistances at 14 bar mean pressure .....	210
Figure A4-82: Measured drive ratio versus heating power for various load resistances at 28 bar mean pressure .....	211
Figure A5-1: Measured drive ratio versus heating power for various load resistance at 28 bar mean pressure with insulating gasket.....	213
Figure A5-2: The effect of mean pressure on the piston displacement with insulating gasket installed for various load resistance at 28 bar mean pressure .....	213
Figure A5-3: Performance of the engine with insulating gasket at different heating power for various load resistance at 24 bar mean pressure.....	213
Figure A5-4: Thermal-to-electric efficiency at different heating power for various load resistance for engine with insulating gasket at 24 bar.....	214
Figure A5-5: Fraction to Carnot efficiency versus heating power for engine with insulating gasket for various load resistance at 24 bar .....	214
Figure A5-6: Acoustic efficiency versus heating power for engine with insulating gasket for various load resistance at 24 bar .....	214
Figure A5-7: Alternator efficiency of the engine with insulating gasket at different heating power for various load resistance at 24 bar mean pressure .....	215
Figure A5-8: Drive ratio at different heating power for various load resistance with the insulating gasket at 24 bar mean pressure.....	215
Figure A5-9: The effect of heating power on the piston displacement with insulating gasket installed for various load resistance at 24 bar mean pressure .....	215
Figure A5-10: The effect of heating power on the temperature difference across the regenerator for engine with insulating gasket for various load resistance at 24 bar mean pressure .....	216
Figure A5-11: Performance of the engine with insulating gasket at different heating power for various load resistance at 20 bar mean pressure.....	216
Figure A5-12: Thermal-to-electric efficiency at different heating power for various load resistance for engine with insulating gasket at 20 bar mean pressure .....	216
Figure A5-13: Fraction to Carnot efficiency versus heating power for engine with insulating gasket for various load resistance at 20 bar mean pressure ..	217
Figure A5-14: Fraction to Carnot efficiency versus heating power for engine with insulating gasket for various load resistance at 20 bar mean pressure ..	217
Figure A5-15: Alternator efficiency of the engine with insulating gasket at different heating power for various load resistance at 20 bar mean pressure .....	217

Figure A5-16: Drive ratio at different heating power for various load resistance with the insulating gasket at 20 bar mean pressure .....	218
Figure A5-17: The effect of heating power on the piston displacement with insulating gasket installed for various load resistance at 20 bar mean pressure .....	218
Figure A5-18: The effect of mean pressure on the temperature difference across the regenerator for engine with insulating gasket for various load resistance at 20 bar mean pressure .....	218
Figure A5-19: Performance of the engine with insulating gasket at different mean pressure for various load resistance at 1800 W heating power .....	219
Figure A5-20: Fraction to Carnot efficiency versus mean pressure for engine with insulating gasket for various load resistance at 1800 W heating power.....	219
Figure A5-21: Acoustic efficiency versus mean pressure for engine with insulating gasket for various load resistance at 1800 W heating power .....	219
Figure A5-22: Alternator efficiency of the engine with insulating gasket at different mean pressure for various load resistance at 1800 W heating power.....	220
Figure A5-23: Drive ratio at different mean pressure for various load resistance with the insulating gasket at 1800 W heating power .....	220
Figure A5-24: The effect of mean pressure on the piston displacement with insulating gasket installed for various load resistance at 1800 W heating power.....	220
Figure A5-25: The effect of mean pressure on the temperature difference across the regenerator for engine with insulating gasket for various load resistance at 1800 W heating power .....	221
Figure A5-26: Performance of the engine with insulating gasket at different mean pressure for various load resistance at 1600 W heating power .....	221
Figure A5-27: Thermal-to-electric efficiency at different mean pressure for various load resistance for engine with insulating gasket at 1600 W heating power.....	221
Figure A5-28: Fraction to Carnot efficiency versus mean pressure for engine with insulating gasket for various load resistance at 1600 W heating power.....	222
Figure A5-29: Acoustic efficiency versus mean pressure for engine with insulating gasket for various load resistance at 1600 W heating power .....	222
Figure A5-30: Alternator efficiency of the engine with insulating gasket at different mean pressure for various load resistance at 1600 W heating power.....	222
Figure A5-31: The effect of mean pressure on the temperature difference across the regenerator for engine with insulating gasket for various load resistance at 1600 W heating power .....	223

Figure A5-32: Drive ratio at different mean pressure for various load resistance with the insulating gasket at 1600 W heating power .....	223
Figure A5-33: The effect of mean pressure on the piston displacement with insulating gasket installed for various load resistance at 1600 W heating power.....	223
Figure A5-34: Performance of the engine with insulating gasket at different mean pressure for various load resistance at 1400 W heating power .....	224
Figure A5-35: Thermal-to-electric efficiency at different mean pressure for various load resistance for engine with insulating gasket at 1400 W heating power.....	224
Figure A5-36: Fraction to Carnot efficiency versus mean pressure for engine with insulating gasket for various load resistance at 1400 W heating power.....	224
Figure A5-37: Acoustic efficiency versus mean pressure for engine with insulating gasket for various load resistance at 1400 W heating power .....	225
Figure A5-38: Alternator efficiency of the engine with insulating gasket at different mean pressure for various load resistance at 1400 W heating power.....	225
Figure A5-39: The effect of mean pressure on the temperature difference across the regenerator for engine with insulating gasket for various load resistance at 1400 W heating power .....	225
Figure A5-40: Drive ratio at different mean pressure for various load resistance with the insulating gasket at 1400 W heating power .....	226
Figure A5-41: The effect of mean pressure on the piston displacement with insulating gasket installed for various load resistance at 1400 W heating power.....	226
Figure A5-42: The effect of extra heating power on the piston displacement with insulating gasket installed for various load resistance at 28 bar mean pressure.....	226
Figure A5-43: The effect of extra heating power on the temperature difference across the regenerator for engine with insulating gasket for various load resistance at 28 bar mean pressure .....	227
Figure A8-1: The first part of the acoustic section, showing the reducer and tee branch.....	236
Figure A8-2: the last part of the acoustic section, showing the reducers and 1 inch diameter tube .....	237

## List of symbols

$A$	Cross sectional area, $m^2$
$a$	Speed of sound, $m/s$
$c_p$	Specific heat capacity, $J/kg \cdot K$
$COP$	Coefficient of performance
$d$	Diameter, $m$
$E$	Acoustic power, $W$
$f$	Frequency, $Hz$
$G$	dimensionless function
$H$	Total power flux, $W$
$i$	$\sqrt{-1}$
$k$	Thermal conductivity, $W/m \cdot K$
$p$	Pressure, $Pa$
$Q$	Heat, $J$
$\dot{Q}$	Heat transfer rate, $W$
$R$	Gas constant, $J/kg \cdot K$
$r$	Radius, $m$
$r_h$	Hydraulic radius, $m$
$s$	Entropy per unit mass, $J/kg \cdot K$
$T$	Temperature, $K, ^\circ C$
$t$	Time, $s$
$U$	Volumetric flow rate, $m^3/s$
$v$	Velocity in x direction, $m/s$
$V$	Volume, $m^3$
$Im$	Imaginary part of
$Re$	Real part of

### Greek Letters

$\lambda$	Wavelength, $m$
$\delta$	Penetration depth, $m$
$\eta$	Efficiency
$\mu$	Dynamic viscosity, $kg/m \cdot s$
$\nu$	Kinematic viscosity, $m^2/s$
$\xi$	Displacement of gas, $m$
$\pi$	3.14159
$\rho$	Density, $kg/m^3$
$\varphi$	Volumetric porosity
$\omega$	Angular frequency, $s^{-1}$
$\sigma$	Prandtl number

$\gamma$	specific heat ratio
$\beta$	thermal expansion coefficient
$\nabla$	Nabla Operator
$\Phi_{pU}$	phase angle between the volume flow rate phase and the pressure phase

#### Subscript

$A$	Ambient
$c$	cooling
$H$	Hot
$k$	thermal
$v$	viscous
$m$	mean
$o$	ambient
$O$	mean
$l$	amplitude
$\tau$	transverse
$s$	gas

#### Abbreviations

AHX	Ambient heat exchanger
DeltaEC	Design Environment for Low-amplitude Thermoacoustic Energy Conversion
HHX	Hot heat exchanger
LDV	Laser Doppler Velocimetry
BV	Ball Valve
2 <sup>nd</sup> AHH	Secondary ambient heat exchanger
TBT	Thermal buffer tube
Reg	Regenerator
TA	Thermoacoustic
LA	Linear alternator

# Chapter 1

## Introduction

### 1.1 Introduction to Thermoacoustics

Day by day, the demand for energy rises all over the world. In recent years a lot of environmental impacts have been discovered and proven as being caused by power generation technologies. These impacts range from local environmental impacts to changes in the whole Earth's climate. This creates a thoughtful approach towards clean and environmentally friendly technologies. Thermoacoustic power generation technology could be considered as one such technology. Sound waves in fluids are normally regarded as coupled oscillations of pressure and velocity; however these are also associated with temperature oscillations. These temperature changes are too small to be noticed in the typical sound propagation processes in air at atmospheric pressure. However, in highly pressurised gases (e.g. at pressures of the order of 30-60 bar) and at high acoustic intensity the temperature changes become significant. The intensity is typically represented by a "drive ratio", a ratio of oscillation amplitude to mean pressure. It is not unusual for thermoacoustic technologies to use drive ratios in the range of 10%.

The above temperature effects can be utilised for energy conversion processes when the acoustic wave propagates next to the solid body. Using a sound source, a temperature gradient can be built up in the solid. Imposing a temperature gradient on the solid may lead to the generation of acoustic power. These processes form the backbone of thermoacoustic technologies (Bao *et al.*, 2006). Thus, thermoacoustics is the interaction between thermodynamics and acoustics in the fluid medium inside a special solid configuration within acoustic resonance conditions. Thermoacoustic technologies have two main applications: engines and refrigerators. Engines, or prime movers, convert thermal energy to sound, and refrigerators or heat pumps convert sound to thermal energy. The sound oscillations take place in the gases trapped inside the thermoacoustic device. Thermoacoustic technology can be recognized as clean and environmental friendly because it can use noble/inert gases (e.g. helium, argon, nitrogen, etc.) as thermodynamic media. Their loss from the system does not lead to

environmental releases of toxic, ozone depleting or environmentally harmful substances. Studies conducted in this field also demonstrated that this technology has other advantages as the devices could be built with no moving parts, using gas as the working fluid, and hence no maintenance is required. The simplicity of configuration with no need for sliding parts potentially makes the construction costs relatively low.

## 1.2 Motivation for the Study

Internal combustion engines are heat engines that combust fuel with an oxidizer inside the engine. The combustion process will cause an increase in gas temperature, make it expand and produce direct forces on the pistons. Their movement in the engine is converted into useful work. The thermal energy released by burning the fuel will leave the engine as thermal energy rejected by the cooling water, exhaust gases, miscellaneous losses or as brake power. Taymaz (2006) reported results for the heat balance of a standard four stroke diesel engine with a capacity of 6.0 Liter. The heat rejected to the exhaust system ranged from 24% to 29% of the total energy released from the fuel depending on the engine load (shown in Figure 1.1).

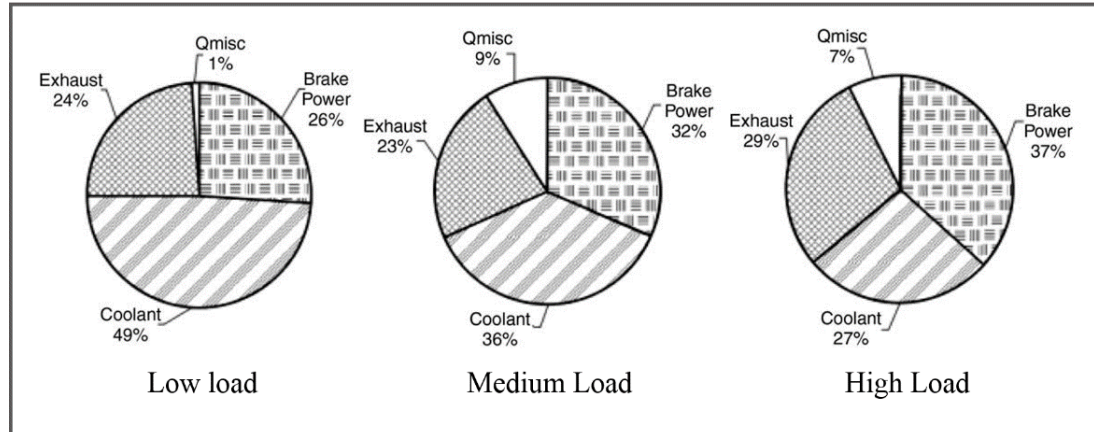


**Figure 1-1** Energy balance in different loads (Taymaz, 2006)

The availability of this large amount of waste energy gives the potential to harvest waste heat and convert it to useful work. Johnson (2002) outlined the technologies to generate cooling power from waste heat from exhaust gases. Thermoacoustic technology has been listed as one of the four vital technologies besides metal hydride cooling, absorption heat pumps and zeolite heat pumps. Johnson presented the advantages of using thermoacoustic technology in vehicle cooling as the system is elegant, reliable, low cost, environmentally safe and has no moving parts. The

disadvantages were low efficiency and power density in comparison with the vapour compression refrigeration, typically large size of the system and sensitivity to shocks and vibration. Later on, Jadhao and Thombare (2013) highlighted thermoacoustic technology as a direct electricity generator in their review of internal combustion engine exhaust gas heat recovery.

In this research, a thermoacoustic engine that is able to recover part of the exhaust gases waste heat and use it to generate electricity will be modelled, designed, constructed and tested. The conceptual configuration of the engine is shown in Figure 1.2. The engine uses the exhaust gases as the heat source ( $\dot{Q}_H$ ) and an ambient cooling system as heat sink ( $\dot{Q}_A$ ) to maintain the temperature gradient across the porous medium and hence generate acoustic power ( $\dot{E}$ ). The linear alternator converts some of the acoustic power to electricity and the rest will be delivered back to the engine by a feedback loop.

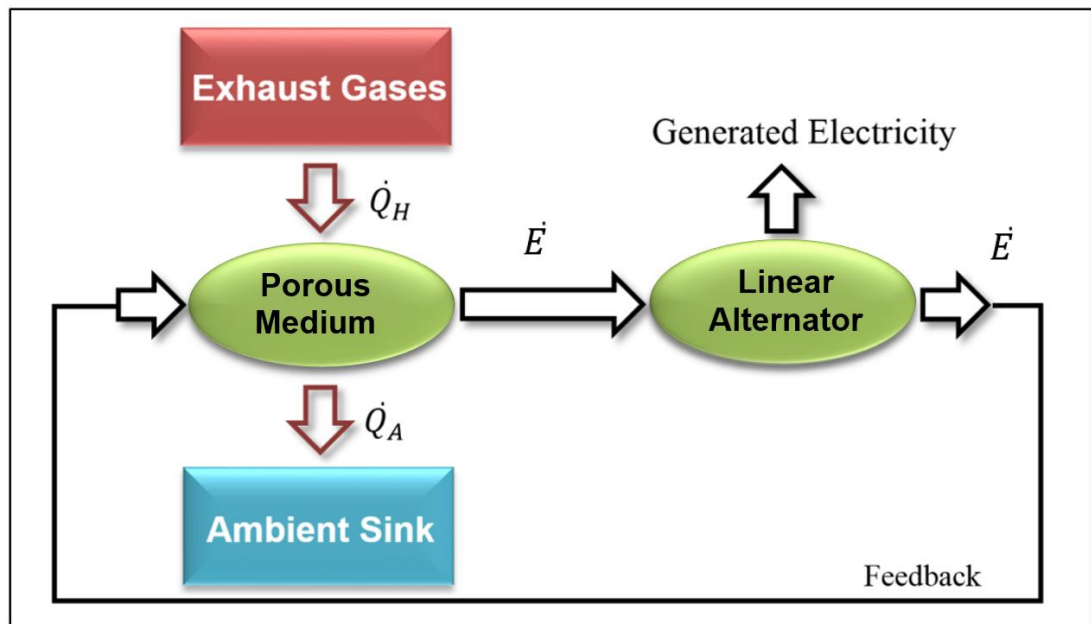


**Figure 1-2:** Function diagram of the proposed thermoacoustic engine.

### 1.3 Aim and Objective of the Study

The previously mentioned advantages of thermoacoustic engines, and their potential use to recover the waste heat from exhaust gases, have encouraged research for a conceptual design. The main aim of this study is to model, design, build and test a thermoacoustic engine generating electricity by running a push-pull linear alternator.

Apart from that, it is aimed at comparing the predicted and experimental results, understanding the thermodynamic and acoustic networks to give development recommendations and publish the work afterwards.

In order to achieve these aims, the current work addressed the following specific objectives:

- 1) To model a two-stage thermoacoustic engine generating electricity by running a push-pull linear alternator using exhaust gases as the heat source. The DeltaEC (Design Environment for Low-amplitude ThermoAcoustic Energy Conversion) is the code to predict the performance of the engine. From an efficiency point of view, the engine will be designed to operate with helium as the working gas at a mean pressure of 28 bar.
- 2) To design and construct the engine at the modelled dimensions from selected materials capable of holding a high mean pressure. The design should supply a heat source and heat sink to maintain a temperature gradient across the regenerator.
- 3) To test the engine and validate the predicted data.
- 4) To investigate the effect of mean pressure, resistive load and heat input on the performance of the engine and alternator system.
- 5) To optimize the design based on the experimental results.
- 6) To investigate theoretically the development opportunity from two-stage to four-stage engine.

## **1.4 Thesis Structure**

The overall structure of the thesis takes the form of eight chapters, including this introductory chapter.

**Chapter 2** starts with a brief review of the early history of thermoacoustics. The principles of the thermoacoustic effect and thermoacoustic technology classification are outlined. Explanation focuses on the differences between the standing wave and

travelling wave devices. Then, a review of the linear thermoacoustic theory and the acoustic streaming that can occur in thermoacoustic devices is given. A literature review of the relevant works related to the design and experimental evaluation of thermoacoustic traveling wave engine devices is presented at the end of this chapter.

**Chapter 3** presents the DeltaEC simulation of the two-stage thermoacoustic electricity generator with push-pull linear alternator. The coupling effect on the performance of the linear alternator with both push-pull and conventional compliance housing is studied and discussed first. Parts selection and optimization graphs are presented for most parts of the engine. The last section of this chapter is the simulation results and discussion. The work presented in this Chapter covers the objective (1) of this study, presented in section 1.3.

**Chapter 4** describes the design and construction of the two-stage thermoacoustic engine. Part by part design and material selection for both thermodynamic and acoustic section are detailed. Measurement techniques used in this research are located in this chapter, showing the sensors and locations. The work presented in this Chapter covers the objective (2) of this study.

**Chapter 5** presents the experimental results and discussion for the prototype engine. The experiments were carried out in order to evaluate the performance and measure the acoustic power generated from the engine. In practice, the engine failed to self-start. An excitation to run the engine method is explained in this chapter. Performance obstacles are listed in this chapter. Comparisons are made between the simulation and experimental results whenever convenient. The effect of the mean pressure, heating power and load resistance on the performance of the engine is presented and discussed. The work presented in this Chapter covers the objectives (3) and (4) of this study.

**Chapter 6** illustrates the experimental optimization of the engine. It starts with installing an insulating gasket to reduce the heat leak. Based on the trend of the results, the effect of increase the heating power was experimentally investigated. The regenerator thickness as a solution to self-start issue is proposed and its effect on the engine performance discussed. The chapter ends in presenting the experimental

results of placing an elastic membrane to suppress streaming along the engine. The work presented in this Chapter covers the objective (5) of this study.

**Chapter 7** presents a further design work, based on DeltaEC simulations aimed at developing the two-stage engine to four-stage engine. The design and optimisation lead to the design of a compact device generating more electricity. The work presented in this chapter fulfils objective (6) of this study.

**Chapter 8** presents the conclusions drawn from this work and recommendations for future work. In particular, it focuses on the summary of achievements of this project versus the set objectives as presented in Section 1.3.

## Chapter 2

### Background and Literature Survey

#### 2.1 Thermoacoustics

The common definition of thermoacoustics is the area of acoustics dealing with the interactions between heat and sound, and importantly the interaction between temperature, density and pressure variations of an acoustic wave. A sound wave which propagates in a gas medium is considered as consisting of coupled pressure and displacement/motion oscillations, however temperature oscillations are always present as well. When a sound wave oscillates in a small channel, heat flows to or from the channel walls.

The study of thermoacoustics has a rich and interesting history. In 1777, Byron Higgins presented acoustic oscillations in a large pipe excited by a hydrogen flame inside it, known as a singing flame (Putnam and Dennis, 1956). Figure 2.1a shows a simple illustration of the experiment. Placing a flame in a certain location inside a glass tube produces acoustic oscillations. Higgins noticed that the acoustic oscillations generated depended on the position of the flame and the dimensions of the tube. He tried tubes of different diameters, small diameter tubes tended to extinguish the flame. As he tried bigger and bigger tubes, he witnessed several tones according to the width, length and thickness of the tube. In relatively large diameter tubes, the sound became weaker and disappeared.

The Rijke tube, named after experiments presented by Rijke in 1859, as reported by Feldman (1968a), is an experimental set-up of a tube and heater producing sound out of heat. He used a tube which had gauze placed in the lower half, as shown in Figure 2.1b. As he heated the wire gauze, the tube generated a strong sound. Sound oscillations were stronger when the wire gauze was placed at one fourth of the tube length from the lower end. An explanation of this phenomena was published later by Rayleigh (1877), (1878), where he stated, "If heat be given to the air at the moment of greatest condensation, or taken from it at the moment of greatest rarefaction, the vibration is encouraged". This statement is well known as the Rayleigh Criterion.

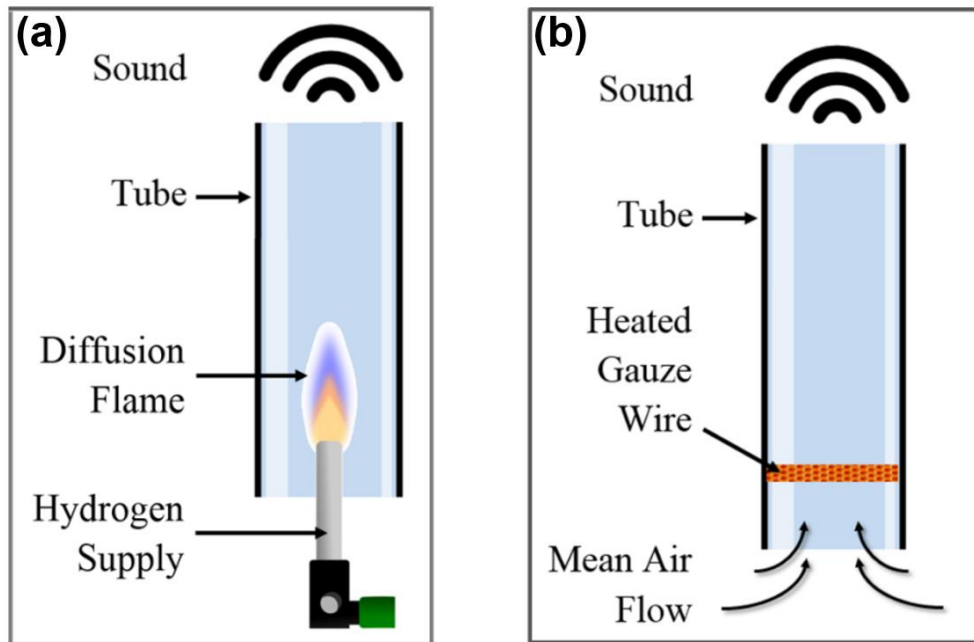


**Figure 2-1:** a) The singing Flame apparatus (Putnam and Dennis, 1956), b) Rijke tube (Feldman, 1968a).

The first conceptual thermoacoustic engine has been proposed by Sondhauss in 1850 as reported by Feldman (1968b). This research presented the thermoacoustic oscillations in a modern way. The heat-generated sound was studied experimentally using a glass-blower by blowing a hot bulb connected to a cold tube. Figure 2.2 shows the experimental set-up which Sondhauss used. He presented that by supplying a steady heat to the bulb, the air in the tube oscillates producing sound. He noticed that the sound intensity depended on the tube and bulb geometries and on the flame temperature. Lord Rayleigh gave an extensive explanation of the Sondhauss tube in 1896. Carter et al. (1962), improved the performance of the Sondhauss tube by applying parallel plates in the tube. This was considered to be a step towards a certain performance improvement by increasing the work out by increasing the heat input. These plates are positioned right next to the heat source on the side closest to the open end, and serve three specific purposes. First, they provide a small contribution to the system by acting as a porous medium. Also, the plates operate as an insulator between the hot and cold regions of the tube. This creates a steeper temperature gradient, thereby improving the system's efficiency. Lastly, the plates act as an acoustic impedance, creating a phase shift (importance will be explained in chapter three and chapter four).

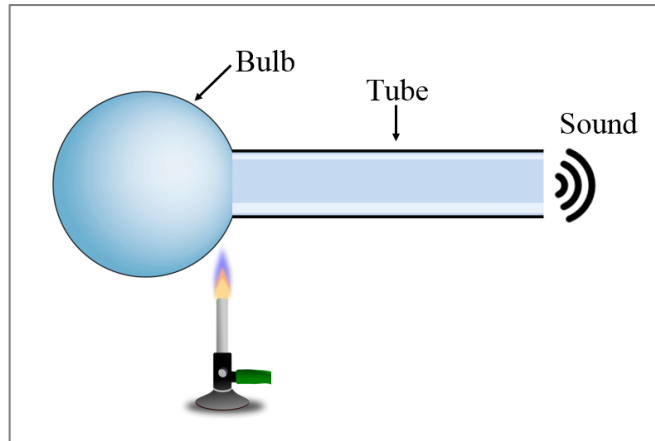


**Figure 2-2:** Sondhauss tube (Feldman, 1968b).

Many experiments and effort were devoted over the intervening decades towards the understanding of thermoacoustics. However, the main breakthrough in thermoacoustics has been made by the pioneering work of Rott in 1969. He explained the thermoacoustic oscillations and developed a successful linear theory of thermoacoustics, this work was published in several papers (1969, 1973, 1975, 1976 and 1985). His expressions of the linear theory linked the motion and pressure amplitude and acoustic oscillation with the temperature gradient. Nowadays, the thermoacoustics devices are designed and investigated based on this linear theory.

## 2.2 Key Parameters

It is important to define some of the length scale parameters before going into more detailed thermoacoustics. The explanation of these three parameters will help in understanding the operation of thermoacoustic devices. The three parameters are: wavelength, thermal penetration depth and viscous penetration depth.

The wavelength,  $\lambda$ , of a wave is the distance from any point on one wave to the same point on the next wave along. The relationship between the wavelength and frequency in the wave propagation direction is:

$$\lambda = \frac{a}{f} \quad \dots 2.1$$

where  $a$  is the speed of sound and  $f$  is the oscillating frequency. The wavelength is the main determinant of the thermoacoustic device length. At resonance behaviour the length of the thermoacoustic device is one half or quarter wavelength. The speed of sound for ideal gases can be expressed as follows:

$$a = \sqrt{\frac{\gamma p_m}{\rho}} = \sqrt{\gamma RT} \quad \dots 2.2$$

where  $\gamma$  is the specific heat ratio of the working gas,  $p_m$  is mean pressure,  $\rho$  is density,  $R$  is the gas constant and  $T$  is temperature.

The other parameters namely: thermal and viscous penetration depth, are in a direction perpendicular to the wavelength. The thermal penetration depth,  $\delta_K$ , is roughly the distance that heat can diffuse through the medium during the time interval related to the period,  $Time = 1 / frequency$ , of the acoustic oscillation. The thermal penetration depth is given by:

$$\delta_K = \sqrt{\frac{2k}{\omega \rho_m c_p}} = \sqrt{\frac{2\kappa}{\omega}} \quad \dots 2.3$$

where  $k$  is the thermal conductivity of gas,  $\omega$  is the angular frequency,  $\rho_m$  is the mean of gas density,  $c_p$  is the isobaric heat capacity of the working gas and  $\kappa$  is the thermal diffusivity of the gas. As the thermoacoustic engine is a heat engine, this parameter will determine the heat transfer efficiency between the gas and solid.

The viscous penetration depth,  $\delta_v$ , is approximately the distance over which viscous shear forces diffuse in a time ( $1 / frequency$ ). The viscous penetration depth is given by:

$$\delta_v = \sqrt{\frac{2\mu}{\omega \rho_m}} = \sqrt{\frac{2\nu}{\omega}} \quad \dots 2.4$$

where  $\mu$  and  $\nu$  are the dynamic and kinematic viscosities, respectively. Within a boundary layer of  $\delta_v$  thickness, the dissipation of acoustic power by a resistive viscous shear forces occurs.

### 2.3 Thermoacoustic Technology

Thermoacoustic devices are generally considered as acoustic resonators filled with a gas and containing a porous medium (stack or regenerator) with heat source and heat sink (i.e. heat exchangers) adjacent to it (Swift, 2002). The gas inside the resonance tube (within the porous medium limits) will undergo a thermodynamic cycle

somewhat similar to the Stirling cycle (Swift, 2002), the cycle will be explained in Section 2.4.1.

There are two main ways to classify thermoacoustic devices: firstly, with respect to their function as engines or refrigerators; secondly, with respect to the properties of the sound wave as standing or travelling wave devices.

The function of the thermoacoustic engine or prime mover is to produce acoustic power out of thermal power while the refrigerator or heat pump is to remove heat at low temperature using acoustic power

In a thermoacoustic engine, the working gas absorbs heat,  $\dot{Q}_H$  from the high temperature side,  $T_H$  of the porous medium and rejects heat  $\dot{Q}_O$ , to the low temperature side  $T_O$  while producing work by the means of acoustic power  $\dot{E}$  as an output. In a refrigerator, working gas removes heat  $\dot{Q}_C$  from the low side at  $T_C$  and supplies a heat quantity  $\dot{Q}_O$  to the surroundings at a high temperature  $T_O$  with the aid of excited sound oscillations,  $\dot{E}$  as input mechanical work (Figure 2.3).

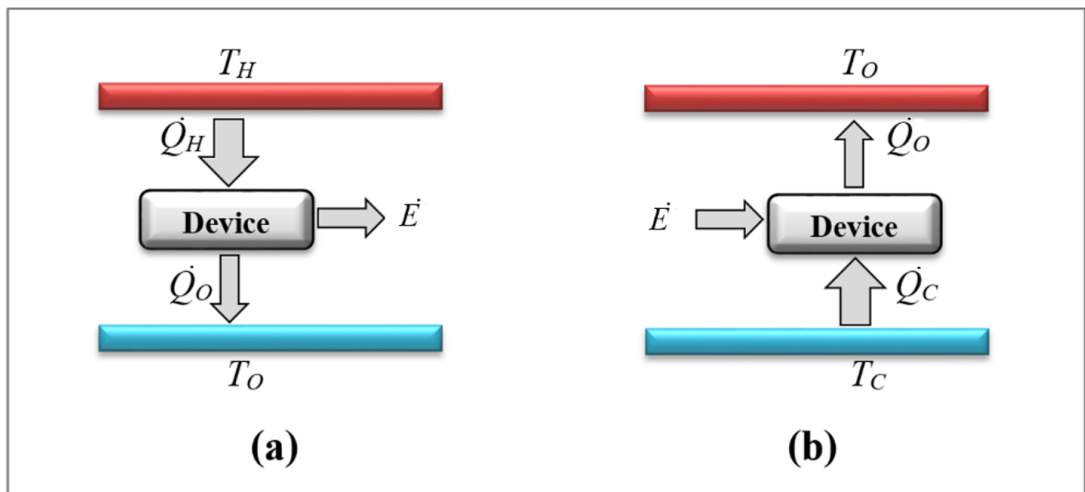


**Figure 2-3:** Work principles of (a) engine and (b) refrigerator.

The laws of thermodynamics introduced the efficiency of the thermoacoustic devices. At steady state, the First Law implies (quantities in equations are not per unit time):

$$Q_H = E + Q_O \quad \dots 2.5$$

for the engine,

and:

$$Q_O = E + Q_H \quad \dots 2.6$$

for the refrigerator.

The Second Law at steady state, which means no change in entropy, the engine equations can be combined to give:

$$\frac{Q_O}{T_O} - \frac{Q_H}{T_H} \geq 0 \quad \dots 2.7$$

and for the refrigerator:

$$\frac{Q_O}{T_O} - \frac{Q_C}{T_C} \geq 0 \quad \dots 2.8$$

Combining equations 2.5 and 2.7 and eliminating  $Q_O$ , produces an expression for the efficiency which is the generated acoustic power  $E$  divided by the heat input  $Q_H$ :

$$\eta = \frac{E}{Q_H} \leq \frac{T_H - T_O}{T_H} \quad \dots 2.9$$

The temperature expression to the right expresses the Carnot efficiency, which limits the actual efficiency of any heat engine. Similarly for the refrigerator, the efficiency is the heat rejected at the cold side divided by the input acoustic power, which could be written by eliminating  $Q_O$  from equations 2.6 and 2.8.

$$\eta = \frac{Q_C}{E} \leq \frac{T_C}{T_O - T_C} \quad \dots 2.10$$

## 2.4 Standing Wave and Travelling Wave Thermoacoustic Engine

Thermoacoustic devices can be categorized depending on whether the sound wave is travelling or standing. The standing wave device and the travelling wave device will be explained in details in Sections 2.4.1 and 2.4.2, for an engine only.

It is essential for the thermoacoustic engine to generate or amplify acoustic power. So the temperature gradient across the porous medium must be higher than the critical temperature gradient. The critical temperature gradient is the achieved by adiabatic

compression and expansion (as will be explained in details in Sections 2.4.1 and 2.4.2).

A standing wave has a unique form with certain points which have no oscillation located at the centre of the points of maximum vibration. It results from a combination of two waves travelling in opposite directions both having the same frequency and amplitude, so it is generated whenever a wave is confined within boundaries. Travelling waves are observed when a wave is not confined to a given space along the wave propagation direction. All the points along the wave propagation direction gradually vibrate from positive maximum amplitude to negative minimum, see Figure 2.4.

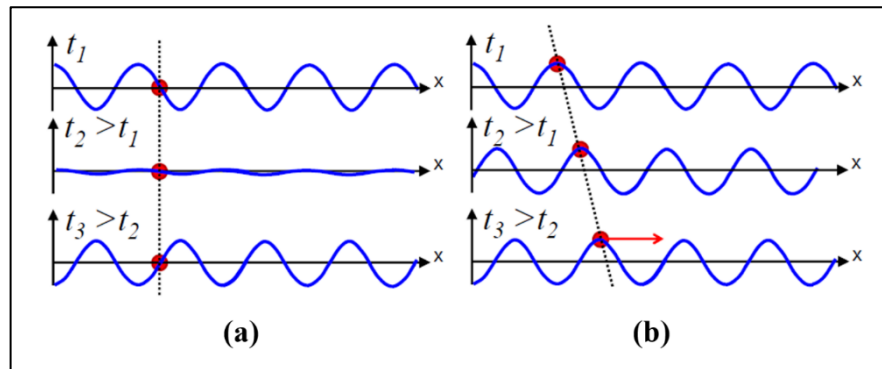


**Figure 2-4:** Wave propagation of (a) standing wave and (b) travelling wave.

### 2.4.1 Principles of a standing-wave thermoacoustic engine

As a thermoacoustic device, the standing wave engine consists of a resonance tube with a length of a quarter, half or a full wavelength of the sound wave travelling and reflecting inside the tube. Both ends of the tube should be closed (one left open in a special case) to allow the wave to reflect and form the standing wave form.

The perfect standing wave has a pressure out of phase with the velocity and in phase with the displacement, as shown in Figure 2.5a. The porous medium used in this kind of engine should be fabricated with small channels having dimensions which will produce imperfect thermal contact between the oscillating gas parcels and the porous medium. The porous medium with such a configuration is usually named a stack. Figure 2.5b shows an example of stack. Heat exchangers add to the sides of the stack to supply and extract heat to and from the stack to maintain a large temperature difference across the stack.

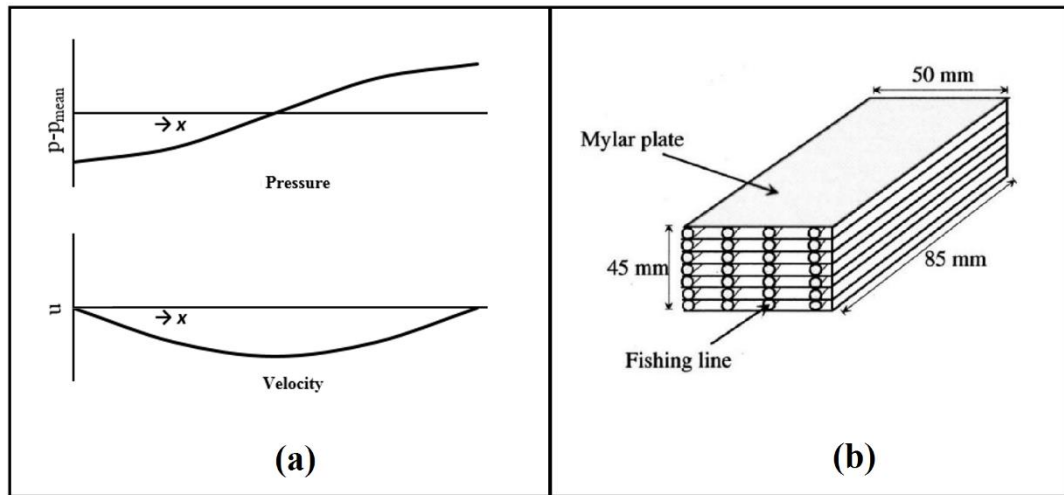


**Figure 2-5:** a) Acoustic pressure and velocity as a function of the position in a resonator having both sides closed, b) example of a stack Bhansali (2009).

Following a gas parcel oscillating between the stack plates the displacement and pressure are in phase. Figure 2.6 shows the four stage working principles of the standing wave engine. To simplify the explanation, the movement at the far end of the oscillation will be neglected. At first, the parcel will move from the hot side towards the cold side (A→B) which has lower local pressure causing the parcel to expand and cool down. When the parcel reaches the right most position (B→C), it will be at the lowest local pressure and the stack wall temperature is lower than that of the parcel. The temperature difference will lead to heat being transferred from the gas parcel to the stack  $Q_C$ . After that, the gas parcel moves to the left to the higher local pressure area (C→D), which causes a compression and heating-up of the gas parcel. Finally, when the gas is in the leftmost position (D→A) which has a wall temperature higher than the parcel; the temperature difference will lead to heat being transferred from the stack walls to the gas parcel  $Q_H$ . Then the cycle will start again from (A→B).

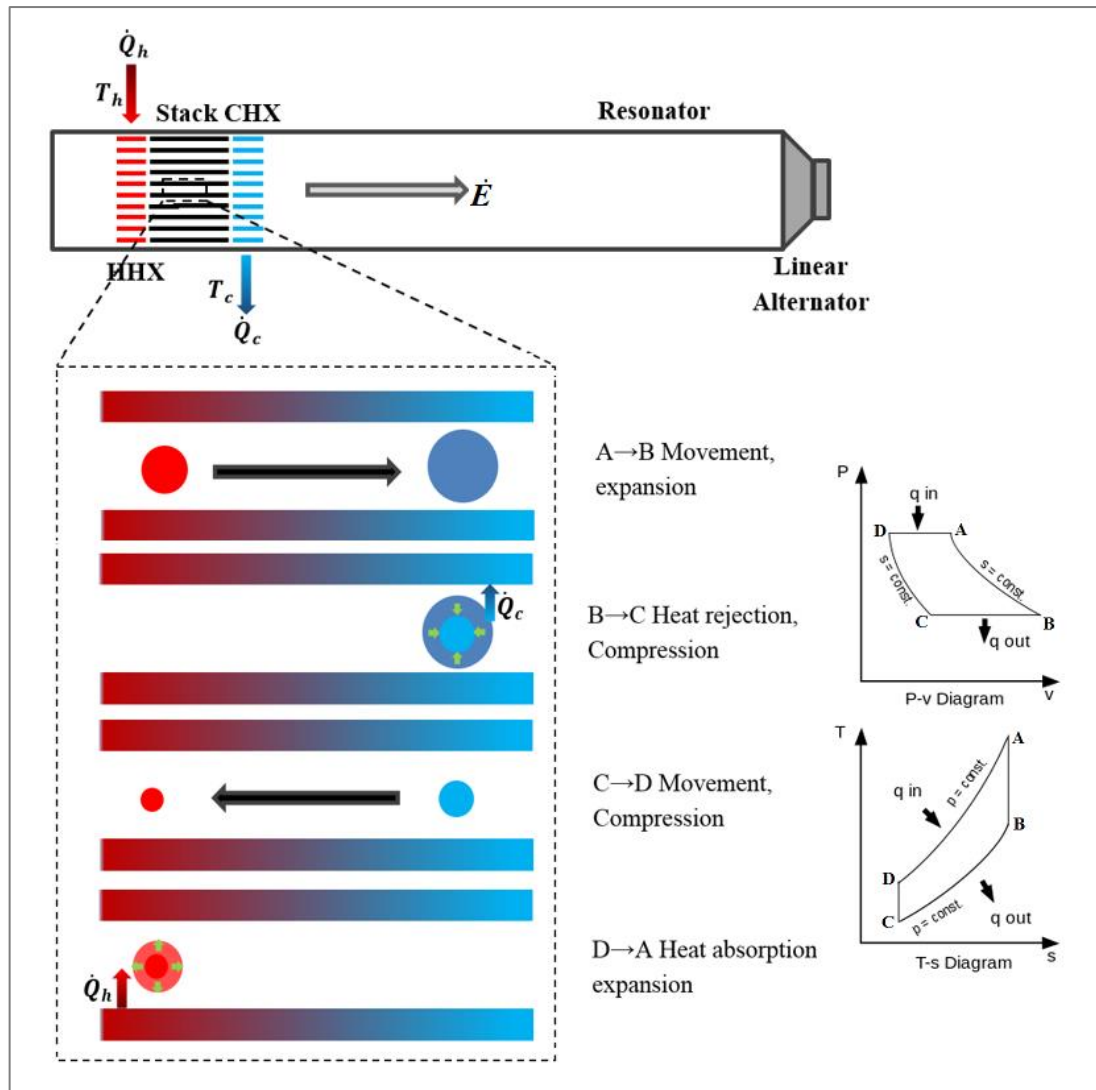


**Figure 2-6:** Simplified thermoacoustic effect in a standing wave thermoacoustic engine showing the schematic diagram and the cyclic thermodynamics of the gas parcel inside the stack.

The temperature location is shown in Figure 2.7a. It summarizes the information of the temperature of the gas parcel and links it to the stack wall temperature. This graph illustrates the importance of weak/imperfect thermal contact between the gas parcel and the stack walls. The main reason is that high thermal contact will lead to high heat transfer and the gas parcel will track the stack wall temperature and this will shift the expansion and contraction time phasing. At such phasing, the relation between the pressure and the volume, shown in Figure 2.7b, will become linear instead of an ellipse which leads to no work gained. On the other hand, if the thermal contact is too weak, very low heat will be transferred between the stack walls and the gas parcel when the parcel reverses direction. The thermal contact between the gas parcel and the stack channel walls must be imperfect. The way to achieve that is to apply a plate

spacing which serves to avoid too weak or too strong a thermal contact. The successful plate spacing is a few  $\delta_k$ .

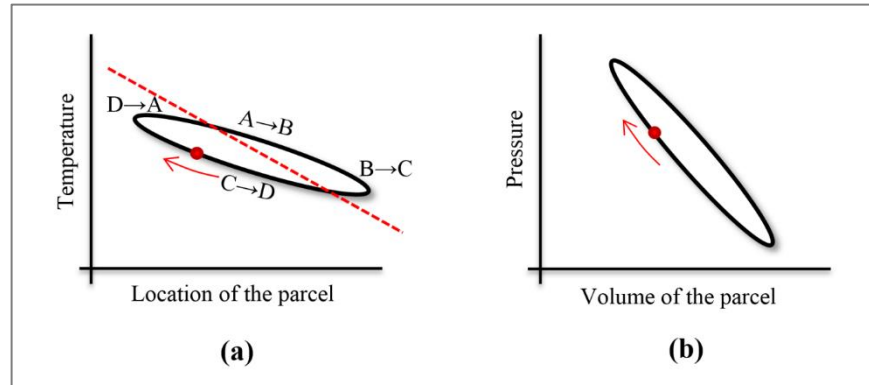


**Figure 2-7:** Standing wave engine processes showing a parcel of gas oscillating inside a stack channel: (a) Temperature-position diagram (b) Pressure-volume diagram (Swift, 2002).

The above issues illustrate the amplification of the sound wave in the standing wave thermoacoustic engine. There will be some gas parcels that are not in perfect contact with the stack walls and are isolated from the heat transfer process, therefore, the gas parcel will not transfer heat instantaneously. The gradual/delayed heat transfer will lead to the oval shaped relation between the pressure and temperature shown in Figure 2.7. In other words, the additional heating of the gas parcel which happens in the process D→A in Figure 2.6 will force the gas parcel to expand and the additional cooling after the expansion stage B→C will force the gas to compress. This will maintain the oscillation as the additional heating and the expansion will send the gas parcel to the cold side and the additional cooling and the compression will send it back to the hot side. The imperfect thermal contact between the gas parcel and the stack walls leads to heat transfer over finite temperature differences and this is considered to be an irreversible process. This irreversible process leads to limiting the conversion efficiency of thermal to acoustic power.

## 2.4.2 Principles of travelling-wave thermoacoustic engine

Unlike standing wave thermoacoustic engines, travelling wave thermoacoustic engines act as an amplifier; this requires that some acoustic power has to be fed to the porous medium to be amplified there by temperature difference.

The main components of the travelling wave engine are the same as those of the standing wave engine except for the resonance tube configuration. The resonance tube of the travelling wave engine should be looped unlike the closed tube of the standing wave engine, to allow the wave to travel through it. The porous medium for this kind of engine has a very high thermal contact with the gas and is called a regenerator. This high thermal contact shifts the phase between the pressure wave and velocity wave so as to be zero producing a pure travelling wave. The high thermal contact will also lead to an identical temperature distribution of the oscillatory gas and regenerator wall temperature as shown in Figure 2.8. This means that the heat transfer between the gas and regenerator walls is a reversible process, and hence it has a higher efficiency than the standing wave engine which has some irreversibility.

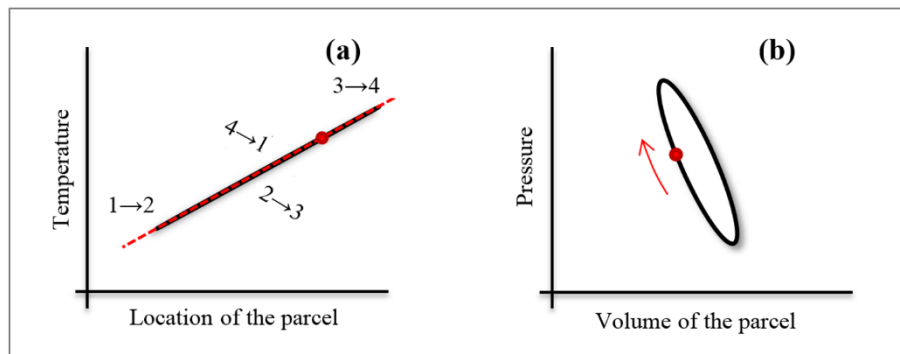


**Figure 2-8:** Travelling wave engine processes showing a parcel of gas oscillating inside a regenerator channel: (a) Temperature-position diagram (b) Pressure-volume diagram (Swift, 2002).

The high thermal contact of the regenerator is maintained by using a high density porous material with high porosity. Swift (2002) has illustrated that the thermal penetration depth  $\delta_K$  and the viscous penetration depth  $\delta_v$  of a gas parcel oscillation within the regenerator should be higher than the hydraulic radius  $r_h$ . The hydraulic radius is the ratio of the cross-sectional area of a regenerator channel to its perimeter and also could be thought of as the ratio of gas volume to the gas-solid contact area. Yu et.al (2005), showed that the ratio of the  $\delta_K / r_h$  can be controlled by the regenerator porosity selection and he showed that travelling wave engines can achieve their best performance when this ratio is within 4-7.

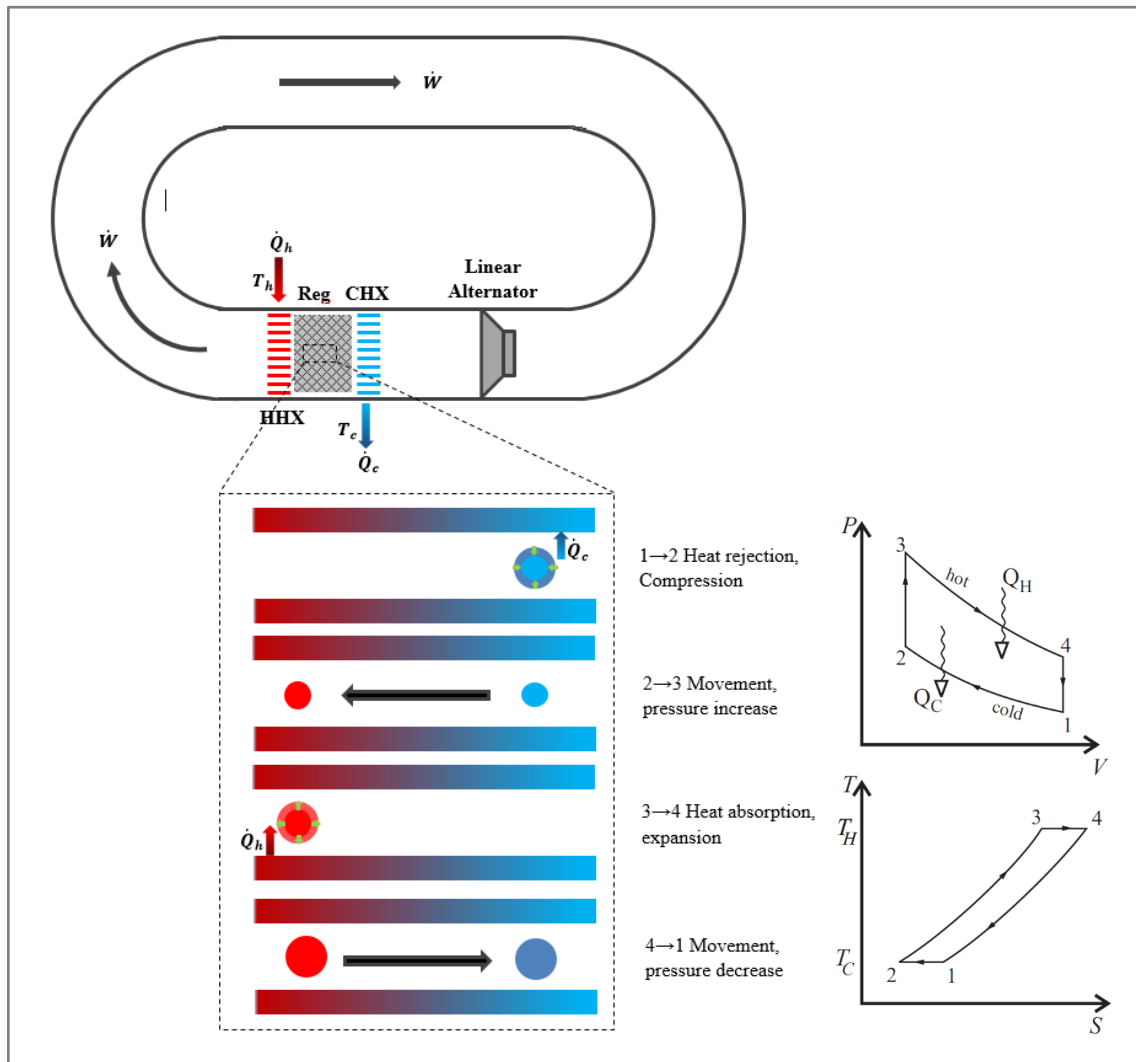


**Figure 2-9:** The simplified thermoacoustic effect in a travelling wave thermoacoustic engine showing the schematic diagram and the cyclic thermodynamics of the gas parcel inside the stack.

Ceperley (1979) was the first to realize that the phasing between the pressure and velocity of the travelling wave is the same as the phasing of the Stirling engine. Since then travelling wave engines have been known as the Stirling thermoacoustic engine. A qualitative understanding of a travelling wave engine can be obtained by following a gas parcel oscillating through the porous medium, as presented previously for the standing wave engine. Figure 2.9 shows the gas parcel oscillating within the regenerator and links it to the Stirling cycle. The cycle started when the gas parcel was compressed at a uniform temperature  $T_C$  (1→2). Then the gas parcel travels towards the higher local pressure from the cold side  $T_C$  to the hot side  $T_H$  at a constant volume absorbing heat  $Q_H$  (2→3). Then the gas parcel expands at a uniform

temperature after (3→4). Finally, the gas parcel is displaced back to the cold side releasing the heat  $Q_C$  at a constant volume (4→1).

## 2.5 Linear Thermoacoustic Theory

The linear thermoacoustic theory was developed by Rott (1969, 1973, 1975, 1976 and 1985). It is valid for both engines and refrigerators, the only difference is the temperature gradient across the porous medium. Arnott *et al.* (1991) reviewed and presented simplified expressions for temperature, density, particle velocity, heat flow and work flow, within the porous medium, heat exchangers and fine tubes having non-uniform cross-sectional geometry. He developed a parameter,  $F$ , which is a function of frequency, pore geometry, and gas properties.

There are some assumptions to be considered in this theory. Firstly, the working gas oscillating inside the porous medium of the thermoacoustic core is considered to be within a single pore or channel. This pore is, by definition, narrow and has infinite length. The gas oscillates longitudinally within this pore which will be considered as the  $x$ -direction. The other directions which are the  $y$  and  $z$  directions follow the Cartesian co-ordination notations. The porous medium channel wall temperature is a function of  $x$  and the channel wall has high thermal capacity to maintain its temperature. Finally, all temperature gradient variables are functions of  $x$  and all the acoustic variables are in harmony with the frequency.

Starting from Arnott *et al.* (1991) expressions of pressure, velocity, temperature, entropy and density:

$$p(x, t) = p_0 + p_1(x)e^{-i\omega t} \quad \dots 2.11$$

$$v(x, y, z, t) = [v_\tau(x, y, z) + v_x(x, y, z)]e^{-i\omega t} \quad \dots 2.12$$

$$T(x, y, z, t) = T_0(x) + T_1(x, y, z)e^{-i\omega t} \quad \dots 2.13$$

$$s(x, y, z, t) = s_0(x) + s_1(x, y, z)e^{-i\omega t} \quad \dots 2.14$$

$$\rho(x, y, z, t) = \rho_0(x) + \rho_1(x, y, z)e^{-i\omega t} \quad \dots 2.15$$

The subscripts  $0$  and  $1$  indicate the mean and amplitude values. The components  $v_\tau$  and  $v_x$  in velocity expression represent the transverse and longitudinal velocities, respectively. As the local temperature is a function of position, the temperature-dependent parameters density, viscosity, thermal conductivity, speed of sound and the coefficient of thermal expansion are functions of position.

Arnott *et al.* (1991) used these expressions to expand and reduce the order of the momentum equation, continuity equation and energy equation. He started from:

$$\rho \left[ \frac{\partial \mathbf{v}}{\partial t} + (\mathbf{v} \cdot \nabla) \mathbf{v} \right] = -\nabla p + \mu \nabla^2 \mathbf{v} \quad \dots 2.16$$

$$\frac{\partial \rho}{\partial t} + \nabla \cdot (\rho \mathbf{v}) = 0 \quad \dots 2.17$$

$$\frac{\partial}{\partial t} \left( \frac{\rho v^2}{2} + \rho \epsilon \right) = -\nabla \cdot \left[ \rho \mathbf{v} \left( \frac{v^2}{2} + h \right) - K \nabla T - \mathbf{v} \cdot \Sigma \right] \quad \dots 2.18$$

And the results showed as:

$$-i\omega \rho_0 v_x = -\frac{dp_1}{dx} + \mu \nabla_\tau^2 v \quad \dots 2.19$$

$$-i\omega \rho_1 + \frac{\partial}{\partial x} (\rho_0 v_x) + \rho_0 \nabla_\tau v_\tau = 0 \quad \dots 2.20$$

$$-i\omega \rho_0 c_p T_1 + \rho_0 c_p v_x \frac{\partial T_0}{\partial x} = -j\omega \beta T_0 \rho_1 + K \nabla_\tau^2 T_1 \quad \dots 2.21$$

where the operators  $\nabla_\tau$  and  $\nabla_\tau^2$  are  $\nabla_\tau = \frac{\partial}{\partial y} \hat{y} + \frac{\partial}{\partial z} \hat{z}$  and  $\nabla_\tau^2 = \frac{\partial^2}{\partial y^2} + \frac{\partial^2}{\partial z^2}$ , and the thermal expansion coefficient is  $\beta = -\frac{1}{\rho_0} \left( \frac{\partial \rho}{\partial T} \right)_p$

To identify the transverse velocity profile in a pore, the x component of the velocity in Equation (2.19) is taken to be:

$$v_x = \frac{1}{i\omega \rho_0} \frac{dp_1}{dx} F(y, z, \lambda_v) \quad \dots 2.22$$

Here  $\lambda_v = 2r_h \sqrt{\frac{\rho_0 \omega}{\mu}}$  and F is a boundary condition which is zero at the walls. At any point far from the wall within a few thermal penetration depths, F must satisfy:

$$F(y, z, \lambda_v) - \left(\frac{2r_h}{i\lambda_v}\right)^2 \nabla_\tau^2 F(y, z, \lambda_v) = 1 \quad \dots 2.23$$

An algebraic rearrangement and thermodynamic relations are applied to Equation (2.21) to present a transverse temperature profile in a pore. Substituting Equation (2.22) into Equation (2.21) and using  $\frac{\beta^2 T_0}{c_p} = \frac{(\gamma-1)}{a^2}$ , where  $\gamma$  is the specific heat ratio and  $a$  is the speed of sound, results in:

$$T_1 + \left(\frac{2r_h}{i\lambda_v}\right)^2 \nabla_\tau^2 T_1 = \frac{(\gamma-1)}{a^2 \beta \rho_0} p_1 - \frac{F(y, z, \lambda_v)}{\omega^2 \rho_0} \frac{dT_0}{dx} \frac{dp_1}{dx} \quad \dots 2.24$$

Assume that the temperature profile  $T_1$  can be written as

$$T_1 = G_a(y, z, \lambda_k) \frac{(\gamma-1)}{a^2 \beta \rho_0} p_1 - G_b(y, z, \lambda_k, \lambda_v) \frac{1}{\omega^2 \rho_0} \frac{dT_0}{dx} \frac{dp_1}{dx} \quad \dots 2.25$$

here  $\lambda_k$  is the thermal disturbance number,  $\lambda_k = 2r_h \sqrt{\frac{\rho_0 \omega c_p}{K}}$

Equation 2.25 can be split into:

$$G_a - \left(\frac{2r_h}{i\lambda_k}\right)^2 \nabla_\tau^2 G_a = 1 \quad \dots 2.26$$

$$G_b - \left(\frac{2r_h}{i\lambda_k}\right)^2 \nabla_\tau^2 G_b = F(y, z, \lambda_v) \quad \dots 2.27$$

The boundary condition of  $T_1 = 0$  implies that  $G_a = 0 = G_b$  on the pore wall. Equation (2.26) could be solved to be:

$$G_a = F(y, z, \lambda_v) \quad \dots 2.28$$

And Equation (2.27) could be solved to be:

$$G_b = \frac{F(y, z, \lambda_k) - \sigma F(y, z, \lambda_v)}{1 - \sigma} \quad \dots 2.29$$

where  $\sigma$  is the Prandtl number of the gas. The temperature profile could be written as:

$$T_1 = \frac{(\gamma-1)}{a^2 \beta \rho_0} F(y, z, \lambda_k) p_1 - \frac{1}{\omega^2 \rho_0} \frac{F(y, z, \lambda_k) - \sigma F(y, z, \lambda_v)}{1 - \sigma} \frac{dT_0}{dx} \frac{dp_1}{dx} \quad \dots 2.30$$

Starting from the time average total energy flow equation:

$$\dot{H}(x) = \dot{Q}(x) + \dot{E}(x) - \dot{Q}_{loss}(x) \quad \dots 2.31$$

All components of this equation are time averaged, where the  $\dot{Q}$  is the heat flow and the  $\dot{E}$  is the acoustic power.

The time averaged heat flow  $\dot{Q}$  could be written as:

$$\dot{Q} = \frac{A_0}{2} Re \left[ \frac{1}{A} \int_A (\rho_0 c_p v_x T_1 - \beta T_0 v_x p_1) dx dy \right] \quad \dots 2.32$$

The time averaged acoustic power  $\dot{E}$  could be written as:

$$\dot{E} = \frac{A_0}{2} Re \left[ \frac{1}{A} \int_A v_x p_1 dx dy \right] \quad \dots 2.33$$

and the time average conductive heat flow losses  $\dot{Q}_{loss}$ :

$$\dot{Q}_{loss} = (A_0 K T_0 + (A - A_0) K_s T_0) \quad \dots 2.34$$

where  $A$  represents the total porous medium cross-sectional area,  $A_0$  is the solid cross-sectional area,  $K$  is the thermal conductivity of the solid and  $K_s$  is the gas conductivity.

Substituting Equations 2.22 & 2.30 into the work and heat flow equations will produce dimensionless equations:

$$\dot{Q} = \frac{A_0 \beta T_0}{2 \rho_0 \omega} \left( Im \left[ \frac{F(\lambda_k) - F(\lambda_v)}{1 + \sigma} \frac{dp_1}{dx} p_1 \right] - \frac{c_p}{\beta T_0 \omega^2} \left| \frac{dp_1}{dx} \right|^2 \frac{dT_0}{dx} Im \left[ \frac{F(\lambda_k) - \sigma F(\lambda_v)}{1 + \sigma^2} \right] \right) \quad \dots 2.35$$

and

$$\dot{E} = \frac{A_0}{2} Im \left[ \frac{F(\lambda_v)}{\rho_0 \omega} \frac{dp_1}{dx} p_1 \right] \quad \dots 2.36$$

Arnott *et al.* (1991) and Swift (2002) suggested many expressions for the function  $F$  for many pore geometries.

## 2.6 Mass Streaming in Thermoacoustic Devices

The term “streaming” is widely used in thermoacoustics, and it refers to a steady mass-flux velocity in one direction. This is usually expressed as a second order oscillation

superimposed on the main first-order oscillating acoustic mass-flux velocity. The gas parcels in oscillatory flow with streaming do not travel the same distance in oscillation direction. A well-known mechanism for the origin of streaming in thermoacoustic devices is the effect of the viscosity and friction. A gas parcel oscillating at a distance of a thermal penetration depth from the wall will be oscillating at varying temperatures because of the thermal contact with the wall and phasing between the oscillatory pressure and motion. This means that the gas parcel will experience various amounts of viscous drag as the viscosity depends on the temperature. In the presence of streaming, a gas parcel in oscillatory flow does not return to its initial starting point.

Generally, there are four known types of undesirable streaming as presented by Swift (2002), see Figure 2.10. Figure 2.10a and b show the time averaged toroidal streaming which takes place inside the Thermal Buffer Tube (TBT). The first one is called “Rayleigh streaming” which is caused by the boundary layer effect, while the second is “Jet-driven streaming” which is caused by the deficient flow straightening at the end on the thermal buffer tube (TBT), shown in figure 2.10. Figures 2.10c and d show the streaming driven by the regenerator. “Gedeon streaming” which is a net time-averaged streaming with the oscillating direction happening in annular travelling-wave devices, and “internal streaming” within the limits of the porous medium. These four types will be explained in the next sections.

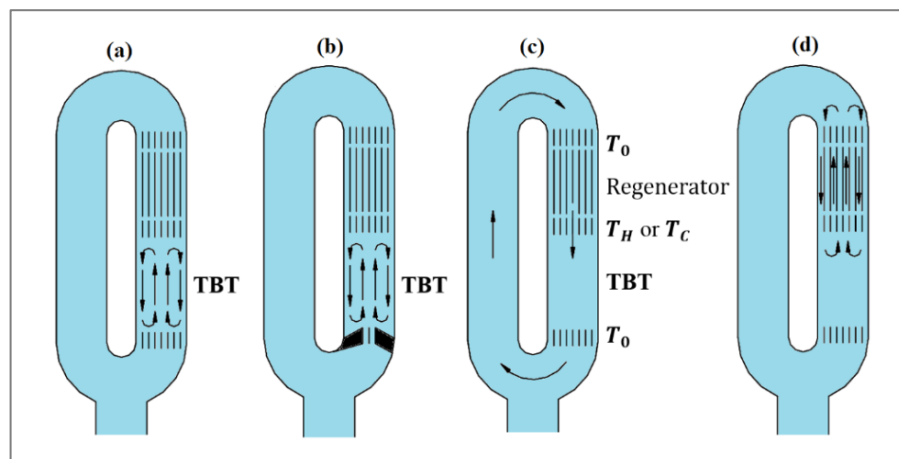


**Figure 2-10:** Sketches of streaming: (a) Rayleigh streaming (b) Jet-driven streaming (c) Gedeon streaming (d) streaming within the regenerator or stack (Swift, 2002)

Streaming could be desirable and have an advantage if it is employed in a way which improves heat transfer. Streaming could be achieved by applying a steady flow parallel or perpendicular to the direction of oscillation, as shown in Figure 2.11. The

flow can transfer heat in a second order manner and hence could be treated as a form of streaming.

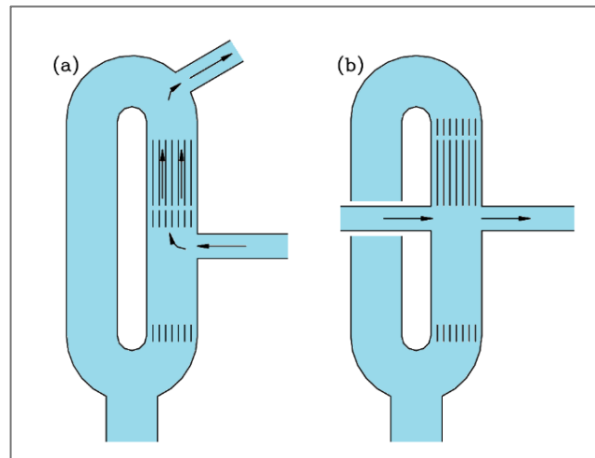


**Figure 2-11:** Desirable mass streaming: (a) flow parallel to the oscillating flow (b) flow perpendicular to the oscillatory flow, (Swift, 2002).

### 2.6.1 Gedeon streaming

This type of streaming can exist in toroidal devices only. The reason is that it encourages a steady flow to circulate along a toroidal tube. In non-toroidal devices, there is no Gedeon streaming as it would lead to accumulation/depletion on one side unlike the toroidal devices where there is a chance of steady flow. Gedeon (1997) explained it as mass flow in the Stirling engine and pulse tube cryo-coolers with a closed loop which leads to time-averaged convection enthalpy flux from the hot to the cold side. This phenomenon wastes heat in a thermoacoustic engine by removing heat from the hot side to the ambient without generating acoustic power. In a thermoacoustic refrigerator, it adds cooling load to the cold side by transferring heat from the ambient side. The devices suffering from a non-zero mass flow through the porous medium will show a non-uniform temperature distribution within the porous medium.

Many researchers (Wilcox, 2014, Swift 2003, Tijani 2012) summarized that this kind of streaming can be suppressed either by placing a latex membrane or applying a flow resistance by use of a jet pump. The latex or elastic membrane will be transparent to the acoustic power while it is not to the second order mass flow, and hence will eliminate the steady mass flow rate. A jet pump is the other effective way to suppress Gedeon streaming, see Figure 2.12. It applies a flow resistance in one flow direction

more than the other by applying a small pressure drop, as presented by Backhaus and Swift, 2000; Backhaus and Swift, 2003. This amount of pressure drop will create a back-pressure in the loop eliminating the one created within the regenerator limit. Despite the above mentioned techniques being able to eliminate the streaming as heat wasting phenomenon, it was reported that they dissipate acoustic power.

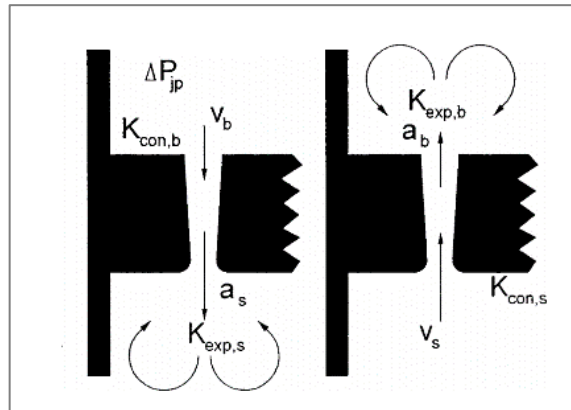


**Figure 2-12:** Schematic diagram of a jet pump (Backhaus and Swift, 2000).

### 2.6.2 Rayleigh streaming

The thermal buffer tube acts as a thermal insulator. It insulates the hot heat exchanger in the engine and the cold heat exchanger in the refrigerator from the rest of the system. Theoretically, gas in the TBT acts as an insulator by transmitting the pressure and velocity oscillations from one end to the other. In fact, convection may carry some heat load to or from the heat exchanger. This may waste heat from the hot heat exchanger in an engine or add a heat load to the cold heat exchanger in the refrigerator. Rayleigh streaming can be encouraged by the forced convection in the TBT driven by the viscous and thermal boundary layer at the side walls of the TBT (Swift, 2002). Poor flow straightening at either end of the TBT may encourage a jet-driven streaming which will enforce the Rayleigh streaming.

Swift (2002) presented an effective way to imagine this phenomenon by following an oscillating gas parcel as shown in Figure 2.13. Figure 2.13a shows a gas parcel oscillating up and down near the wall of a uniform cross-section TBT at a distance smaller than viscous penetration depth. The oscillating gas parcel temperature during the downward motion is different to that of the upward motion, due to the imperfect thermal contact between the parcel and the wall. As a result, the gas parcel will

experience a different amount of viscous drag and hence it will fail to travel the same distance back to the original position.

It is expressed that tapering the TBT will eliminate the Rayleigh streaming. In the tapered TBT, the gas parcel will undergo the same procedure mentioned above, as can be seen in Figure 2.13b. In general, a gas parcel close to the wall will be farther from the wall during, say, its upward motion than during its downward motion. Hence, the moving parcel will experience amount of viscous drag during its upward and downward motion, and so the parcel will fail to return to its starting point after a full cycle. The combination of the Rayleigh streaming and tapering the TBT lead to equal motion upward and downward.

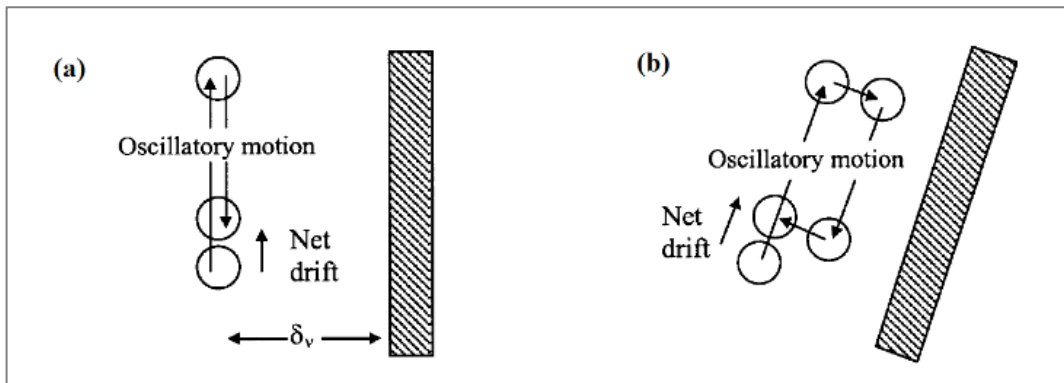


**Figure 2-13:** The net draft near the wall which causes Rayleigh streaming: (a) near a vertical wall (b) inclined wall, (Swift, 2002).

### 2.6.3 Jet-driven streaming

Jet driven streaming is a time-averaged convection which occurs when a viscous fluid oscillates through a cross-section change or small channels. Figure 2.14 shows an example of jet driven streaming at a small channel or an orifice. As the ratio of the cross-section of the space to the cross-section of the orifice is high, the orifice is considered to be connected to an infinite open space. In oscillatory flow, the gas experiences ejection and suction. In the ejection period, the viscous gas leaves the orifice in straight jet streamlines, and hence the fluid will lose a share of its kinetic energy due to downstream turbulence. The turbulence is caused by the transition from high speed region through the channel to the low speed channel through the open space. In contrast, the gas flows smoothly inside the orifice in the suction period from all directions. This will add some flow resistance caused by the edges of the orifice

entrance. Therefore, rounding the orifice edge by increasing the edge radius will decrease the section flow resistance (Swift, 2002).

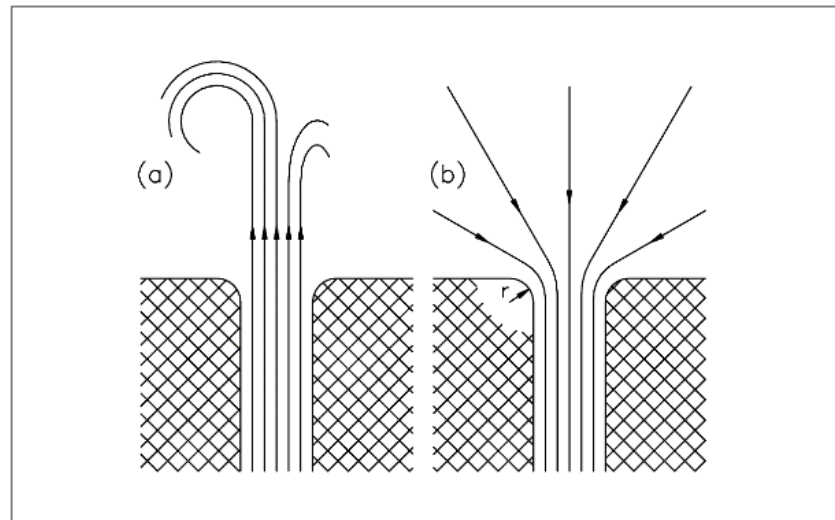


**Figure 2-14:** Oscillatory flow at a small orifice to an open space: (a) ejection (b) suction, (Swift, 2002).

#### 2.6.4 Streaming within a regenerator or stack

So et al (2006) clarified a streaming which happens within the regenerator in travelling wave refrigerators, to which the engine's regenerators are resistant. As the regenerator is made out of stacking woven meshes of circular wires, this produces a non-linear flow resistance which makes the oscillatory flow interact with the steady flow. The value of the flow resistance depends on the local temperature. The mean temperature across the regenerator has a small disturbance, and hence the regenerator has different flow resistance which leads to streaming flows in different regions of the regenerators, as shown in Figure 2.15. The streaming solution assumed at region (A) has a local temperature hotter than it should be and another region (W) at a transverse distance which is cooler than it should be. Heat will be moved from region A to region B through some consequences of conduction and total energy flow. All the studied cases showed that the steady mass flow is always directed from  $T_a$  to  $T_w$ . In engines, the heat flows from region A to region W which eliminates the temperature disturbance and leads to stability of the engines for this type of streaming. In contrast, the refrigerators suffer from this streaming as the heat flows from region A to region W and hence the temperature disturbance will be reinforced by the natural heat flux.

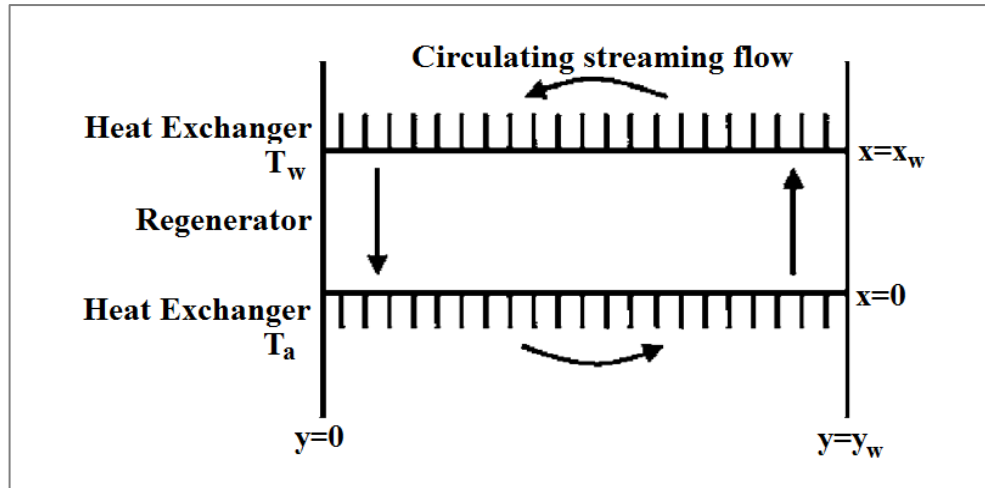


**Figure 2-15:** Schematic drawing of an internal streaming flow in a regenerator (So *et al*, 2006).

## 2.7 Development Review of Travelling-Wave Thermoacoustics Engines

Over the past three decades, the interest in thermoacoustic engines has encouraged lots of researches globally to investigate further. In this review, only travelling wave thermoacoustic engines will be presented as it is the area of interest of this research. These engines could be classified as per the resonator configuration: torus and looped tube engine. The looped tube could be classified as a singular and multi-stage thermoacoustic engine. The detailed literature reviews will follow on the torus thermoacoustic engines (Section 2.7.1), looped tube thermoacoustic engines (Section 2.7.2) and the multi-stage thermoacoustic engine (Section 2.7.3).

In this review, the performance of the engines will be evaluated based on the generated electricity and three efficiencies; thermal-to-electric, thermal-to-acoustic and fraction to Carnot efficiency. The thermal-to-electric or total energy is the ratio of the generated electricity and supplied heat. Some engines dissipate acoustic power by an acoustic load, and hence, the total efficiency is the ratio of the acoustic power dissipated to the supplied heat. The thermal-to-acoustic or acoustic efficiency is the ratio of the generated acoustic power to the supplied heat. Finally, the fraction to Carnot efficiency is the ratio of the acoustic efficiency to the Carnot efficiency. The Carnot efficiency is calculated by using the hot and ambient side temperatures using the formula ( $\eta_{Carnot} = \frac{T_H - T_A}{T_H} * 100\%$ ).

### 2.7.1 Torus thermoacoustic engines

The torus configuration of a thermoacoustic engine consists a loop (containing the thermodynamic section and the acoustic network) and the straight resonator. All the thermoacoustic engine parts are shown in Figure 2.16. The thermodynamic section consists of the regenerator, three heat exchangers and a thermal buffer tube, while the acoustic network consists of the feedback inertance and compliance. The oscillating wave in these two sections is in travelling wave mode. The total length of these two sections is a fraction of a wavelength, and hence they are connected to a long standing wave resonator to set the acoustic oscillating frequency. The resonator which is normally a quarter-wavelength is connected to the loop to form the engine.

The first successful attempt to build a travelling-wave torus thermoacoustic engine was made by Backhaus and Swift (1999, 2000). The main task of this engine was to generate acoustic power out of heat. The engine was designed to have the thermoacoustic core placed in a loop tube which is connected to a quarter wavelength resonator pipe, as shown in Figure 2.16. The thermoacoustic core retained all the components of the travelling wave core, and the working gas was helium at 30 bar. At the highest efficiency run, the engine delivered 710 W of acoustic power to the resonator at an efficiency of 0.3 which is equivalent to 41% of the Carnot efficiency. The generated acoustic power was dissipated through the resonator and a variable acoustic load connected to the resonator. The maximum acoustic power delivered to the resonator of 890 W achieved at an efficiency of 0.22. This was achieved by applying some improvements. The torus loop which contains the thermoacoustic core made the loop much shorter than one-wavelength. The shorter loop led to a relatively low surface area, and hence low losses due to viscous drag and thermal hysteresis at the walls. The design of the feedback loop of the acoustic network served to maintain the travelling wave phase difference between the pressure and velocity, by using an inertance-compliance section prior to the thermoacoustic core. Gedeon streaming was suppressed by applying a jet pump placed prior to the ambient heat exchanger as shown in Figure 2.16, Rayleigh streaming was suppressed by tapering the thermal buffer tube, and a flow straightener was placed at the end of the thermal buffer tube to reduce jet streaming.

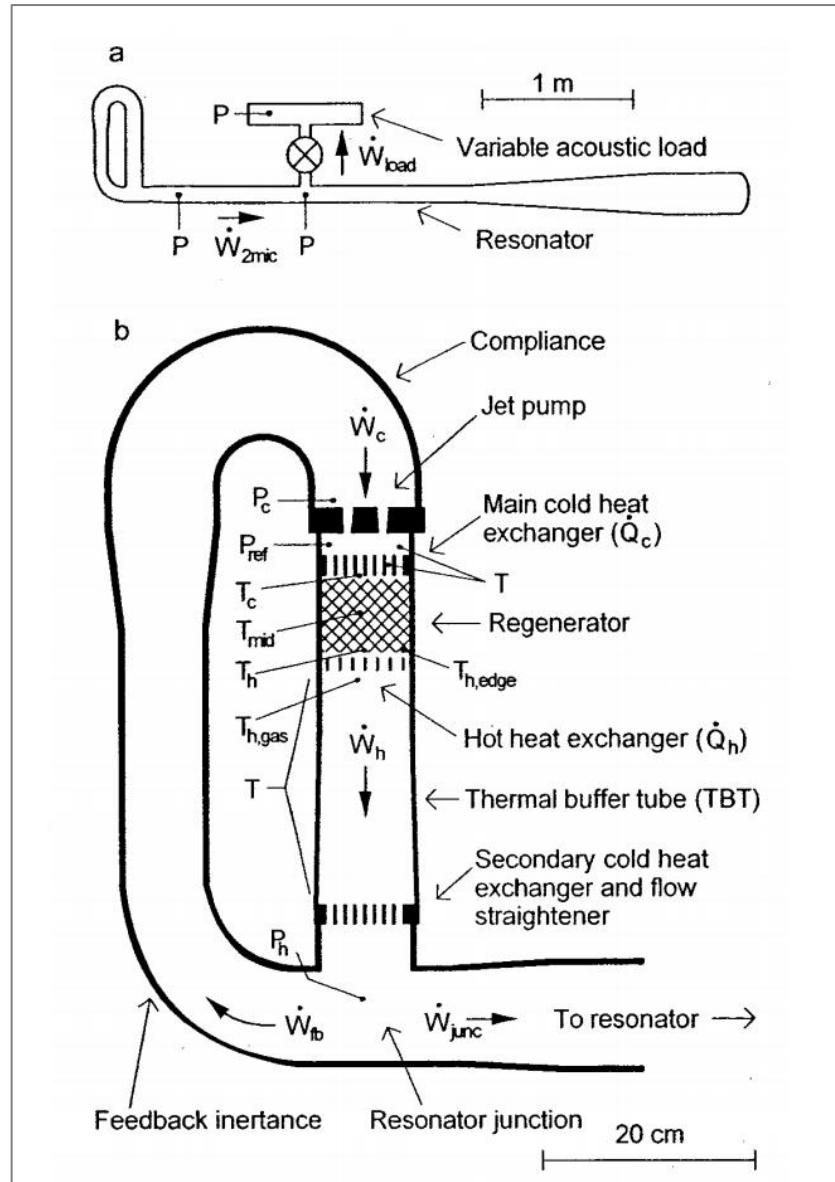


**Figure 2-16:** Scale drawing of the thermoacoustic engine showing all the parts, (Swift, 2000)

Backhaus *et al.* (2004) continued, matching a thermoacoustic engine to a linear alternator to generate electricity out of the acoustic power produced. He presented his electricity generator to be used aboard a spacecraft. This engine retained the same configuration, however, the mean pressure increased to 55 bar. The engine run at a frequency 120 Hz. At the most efficient run, the engine generated 39 W of electricity at a total efficiency (generated electricity W/heating power W) of 18%. The maximum generated power of 58 W was recorded at a total efficiency of 15%.

Meanwhile, a thermoacoustic engine was developed at Nagoya University in Japan. A Pyrex engine was fabricated (shown in Figure 2.17) to study travelling wave device

characteristics and the possibility of combining a thermoacoustic cooler core with the engine core in one loop and generate cooling. It run at 41 Hz frequency. Ueda *et al.* (2002) summarized that the engine achieved higher efficiency at a phase difference between the velocity and pressure of the acoustic wave at the regenerator of  $-20^\circ$  rather than the travelling wave phasing of  $0^\circ$  recommended by Backhaus and Swift (2000). Biwa *et al.* (2002) developed a torus engine with ceramic stack as a porous medium. This engine produced 70 mW of acoustic power at a frequency of 274 Hz, however, the main achievement was the success in the transition from the standing wave to travelling wave mode. Ueda *et al.* (2004) continued and improved this work to generate higher acoustic power and to generate cooling by placing another thermoacoustic core (regenerator based) as a heat pump to dissipate the acoustic power. The heat pump core was placed in the engine loop. The heat pump reached  $-25^\circ\text{C}$  and a cooling power of 11 W at  $0^\circ\text{C}$  at an input power of 210 W. Biwa *et al.* (2010) continued to work in another Japanese university (Tohoku University) on a very similar device. They studied the critical temperature ratio across the regenerator (hot side (K)/cold side (K)), at an oscillation frequency of 31 Hz. They concluded that installing more regenerators in the loop will reduce the critical temperature ratio, as They managed to reduce the ratio from 1.76 (one regenerator) to 1.19 by installing five regenerators.

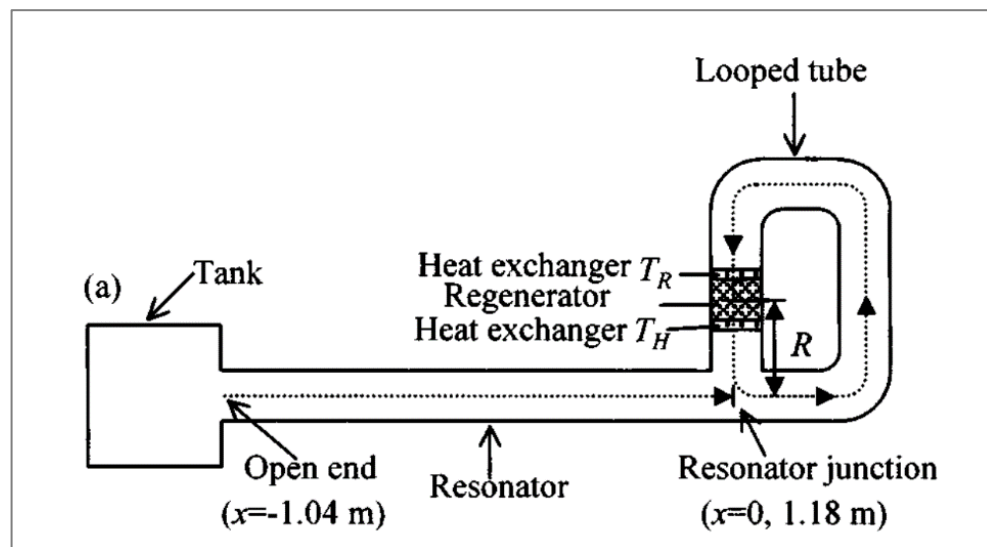


**Figure 2-17:** A schematic diagram of Ueda *et al.* (2002) thermoacoustic engine.

In the Chinese Academy of Sciences, there was a potential interest in thermoacoustic torus engines. Luo *et al.* (2005 and 2006) developed Backhaus and Swift's (2000)

thermoacoustic engine by changing the resonator shape. The previous resonator had a uniform cross-section, while the improved one was tapered. Figure 2.18a shows a simplified schematic drawing of Luo *et al.*'s. (2005 and 2006) engine, which oscillates at a frequency of 87 Hz. For the same loop running at the same frequency, the engine generated higher acoustic power at higher efficiency. To measure and dissipate the generated acoustic power, an acoustic load was connected close to the loop-resonator tee. The acoustic (R-C, resistance-compliance) load consisted of a needle and reservoir. Using pressurized helium at 30 bar as a working pressure, the engine with a tapered resonator generated 200 W of acoustic power as compared to 160 W generated with a uniform cross-section resonator. The tapered resonator helped to reduce the non-linear dissipation losses compared to the uniform cross-section resonator. Later, Luo *et al.* (2008) replaced the acoustic load with a linear alternator, as shown in Figure 2.18b. The importance of the phase difference (velocity and pressure) at the linear alternator was highlighted in addition to its value at the regenerator. The engine was filled with helium at 2.5 MPa. It was found that the engine was capable of generating 100 W of electricity out of 2850 W heat input. Wu *et al.* (2011) improved this work to increase the power output and identify the coupling law of the linear alternator by means of acoustic impedance. A pair of linear alternators were connected in opposite directions at the tee (the connection point between the loop and resonator). The working fluid was helium at 3.54 MPa, and the working frequency was 74 Hz. A maximum thermal to electrical efficiency of 15.03% was measured at a 450.9 W generated electricity, and the maximum electricity produced was 481.0 W at 12.65% thermal to electrical efficiency.

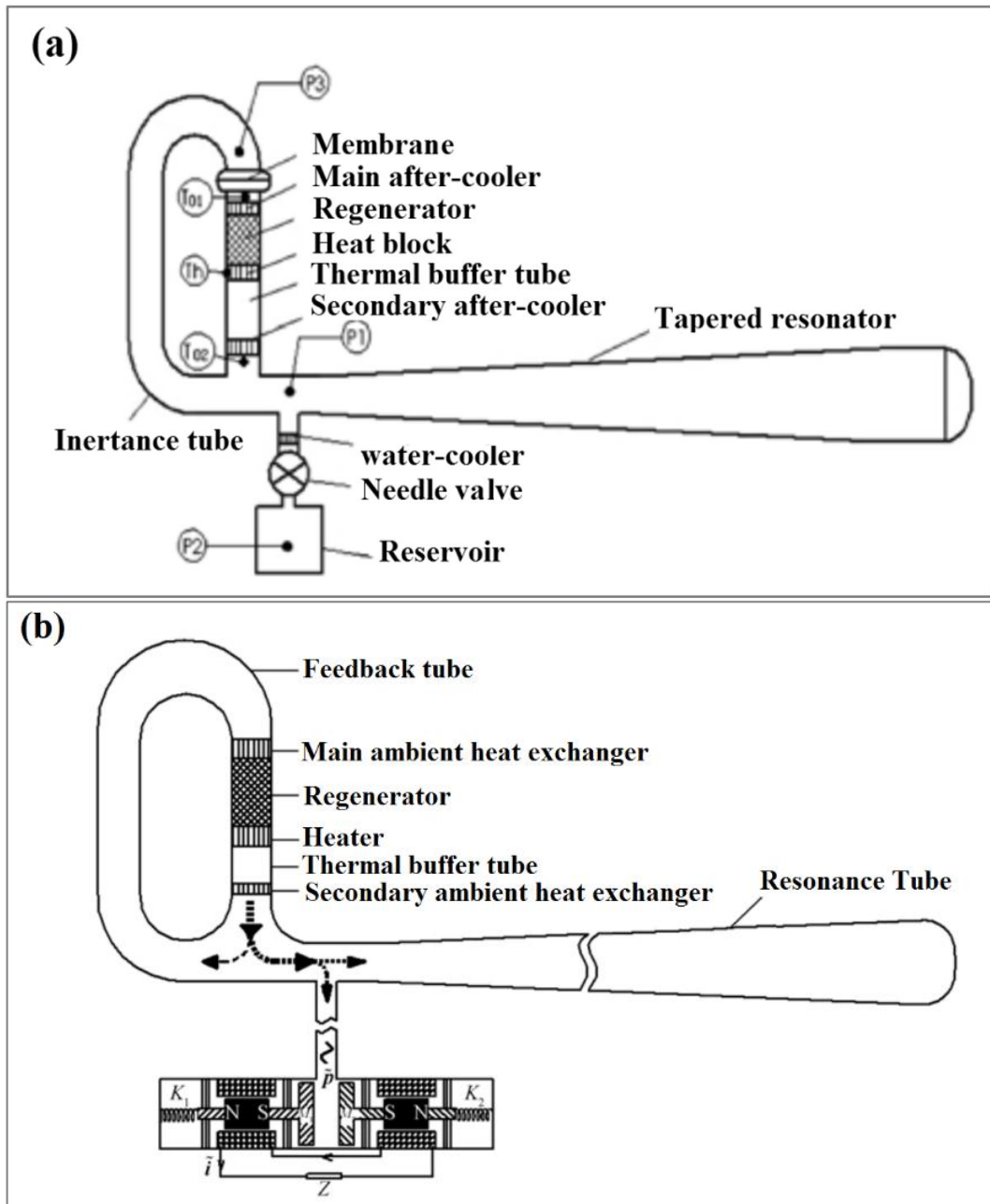


**Figure 2-18:** Engine's schematic diagrams of: (a) Leo et al. (2005 and 2006); (b) Leo et al. (2008)

Wu *et al.* (2014a) pushed the electricity generation to reach one kilowatt. A new engine was built retaining the same configuration, but with slightly larger dimensions, more powerful linear alternators and the helium mean pressure was 4.0 MPa. The working frequency was decreased in the experiments from 74 Hz to 64 Hz. The highest recorded electricity of 1043 W was generated at 17.7% thermal to electrical efficiency and the highest efficiency was 19.8% at 970 W of electricity. All the engines described above used electrical heaters as a heat source, unlike Wu *et al.* (2012). In this work, a solar dish collector was used to heat the hot heat exchanger as

shown in Figure 2.19. The newly built engine followed the same configuration and used the resonator (4.3 m) as a loop carrier, as shown in Figure 2.19. The interesting solar dish collector consists of 144 mirror units and a sun-tracking unit. The total solar collector area is 13 m<sup>2</sup> and it focuses the reflection onto a 15 cm<sup>2</sup> area. A pool-boiler type heat receiver was used at the heat receiver to maintain a uniform temperature at the hot heat exchanger, which utilizes sodium as an intermediate heat transfer fluid. Two fan-coil units were used for the cooling of the ambient heat exchanger coolant. As was the case with the previous engines, helium was used as the working medium, pressurized at 3.5 MPa. The engine was tested first using electrical heaters, it generated 481 W of electricity at 15.0% thermal-to-electrical efficiency. However, it generated 200 W due to solar collector issues.



**Figure 2-19:** Photograph of the solar-powered engine of Wu *et al.* (2012).

Another contribution from this group is their efforts in thermoacoustically-driven refrigerators. Unlike the previously presented device of Ueda *et al.* (2003) who placed the refrigerator core inside the engine loop, Luo *et al.* (2006) and Yu *et al.* (2011) placed the refrigerator core in a branch near the tee (between the loop and the resonator). Both devices used helium at 30 bar as the working gas. Luo *et al.* (2006) attached a full loop to the branch. He expressed his coupling strategy by following a gas parcel through an ideal PV diagram, as shown in figure 2.20. Firstly, the whole

system could be understood as a series of gas parcels acting as pistons delivering power to one another, and the PV diagram could be understood in the same way as the Stirling cycle. The PV diagram of the engine/prime mover is a clockwise closed area, which means heat is converted to mechanical work, in other words, it is generating acoustic power. The PV diagram of the refrigerator/cooler forms a counter-clockwise closed area, which means that it is consuming work and hence dissipating acoustic power. The experimental investigations showed that a combined system at this configuration generated cooling at a lowest temperature of  $-64.4\text{ }^{\circ}\text{C}$  and 250 W cooling power at  $-22.1\text{ }^{\circ}\text{C}$ . Yu *et al.* (2011) improved this work by replacing the refrigerator loop with a co-axial one with some advanced design features. The compactness of the refrigerator has been served by rounding the thermal buffer tube (which is a group of ten tubes) around the core to reduce the dead volume and the inertance is imbedded into the compliance cavity. The Gedeon streaming in the refrigerator was successfully suppressed by a loaded membrane. At a frequency of 57 Hz, the highest cooling power at  $0\text{ }^{\circ}\text{C}$  was 469 W at a total coefficient of performance of 0.216 and it dropped to 340 W at  $-20\text{ }^{\circ}\text{C}$  leaving the total coefficient of performance at 0.16.

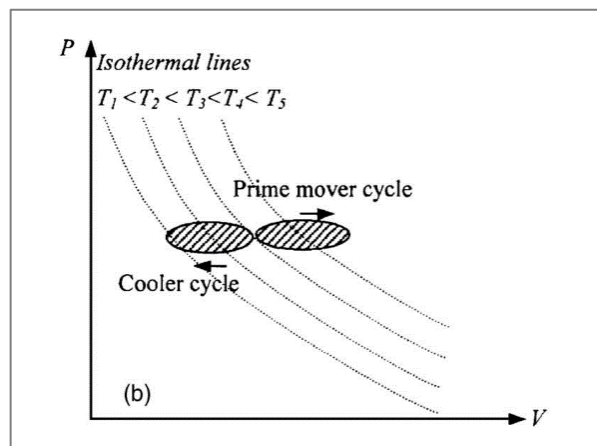


**Figure 2-20:** PV diagram of the thermoacoustically driven refrigerator (Luo *et al.*, 2006)

Not so far from the previous group, there were some researchers working on developing a torus travelling wave thermoacoustic engine in Zhejiang University in China. Qiu *et al.* (2003) and Sun *et al.* (2005) presented their nitrogen-filled torus travelling wave engine which aimed to drive a pulse tube refrigerator. Their torus thermoacoustic engine is very similar to the engines built by Backhaus and Swift

(2000). The start onset and damping behaviour were studied. The experiments showed the effect of the filling pressure and heating power on the drive ratio, and the heating temperature at 12 bar mean pressure and the operation frequency was steady at 25 Hz. Sun *et al.* (2013) theoretically studied the coupling mechanism between the thermoacoustic engine and the linear alternator by means of mechanical and electrical resonance and their effect on electricity generation and total efficiency. The travelling wave engine of the previous research evolved by matching a pair of linear alternators with a variable acoustic load and using helium at 30 bar as the working gas. The theoretical and experimental results confirmed that the mechanical and electrical resonance is crucial for productivity and efficiency of the engine and linear alternator. At the most efficient run of the engine it generated 321.8 W of electricity at 12.33% thermal-to-electrical efficiency, and the highest generated electricity was 345.3 W at 9.34% efficiency. Wang *et al.* (2015) built their new engine which was matched to a pair of linear alternators with a larger swept volume and appropriate acoustic impedance which was studied in depth. Detailed study results were presented at values of many operational parameters.

A remarkable quantitative study of the acoustic losses was presented as shown in Figure 2.21. It shows that the greatest share of losses occurred in the resonator and this share increased directly with the pressure amplitude. Using pressurized helium at 24.8 bar as the working gas, the engine generated 473.6 W of electricity at 14.5% heat-to-electric efficiency. Comparing the two 500 W class thermoacoustic engines of Wang *et al.* (2015) and Wu *et al.* (2011), the two are very similar in configuration, and working temperatures, and both have used helium as the working gas, however, Wang *et al.* (2015) engine's ran at a higher efficiency despite the mean pressure being 30% lower.

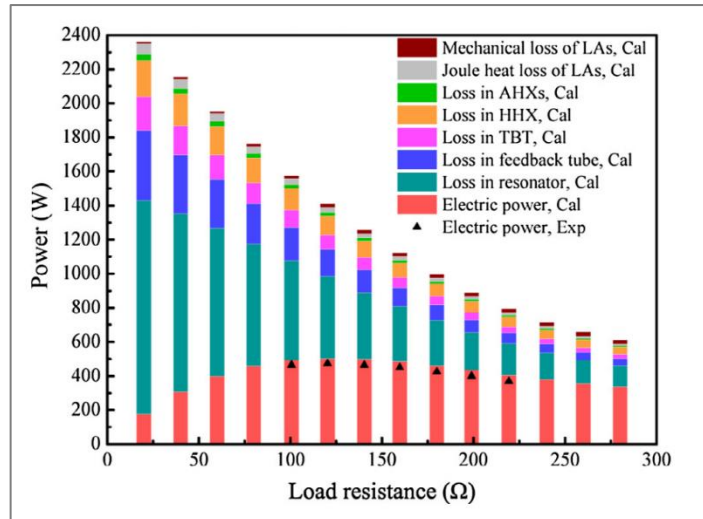


**Figure 2-21:** Dissipation distributions at variable load resistance when the heating temperature is 650 C at 2.48 MPa, (Wang *et al.*, 2015)

Recently, Wang *et al.* (2016a) presented a matching focused research. This research targeted better matching by optimizing/modulating the acoustic impedance of the engine and the alternators. The maximum electric power of 750.4 W was achieved at 16.3% thermal-to-electric efficiency. Wang *et al.* (2016b) continued his matching focused work and studied connecting the linear alternators to the loop instead of the resonator. As the imaginary part of load acoustic impedance should be close to zero in any location, it was found that the real part of the load acoustic impedance is higher at the resonator and hence it can generate higher electricity. The electric power and the thermal-to-electrical efficiency were reduced to 506.4 W and 14.6%, respectively, when the linear alternators were connected to the loop.

In The Netherlands, Tijani *et al.* studied the acoustic field in torus configuration. Their thermoacoustic engine was connected to an acoustic load to dissipate the generated acoustic power. Tijani *et al.* (2008) presented the design and some performance measurements of the study. The engine is similar to the Backhaus *et al.* (2004) engine. It uses cartridge heaters as heat source and helium at 40 bar as the working gas. It generated 190 W of acoustic power at a thermal-to-acoustic efficiency of 22.5%. The fraction to Carnot efficiency (acoustic efficiency divided by the Carnot efficiency) was calculated to be 36%. Tijani and Spoelstra (2011) developed a new engine (which is similar to Backhaus and Swift, 2000) aiming to achieve higher efficiency. Compared to the previous engine, the helium was at a higher mean pressure of 40 bar at working frequency of 150 Hz, and some design improvements had been made. The

heat exchangers provided a higher thermal contact area to the working gas and the regenerator had a smaller hydraulic radius, providing, better thermal contact. The acoustic network was designed carefully to provide an appropriate phasing condition in the generator. In addition to the elastic membrane (suppressing Gedeon streaming), flow straighteners were placed in the thermal buffer tube to suppress jet-streaming. This engine ran at the highest recorded relative to Carnot efficiency (to the author's knowledge) of 49%. At the most efficient point, it generated 280 W of acoustic power at a thermal-to-acoustic efficiency of 32%. Tijani and Spoelstra (2012) combined a heat pump with the engine to generate high temperature cooling out of the produced acoustic power. A step towards a better presentation of a thermoacoustic device, this device operated using hot air instead of electrical heaters. The air was blown by an air gun and heated by electrical heaters to simulate the flue gases of a gas burner. The heat pump used the acoustic power generated by the engine to lift heat from a low temperature source at 10°C to a high temperature source at 60°C or 80°C. The thermoacoustic engine and heat pump were coupled by the resonator. At a fraction to Carnot efficiency of 40%, the heat pump generated a cooling power of 250W at 60°C hot side temperature and 200 W of cooling at 80°C hot side temperature. Later on, Tijani and Spoelstra (2013) tested the engine separately using hot air as the heat source instead of electrical heaters. The hot pieces; regenerator holder, hot heat exchanger and thermal buffer tube were manufactured out of a single high temperature steel block to avoid gas leaks at high temperature. A fin-fin cross-flow hot heat exchanger was designed to exchange 2 kW of heat from the hot air to the helium at a minimal pressure drop. Comparing to Tijani and Spoelstra (2012) who used electrical heaters, this engine showed a drop in fraction to Carnot efficiency, to 41% when generating 300 W of acoustic power, at a working frequency of 120 Hz.

### **2.7.2 Looped tube thermoacoustic engines**

The first looped tube thermoacoustic engine was presented by Yazaki *et al.* (1998). The new configuration of travelling wave engine was a one wavelength loop which contained the thermoacoustic core at a specific location, as shown in Figure 2.22. Yazaki *et al.* (1998) designed and built their air filled engine to study the spontaneous gas oscillations of a travelling wave. The experimental results showed that the travelling wave engine acts as an acoustic amplifier and it outperformed the standing

wave engines at the same frequency and wavelength. The other main observation was that the onset temperature of the travelling wave engines is lower than that of the standing wave engines. A stack was used as a porous medium in this engine, however, it was proposed to use a regenerator in travelling wave engines to enhance the heat transfer between the gas parcel and porous medium. The low efficiency of this engine was discovered to be caused by low acoustic impedance. Yazaki *et al.* (2002) continued this work and combined the engine with a thermoacoustic cooler. The working gas was changed to helium. The position and length of the stack-based refrigerator core was investigated experimentally aiming for the lowest refrigerating temperature. The combined device was tested at various mean pressures using helium and a mixture of Helium and Argon as working gas. It was concluded that the combined device performed better at lower mean pressure and with a mixture of helium and argon, as these two can provide better heat transfer in the thermoacoustic core of large pores used in this device. The lowest cooling temperature achieved was  $-27^{\circ}\text{C}$ , at 240 Hz working frequency.

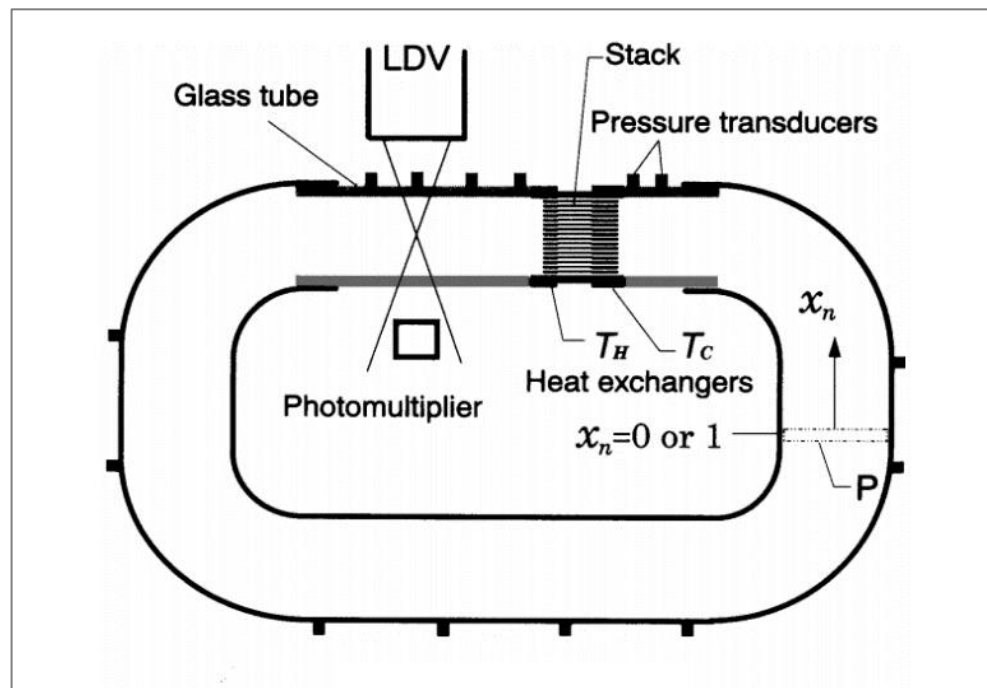


**Figure 2-22:** Schematic of experimental looped tube thermoacoustic engine, Yazaki *et al.* (1998)

The encouraging results of Yazaki *et al.* (1998, 2002) attracted the interest of Japanese researchers from Doshisha University. Sakamoto *et al.* (2004) and Sakamoto and Watanabe (2004) built a combined device (engine and refrigerator as shown in Figure

2.23) having a loop longer than Yazaki (1999), and hence it ran at a lower frequency. They noticed that the oscillation start-up time of a mixture of air and helium as working medium was half that for air. The effect of the heating power was investigated to study the effect of the heating power on the cooling effect. The heating power was found to directly affect the cooling power and the cooling onset time. The results failed to meet the success of Yazaki (1999) as the lower temperature was about 6.5°C at a temperature reduction of 16°C. The estimated thermal-to-refrigeration efficiency of this device was 0.13% when air was used as the working medium, and 1.5% with helium. Sakamoto *et al.* (2004) continued the study by investigating the effect of some design and operational parameters on the resonance frequency. The experiments confirmed that increasing the tube length decreased the resonance frequency. The inner mean pressure does not show a significant effect on the resonance frequency. It was concluded that the thickness of the boundary layer is smaller than the stack channel radius, to prevent viscosity from obstructing the energy conversion and sound amplification.

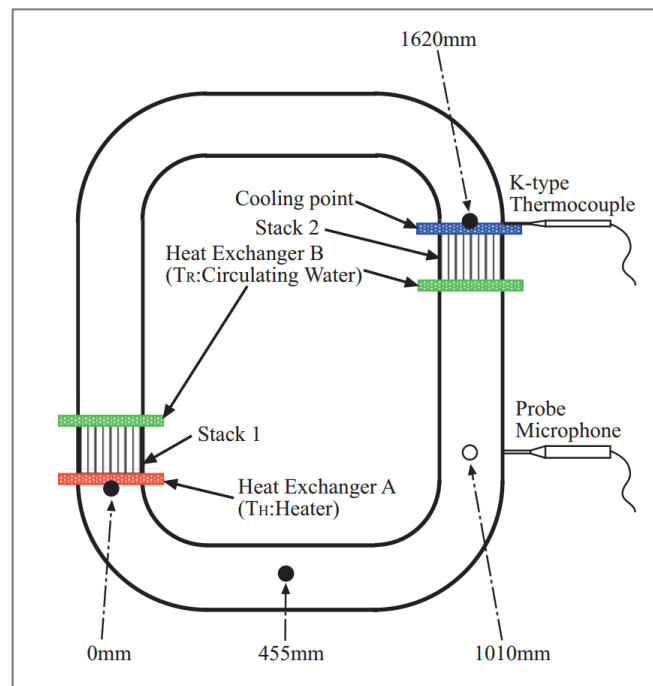


**Figure 2-23:** Schematic drawing of the combined thermoacoustic device of Sakamoto *et al.* (2004)

Kitadani *et al.* (2010) investigated the electricity generation from a looped tube engine. A loudspeaker was connected within the loop to convert the acoustic power to electricity and was placed at the end of a branch optimised to be a quarter

wavelength. The branch tee was located at a high sound pressure location, normally called the “pressure antinode”. The dependence of sound amplification on the phase difference between the acoustic pressure and velocity was highlighted here, and it was clarified that there are not many controlling parameters to adjust the phase difference. The engine generated 1.1 W of electricity out of only 330 W input heat, leaving the thermal-to-electrical efficiency to be 0.3%. The idea of the branch was adopted and tested in the cooler again. Compared to the location of Sakamoto *et al.* (2004) shown in Figure 2.23, the cooling core was placed in a branch and at a position in the loop after the branch. Placing the cooler in the branch increased the temperature reduction to 25°C.

Sakamoto *et al.* (2012) and Sakamoto *et al.* (2008) proposed a phase adjuster mechanism to improve the thermal-to-acoustic conversion. The proposed phase adjustment is a thick tube inserted to reduce the internal diameter of the loop tube at a certain location. The phase adjuster is a sudden reduction of the inner diameter of the tube. The experiments showed an improvement in the energy conversion from heat to acoustic power. In Sakamoto *et al.* (2008) a three phase adjuster inner diameter was studied and the change in sound pressure, velocity, and phase difference between sound pressure and particle velocity, as it led to higher acoustic intensity. Sakamoto and Watanabe (2011, 2013) tested the looped tube combined system to act as heater instead of cooler. The difference between thermoacoustically driven cooler and heater is the location of the reference temperature section at the heat pump being reversed. In this experiment, an electric heater was used to amplify acoustic power through the system which converts back through the second stack to heat. In experiments, a thermoacoustic heating temperature of 100°C was reached.

In the United Kingdom there is group of researchers supervised by Professor Artur Jaworski who have constructed looped tube devices and presented a remarkable contribution in this area. They have started their work at the University of Manchester and then they moved to the University of Leicester and then move to the University of Leeds. Yu *et al.* (2009, 2010a) proposed the looped tube thermoacoustic electricity generator for remote and rural areas. The engine was constructed from commercially available materials targeting a low-cost product, as shown in Figure 2.25, a low-cost loudspeaker was connected along the loop to convert the acoustic power to electricity.

Electrical heaters were installed in the hot heat exchanger to simulate the heat of a burner. A blind tube called a “stub” was introduced to the engine loop to act as a phase adjuster to help in tuning the impedance matching between the alternator and thermoacoustic engine, shown in Figure 2.25. The working frequency was 75 Hz. The experimental results were lower than expected, the engine generated electricity of 5.17 W at a thermal-to-electrical efficiency of 0.65%. Later on, Yu *et al.* (2010b) applied some dimensional optimization to the previous design for a better matching between the engine and the loudspeaker. The electricity generated doubled to 11.58 W at a thermal-to-electrical efficiency of 1.65%. Yu *et al.* (2012) detailed the guidelines for developing ultra-compliant alternators (like loudspeakers) and their application in thermoacoustic power generation. The summarized specifications discussion of this work helps to select/build the correct loudspeaker/ultra-compliant alternator for low acoustic impedance engines. Yu and Jaworski (2012) took a step towards demonstrating the practicality of this engine and its suitability to be driven by burning gases. The electrical heaters were replaced with a shell and tube heat exchanger. A propane burner and ventilation chimney were introduced as shown in Figure 2.24a. The oscillating gas flowed inside the parallel pipes while the propane burner gases passed through the heat exchanger tubes. The results confirmed that it is suitable and ready to use as it has generated 8 W of electricity at a regenerator temperature difference of 290°C. Abdoulla *et al.* (2013) aimed to increase the generated electricity of this set-up, therefore, the linear alternator matching arrangement of Kitadani *et al.* (2010) has been adopted. The linear alternator was placed at the end of a side branch (resonance tube) connected close the antinode of the sound pressure, as shown in Figure 2.24a. The current configuration increased the generated electricity to 13 W from a higher temperature difference of 420°C (compared to the previous configuration). Connecting the linear alternator in the tube line (as shown in Figure 2.25) has proven to damp/limit the sound amplification, however, it has the advantage of suppressing the Gedeon streaming as the linear alternator acts as a membrane. Saechan *et al.* (2013) investigated the opportunity to generate cooling by converting this engine to a combined system (thermoacoustic engine-refrigerator), as shown in Figure 2.24b. The aim was to present a low-cost combined thermoacoustic system that can be driven by burning gases. A thermoacoustic regenerator was placed a half wavelength away from the

thermoacoustic engine core to generate cooling. The rig retained all the parts of the engine's thermoacoustic core, feedback loop and stub as in the previous configuration. For matching purposes, the feedback loop length was increased, and hence the combined system ran at lower frequency. The lowest cooling temperature achieved was  $-3.6^{\circ}\text{C}$ . Later on, Abdoulla *et al.* (2012) proposed adding a second thermoacoustic engine core to this configuration. The numerical design considered the use of air at 2 bar as working medium in a loop of about 2.8 m long. The simulation showed that the engine can generate 130 W of electricity at 6% thermal-to-electrical efficiency.

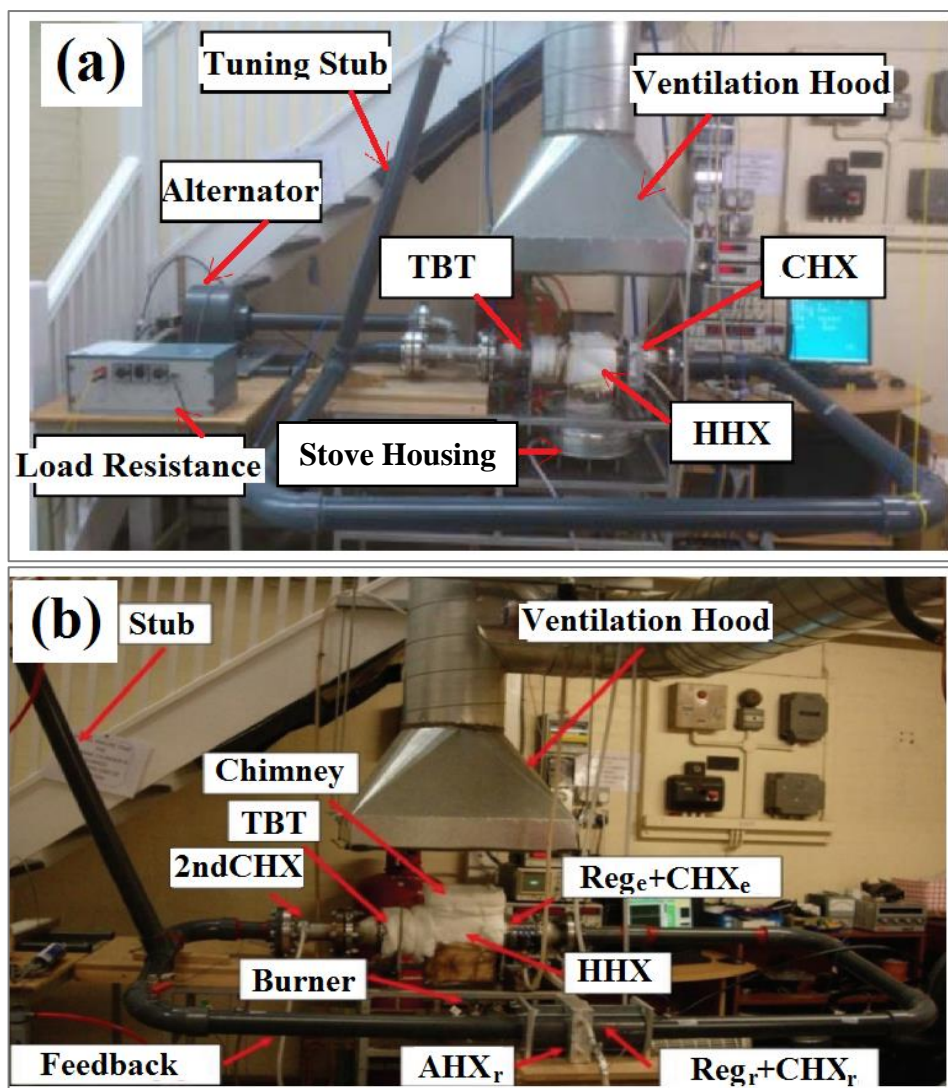


**Figure 2-24:** (a) labelled photograph of a thermoacoustic electricity generator (Abdulla *et al.*, 2013); (b) labelled photograph of a thermoacoustic combined system (Saechan *et al.*, 2013).

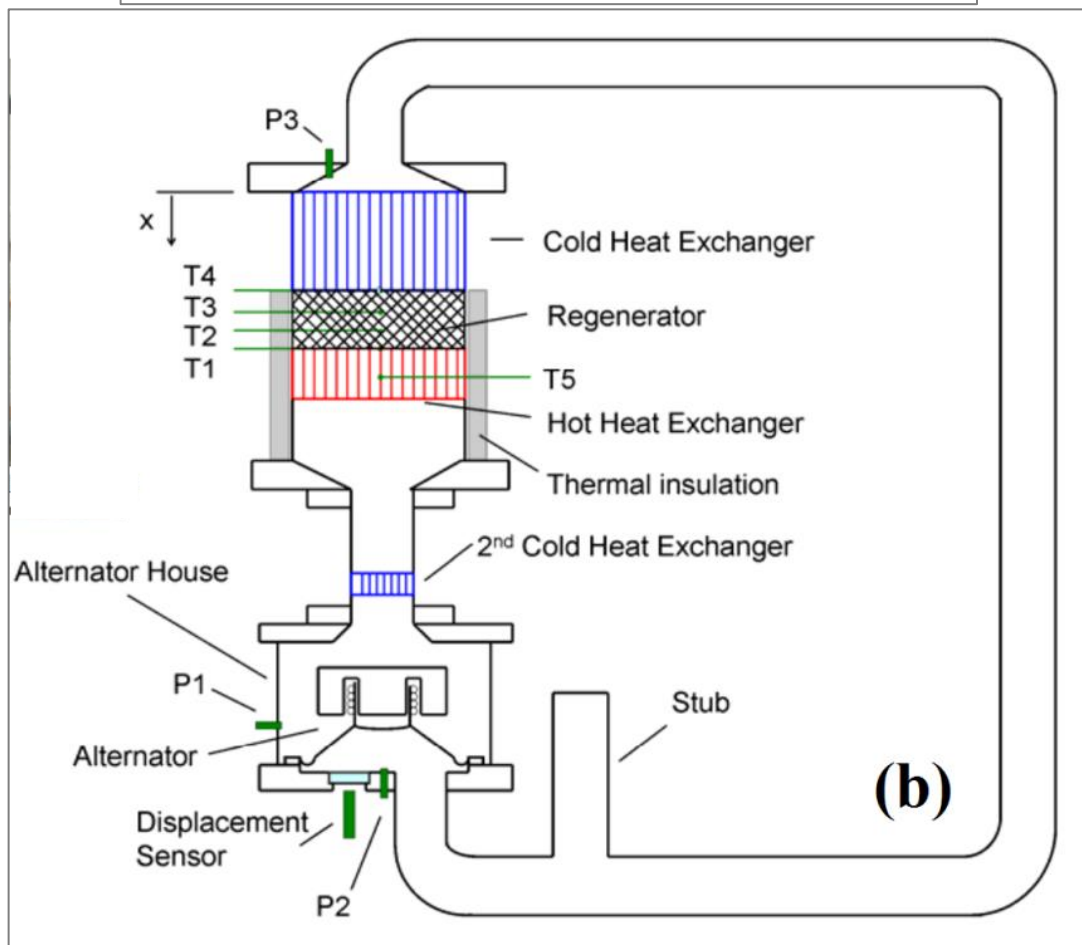
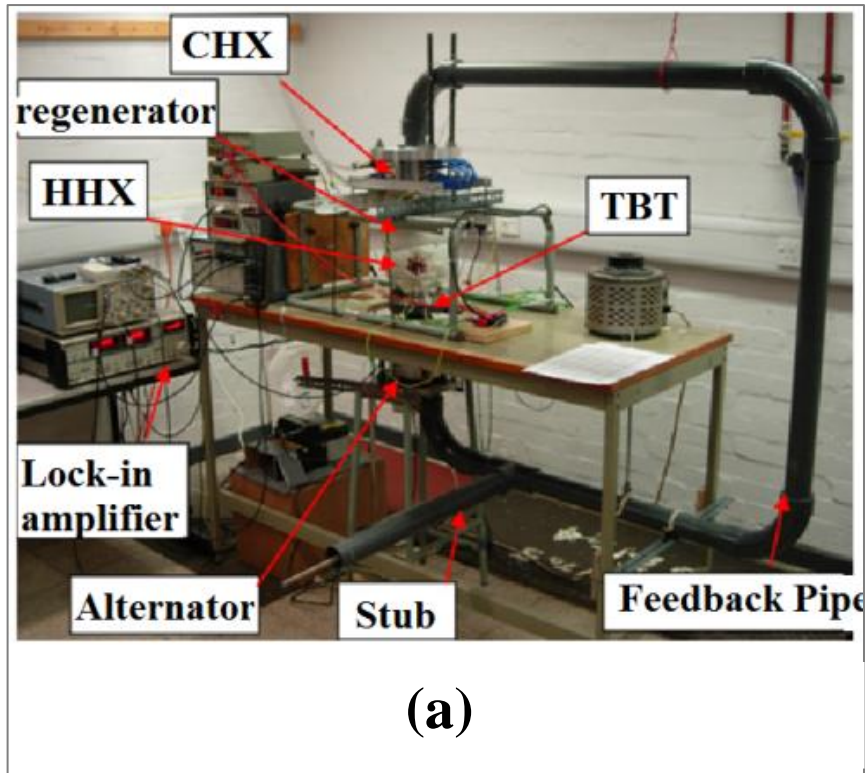


**Figure 2-25:** (a) photograph of a thermoacoustic electricity generator (b) schematic drawing of the proposed engine, Yu and Jaworski (2012)

Abduljalil *et al.* (2009) built a travelling wave thermoacoustic engine to study the regenerator characterization. Abduljalil *et al.* (2009, 2011a) presented the design and construction of a table top travelling wave engine, shown in Figure 2.26a. This engine is proposed to be developed to use solar energy instead of the electrical heaters as the heat source. The working medium was pressurised air at 10 bar, and the working frequency was 110 Hz. The regenerator was made from Corning Cellular Ceramic Catalyst Support, which has square channels of about 900 channels per square inch, shown in Figure 2.26b. Firstly, the engine performance was tested in three different orientations: horizontal, inclined at 15° and vertical. At the same design and operational parameters; the natural convection helped the vertical orientation to run at the highest regenerator temperature difference among the three cases, and the vertical orientation had the shortest onset time. The onset regenerator temperature difference was studied against the mean pressure from 1 - 9 bar. It was found that the lowest onset temperature is at a mean pressure between 2.5 - 4 bar, and increases directly with mean pressure between 4 and 9 bar. Abduljalil *et al.* (2009b, 2009c and 2011b) investigated the suitability of selected low-cost porous materials as regenerator material for a travelling wave engine. The vertical orientation of the thermoacoustic engine was adopted in this study. In addition to the ceramic regenerator, three kinds of materials were tested, namely; steel “scourers”, stainless steel “wool” and wire mesh screens, all shown in Figure 2.27. Having a wire mesh screen regenerator, the engine has a lower onset temperature and higher pressure amplitude as compared with scourers and steel wool regenerators of the same hydraulic radius (except for the steel wool regenerator at high mean pressure). The low flow resistance and high porosity are the possible reasons for the very low performance of the scourer regenerator. At a range of low pressures, the ceramic regenerator offers reasonable performance compared to the wire mesh screens. The steel wool performed quite well in comparison with the wire mesh screens. However, to achieve a similar hydraulic radius the porosity of the steel wool will be low and this will increase the flow resistance.

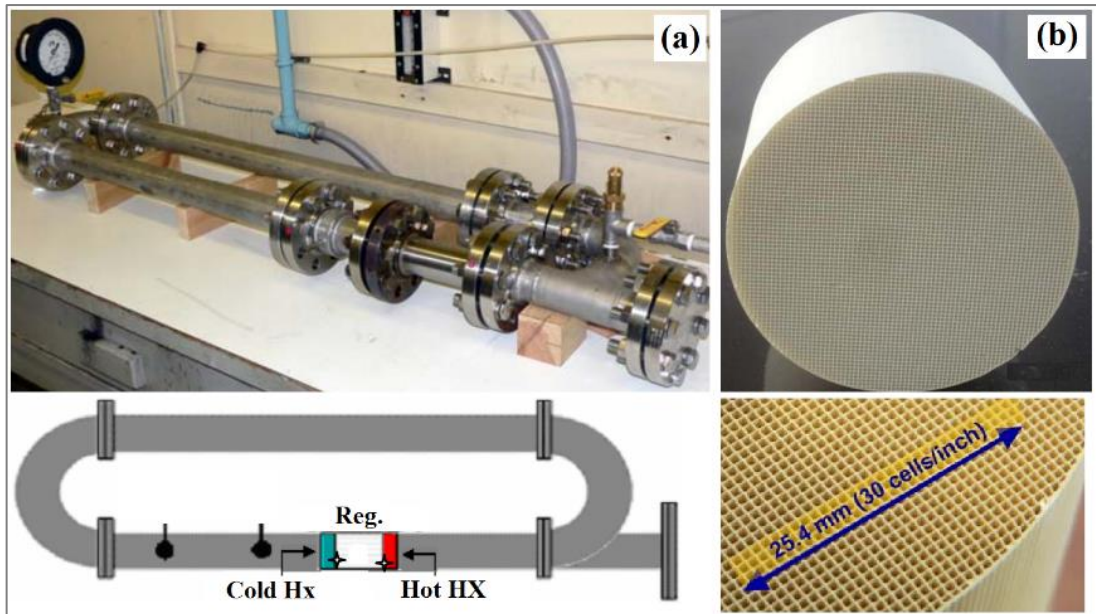


**Figure 2-26:** (a) photograph and schematic diagram of a thermoacoustic engine (Abduljalil *et al.*, 2009); (b) general and close-up views of the ceramic regenerator (Abduljalil *et al.*, 2011)

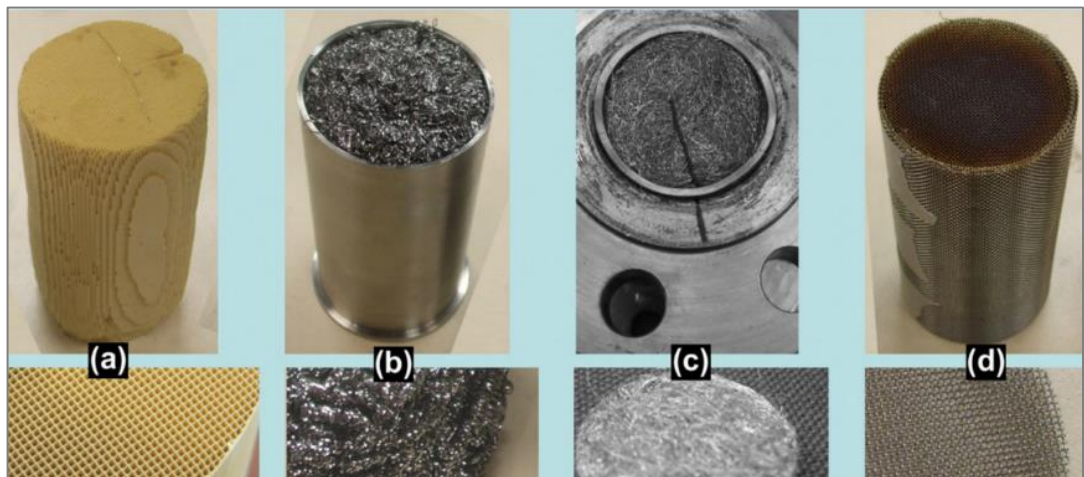


**Figure 2-27:** Photographs of regenerator set-ups and close-ups of materials: (a) ceramic catalyst support; (b) steel “scourers”; (c) stainless steel “wool” and (d) wire mesh screens (Abduljalil *et al.* (2011b).

The main target of the studies presented by the University of Nottingham is to demonstrate a low-cost thermoacoustic generator operating by waste heat from a cooking stove. Chen *et al.* (2012) presented a low-cost thermoacoustic engine which had a loudspeaker as the linear alternator, able to convert the waste heat from a wood-burner cooking stove to useful electricity. The engine was constructed to be driven by a propane burner or wood burner. The engine driven by a propane burner was fabricated first as shown in Figure 2.28, which consisted of two identical half-wavelength stages. After testing this engine, the design target was up-dated to achieve

a lower onset temperature and a further reduction in the fabrication costs, as shown in Figure 2.28. These goals were fulfilled by changing the identical stage lengths to a quarter and three quarter length stages and combining the two stages, respectively. At 80 Hz working frequency, experiments showed that the engine driven by a propane burner can generate 15 W of electricity, while when driven by a wood burner it was able to generate 12.6 W and 22.7 W at atmospheric and 2 bar mean pressure, respectively. More detailed study and cost analysis of the wood-burner has presented by Chen *et al.* (2013). The unit was found to cost less than £150. Ehsan *et al.* (2015a) modified the wood-burner engine to a kerosene-burner to enable evaluations to take place in three regions of Bangladesh. The engine was acceptable at limited field trials as it could generate electricity using air at atmospheric pressure as the working gas. The power generation was lower than expected as it generated 3.5 W of electricity only. Ehsan *et al.* (2015b) doubled the engine generated electricity by increasing the mean pressure to 1.4 bar. Recently, Hossain *et al.* (2016) studied a step towards a compact design to reduce the engine size. More bends were introduced and the straight PVC pipes were replaced by corrugated flexible PVC pipes. This method led to a massive reduction in spatial volume occupied by the engine, and the generated electricity was limited to 4 W.

Kang *et al.* (2015) constructed a two-stage looped tube engine using two linear alternators in different configurations; within the loop line and in a branch, as shown in Figure 2.29. This engine used loudspeakers as linear alternators in a manner similar to the previous two-stage engines, however, pressurized helium (18 bar) was used as the working gas. The coupling mechanism of the two loudspeakers was studied numerically and experimentally. The idea was to put a thermoacoustic core in each of the two high impedance zones and a loudspeaker in each of the two low impedance zones, to avoid acoustic losses. The loudspeaker connected within the loop line will suppress the Gedeon streaming and the branch of the other alternator will help to tune and set the acoustic phasing difference (velocity and pressure). Between tubes 5 and 6, see figure 2.29, a Ball Valve (BV) was introduced as an acoustic load to correct the acoustic field. At 171 Hz working frequency, the maximum generated electric power was 204 Watts at 3.41% thermal-to-electric efficiency and a maximum efficiency of 3.43% was obtained at 183 W electric power.

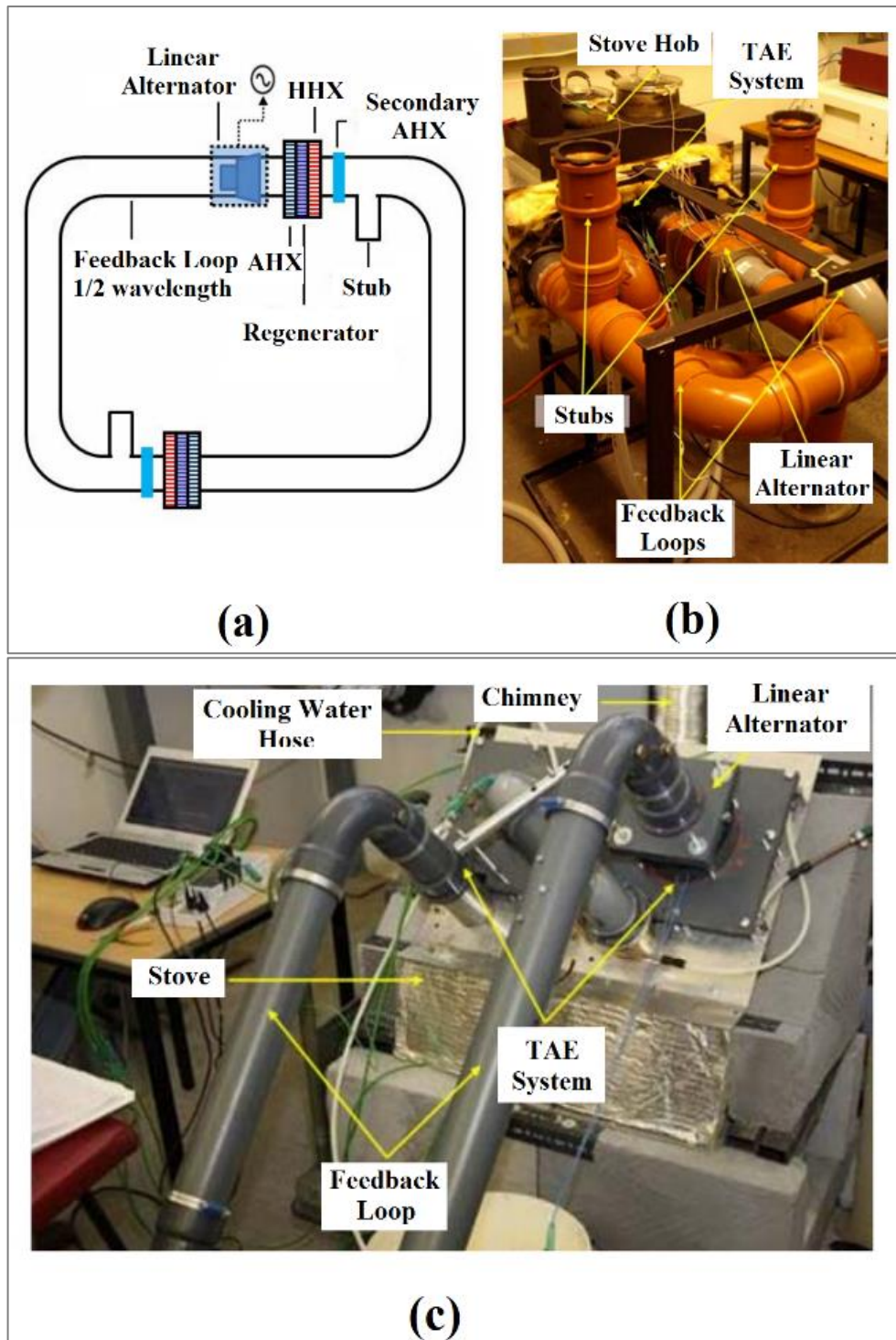


**Figure 2-28:** (a) simplified sketch of the two-stage thermoacoustic electricity generator; (b) photograph of propane-burner driven engine; (c) photograph of wood-burner driven engine, (Chen *et al.* (2012)).

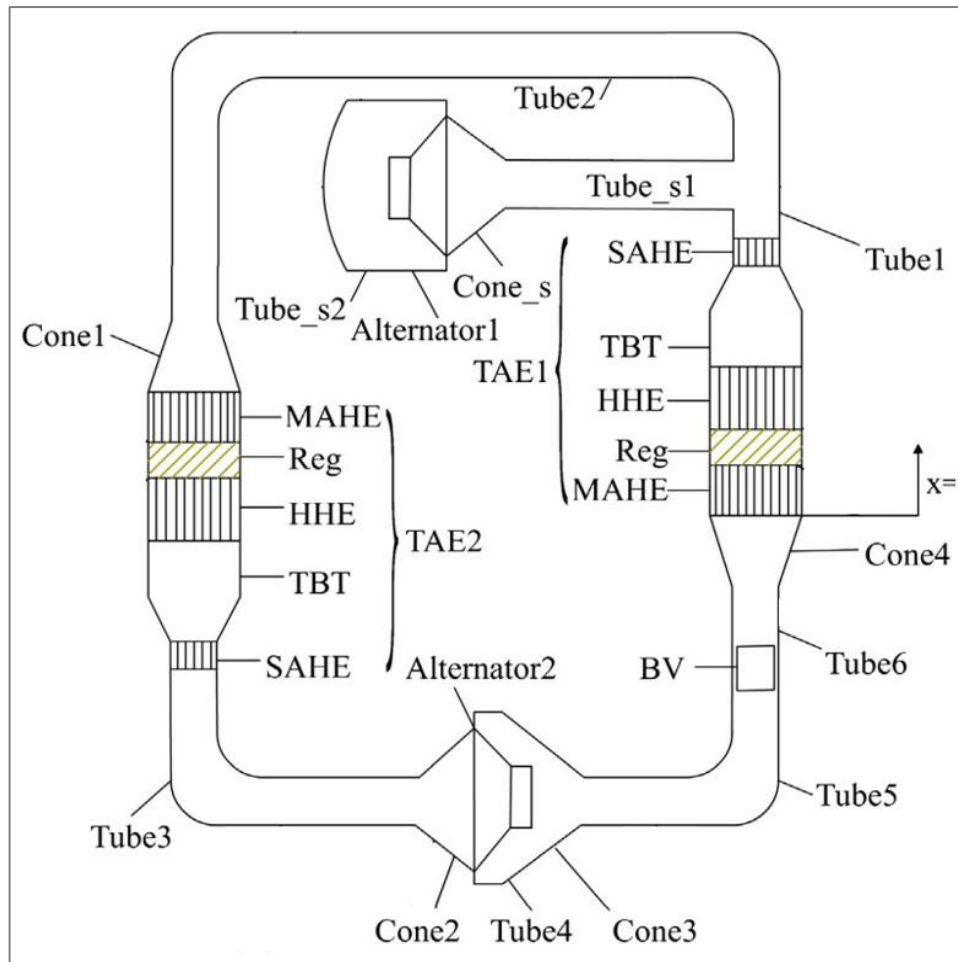


**Figure 2-29:** Schematic of the two-stage thermoacoustic generator prototype, Kang *et al.* (2015).

### 2.7.3 Multi-stage thermoacoustic engines

The thermoacoustic engine could have more than one regenerator unit in the same engine. However, all attempts to put more than two regenerator units in the torus tube with a standing wave resonator have failed. Such an arrangement seems very difficult to build (de Blok, 2010)(Swift, 2001). The looped tube TA engine was found to be more convenient to use with multiple regenerator units. The multi-stage engine is simply a looped configuration working at one or more wavelengths which has many regenerator units, as shown in Figure 2.30. The initial idea behind multi-stage TA engines was that they could be built whenever there is a heat source of kilowatts to be used. Later, it was found that the multi-stage TA engine is a solution for a low onset temperature too, Chen *et al.* (2012).

Multi-stage engines were pioneered by de Blok (2010, 2012). Four novel engines were built with four identical self-matching stages. Basically, they have low acoustic loss because of lower acoustic dissipation in the resonance and feedback loop. The identical four stages were presented as feasible from the construction point of view because of having identical components per stage. The name “self-matching” indicates that each stage has an independent power extractor. On other hand, if the engine has a single alternator, the cross section of the regenerator should be increased with the wave direction (Backhaus and Swift, 2002) (de Blok, 2010). From loss point of view, it is better to design a self-matching engine in order to avoid high power spots and minimize losses. Four novel TA four stage engines were presented by de Blok (2010), each of which was self-matching. The first rig was designed to use air at atmospheric pressure as working gas and had acoustic loads instead of alternators, as shown in figure 2.30. At temperature differences across the regenerator of 132°C, the engine could deliver an electric power of 18 W to the loads out of 64 W of acoustic power circulating in the loop. The input power was 656 W of which 449 W was lost through the regenerator in the form of static heat flow. The thermal efficiency, excluding the amount of heat lost in static heat, flow was 8%. Another atmospheric pressure engine was constructed to operate as a cooking device for developing countries. The aim was to generate electric power besides the main function of cooking. The low efficiency of alternators used led to generated electrical power of 5.4 W out of 34 W of acoustic loop power. A more powerful engine was constructed and introduced in the European THATEA project (THERmoacoustic Technology for Energy Applications) as a solution to recover low temperature waste heat. This engine was tested using Argon and Helium as working gases, at 95 Hz working frequency. The onset oscillation temperature difference across the regenerator for argon was found to be lower than 30°C, while for helium it was about 42°C. The engine working with helium could generate up to 250 W of electricity while the argon-based engine generated 140 W at the same temperature difference. The fourth engine seemed to be the largest multi-stage engine in this group. It is named ThermoAcoustic Power (TAP). The design and construction details and the results were presented by de Blok (2012). This engine generated 1.64 kW of electricity using available waste heat of 20 kW, at working frequency of 40 Hz.

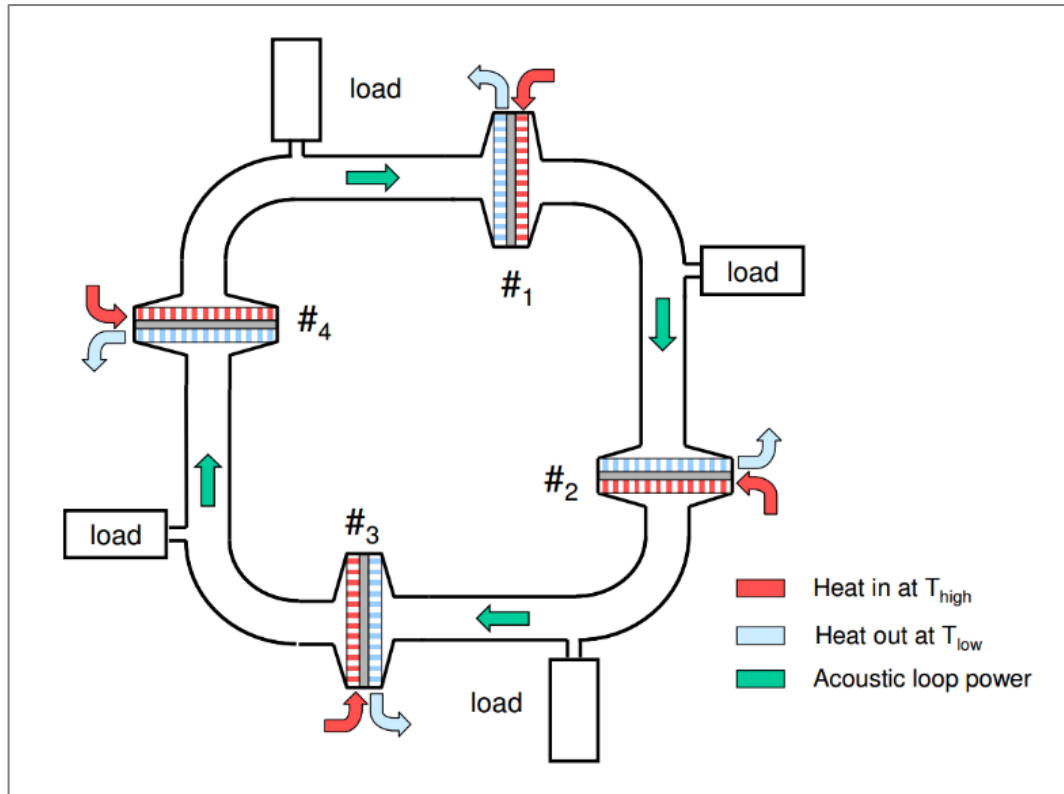


**Figure 2-30:** Four stage thermoacoustic engine scheme (Blok, 2010).

The interesting four identical stages attracted two groups from China and Japan in the last four years. The facts highlighted in de Blok (2012, 2012) and Biwa *et al.* (2010) that the multi-stage configuration has a lower onset temperature than the singular, encouraged researchers to build a four stage thermoacoustic device at Tokai University in Japan. Hasegawa *et al.* (2013) presented a numerical model for a three stage cascade engine loop (the cores are in series) driving a refrigerator loop. Despite being designed to run using air at atmospheric pressure as working gas, the multistage configuration started at a low onset temperature of 110.8°C and a high Carnot relative efficiency of 21%. Senga and Hasegawa (2016) built a four-stage engine similar to the de Blok (2010) configuration, using air at atmospheric pressure as working medium. The main difference is that it has one load and hence the cross section area of the regenerators increased with the acoustic power flow direction after the load. The acoustic power generated did not reach 1 W on this rig. Xiaoqing Zhang from Huazhong University of Science and Technology in China studied the multi-stage configuration theoretically. Zhang and Chang (2015) numerically studied the onset temperature, mean pressure, working gas, hydraulic radius and the number of stages of a four-stage engine similar to the de Blok (2010) configuration. The results were

used to develop another numerical study replacing one of the engine stages with a refrigerator, by Zhang (2016). The simulation results showed that it can reach a relative Carnot coefficient of performance of 28.5% at a refrigeration temperature of 5°C.

As in the torus thermoacoustic engine, the impressive contribution in the multi-stage engine was carried out by the Chinese Academy of Science. They have innovated the three-stage thermoacoustic devices that have a high performance capacity. Yang et al. (2014) presented the first numerical model for a three-stage thermoacoustic heat pump. The aim of the heat pump is to increase the temperature of a waste heat source to a higher useful grade. Unlike the previous looped tube and multi-stage engines, there is no need to construct the engine to a full one wavelength. The reason behind is the use of a linear motor having dual-opposed pistons in between each of the two stages (as shown in Figure 2.31), which shift the volumetric flow rate by 120°. The phase shifting was previously achieved by use of a long resonator. This will reduce the system size and acoustic load. The linear motor acts as a compressor at the start of each heat pump and as an expander at the end of it. With this arrangement, around 30% of the acoustic power produced on the compression side is consumed by the regenerator, and the system can use a low grade heat source to obtain heat energy at a much higher temperature. The system was designed to run using helium at 50 bar as working medium. The numerical results showed that each stage pump 1038.7 W of heat at a coefficient of performance of 2.99 with 56.5% relative to Carnot efficiency by absorbing 713.4 W of heat and consuming 347.1 W of acoustic power.

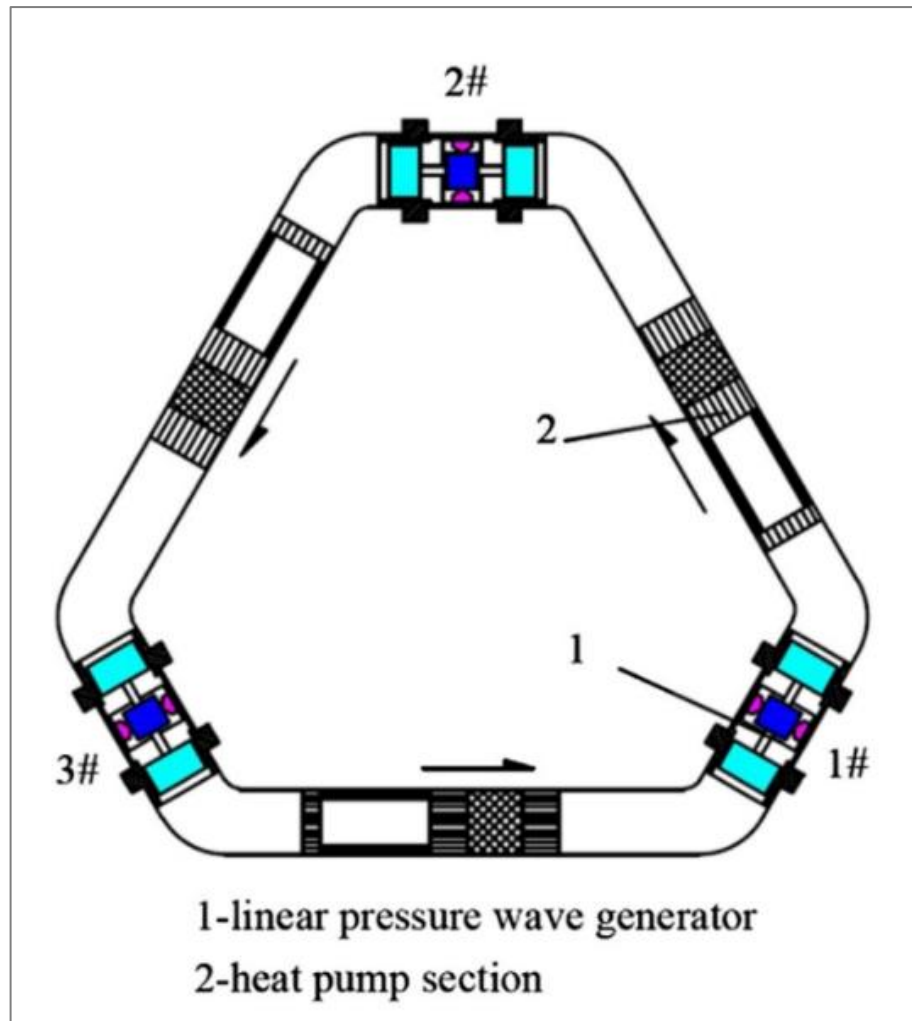


**Figure 2-31:** Schematic of the travelling-wave thermoacoustic heat pump (Yang *et al.*, 2014).

Li *et al.* (2014) adopted the three-stage configuration and built a three-stage thermoacoustic engine to study the heat to acoustic power conversion. As an engine, the compression alternator provides acoustic power. The regenerator amplifies the acoustic power in the direction of positive temperature gradient. This acoustic power will be dissipated by the expansion alternator to generate electricity. At this configuration, the acoustic impedance of the expansion alternator can be used to adjust the acoustic phasing conditions. At a mean pressure of 40 bar of helium, each stage of the engine generated 1080 W of acoustic power at 36% total efficiency. Wu *et al.* (2014b) developed the system aimed at generating useful electricity. The mean pressure was increased to 50 bar and 86 Hz working frequency. At hot side temperature to 650°C, the engine produced 1.57 kW of electricity by the three alternators at thermal-to-electric efficiency of 16.8%. Bi *et al.* (2015) improved the engine and pushed the power generation to the most generated recorded to date. Not

only have the linear alternators been changed, the acoustic network has also been adapted. The feedback tubes were replaced by narrow tubes. The mean pressure was to 60 bar and the working frequency was 70 Hz. The maximum generated electricity was 4.69 kW at 15.6% of thermal-to-electric efficiency and the highest efficiency was 18.4% at generated electricity of 3.46 kW.

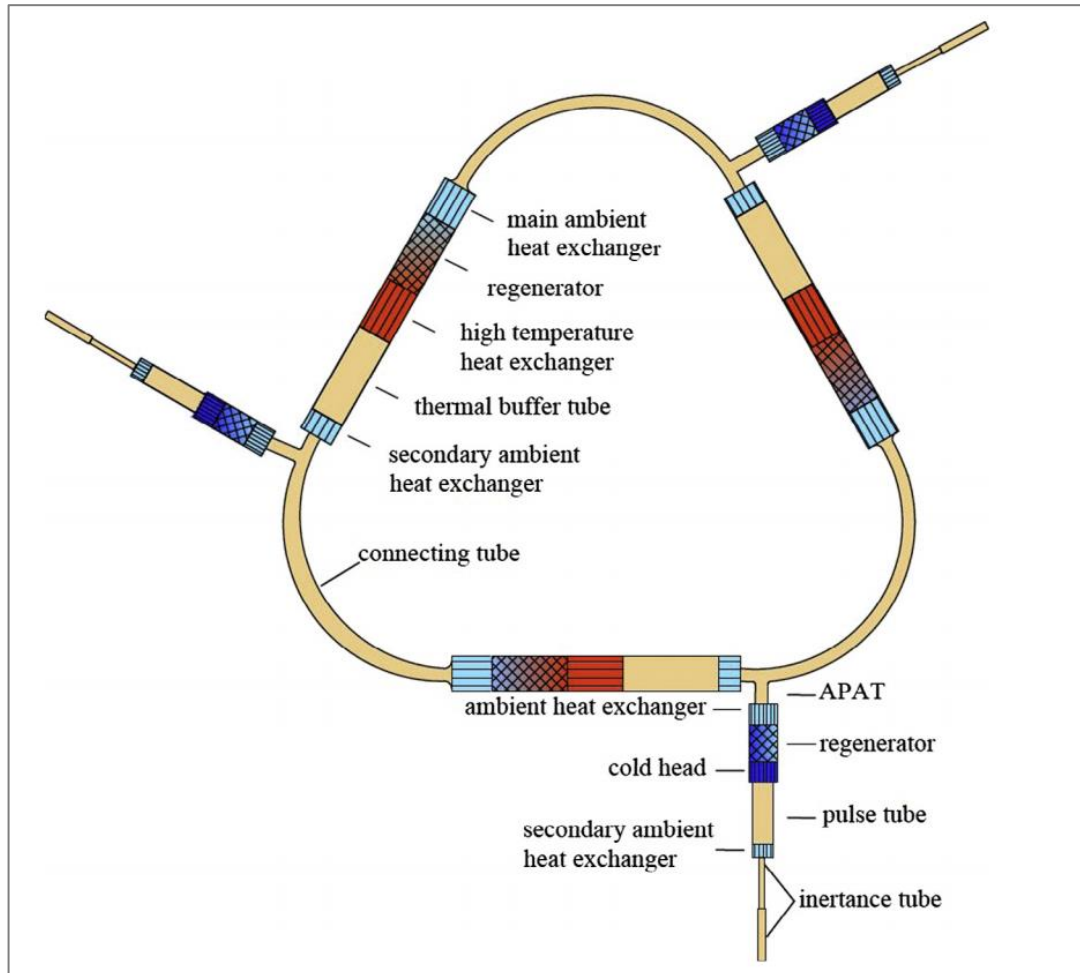


**Figure 2-32:** Schematic of a three-stage combined system Xu *et al.* (2015a)

The success of the high acoustic power generation of the three-stage engine encouraged the combination of a refrigerator instead of the linear alternator as a combined thermoacoustic system. Firstly, the coupling method and position were numerically studied by Xu *et al.* (2015a). The refrigerator cores were placed in branches as it has proven to perform better than the in-tube coupling. The coupling location was studied experimentally in the inlet, middle and outlet of the resonance tube. There are no linear alternators in this configuration, therefore, a phase adjuster of the inertance- reservoir type was attached after each refrigerator unit, as shown in Figure 2.32. The outlet coupling location was found to be the most efficient, the inlet

was 10% less and the outlet was the worst. The inlet location was chosen for further studies. Xu *et al.* (2015b) numerically optimized the combined system. The optimised design is promising to generate a cooling power of 7.75 W at a very low temperature of  $-196^{\circ}\text{C}$  and frequency of 300 Hz. Zhang *et al.* (2015) and Xu *et al.* (2016) built and tested the combined system. Using pressurized helium at 70 bar, the system generated 0.88 kW of cooling at  $-163^{\circ}\text{C}$  and 1.2 kW at  $-143^{\circ}\text{C}$ . Recently, Li *et al.* (2016) numerically up-graded the system into a four-stage combined system. The inertance-reservoir was replaced with dual linear alternators in the proposed design to adjust the phasing of the acoustic field and to generate useful electricity, as shown in Figure 2.33. The simulation results showed that this configuration can achieve a cooling power of 463.1 W at  $-163^{\circ}\text{C}$  while generating useful electricity of 553.7 W.

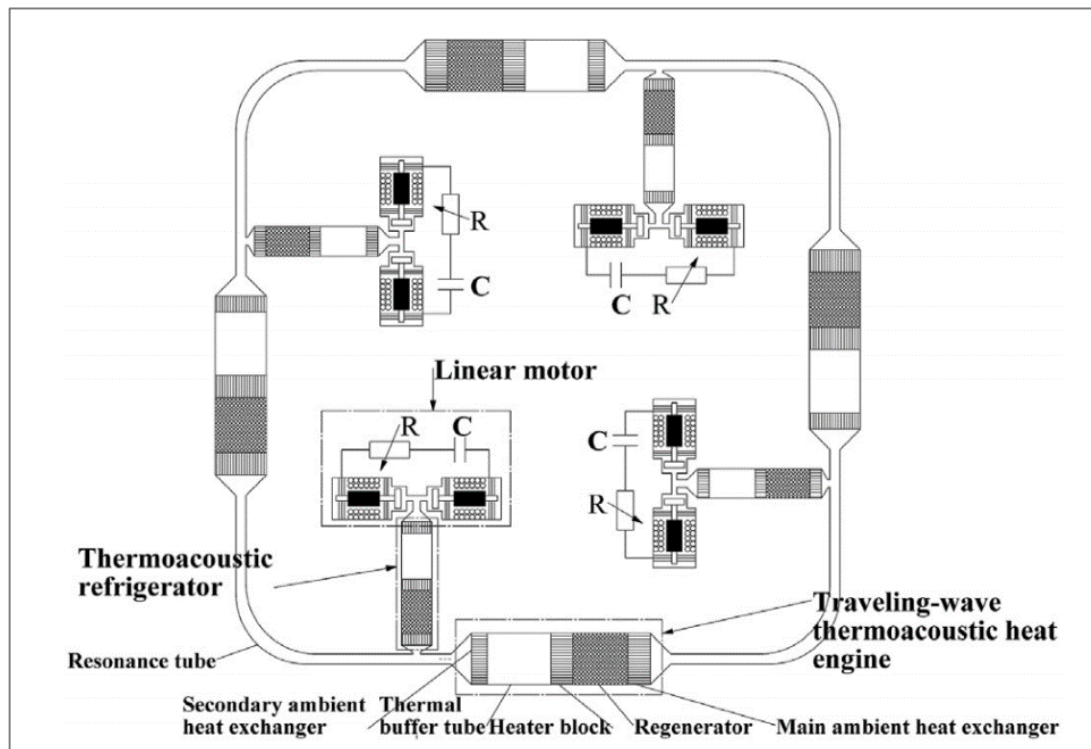


**Figure 2-33:** Schematic drawing of the four-stage combined system (Li *et al.* 2016).

## 2.7.4 Concluding remarks

The literature survey shows that the performance of the torus engine is higher than the looped tube thermoacoustic engine. The main reason is that the loop of the torus is a fraction of a wavelength, unlike the full wavelength of the looped tube, therefore it can run at a high acoustic impedance. The proposed solution for that is the multi-stage configuration which can run at a high acoustic impedance. Mainly there are two

problems with multi-stage engines; they are complex and expensive and require many linear alternators.

The present research offers an alternative solution to run the multi-stage looped tube with one linear alternator. The novel configuration of the engine consists of two identical half-wavelength stages with a linear alternator connected between them. The identical stages that generate acoustic power have the same identical acoustic pressure and volume flow rate amplitudes but are  $180^\circ$  out of phase. The out of phase acoustic power enables the linear alternator to be operated in push-pull mode. In fact, the acoustic intensity value will not reach the values of the torus engine. However, the linear alternator, if isolated from the acoustic network, can generate the same power at half the acoustic impedance as active acoustic power is beneficially applied from two sides.

## Chapter 3

### **Modelling and Optimization of a Two-Stage Thermoacoustic Engine Coupled to a Push-Pull Linear Alternator**

In this chapter, the modelling and numerical results of a two-stage thermoacoustic engine coupled to a push-pull linear alternator are presented. The conceptual design is introduced at the beginning of the chapter (Section 3.1). The linear alternator coupling and design description and optimization procedures using the DeltaEC programme are discussed in Section 3.2. Lastly in Section 3.3, the results of the simulations are presented.

#### **3.1. Conceptual Design**

As presented in Section 1.2, a third of the energy released from the burnt fuel of an internal combustion engine is typically released to the exhaust system. That amount of heat has attracted researchers to study the opportunity to recover it for power generation. Johnson (2002) listed thermoacoustic technology as a method to generate cooling from the waste heat of exhaust gases. Later on, Jadhao and Thombare (2013) highlighted the suitability of thermoacoustic technology for direct electricity generation. The looped tube thermoacoustic engine configuration was chosen in the present work to study electrical power generation from internal combustion engine exhaust gases. There are two main reasons for this. First, the acoustic wave of the looped tube engine is in traveling wave mode which offers potentially high efficiency. Second, the one wavelength configuration allows the engine to be designed in two identical stages, each having a power extraction point. This gives the opportunity for the second target of this study which is to connect one linear alternator to two points to run it as a push-pull alternator.

The configuration consists of two identical stages each having a power extraction point and the linear alternator connecting these two points as shown in Figure 3.1. The two power extraction points help to avoid high power spots and allow the stages to self-match. The self-matching stages have the same identical acoustic pressure and volume flow rate amplitudes but are out of phase by  $180^\circ$ . This means that each of the

two identical points of the two stages have the same acoustic pressure and volumetric flow velocity but shifted 180° in phase. This configuration allows the connection of the linear alternator to two points having the same amplitudes acting out of phase. The idea behind it is to increase the system efficiency by increasing the power output, at a specific acoustic impedance.

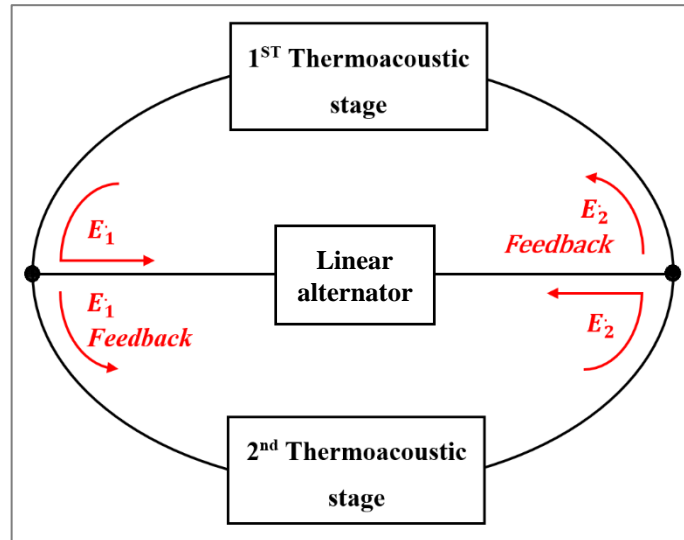


**Figure 3-1:** Conceptual drawing of the proposed two-stage engine.

As the engine was designed to use exhaust gases from an internal combustion engine, it was considered to simulate the exhaust gases heat quantity and quality for a Caterpillar 6.6L engine. Allis Chalmer (2009) showed that the exhaust gas temperature ranges between 400°C and 500°C depending on the load. The hot heat exchanger temperature was limited to 400°C in this project for two reasons. First, the temperature of low load was considered. Second, the temperature of the exhaust gases leaving the engine cools down before reaching the exhaust system, therefore, the high limit of the exhaust gases temperature was avoided. Helium was chosen to be the working gas because it has low Prandtl number and low viscosity which leads to low viscous dissipation. Also, helium has a high sound speed because it is a light gas, which leads to high power density (Swift, 2002). Added to that, helium has relatively high thermal penetration depth caused by the high thermal conductivity (direct relationship of Equation 2.3). This is preferred as it allows a relatively large channel width to be used and ease fabrication. The mean pressure of the thermoacoustic engines is proportional to the power density, and hence, the mean pressure needs to be as high as possible (Swift, 1988). High power density leads to high power generation and efficiency. However, there is a trade-off between the thermoacoustic

power density and the fabrication as high pressure requires a lot of fabrication considerations. These considerations are associated with the pressure sealing and heat exchanger channels width. Adding to these considerations is the fact that the hot parts of the engine will reach 400°C, and hence the metal will be softer and have less pressure endurance. Therefore, the mean pressure used in this project was limited to 28 bar. The linear alternator available for this project was a Q-Drive Model 1S132M, which has an optimum frequency of 60 Hz. The linear alternator frequency and the working gas defined the length of the engine. The engine was designed to be a one wavelength looped tube, and as shown in Equation 2.1 the wavelength is the ratio of sound speed to frequency. The relatively high sound speed of the helium and the limited frequency of the linear alternator results in a long wavelength.

### 3.2. DeltaEC Modelling

In the current work, DeltaEC was used to simulate the acoustic field in the thermoacoustic device. It is software created by the Los Alamos National Laboratory. The acronym DELTAEC is the abbreviation of Design Environment for Low Amplitude ThermoAcoustic Energy Conversion. The software performs calculations by integrating the one-dimensional wave equation for a pre-defined geometry, set of thermal conditions and working fluid. It does this through each of the user-defined elements, called "segments", such as ducts, heat exchangers, compliances, porous medium, etc., and ensures that the pressure and volumetric flow rates, both real and imaginary, are matched the boundaries of the sequent segments. The integration solves a series of equations that the acoustic pressure ( $p_1$ ), volumetric flow rate ( $U_1$ ), the gas mean temperature ( $T_m$ ) and the total power ( $\dot{H}$ ), of the acoustic field through the pre-defined series of segments Ward *et al.* (2012). Ward *et al.* (2012) presented the equations as follows:

$$\frac{dp_1}{dx} = -\frac{i\omega\rho_m}{A(1-f_v)}U_1 \quad 3.1$$

$$\frac{dU_1}{dx} = -\frac{i\omega A}{\rho_m a^2} \left[ 1 + \frac{(\gamma-1)f_k}{1+\varepsilon_s} \right] p_1 + \frac{\beta(f_k-f_v)}{(1-f_v)(1-\sigma)(1+\varepsilon_s)} \frac{dT_m}{dx} U_1 \quad 3.2$$

$$\frac{dT_m}{dx} = \frac{\dot{H}_2 - \frac{1}{2} \operatorname{Re} \left[ p_1 \tilde{U}_1 \left( 1 - \frac{T_m \beta (f_k - \tilde{f}_v)}{(1 + \varepsilon_s)(1 + \sigma)(1 - \tilde{f}_v)} \right) \right]}{\frac{\rho_m c_p |U_1|^2}{2A\omega(1 - \sigma)|1 - f_v|^2} \operatorname{Im} \left( \tilde{f}_v + \frac{(f_k - \tilde{f}_v) \left( 1 + \frac{\varepsilon_s f_v}{f_k} \right)}{(1 + \varepsilon_s)(1 + \sigma)} \right) - (Ak + A_{solid} k_{solid})} \quad 3.3$$

$$\begin{aligned} \dot{H}_2 = & \frac{\rho_m c_p |U_1|^2}{2A\omega(1 - \sigma)|1 - f_v|^2} \frac{dT_m}{dx} \operatorname{Im} \left( \tilde{f}_v + \frac{(f_k - \tilde{f}_v) \left( 1 + \frac{\varepsilon_s f_v}{f_k} \right)}{(1 + \varepsilon_s)(1 + \sigma)} \right) - (Ak + \\ & A_{solid} k_{solid}) \frac{dT_m}{dx} + \frac{1}{2} \operatorname{Re} \left[ p_1 \tilde{U}_1 \left( 1 - \frac{T_m \beta (f_k - \tilde{f}_v)}{(1 + \varepsilon_s)(1 + \sigma)(1 - \tilde{f}_v)} \right) \right] \end{aligned} \quad 3.4$$

The generation or dissipation of the acoustic power can be represented by (Swift, 2002):

$$\frac{d\dot{W}_a}{dx} = \frac{1}{2} \operatorname{Re} \left[ \tilde{U}_1 \frac{dp_1}{dx} + \tilde{p}_1 \frac{dU_1}{dx} \right] \quad 3.5$$

Here  $A$  is the cross-sectional area of the channel.  $\omega$  is the frequency.  $i$  is the imaginary unit.  $\operatorname{Re}$ ,  $\operatorname{Im}$  and superscript  $\sim$  indicate the real, imaginary parts and conjugation of a complex component.  $f_k, f_v$  are thermal and viscous functions.  $\varepsilon_s$  is the ratio of gas to solid heat capacities.  $a, c_p, k, T_m, \rho_m, \beta, \gamma, \sigma$  are the speed of sound, isobaric specific heat capacity, thermal conductivity, mean temperature, mean density, gas expansion coefficient, specific heat ratio and Prandtl number of the working gas.

The first step in modelling the thermal and acoustic network is to determine the required acoustic field at the linear alternator to generate electricity efficiently. A simulation was undertaken for this purpose to investigate the linear alternator performance for both the push-pull and compliance housing coupling at various acoustic impedances and phase differences (between volume flow rate and the pressure) at a specific frequency and stroke. The performance was represented by the electricity generated and the acoustic-to-electrical efficiency. The linear alternator specifications listed in Table 3.1 were used as input values to a DeltaEC simulation model. The simulation was undertaken at 56 Hz which was pre-defined by the manufacturer to be the best working frequency for this linear alternator. The piston stroke was assumed to be 12 mm. Figure 3.2 shows the coupling configuration of the push-pull and compliance coupling. In the push-pull coupling, acoustic power flows

from each side of the housing acting out of phase on the linear alternator piston, while there is an active acoustic power from a side and a dead volume acting as an acoustic compliance from the other side in compliance coupling.

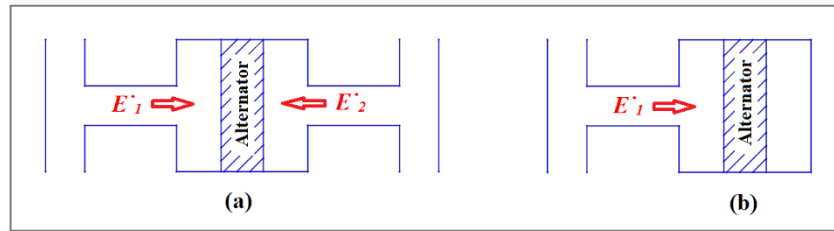


**Figure 3-2:** Linear alternator coupling configurations (a) push-pull (b) compliance housing

**Table 3-1** Linear alternator specifications (Q-Drive 1S132M)

Parameter	Value
Core impedance	2 ohm DC, (18 @ 60 Hz)
Stator inductance	46 mH
Rated operating voltage/current	110 VAC rms @ 60 Hz/4.0 A rms
Peak-to-peak stroke limit	14 mm
Nominal BL product	47 N/Ampere (approximate)
Intrinsic Stiffness	6 kN/m (approximate)
Damping, Rm	7.0 N-s/m (approximate)
Moving mass	0.721kg

Swift (2002) defined the acoustic impedance as the ratio of pressure to volume flow rate ( $Z = p_1/U_1$ ). As we have already considered that frequency and piston stroke are the same for all the cases studied, this means that the volumetric flow rate is constant as:

$$U_1 = \omega A \xi \tag{3.6}$$

where  $\omega$  is the angular frequency, A is the piston cross-section and  $\xi$  is the piston displacement. This means that the simulation considers the change in the acoustic impedance was caused by the change in pressure amplitude. The push-pull coupling is expected to generate double the electricity as compared with the compliance housing coupling at a specific local acoustic impedance and a phase difference, as the acoustic power is:

$$E = \frac{1}{2} |p_1| |U_1| \cos \Phi_{pU} \quad 3.7$$

where  $\Phi_{pU}$  is the phase angle between the volume flow rate phase and the pressure phase.

Normally, the performance study of the linear alternator is based on the acoustic impedance across the alternator and the phase difference (between the pressure and volume flow rate phases). The acoustic impedance across the alternator is the ratio of the pressure difference before and after the alternator to the volumetric flow rate ( $Z_a = \Delta P/U$ ). The phase difference is the pressure phase difference across the alternator ( $Ph(P_x)$ ) and the volumetric flow rate phase ( $Ph(U)$ ).

In the current study a different approach is followed. To highlight the impact of the coupling method on the required local acoustic impedance, the alternator performance study is based on the local acoustic impedance acting on the alternator piston instead of the pressure difference across the alternator. The push-pull model considers equal and out of phase acoustic impedance acting on the piston from both sides. Therefore, the simulation result graphs will show the local acoustic impedance value of one side, assuming the same value acting on the other side. The compliance housing model is based on local acoustic impedance acting from one side and there is a compliance from the other side representing the gas volume between the alternator body and the housing. As the study focuses on the local acoustic impedance, the phase difference is the difference between volumetric flow phase and pressure phase ( $Ph(U)-Ph(P)$ ).

The simulation results shown in Figure 3.3 confirm that the push-pull configuration can generate approximately double the electricity at the same local acoustic impedance as compared with the compliance coupling. Comparing the linear alternator performance at an amount of local acoustic impedance at the push-pull configuration to the linear alternator performance at double the local acoustic impedance for the compliance housing configuration, the compliance configuration was able to generate electricity higher than the push-pull configuration by 2 - 4%. This increment was caused by the linear alternator as it ran at a higher efficiency at higher local acoustic impedance. The graphs below can be used to decide the acoustic

impedance and phase difference at the linear alternator after deciding the performance level of the engine.

These graphs are useful in designing the thermoacoustic network and decide a coupling location. Firstly, they can be used to define the required local acoustic impedance and phase difference required at the coupling location. For a specific electricity generation and efficiency, a range of acoustic impedances can be selected. The selection of the local phase difference can determine the exact amount of local acoustic impedance. Alternatively, the graphs can be used during the modelling optimization. Optimizing any part of the acoustic network will have an influence on the acoustic impedance and phase difference along the engine. These graphs help to track the influence on the performance of the alternator.

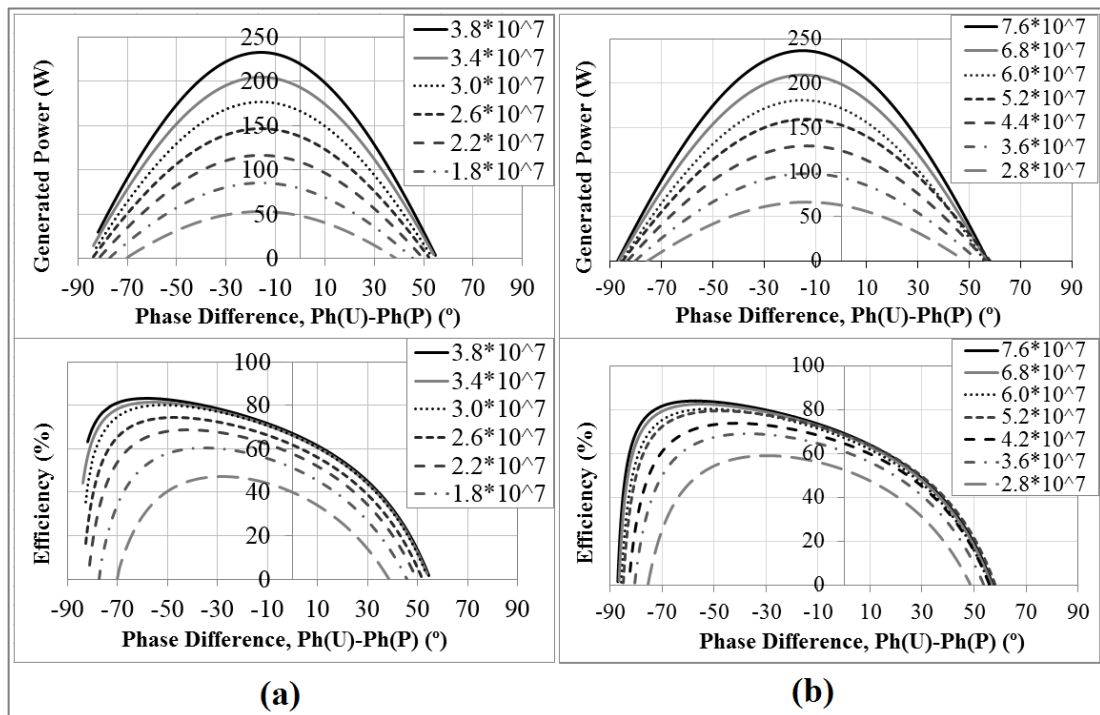


**Figure 3-3:** Linear alternator behaviour at various acoustic impedances and phase differences at the piston (a) push-pull coupling and (b) compliance housing coupling.

The shooting method (Ward *et al.*, 2012) was used in this code to find the guess values consistent with the target results. As a first step, the boundary conditions were set up and the geometries of each component were defined. The solutions were then guessed in order to meet the targets by solving the set of linear thermoacoustic equations. The DeltaEC shooting method, Ward *et al.* (2012), showed that it was not possible to run

two identical stages as expected. The two identical stages, when each has a power extraction point, should have the same thermal and acoustical performance and this is what the shooting method failed to follow. The modelling was done as half of the engine which is one stage and the other stage was represented as a self-excited hypothetical flow. There are two self-excited hypothetical flows in this engine, each has a specific flow characterisation based on the author's understanding of the identical stages and push-pull connection. The first self-excited hypothetical flow is the flow entering the first stage which represents the flow at the end of the second stage. The characterisation of this flow was suggested based on the wave behaviour at two identical stages. To apply this behaviour the following boundary conditions were made. The pressure amplitude, volumetric flow rate and total power was set to be equal at the beginning and the end of the simulated stage, as they are expected to repeat themselves over the two identical stages. In contrast, the phase between pressure and velocity was set to be shifted by  $180^\circ$  at the end of the stage with reference to the beginning, so the wave phases will repeat. The six boundary conditions shown in equations 3.8-3.13, were set as targets at  $x=\lambda/2$  shown in figure 3.5, relating  $x=\lambda/2$  to  $x=0$ .

$$\frac{T_{x=\lambda/2}}{T_{x=0}} = 1 \quad 3.8$$

$$\frac{P_{x=\lambda/2}}{P_{x=0}} = 1 \quad 3.9$$

$$\frac{Ph(P)_{x=\lambda/2+180^\circ}}{Ph(P)_{x=0}} = 1 \quad 3.10$$

$$\frac{U_{x=\lambda/2}}{U_{x=0}} = 1 \quad 3.11$$

$$\frac{Ph(U)_{x=\lambda/2+180^\circ}}{Ph(U)_{x=0}} = 1 \quad 3.12$$

$$\frac{H_{x=\lambda/2}}{H_{x=0}} = 1 \quad 3.13$$

Where  $T$  is temperature,  $P$  is pressure amplitude,  $Ph(P)$  is pressure phase,  $U$  is volumetric flow,  $Ph(U)$  volumetric flow phase and  $H$  is the total power.

The second self-excited hypothetical flow is applied to the other side of the linear alternator. Based on the push-pull run characterization, the pressure amplitude, volumetric flow and velocity phase was set to be equal on both sides of the alternator piston. While, only the pressure phase was set to be out of phase (phase difference of  $180^\circ$ ), and this will push all the other three to act as push-pull. The three boundary conditions shown in equations 3.14-3.16, were set as targets at locations 1 and 2 shown in figure 3.5.

$$\frac{P_2}{P_1} = 1 \quad 3.14$$

$$\frac{Ph(P)_2 + 180^\circ}{Ph(P)_1} = 1 \quad 3.15$$

$$\frac{H_2}{H_1} = 1 \quad 3.16$$

The modelling procedure consisted of two steps. Firstly, the main layout parameters were defined. Secondly, an optimization was made of every detail of the engine parts. There are several parameters which should be considered in the optimization, local acoustic impedance, oscillation peak-to-peak displacement, generated electricity, thermal-to-electrical efficiency and thermal-to-acoustic efficiency as will be presented in this chapter.

The parameters defining the layout of the engine are: total length, cross-sectional area ratio, regenerator location and linear alternator location. The total length was defined by the working gas and the working frequency. Equation 2.1 showed that the wavelength is the ratio of the speed of sound of the working gas to the working frequency. The cross-sectional area ratio is the ratio of the regenerator to the feedback loop cross-sectional area. This ratio is preferred to be higher than one to reduce the local oscillation velocity at the regenerator. This will help to reduce the viscous dissipation of acoustic power in the regenerator. Figure 3.4 shows the effect of the cross-sectional area ratio on the five main parameters. Obviously, high acoustic impedance is more favourable to generate higher electricity as presented previously. However, a ratio higher than six will damp the oscillation and hence reduce both the generated electricity and the thermal-to-electric efficiency. The presented acoustic impedance and oscillation displacement are in the regenerator. Based on these results,

a cross-sectional area ratio of 6 has been chosen. The thermoacoustic core was selected to be 10 cm diameter for the ease of heat exchanger fabrication, leaving the feedback loop to be around 4 cm diameter tube. The uniform cross-section tube feedback loop could be replaced by a compliance-inertance to reduce the total length.

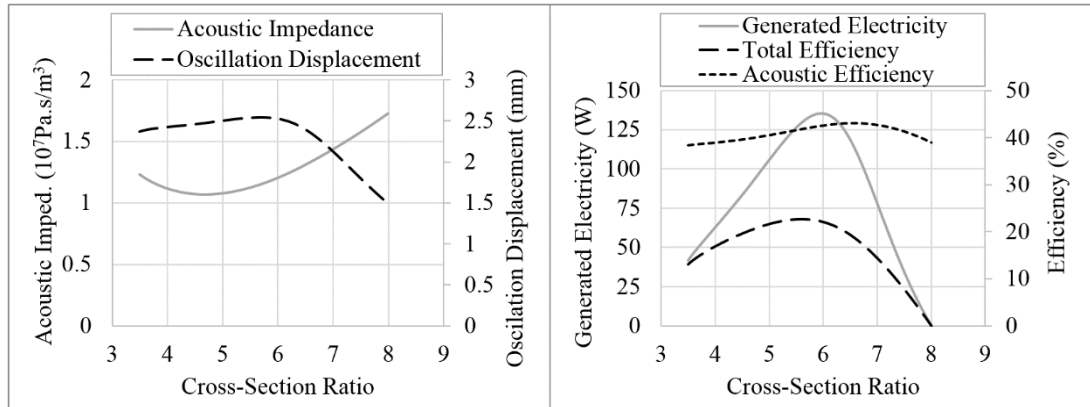


**Figure 3-4:** The effect of the cross-sectional area ratio on various parameters.

For the same aim of reducing the viscous dissipation of acoustic power at the regenerator, the regenerator should be located at the pressure antinode where the acoustic impedance is significantly higher than  $\rho a/A$  (Swift, 2002). The linear alternator branch should be as close as possible to the regenerator to be at a high acoustic impedance to generate higher electricity. The branch needs to be either before or after the regenerator. After the regenerator is favoured as the acoustic power will be higher than at the end of the feedback loop. The acoustic power is lower at the end of the feedback loop because of the acoustic power losses through the feedback loop. A block diagram of the segments in the DeltaEC simulation showing the main layout and parts is shown in Figure 3.5.

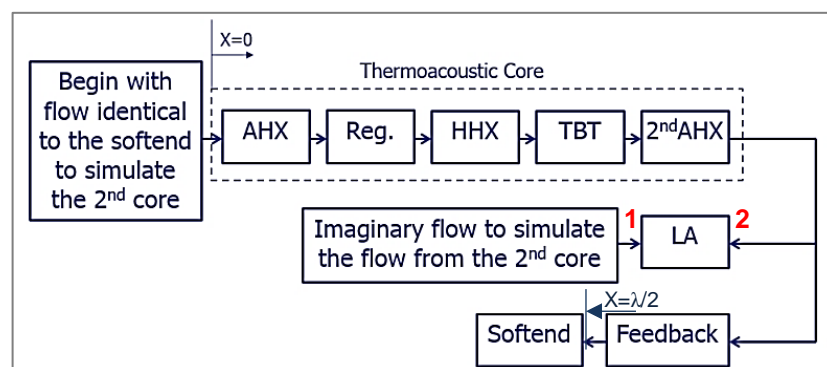


**Figure 3-5:** Block diagram of the segments in the DeltaEC simulation: ambient heat exchanger (AHX), regenerator (Reg), hot heat exchanger (HHX), thermal buffer tube (TBT), secondary cold heat exchanger (2<sup>nd</sup>AHX), feedback pipe (Feedback), linear alternator (LA).

The parts optimization process starts from the heart of the engine which is the regenerator as it amplifies the acoustic power. The temperature must increase through the regenerator in the direction of the acoustic power flow to generate acoustic power (Swift, 2002). The regenerator is defined by the hydraulic radius  $r_h$  and the volumetric porosity. The hydraulic radius is the ratio of gas volume to gas-solid contact area and can be thought of as the distance from a typical gas parcel to the nearest solid surface. Swift (2002) summarizes the relationships between the hydraulic radius and the thermal and viscous penetration depths in the regenerator as  $\delta_v \gg r_h$  and  $\delta_k \gg r_h$ . Yu et al. (2005) concluded that the optimum ratio of the hydraulic radius  $r_h$  to the thermal penetration depth  $\delta_k$  for travelling wave engines is between 4 and 7. Figures 3.6 and 3.7 show the optimization curves of the regenerator  $\delta_k/r_h$  and its length versus the performance parameters. The optimization is a trade-off between the increasing and decreasing parameters. Based on these two charts, the  $\delta_k/r_h$  should be between 4 and 6 and the length between 65 mm and 80 mm, in order to gain high electricity efficiently while maintaining relatively high oscillation displacement. Figure 3.8 shows the effect of regenerator porosity on the five parameters, from which it can be deduced that it should be 70% and 85%. The final selection of the  $r_h$  and porosity will be made based on the results of the optimization process as well as on the available materials on the market.

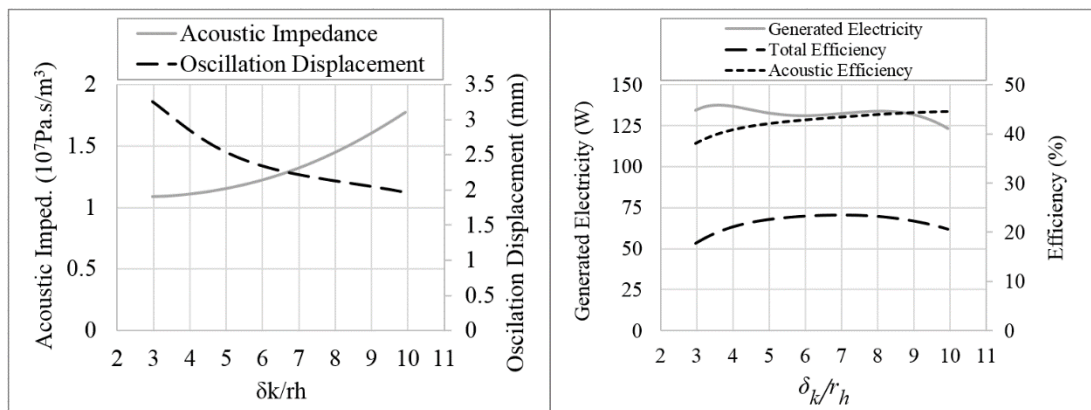


**Figure 3-6:** The effect of  $\delta_k/r_h$  through the regenerator on various parameters

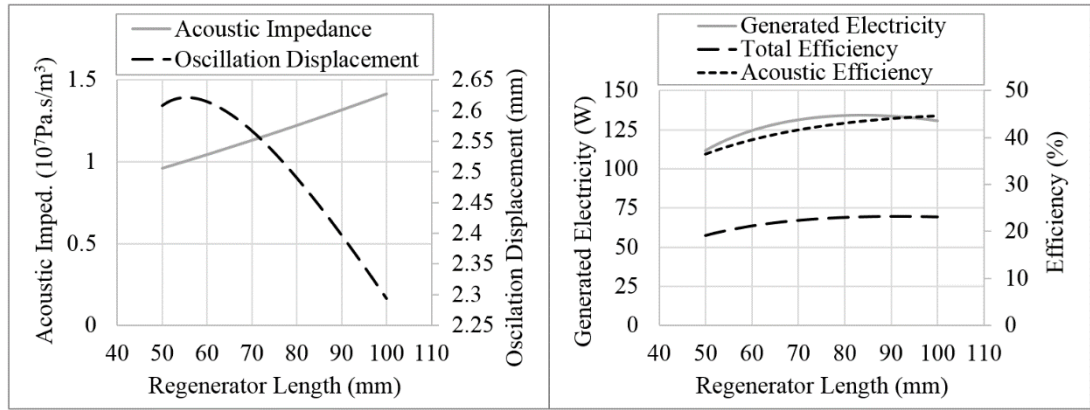


**Figure 3-7:** The effect of the regenerator length on various parameters

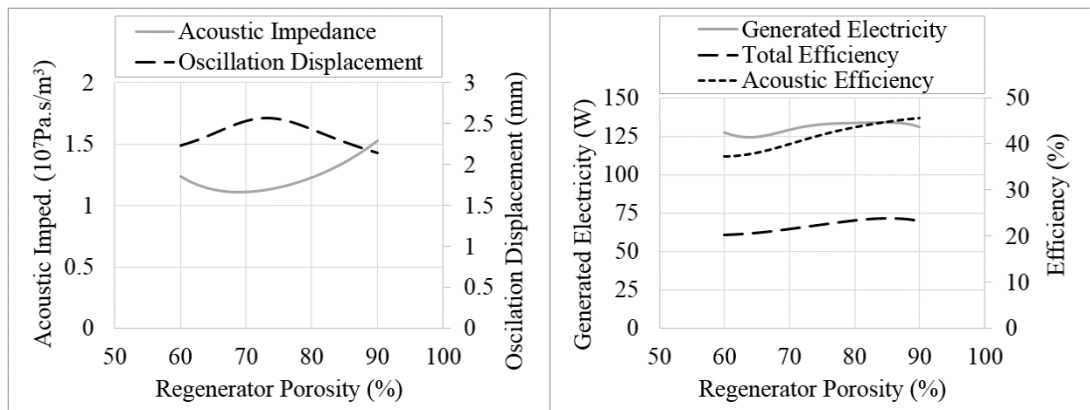


**Figure 3-8:** The effect of the regenerator porosity on various parameters.

The hot heat exchangers selected are cross-flow parallel plate heat exchangers. The optimization of the heat exchangers includes the plate spacing and the blockage ratio. These two parameters were studied for all the three heat exchangers; however, the results of the hot heat exchanger will be presented here. Figure 3.9 shows the effect of the ratio of the plate spacing to the thermal penetration depth. Clearly, a ratio of less than one will reduce the oscillation displacement and hence the heat transfer and any value between 1 and 4 is acceptable (preferably close to one). The effect of the blockage ratio which is the ratio of the solid area to the gas area is shown in Figure 3.10. As expected, the lower the blockage ratio the better the performance will be. The length of the heat exchanger in the oscillation direction should be equal to the peak-to-peak gas displacement in that local region (Swift, 2002). The final values were selected after surveying the manufacturing facilities.

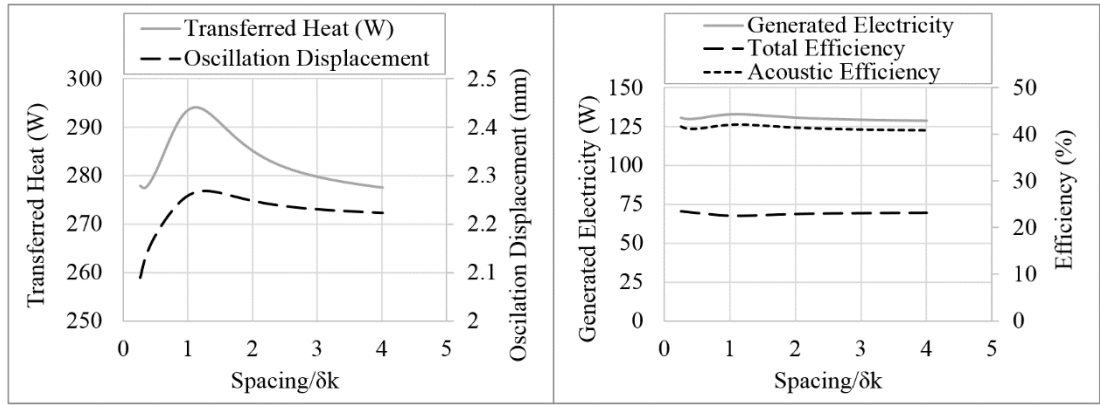


**Figure 3-9:** The effect of *fin spacing*/ $\delta_k$  through the hot heat exchanger on various parameters.

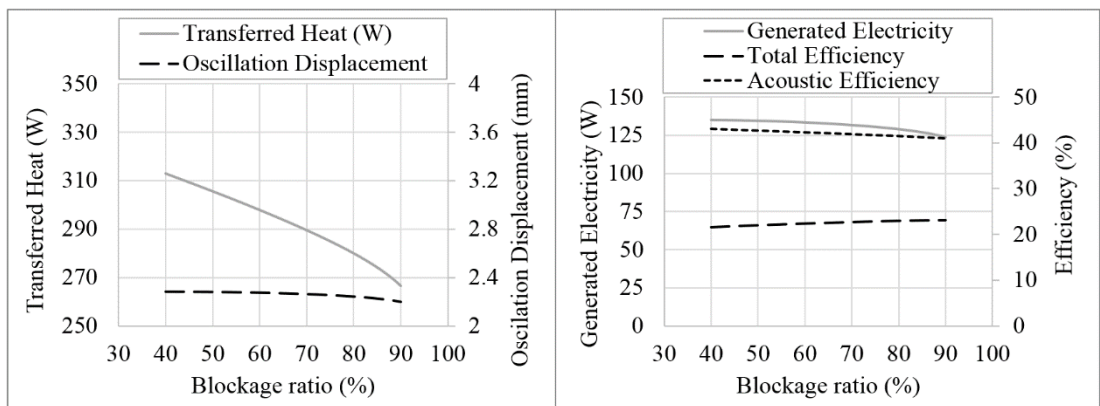


**Figure 3-10:** The effect of the heat exchanger blockage ratio on various parameters.

The thermal buffer tube reduces the area by 50% to suppress Rayleigh streaming, as recommended by (Swift, 2000). Figure 3.11 shows the optimization of the length. It shows that the electricity generated and the thermal-to-electrical efficiency reached the maximum at TBT lengths between 150 mm and 200 mm.

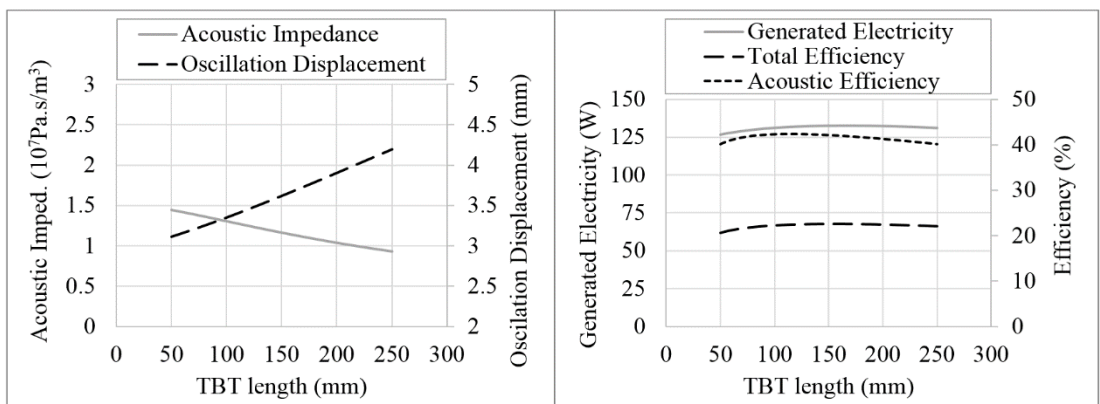


**Figure 3-11:** Effect of the length of the thermal buffer tube on various parameters.

The last parameter is the cross-sectional area/diameter of the feedback loop. The feedback loop cross-sectional area was optimized with the regenerator cross-sectional area previously. The feedback loop diameter was found to be a very sensitive as it changes the electricity generation from nil to its maximum with a 3 mm change only, as shown in Figure 3.12. Decreasing the feedback loop diameter leads to an increase in the acoustic impedance along the engine. However, it shifts the phase difference to the far left end of Figure 3.3a, which reduces the linear alternator efficiency and hence the power generation. The optimum loop length was found to be between 40 mm and 41 mm. The model of a uniform cross-section feedback loop was unable to generate electricity as the phase difference at the linear alternator was at the far left end of Figure 3.3a. For the purpose of adjusting the phase, the last 275 mm of the feedback loop was reduced to a diameter of 26 mm. This tuned the phase difference at the linear alternator to be  $-45^\circ$ .

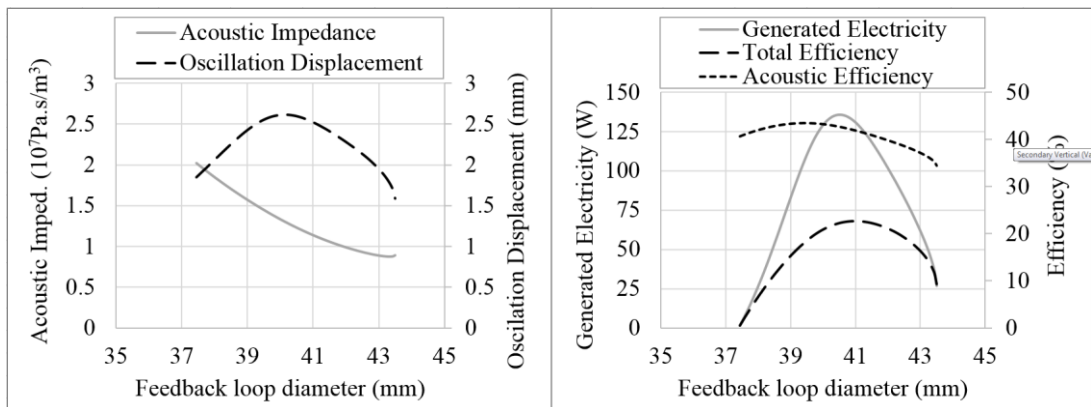


**Figure 3-12:** Effect of the feedback loop diameter on various parameters.

### 3.3. Simulation Results

Following the concept and optimization discussed before, the simulation modelling continued considering several operational and performance parameters. After several trade-off optimization processes, a final model which has dimensions based on the dimensions of parts available in the market showed that this configuration can convert the thermal power to electricity efficiently.

Figure 3.13a shows the calculated pressure amplitude distribution along the engine loop. There are two peaks, both are near the regenerators of the two stages. There is a major pressure drop at the regenerator and a minor drop at the linear alternator. The major drop is caused by the flow resistance at the regenerator and the minor drop is

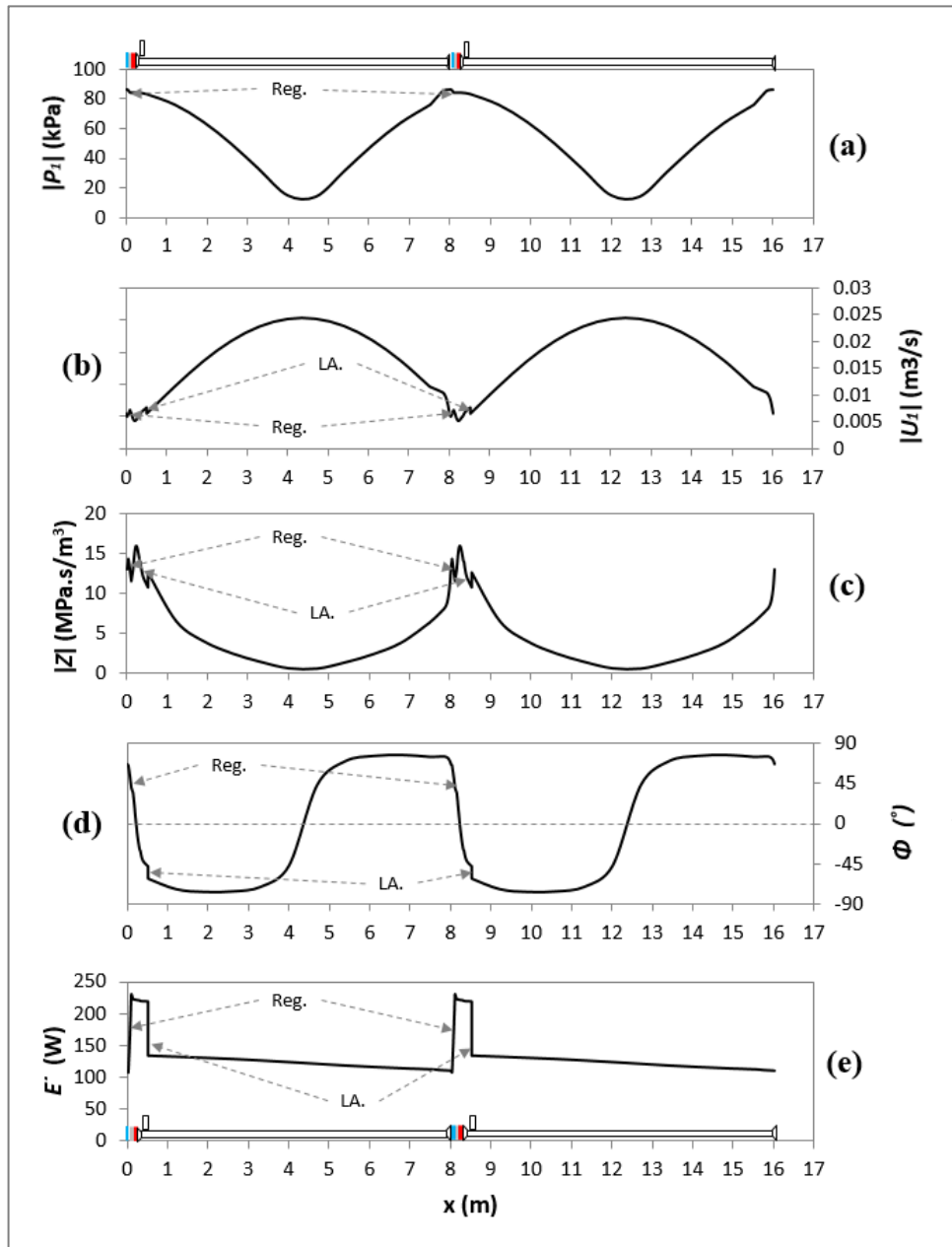
due to power extraction at the linear alternator. Figure 3.13b shows the distribution of volumetric velocity along the thermoacoustic engine. The engine was designed to have the lowest volumetric flow rate at the regenerator. The small volumetric flow velocity at the regenerator is essential to minimize viscous dissipation. The effect of the temperature difference across the regenerator is seen in the volumetric flow rate profile as it increases with the regenerator limits from the cold end towards the hot end. There is a volumetric flow rate drop at the linear alternator branch caused by the power extraction at the linear alternator.

Figure 3.13c is the acoustic impedance profile along the engine. It can be seen that the acoustic impedance is nearly maximum at the regenerators which is one of the design strategies. The acoustic impedance drop within the regenerator, caused by the pressure drop and velocity amplification. The impedance drops until the middle of the feedback loop and increases again as per the fluctuation of the pressure and volumetric flow rate amplitudes.

Figure 3.13d shows the phase difference between the velocity and pressure oscillations along the engine. This graph illustrates that the regenerators were placed at near travelling-wave locations. It is clear that the engine needs to be modified to have a mechanism of phase adjustment in the feedback loop. This figure shows that the engine feedback loop mainly has standing wave phase differences mode of  $90^\circ$  or  $-90^\circ$ . This effect occurs in looped tube travelling wave devices as the operating is neither pure travelling wave mode nor pure standing wave mode. The thermoacoustic effect is a combination of standing and travelling wave. Figure 3.13e shows the acoustic power distribution along the engine. It is shown that the 110.1 W is fed into the ambient end of the regenerator and it is amplified to 234.4 W at the hot end.

The numerical results showed that the engine runs at a frequency of 55.1 Hz. The engine was found to be able to produce 133.2 W of electricity through the linear alternator out of 577.6 W of heat. The heat is injected to the system through the HHXs of the two stages at a value of 293.25 W at each stage. Each stage generates an acoustic power of 124.2 W. The thermoacoustic engine thermal-to-electrical efficiency is 23.06%, while the heat-to-acoustic efficiency is 43.02%. The Carnot efficiency could be calculated using the temperatures at the ends of the regenerators. The hot side

temperature was 400°C and the cold side was 25°C, and hence the Carnot efficiency is 55.7%. The fraction to Carnot efficiency is the heat-to-acoustic efficiency divided by the Carnot efficiency and it is calculated to be 77.2%. Each stage delivered an acoustic power of 85.3 W to the linear alternator, leaving the linear alternator efficiency to be 78.57%. Appendix two gives the full DeltaEC model with all the segments.



**Figure 3-13:** Simulation results (a) pressure amplitude, (b) volumetric flow, (c) acoustic impedance, (d) phase difference angle and (e) acoustic power flow, the schematic drawing at the bottom and top of the figure shows a simplified layout of the engine.

### **3.4 Concluding Remarks**

A model was built using DeltaEC programme. It has been started by investigating the performance behaviour of the linear alternator under both push-pull and compliance coupling. A conceptual design was presented and step-by-step optimization showed how the final configuration was reached. The model showed that the linear alternator could be connected to two identical stages and generate electricity by extracting acoustic power from both sides. The numerical results showed that the engine runs at a frequency of 55.1 Hz. The engine was found to be able to produce 133.2 W of electricity through the linear alternator out of 577.6 W of heat.

## Chapter 4

### Experimental Set-up

In this chapter, the design and fabrication of the experimental rig is presented in Section 4.1. The measurement techniques are explained in Section 4.2 and finally, the heating and cooling systems are discussed in Section 4.3.

#### 4.1 Experimental Apparatus

The experimental apparatus, shown in figure 4.1, consists of two sections: the thermodynamic section and the acoustic section. The thermodynamic section is where heat is transferred to or from the working gas, while the acoustic section is the tubing network transmits the acoustic power from one place to another.

There are some common issues in both sections which will be discussed first. The design, materials and parts selection criteria were based on the availability and durability for the working pressure, pressure sealing of the working gas and moderate cost. Figure 4.1 is a photograph of the experimental rig, the tubes and fittings used in this rig are schedule-40 stainless steel welded pipes. The pipe selection was based on the pressure durability and the internal diameter only, matching the modelling diameter, as there was no concern about the weight at this stage of the research. For the two tubes and reducer of the thermodynamic section, the pressure rating at elevated temperatures was considered as well as the material supplier pressure rating tables.

The rig was constructed so as to have pieces of moderate weight for ease of transportation. The separate pieces were assembled and secured using 300 lb class flanges. The flange-to-flange and flange-to-heat exchanger joints were sealed with O-rings. Considering the working gas is helium at 28 bar, FKM Viton O-rings were selected. The O-ring properties are: 75 hardness shore A, 70 bar tensile strength, 210% elongation and a temperature range of -20-200°C. O-ring grooves were machined in the flanges following the supplier recommended dimensions, an example of an O-ring accommodated by a groove shown in Figure 4.4c. Various feedthrough fittings were

used in this rig. BSPT and NPT sockets were welded directly to the tubes to accommodate these feedthrough fittings.

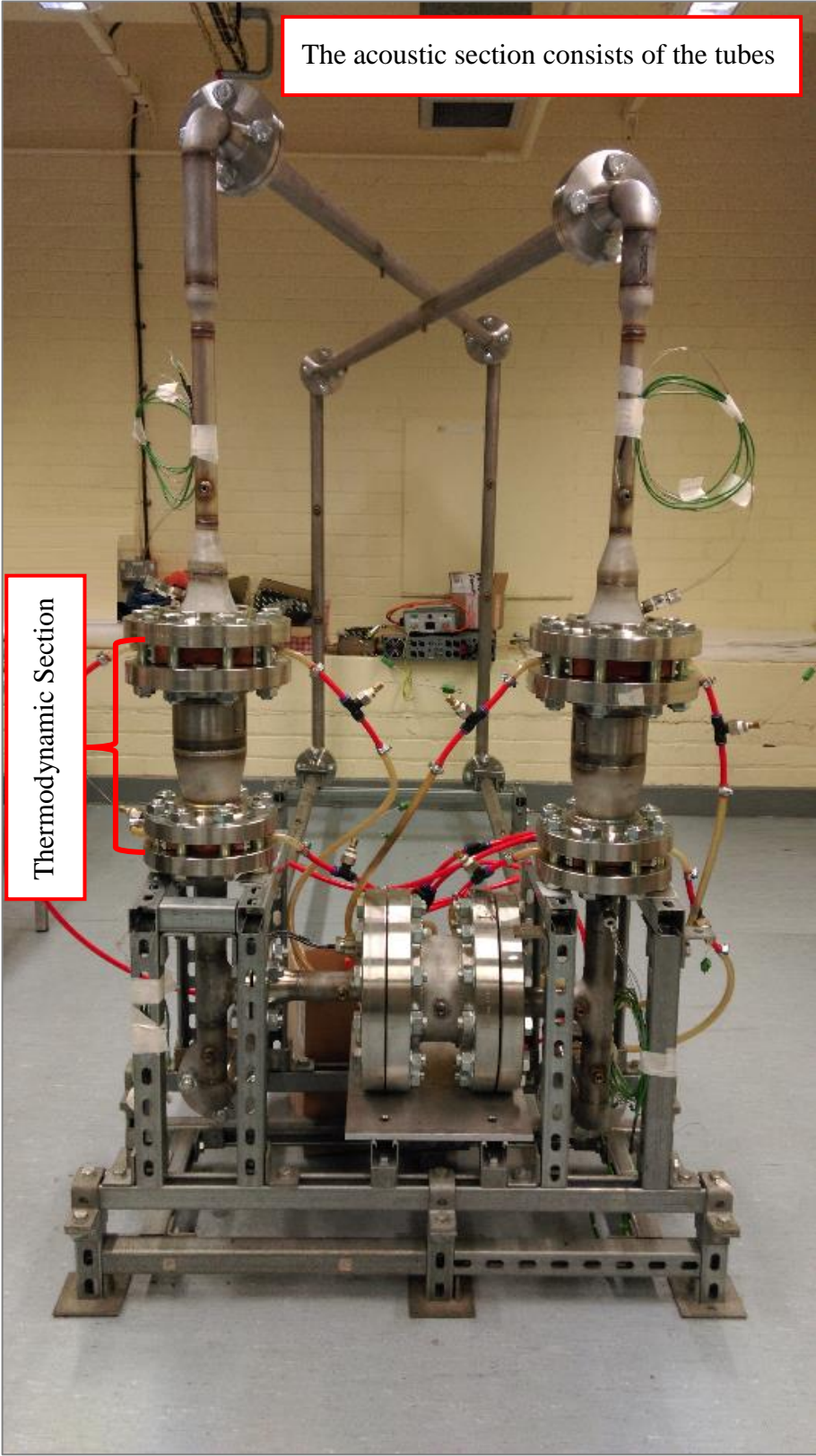


**Figure 4-1:** A photograph of the experimental rig

### 4.1.1 Thermodynamic section

This section consists of an ambient heat exchanger, regenerator, hot heat exchanger, thermal buffer tube and secondary ambient heat exchanger. Figure 4.2 shows a cross-sectional view of this section. The regenerator and the adjacent heat exchangers are 102 mm (4 inch) in diameter. The section diameter then reduces towards the secondary ambient heat exchanger to 77.5 mm (3 inch) through the thermal buffer tube.

To reduce gas leakage problems which might appear at elevated temperatures in sealing the hot parts, the regenerator holder, hot heat exchanger and the thermal buffer tube were fabricated as one piece. The hot section containing the regenerator, hot heat exchanger and thermal buffer tube was thermally insulated to reduce the heat losses to the surroundings. It was wrapped with two layers of 12 mm thick flex wrap insulation blanket, GLOWING EBBERS model 125/150-1M.

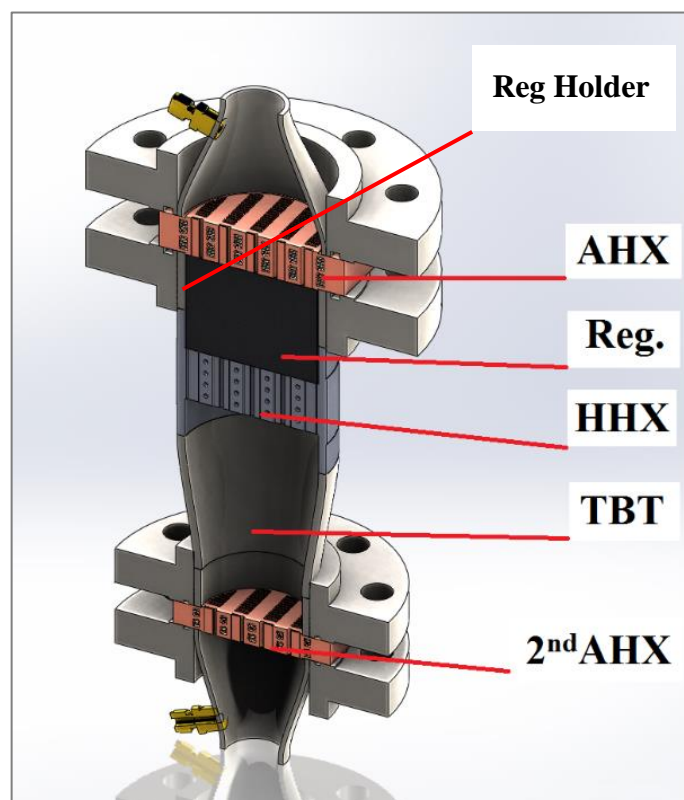


**Figure 4-2:** Cross-section of the thermodynamic section, ambient heat exchanger (AHX), regenerator (Reg), hot heat exchanger (HHX), thermal buffer tube (TBT), secondary cold heat exchanger (2<sup>nd</sup> AHX).

The ambient heat exchanger is a cross flow heat exchanger. The helium oscillates in the small channels of the circular face (101.75 mm diameter) shown in Figure 4.3a. The circular side has 1 mm protruding out of the block for ease of alignment with the regenerator holder from one side and the reducer from the other side. Water at ambient temperature flows in the cross flow channels. The AHX was made out of a block of copper to ensure good heat transfer from the helium to the cooling water. The block sides are 142, 138 and 30 mm. On both the water and oscillatory helium sides, continuous channels were cut out using EDM (Electrical Discharge Machining). The continuous cut of the EDM in a square wave form cuts the material to leave fins in a comb pattern. The staggered fins are each adjacent to a cooling water channel, as shown in Figure 4.3c. The fins are 0.5 mm in width, on the helium side the fins are 9 mm long, and 6 mm long on the water side. The channels between the fins are 1 mm wide. At this configuration, the contact area between the helium and the heat exchanger channel walls is  $0.1317 \text{ m}^2$ , and  $0.1054 \text{ m}^2$  between the cooling water and channel walls. The AHX was designed to have a higher contact area from the helium side as the helium has a lower heat transfer coefficient and as well to reduce the blockage ratio on the helium side. These two areas were used in the conduction-convection heat transfer calculations. The results showed that this configuration of heat exchanger can transfer more than 600 W of heat from the helium to the water side at a temperature difference of  $4^\circ\text{C}$  only. At the right amplitude, the peak-to-peak displacement is roughly a quarter of the heat exchanger length. A more detailed drawing is shown in Appendix 3, Figure A3.1. The blockage ratio of the ambient heat exchanger is 68.8%, leaving the porosity to be 31.2%. The heat exchanger design was tested for pressure endurance using SolidWorks. The simulation showed that the minimum factor of safety is 9.9 located at the inner edge in between the middle channels and the water channel. More details of the stress analysis results and factor of safety of the simulation is shown in Appendix three, figures A3.2 and A3.3.

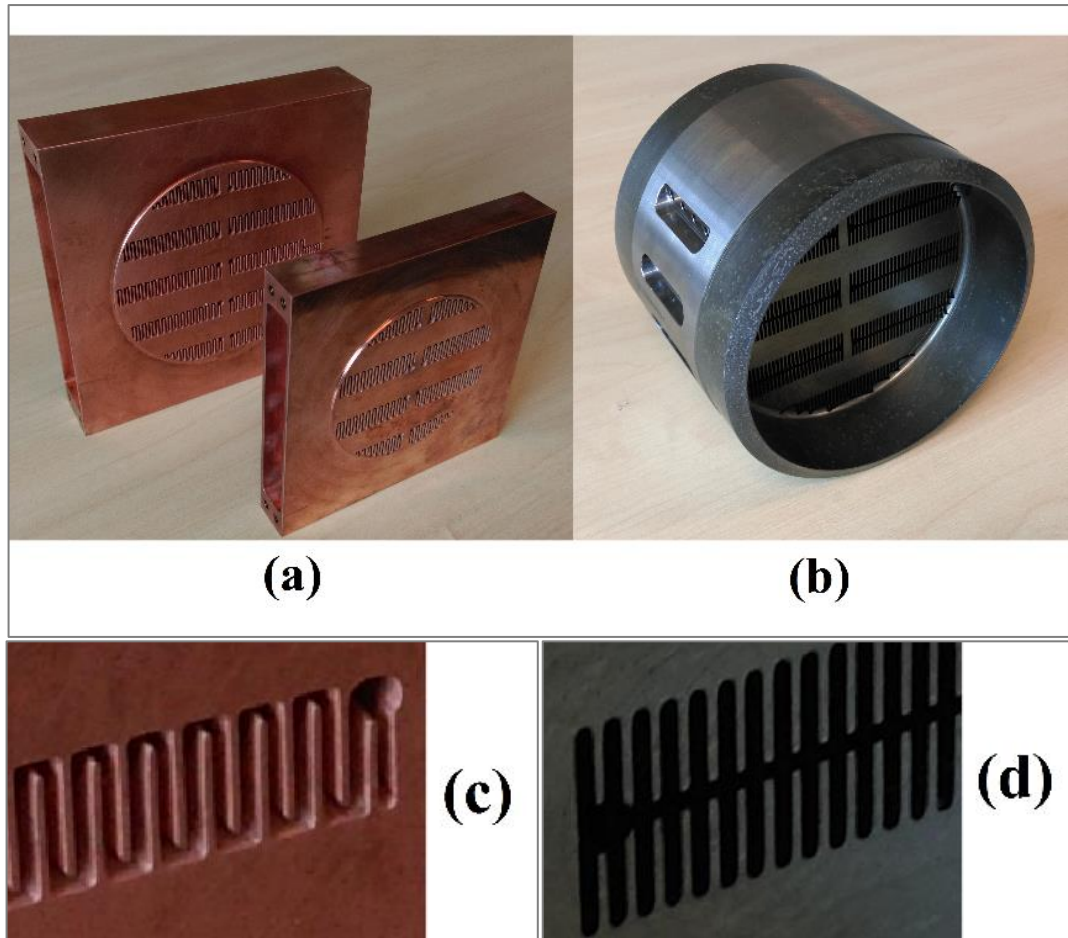


**Figure 4-3:** (a) ambient and secondary ambient heat exchangers; (b) hot heat exchanger; (c) a channel of ambient heat exchanger; (d) a channel of hot heat exchanger.

Below the main ambient heat exchanger is the regenerator, shown in Figure 4.2, made from a 7.3 cm tall piece of 445 stainless steel mesh screen. The diameter of the regenerator is 102 mm. The diameter of the mesh wire is 65  $\mu\text{m}$  and the aperture is 180  $\mu\text{m}$ . The number of stacked mesh screens is about 88% of the calculated/expected number. The stacking procedure started with slipping the screens into the regenerator holder, shown in figure 4.2, one at a time. To ensure that the regenerator has a uniform number of screens per unit length, a uniform amount of force was applied by a cylinder after each pair of screens. Figure 4.4 shows the stacking stages of the regenerator. Starting from 4.4a to 4.4c, Figure 4.4a shows a single screen on a coarse mesh, 4.4b shows a half-filled regenerator and the tight clearance can be seen here and 4.4c shows a full regenerator and some screens and the spacer coarse mesh floating out of the holder. The floating out mesh screens were pressed by the ambient heat exchanger at the assembly stage. On each end of the regenerator, there is a coarse diamond mesh

of 1.3 mm thickness, which act as spacers. These spacers allow the gas leaving the heat exchangers to mix and spread over the entire regenerator cross section. The regenerator hydraulic radius and the volume porosity were calculated using the wire diameter, aperture and the amount of packed mesh per unit volume. The hydraulic radius is 60.5  $\mu\text{m}$  and the volume porosity is 78.9%. The regenerator holder was machined to have an inner diameter of 102.5 mm. The small clearance between the holder and regenerator screens is to avoid bridges of oscillations around the regenerator. These bridges may encourage streaming and transfer heat without generating acoustic power.

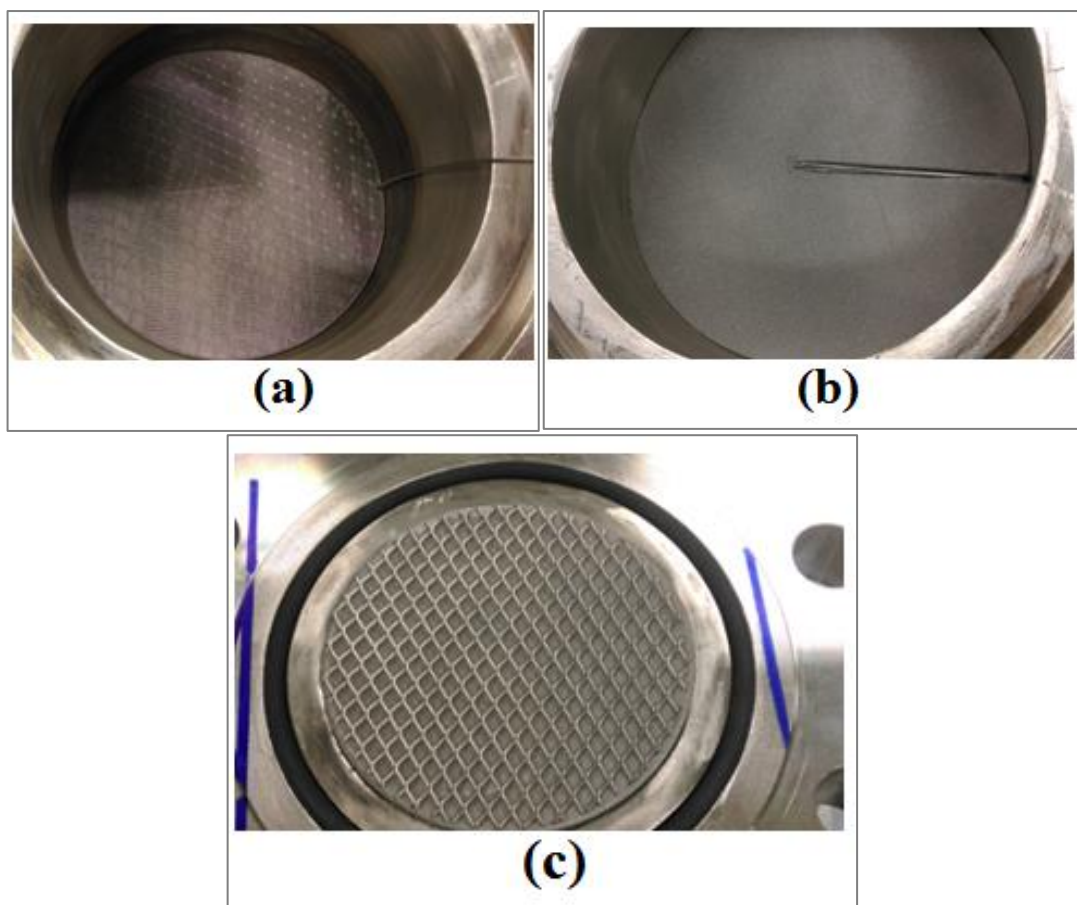


**Figure 4-4:** Regenerator stacking stages (a) one screen; (b) half filled; (c) full regenerator.

The hot heat exchanger was manufactured from a low carbon steel. The choice of material is a trade-off between the thermal conductivity and the material mechanical properties at high temperature. It has a 102.2 mm (4 inch) circular face diameter and 40 mm length in the direction of oscillation. At first, the hot heat exchanger was designed to be cross flow, details could be found in appendix three, figure A3.4. Later

on, the heating source was simulated by electrical heaters. A photograph of the hot heat exchanger is shown in Figure 4.3b. The hot air channels were replaced by 6 pairs of cartridge heaters. The heaters are 100 W each. The accommodating holes were prepared very carefully to have a tight clearance of 0.175 mm, to maintain good thermal contact between the heater and heat exchanger block. The detailed design can be seen in Appendix three, figure A3.5, showing that the hole depths varied with the location. The upper and lower pairs of holes are 68 mm deep and the heaters are placed in the first 50 mm of the hole and the rest is only an extended length to ensure that the heaters heat around the fins only.

On the helium side, a comb was cut using Electrical Discharge Machining (EDM) to form channels of 1 mm width, and fins of 7 mm in length and 0.5 mm in width (the channel shown in Figure 4.3d). The total contact area between the fins and the gas is 0.149 m<sup>2</sup> which allowed the heat exchanger to transfer more than 850 W of heat to the helium. The blockage ratio of the hot heat exchanger is less than the ambient heat exchanger as it had one flow side only, the blockage ratio was 65.5%. At the design amplitude, the peak-to-peak displacement is roughly a quarter that of the heat exchanger length. The heat exchanger design was tested for pressure endurance using SolidWorks. The simulation showed that the minimum factor of safety was 15.37 at 400°C and at 500°C the factor of safety is 5.3 (note that the rig is aimed to run at 400°C). More details of the stress analysis results and factor of safety of the simulation are shown in Appendix three, Figures A3.6 and A3.7. The hot heat exchanger had two circular sleeves protruding 30 mm in length from each side. The regenerator holder and the thermal buffer tube are welded to these two sleeves to ensure that the thermal stresses caused by the welding would never bend the fins.

The thermal buffer tube consisted of three regions, the first and the third have uniform cross-sections while the middle region is a 4-3 inch reducer. The size of the two uniform sections was determined in the manufacturing design process. The first region which is 102.2 mm (4inch) diameter is a hot heat exchanger sleeve. The second one is 77.9 mm (3 inch) in diameter and is an extension for the reducer as the reducer cannot fit for welding inside a slip-on flange. Both sections are 30 mm long. The reducer was selected from the available standard reducers. The length of the reducer

is 102 mm. The total length of the thermal buffer tube is 162 mm which is within the optimum length as shown by the simulation in the previous chapter.

The last part of the thermodynamic section is the secondary ambient heat exchanger. The circular side protrudes 1 mm out of the block for ease of aligning with the thermal buffer tube on one side and the reducer on the other side. As the aim of this part was to avoid heat leaks beyond the thermodynamic section, it was designed to have relatively long fins and low blockage ratio in comparison with the main ambient heat exchanger. The heat exchanger was manufactured out of a copper block which is 120\*116\*20 mm. It has similar fins to the ambient heat exchanger with a length of 9 mm. At this configuration, the contact area between the helium and the heat exchanger channel walls is 0.056 m<sup>2</sup>, and 0.018 m<sup>2</sup> between the cooling water and channel walls. The calculations showed that this heat exchanger can transfer more than 400 W of heat from the helium to the water at a temperature difference of 3°C only. At the design amplitude, the peak-to-peak displacement is roughly one third of the heat exchanger length. A more detailed drawing is shown in Appendix three, Figure A3.8. The blockage ratio of the ambient heat exchanger is 62%. The simulation of the pressure endurance using SolidWorks showed that the minimum factor of safety was 12.3. More details of the stress analysis results and factor of safety of the simulation are given in Appendix three, figures A3.9 and A3.10.

#### **4.1.2 Acoustic section**

The acoustic section comprises all the tubes connecting the thermoacoustic cores to the linear alternator which connects them together. The main target of the feedback loop is to deliver an acoustic power from the end of a stage to the beginning of the other at a convenient acoustic phasing. In this stage of the research, no phase control was used. Therefore, the acoustic feedback is a straight tube. All the tubes of the acoustic sections are standard 1½ inch tubes which have an inner diameter 40.94 mm. An approximate roughness factor of the tubes internal surface was provided by the material supplier and used in the DeltaEC modelling.

The acoustic network starts with a 3 to 1½ inch standard reducer connecting the secondary ambient heat exchanger to the 1½ inch pipe, shown in Appendix 8 Figure

A8.1. Because of the large volume of the linear alternator housing and the width of the 3 inch flange, a 100 mm long tube, 1½ inch in outer diameter is welded after the reducer. The short tube is welded to an equal tee junction connecting the main feedback branch to a trunk connected to the linear alternator housing. Following the branch, a 1½ inch tube was welded to the tee at a total length of 6880 mm. This was divided into five pieces connected by long radius elbows. The total volume consumed by the rig is not a concern at this stage of the research; therefore, the tubes were left straight. The rig’s final dimensions are shown in Figure 4.5. The last piece of the 1½ inch feedback tube is connected to a standard reducer 1½ to 1 inch, followed by a standard 1 inch tube of 275 mm, shown in Appendix 8 Figure A8.2. The last piece of the feedback branch is a 4 to 1 inch standard reducer connecting the 1 inch tube to the ambient heat exchanger.

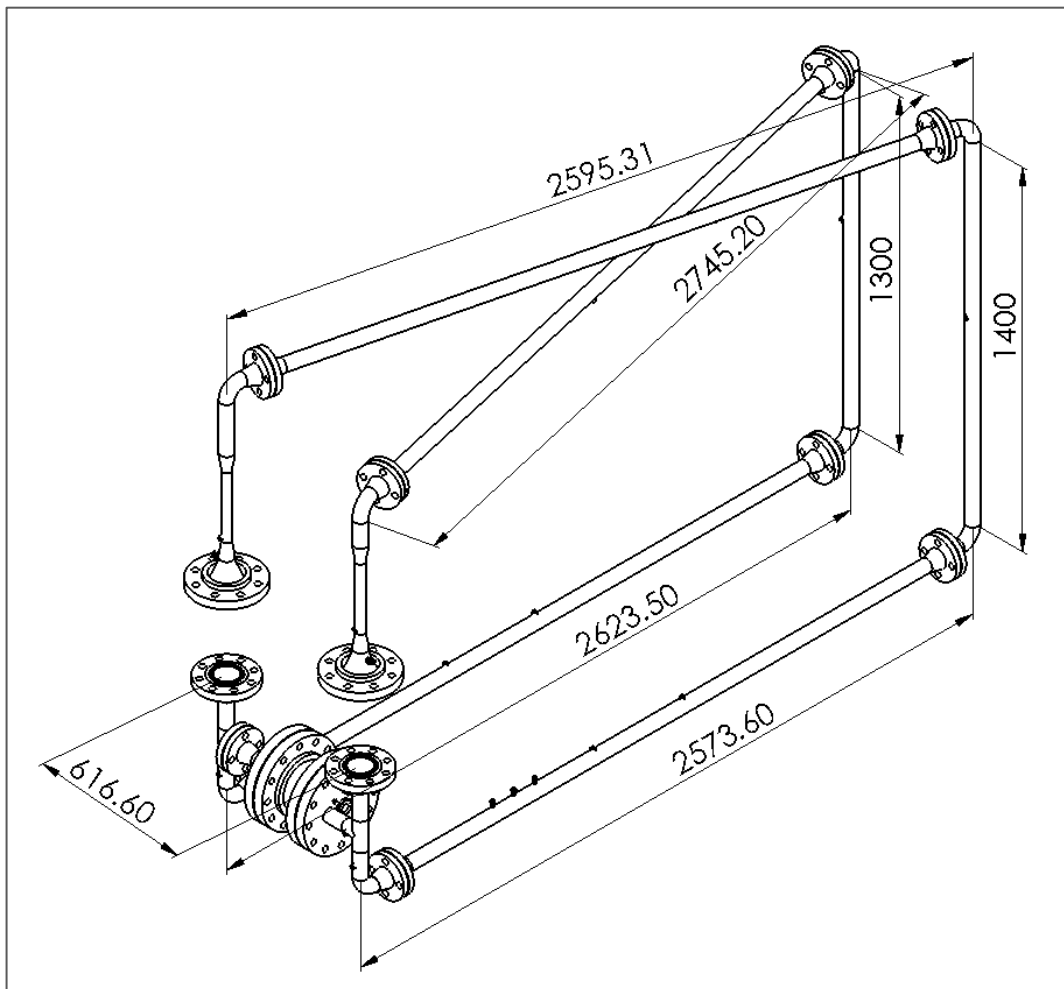


**Figure 4-5:** The acoustic network layout of the experimental rig.

The linear alternator housing was placed between the two branches of the two stages. The total length of the alternator housing was 575.6 mm. As mentioned previously, the linear alternator used in this research is a Q-drive linear alternator model 1S132M. This alternator has one piston from one side, while the research requires an alternator having two back-to-back pistons each extracting acoustic power from a branch side. To overcome/eliminate the effect of the use of this alternator, two design decisions were made. First, it is aimed to position the piston of the linear alternator in the middle of this trunk in between the two branches. The piston of the alternator needs to be in the middle to ensure an out of phase acoustic power is applied to the sides of the piston. Second, a plastic insert shown in Figure 4.6b was placed in the cavity shown in Figure 4.6a to reduce the effect of gas volume. The plastic insert is a machined PVC pieces to fill the cavity between the housing and the linear alternator. The gas volume in the linear alternator housing acts as an acoustic compliance, which leads to a change in the pressure amplitude and phase. Based on a rough estimation of the volume of the linear alternator body, the plastic insert shown in Figure 4.6b was fabricated to fill the cavity between the alternator and the housing, leaving an approximate volume equivalent to the 1½ inch tube. The linear alternator housing is a standard 6 inch pipe of 175 mm length.

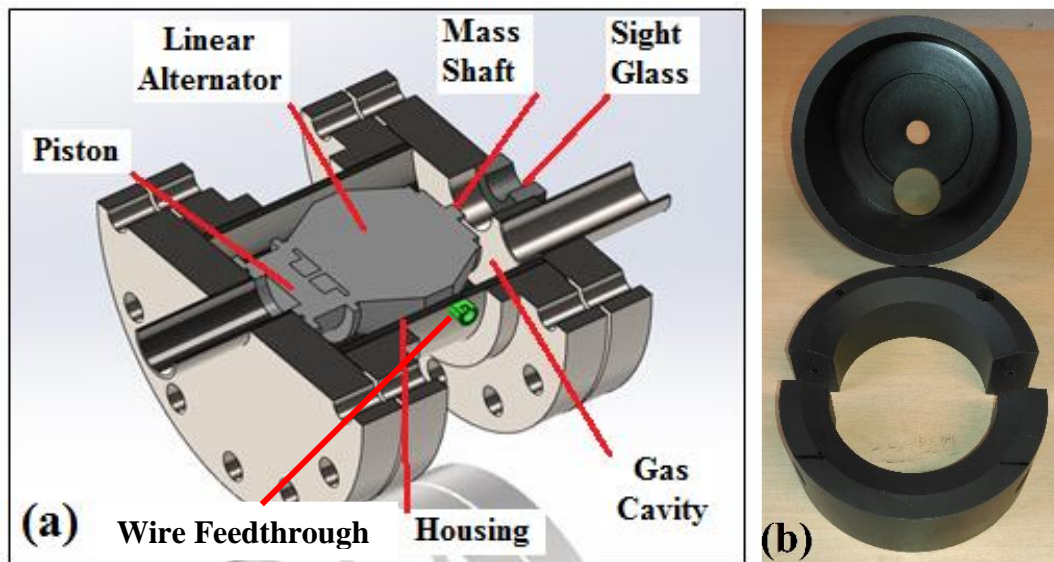


**Figure 4-6:** (a) linear alternator housing cross-sectional view; (b) the plastic insert.

In summary, Table 4.1 shows a list of the parts of the thermodynamic and acoustic sections.

**Table 4-1: Dimensions and Materials Summary**

Component	Length (mm)	Inside Diameter (mm)	Porosit y	Material
AHX	30	102.2	31.2%	Copper
Regenerator	73	102.0	75.8%	Stainless Steel
HHX	40	102.2	34.5%	Mild Steel
TBT-1 <sup>st</sup> part	30	102.2		Stainless Steel
TBT-2 <sup>nd</sup> part	102.5	102.2-77.9		Stainless Steel
TBT-3 <sup>rd</sup> part	30	77.9		Stainless Steel
2 <sup>nd</sup> AHX	20	77.9	38%	Copper
Reducer	89	40.9		Stainless Steel
Tube	100	40.9		Stainless Steel
T-branch	114	40.9		Stainless Steel
Feedback-1 <sup>st</sup> part	6880	40.9		Stainless Steel
Reducer	64	40.8-26.5		Stainless Steel
Feedback-2 <sup>nd</sup> part	275	26.5		Stainless Steel
Enlargement	166	26.5-102.2		Stainless Steel
LA Branches	200,120	40.8		Stainless Steel
LA Holder	175	154.1		Stainless Steel

## 4.2 Measurements

In the experiments, the measured quantities are temperatures and oscillating pressure amplitudes at selected locations along the system and linear alternator piston displacement and generated electrical power.

Twenty one Type-k thermocouples, TC-Direct models 405-010 and 405-011, were used to monitor the helium temperature at different locations along the engine loop. Six thermocouples at each stage and one to monitor the linear alternator temperature were distributed, as shown in Figure 4.7. In each stage, there was a thermocouple in the middle of each heat exchanger channel and at the middle and each end of the regenerator. The regenerator end's thermocouples were placed at the spacers. To pass the thermocouples to the middle of the regenerator, half of the regenerator screens were punched with a 1 mm diameter holes and eight were line cut in the middle, as shown in Figures 4.4a and 4.4b. A multiple feedthrough assembly, TC-Direct model 941-339, were used to pass the thermocouple lead to the engine. This assembly isolated at the reducers above (TC feedthrough 1) and below the thermoacoustic cores; two fed from above and four from below (TC feedthrough 2). The linear alternator

temperature were measured by a thermocouple attached to its body. There are eight thermocouples installed in the cooling system; one at the cooling water inlet and the other at the outlet of each heat exchanger. All these thermocouples are connected to a data acquisition card, OMEGA OMB-Daq Temp Model 7, which is connected to an in-house designed LabVIEW program allowing recording of their values.

The linear alternator piston displacement were measured for two reasons; to calculate the volumetric flow velocity and to ensure that it did not reach its maximum stroke. As shown in Equation 3.6, the volumetric velocity is equal to the multiplication of the angular velocity, the piston area and the displacement amplitude. In this research, the piston displacement amplitude was measured by a laser displacement sensor, KEYENCE model LK-G152. The measured the displacement by applying a laser beam to its surface at a distance of up to 150 mm between the sensor and the object's surface. A high pressure sight glass window, VISILUME toughened line glass type-64, was installed facing the back of the mass shaft of the linear alternator which is part of the moving mass and hence moves with the piston, as shown in Figure 4.6.

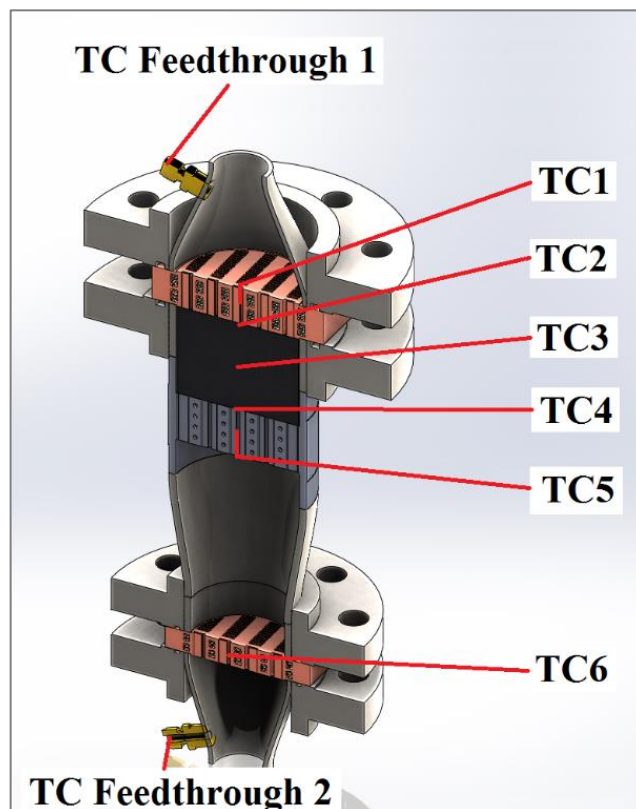


**Figure 4-7:** Thermodynamic cross-sectional view showing the thermocouple (TC) locations.

Seven pressure sensors, PCB PIEZOTRONICS model 112A22, were installed at different positions along the loop to monitor the distribution of the pressure amplitude. Nineteen accommodation holes were prepared for these transducers, as shown in Figure 4.8. All pressure transducers have a resolution of 7 Pa, and were used to measure the pressure amplitude, phase angle and frequency. During the experiments, the sensors were moved to different holes to get a reading at each location then they were placed in permanent locations. These locations are 1, 2, 7, 8, 9, 10 and 17, as shown in Figure 4.8. The pressure transducers are connected to the same data acquisition card and LabVIEW program, which allowed recording of the pressure amplitude and the phase difference between any two sensors at an accuracy of 0.01°. A signal conditioner, PCB PIEZOTRONICS model 480B21, was connected between the sensors and the data acquisition card. The pressure amplitude and the phase difference of each pair of sensors could be applied to the reliable method known as the “two-microphone method” described by Fusco *et al.* (1992) to calculate the acoustic power flowing at the mid-point between them. The acoustic power is:

$$W_{2mic} = \frac{A}{2\rho_m a \sin(\omega\Delta x/a)} \left( Im [p_1 \widehat{p}_2] \left\{ 1 - \frac{\delta_v}{4r_h} \left[ 1 - \frac{\gamma-1}{\sqrt{\sigma}} + \left( 1 + \frac{\gamma-1}{\sqrt{\sigma}} \right) \frac{\omega\Delta x}{a} \cot \left( \frac{\omega\Delta x}{a} \right) \right] \right\} + \frac{\delta_v}{8r_h} (p_1^2 - p_2^2) \left[ 1 - \frac{\gamma-1}{\sqrt{\sigma}} + \left( 1 + \frac{\gamma-1}{\sqrt{\sigma}} \right) \frac{\omega\Delta x}{a} \csc \left( \frac{\omega\Delta x}{a} \right) \right] \right) \quad 4.1$$

$$\text{Here} \quad Im [p_1 \widehat{p}_2] = p_1 p_2 \sin \alpha \quad 4.2$$

where  $p_1$  and  $p_2$  are the pressure amplitudes at the two specific locations,  $\Delta x$  is the distance between the two sensors in the oscillation direction,  $\alpha$  is the phase difference between the sensors,  $\omega$  is the angular frequency,  $\rho_m$  is the gas density,  $\gamma$  is specific heat ratio,  $\sigma$  Prandtl number and  $\delta_v$  is the viscous penetration depth. The phase difference between the pressure sensor at location-17 and the piston needs to be recorded to calculate the acoustic power at the piston by the general acoustic power Equation 3.7. First, the volumetric flow rate was calculated by Equation 3.6 using the measured value of the piston displacement and the frequency. Then the acoustic power was calculated by pressure amplitude at location 17, the calculated volume flow rate and the phase difference recorded between the pressure sensor and the piston displacement. It is important to note the phase difference recorded by the data acquisition card is the phase difference between the pressure amplitude and the piston

velocity, while the phase difference of Equation 3.7 is the difference between the pressure amplitude and volumetric velocity. Therefore, the phase difference value should be shifted by  $90^\circ$  which is the phase difference between the piston velocity and the volumetric velocity.

Using Equations 4.1 and 3.7, the acoustic power entering each core was calculated at the midpoint of 6-7 and 9-10. The acoustic power at the piston was calculated by the piston measurement and the pressure at 16 and 17, the power entering the feedback loop calculated at the mid-point of 1-2 and 9-10. The net generated acoustic power is considered to be the power at the piston plus the power entering the feedback loop minus the power entering the core. Clearly, the calculated net power is less than the real value as the power entering the thermoacoustic core is measured about 2.5 m before the core and the power entering the feedback loop is measured about 1.2 m after the core, and there is an acoustic power loss in the tubes and fittings, and losses in the tee connection and the linear alternator housing and connectors.

The linear alternator generated power was calculated by multiplying the measured voltage and current of the generated electricity. The voltage and current were measured by digital multi-meters, Fluke 28II digital multi-meter (current accuracy  $\pm 0.2\%$ , voltage accuracy  $\pm 0.1\%$ ). A glass-to-metal wire feedthrough, shown in Figure 4.6a, was used to pass the alternator wires through the linear alternator housing vessel.

### **4.3 Heating and Cooling Systems**

The heating and cooling systems are essentials for the thermoacoustic engine to maintain the temperature difference across the regenerator.

#### **4.3.1 Heating system**

As explained in the hot heat exchanger part of Section 4.1.1, the heating was achieved using 100 W electrical heaters, WATLOW model C2M-9410. At first, each heat exchanger was supplied with 12 heaters which were then increased to 18 heaters. As shown in Figure 4.3b and Appendix three, figure A3.5, there are slots machined into the two sides of the hot heat exchanger and there are 4 holes in each slot. These heaters are connected to an electrical autotransformer to control the heating power of the heat

exchanger by controlling the voltage. The electricity consumed by the heaters was measured by an inline power meter, Fluke 28II digital multi-meter (current accuracy  $\pm 0.2\%$ , voltage accuracy  $\pm 0.1\%$ ), and was considered to be the heating power of these heaters.

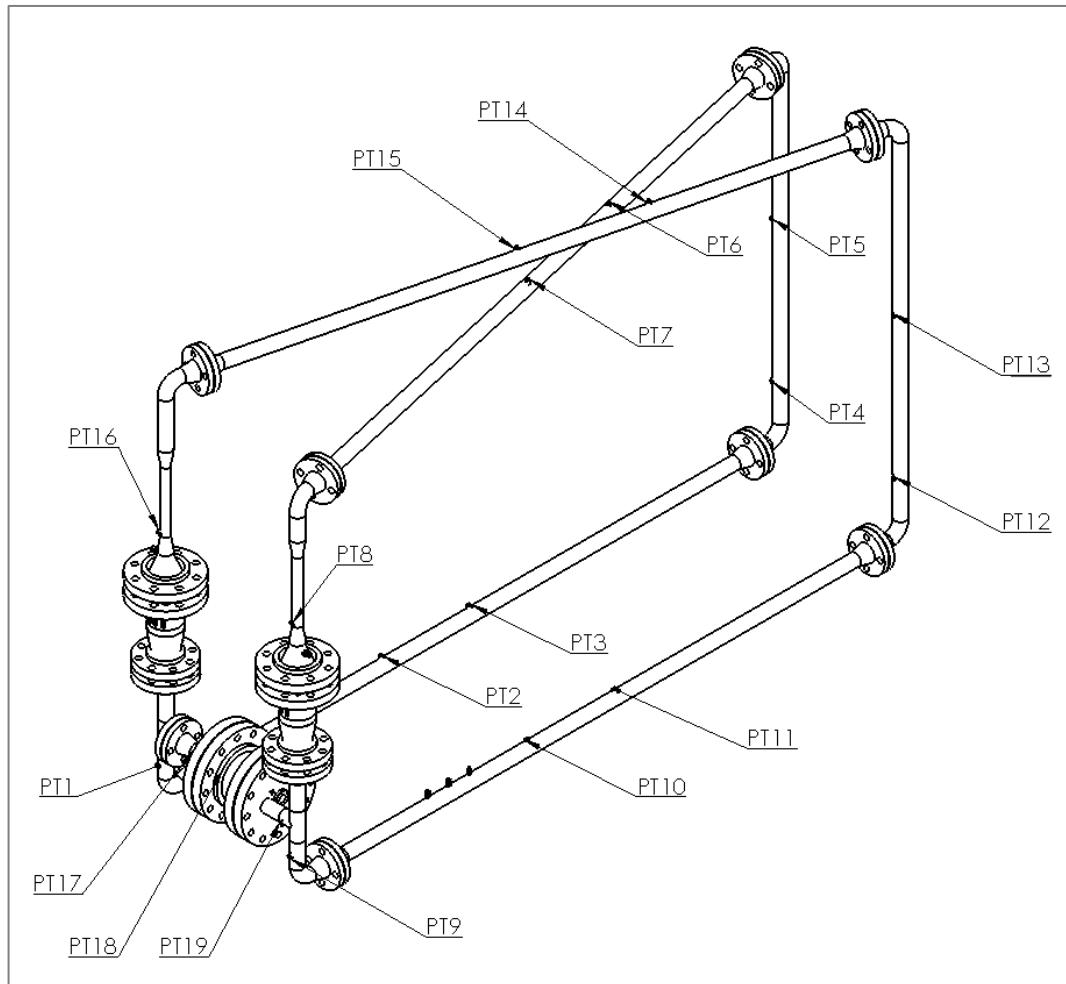


**Figure 4-8:** A schematic drawing of the rig showing the locations of the pressure transducers (PT).

### 4.3.2 Cooling system

The cooling system uses water to maintain the temperature at the two ambient exchangers near air ambient temperature. The cooling system consists of a 91 litre (20 gallon) water tank, high pressure diaphragm pump, hoses and cooling coils. The idea is to circulate the tank water into all the heat exchangers. The heat capacity of water and the natural convection and radiation help to maintain the water at low temperature. However, the water needs to be changed or cooled down when running the engine for more than three hours. To simplify the system, all the four heat exchangers were

connected in series with cooling coils in between. The benefits are the system needs one pump for all the four exchangers to ensure the same flow rate in all the heat exchangers. The cooling coils are copper tube, WICKES model 420700, coiled and immersed in the water tank. The heat transfer calculations showed that each meter of immersed pipe can drop the water temperature up to 2°C at a water flow rate of 1 L/min. The water leaving the pump is split into two lines each has a valve, one is feeding the water back to the tank and the other supplies the cooling line. The control of these two valves can tune the flow rate of the cooling line, which was set at 1 L/min. The cooling line enters a main ambient heat exchanger and then it was connected to 4 meter coiled copper to cool the water down before entering the other main ambient heat exchanger. There are two other cooling coils at 4 and 2 meters connected afterwards.

#### **4.4 Concluding Remarks**

The rig was constructed from materials available in the market. The design, materials and parts selection criteria was based on the availability and durability for the working pressure, pressure sealing of the working gas and moderate cost. The experimental apparatus consists of two sections: the thermodynamic section and the acoustic section. The thermodynamic section is where heat is transferred to or from the working gas, while the acoustic section is the tubing network transmitting the acoustic power from one place to another. In the experiments, the measured quantities are temperatures and oscillating pressure amplitudes at selected locations along the system and linear alternator piston displacement and generated electrical power.

## Chapter 5

### Experimental Results and Discussion

In this chapter, the system start-up issue is discussed in Section 5.1. The experimental results are presented and discussed in Section 5.2. Sub-Section 5.2.1 illustrates the effect of the load resistance on the performance of the engine. The effect of the mean pressure and the heating power are discussed in Sections 5.2.2 and 5.2.3, respectively. Section 5.2.4 shows the results of the full performance tests of all the parameters.

#### 5.1 Start-up and System Debugging

The first step in engine preparation is to charge the engine with helium at 28 bar. The procedure started with evacuating the system to - 0.9 bar (gauge pressure), then charging with helium to 3 bar, twice, to eliminate any traces of air inside the engine, then evacuating and charging to 28 bar. After turning the cooling pump on, the heating process starts. The heating procedure starts with slow heating, from 0°C to 100°C, to avoid thermal stresses at the metal-to-metal contact between the hot heat exchanger and the heaters, then full heating power is applied.

It was expected that the engine excites weak acoustic oscillations at a steep temperature distribution across the regenerator, then the acoustic power is amplified in the regenerator over a period of a few seconds or minutes. The time taken to start is based on the heat flux that is able to maintain and increase the temperature difference, as the hot side temperature decreases when oscillation starts.

The weak oscillation started when the helium at the regenerator hot side reached a temperature of approximately 230°C and the temperature difference was about 185°C. Unfortunately, the regenerator failed to amplify the acoustic power to an intense level enabling it to drive the linear alternator. The hope was that the measured pressure amplitudes at sixteen locations along the engine loop would agree with the calculated predictions, however, the calculated pressure was approximately 200 times the experimental values as shown in Figure 5.1.

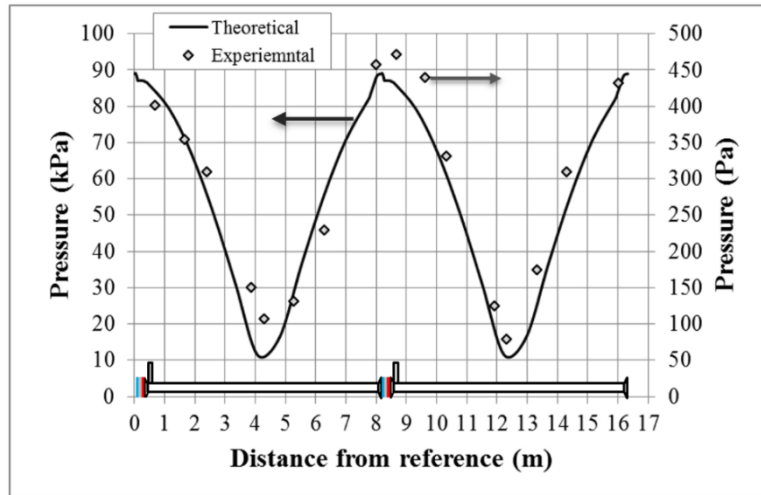


**Figure 5-1:** The preliminary experimental pressure amplitude measurements against the theoretical values along the engine loop, the schematic drawing at the bottom of the figure shows a simplified layout of the engine.

The conclusion of a debugging process investigating how to run the engine was that the engine requires an external excitation to start the amplification of the weak oscillation. The most successful way to excite the engine is to drive the linear alternator as an acoustic driver at a specific frequency. In practice, a few pulses of the acoustic driver piston by a function generator and amplifier at a frequency of 50.8 Hz was enough to excite the intense oscillation. The problem encountered with this method is that once the intense excitation starts, the linear alternator behaves as an open-circuit/no-load and hence the piston exceeds the stroke limit. A continuous knocking of the piston may damage the linear alternator in a few seconds. The piston stroke could be controlled by connecting an external load resistance to the linear alternator. This load resistance will control the piston stroke as well as dissipating the generated electricity. At first, the switching between the function generator and the load resistance was done manually once the piston started knocking. The time taken for the switching to occur, if too long, was a serious danger to the alternator. An electrical control box was designed to protect the alternator and facilitate starting the engine. The control box switches the connection of the linear alternator in three ways: function generator, load resistance and a short circuit, based on piston displacement measured by the laser displacement sensor. The sensor voltage represents the RMS value of the piston peak displacement. The control box connects the linear alternator to the function generator for sensor voltage ranges from 0 to 1.414 V which is equivalent to 0 to 2 mm piston peak displacement. Usually a piston reciprocates with

2 mm peak stroke is able to excite the engine to start the intense oscillation. At a sensor voltage range of 1.414 to 4.242 V, which is equivalent to a piston peak displacement of 2 to 6 mm, the control box connects the linear alternator to the load resistance to control the piston displacement and dissipate the generated electricity. If the voltage exceeds 4.242 V, the switch box connects the alternator to a short circuit connection to stop the alternator from reaching the maximum stroke limit. Figure 5.2 shows a schematic diagram of the connection between the control box and other equipment.

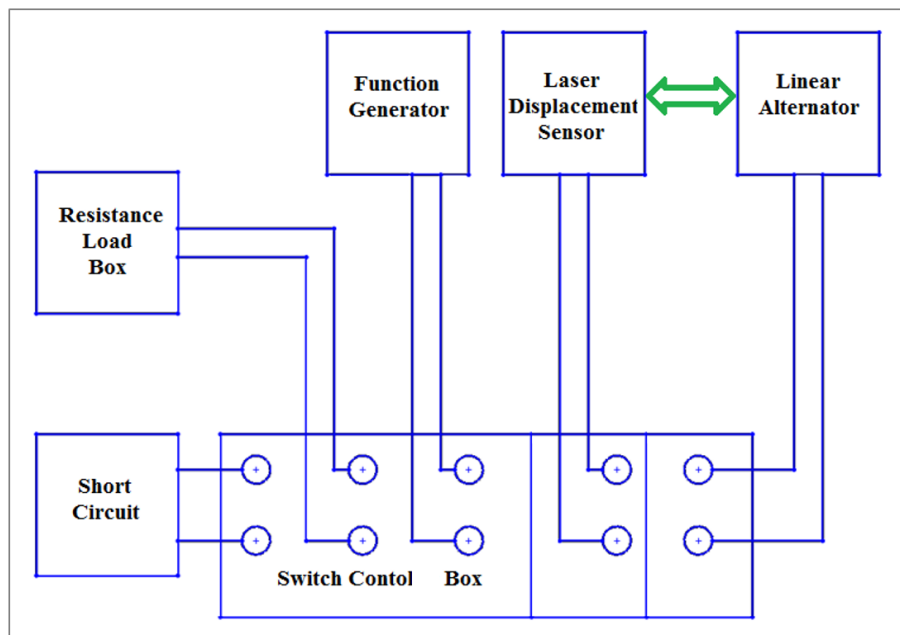


**Figure 5-2:** The connection arrangement of the control box and other equipment

## 5.2 Experimental Results

The preliminary tests of the rig showed promising results. A single set of data is discussed here and more details are presented in the next sections, Sections 5.2.1-5.2.4. After exciting the engine using the control box, the engine starts to drive the linear alternator to generate electricity. The experimental oscillation frequency was found to be less than the simulation frequency. In the experiments, the engine ran at a frequency of 54.7 Hz, which is less than the modelled value of 55.19 Hz. This result may be explained by the relation between the frequency and speed of sound shown in Equation (2.1). The model considers the gas temperature beyond the ambient and secondary ambient heat exchangers is at 25°C. In practice, the feedback tube was not insulated, therefore, the tube and helium were at room temperature, mostly below

20°C. The gas had higher density at lower temperatures, and this led to a decrease in the speed of sound as shown Equation (2.2), which decreases the frequency as per Equation (2.1). Applying the gas temperature of 19°C in the DeltaEC model, resulted in the frequency dropping to 54.69 Hz.

The settling time of the engine was identified for both thermal and acoustical measurements. It is considered that the settling time is the time it takes to get within 1% of the final value, or to 99% of the final value and, most importantly, stay within that 1%. Knowing the settling time is crucial and interesting for a system that has heat transfer and oscillations, enabling an isolated and accurate study of both the performance and operating parameters. The settling time of the current study was influenced by several factors, including past events and degree of any change implemented. A possible example is the large mass of the hot heat exchanger assembly, explained in section 4.1.1, which has a high thermal capacitance. Due to this capacitance the system requires a longer settling time with a cold start than from following runs. Another example, it requires a longer settling time when varying the heating power than when making small changes in load resistance. In general, the settling time of the first run was found to be between 35 to 40 minutes, thereafter, a change in a single parameter requires a settling time of 20-30 minutes only.

In the present study, the measurements were taken with great care and careful thought was given to every step of the measurements procedure. Nevertheless, the measured values failed to produce smooth curves and the tests failed to be repeatable. There are, however, possible explanations for the non-repeatability. The main explanation for the experiments having some inconstant parameters is that the past experiment carried out on the same day may have an effect on the heat stored in the bulk metal around the hot heat exchanger, the cooling water temperature which varied between 25 and 40°C, the quality of helium and the traces of air which were assumed to be the same, and the room temperature. Generally, many experiments were repeated and the spread of results was always been within 2.5%.

Two main problems have been noticed during the experiments; heat leakage and phase difference shifting. Once the oscillation started, heat leakage was detected whereby the heaters could not maintain the hot heat exchanger at 400°C. The DeltaEC

simulation results showed that it requires only 288.8 W to maintain a temperature of 400°C, however, a heating power of 900 W failed to maintain the temperature in practice. This led to a reduction of all the performance parameters of the engine in both the acoustical and electrical generation. A possible explanation for the heat leak is due to heat conduction along the walls and regenerator and minimally by convection to the environment through the insulation. Streaming is another source of heat leak as it pushes the hot gas beyond the ambient heat exchanger, which will be cooled by the feedback loop as explained in the following Sections.

As explained in Section 4.2, there is no measurement were obtained for velocity in this research apart from that of the alternator piston. The phase difference between the volumetric flow rate and the pressure could be measured at the piston of the linear alternator. The simulation phase difference is  $-45.25^\circ$ , while the recorded experimental difference ranges from  $15.5^\circ$  to  $-7.25^\circ$ . These phase differences indicate a serious change in the acoustic field along the engine loop. It seems possible that the shifting is due to the use of an improper linear alternator. The difference between the theoretical and experimental may have influenced the phase difference at the regenerator which affects the power amplification.

The pressure amplitude was measured in all the sixteen locations. The distribution shown in Figure 5.3 illustrates the match between the experimental the theoretical (in the optimized design) results. In this test, the heat input was 900 W at each stage (1800 W for both stages), the mean pressure was 28 bar and the external load resistance was  $30 \Omega$ . Contrary to expectation, the pressure amplitude at identical points before and after the thermoacoustic cores, i.e., at the beginning and the middle of the chart of Figure 5.3, are not equal. Comparing all three LHS point to those of the RHS as shown in Figure 5.3, it is clear that the all the LHS points have higher amplitudes than the RHS. It can thus be suggested that the linear alternator extracts power from the RHS more than from the LHS and hence the RHS has lower pressure amplitudes. This is suggested as the RHS is facing the piston of the linear alternator while the LHS is facing the back of the linear alternator which has a less active area subjected to pressure.

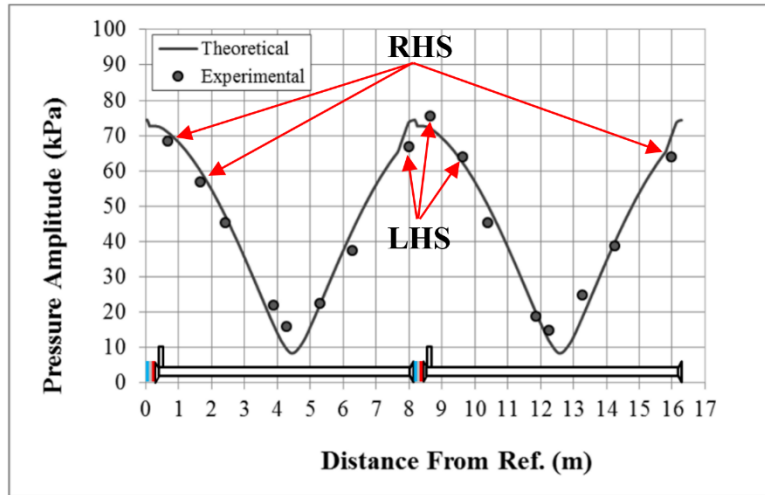


**Figure 5-3:** Pressure waveform of theoretical vs experimental at 28 bar mean pressure, 1800 W heating power and 30.8  $\Omega$  external load, the schematic drawing at the bottom of the figure shows a simplified layout of the engine.

The pressure amplitudes and the phase differences measured between two adjacent pressure measurement points were used to calculate the acoustic power flowing at the middle point between them using Equation (4.1). Figure 5.4 compares the experimental acoustic power to the simulation results. The results show a big difference between the theoretical and the experimental acoustic power, however, there is a good match with the trend. Again, the optimal theoretical results are shown. The experimental results shown in Figure 5.4 confirm that there is higher acoustic power around the LHS higher than the RHS.

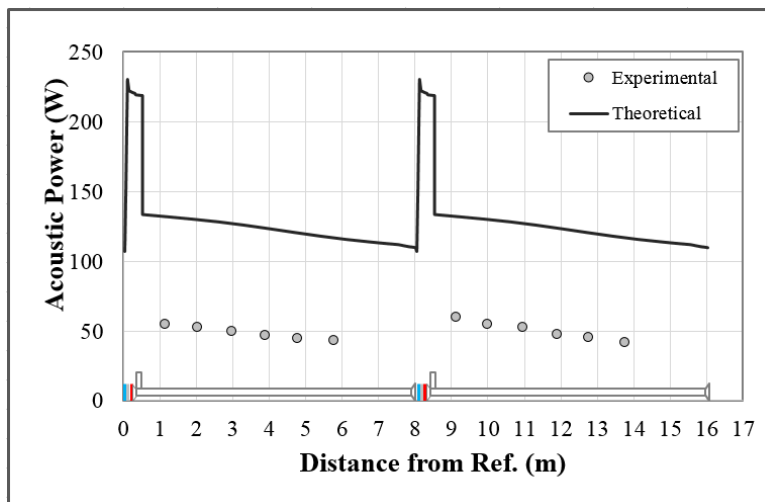


**Figure 5-4:** Acoustic power distribution of experimental vs theoretical results at 28 bar mean pressure, 1800 W heating power and 30.8  $\Omega$  external load, the schematic drawing at the bottom of the figure shows a simplified layout of the engine.

The difference in the pressure amplitudes affected the temperature distribution in the thermoacoustic cores as well, as shown in Figure 5.5. The higher pressure amplitudes of the LHS lead to higher heat being transferred from the hot to the ambient heat exchanger by the oscillatory flow. As they have the same heating power, the LHS hot heat exchanger has a temperature lower than that of the RHS.

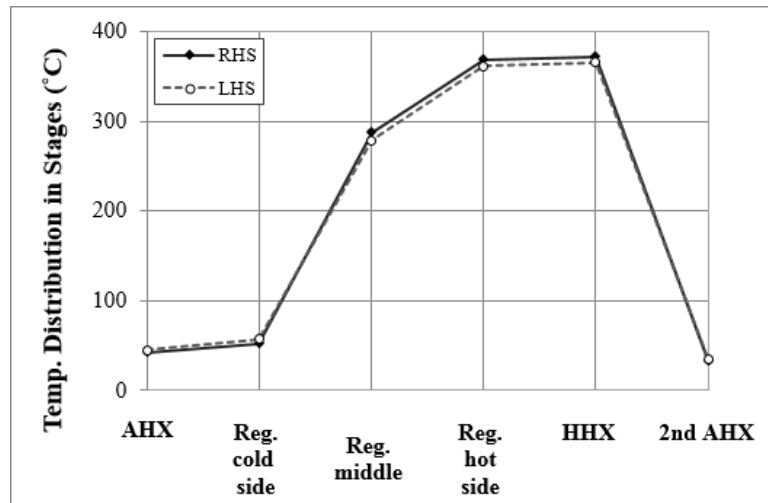


**Figure 5-5:** Temperature distribution at the two thermoacoustic cores at 28 bar mean pressure, 1800 W heating power and 30.8  $\Omega$  external load

The lack of symmetry discussed above led to more investigation of the symmetry of the performance of the two stages. Figure 5.6 shows the experimental phase differences between pairs of pressure measurement locations. Theoretically, the phase difference should be 180°. However, the use of the acoustically asymmetric linear alternator may have changed the phase difference as it went up to 194° around the middle of the feedback loop.

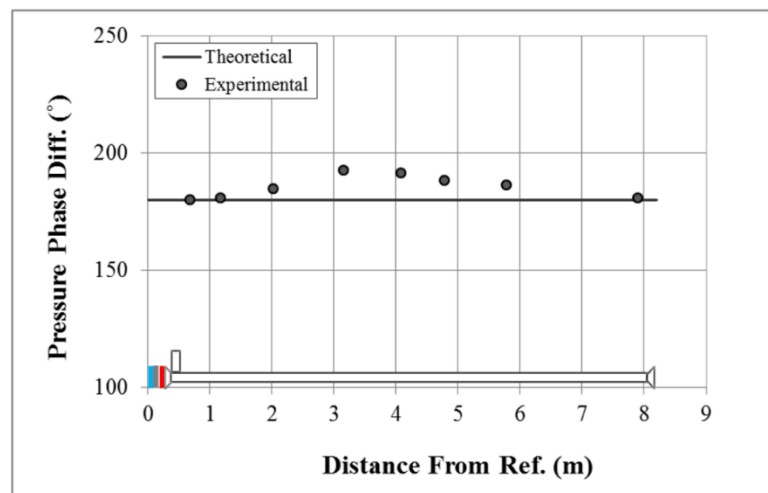


**Figure 5-6:** Pressure phase difference between two identical points on the stage loop at 28 bar mean pressure, 1800 W heating power and 30.8  $\Omega$  external load

### 5.2.1 The Effect of External Load Resistance

The load resistance value affects the acoustic-to-electric energy conversion, which will affect the acoustic field, which in turn can affect the thermal-to-acoustic conversion. Yu *et al.* (2011) studied the application of the loud speaker as a linear alternator from the viewpoint of a parametric and general performance. The study concluded that the linear alternator extracts maximum power from the acoustic field at a load resistance value equal to the alternator coil impedance. It was assumed that the same piston displacement and acoustic impedance was applied to the alternator at all the load resistances. In the current research, the alternator has  $18 \Omega$  at 60 Hz. Therefore, it is expected that the alternator would generate the maximum power at a load resistance around  $18 \Omega$ .

The experiments showed a different optimum load resistance to what had been expected based on Yu *et al.* (2011) conclusions, as the volumetric flow rate and pressure amplitude of the acoustic field are dependent on the load resistance. At a mean pressure of 28 bar and heating power of 1800 W (900 W at each stage), the maximum electricity generated was 48.6 W at a load resistance of  $30.8 \Omega$ , as shown in Figure 5.7. In Figure 5.7, the circles are the measured generated electricity while the solid line shows the predicted results using the DeltaEC model after applying three measured boundary conditions: load resistance, pressure amplitude at the linear alternator and the temperature difference across the regenerator. Each experiment was repeated at least four. The circles represent the average of the experiments and the error bar represents the repeatability of the test. The total efficiency was calculated by dividing the generated electricity by the heating power (1800 W). Figure 5.8 provides the effect of the load resistance on the total efficiency. As shown in Figure 5.8, the maximum total efficiency is 2.7% at a load resistance of  $30.8 \Omega$ .

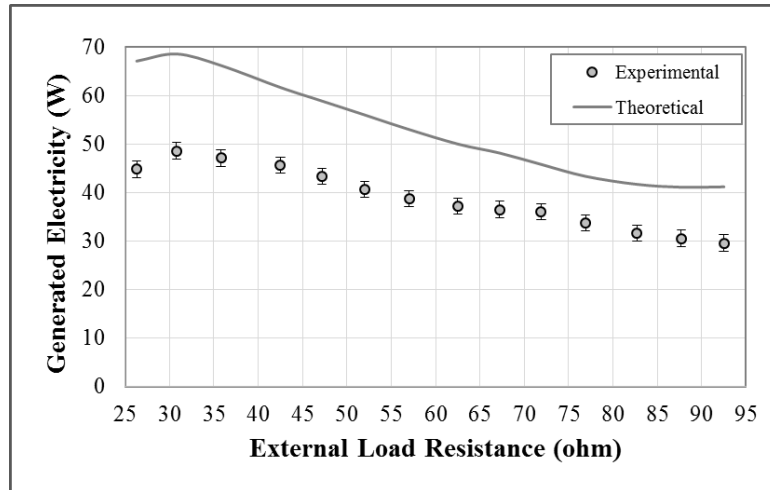


**Figure 5-7:** The performance of the engine as a function of the load resistance at 28 bar mean pressure and 1800 W heating power

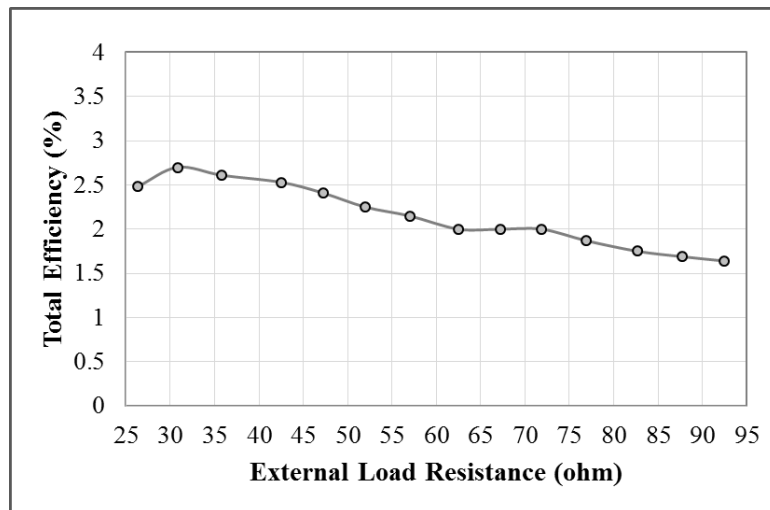


**Figure 5-8:** Total efficiency for different load resistances at 28 bar mean pressure and 1800 W heating power

The alternator efficiency is the ratio of the generated electricity to the consumed acoustic power from both sides of the alternator piston. The acoustic power was calculated using the measured piston displacement, pressure amplitude close to the piston and the phase difference between the piston displacement and pressure amplitude, as explained before. The relationship between the load resistance and the alternator/acoustic-to-electric efficiency, shown in Figure 5.9, shows there is a clear trend of decreasing alternator efficiency by increasing the load resistance. The circles are the measured efficiency while the solid line shows the predicted results using the DeltaEC model. There are several possible explanations for this variance between the experimental and simulated values. Firstly, the use asymmetric linear alternator has a

flow resistance on one side which extracts acoustic more power than the other side value. Secondly, the incorrect experimental phase difference compared to the theoretical value, as explained in Section 5.2.

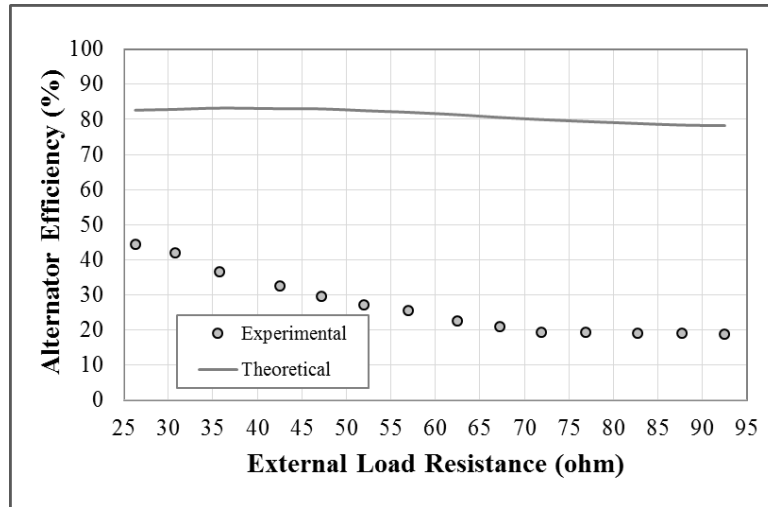


**Figure 5-9:** The effect of load resistance on the linear alternator efficiency at 28 bar mean pressure and 1800 W heating power

The mismatch between the alternator and the load resistance at load values higher than 30.8  $\Omega$  reduces the extracted power by the alternator which encourages more intense acoustic field along the engine. The thermal-to-acoustic conversion increased by increasing the load resistance, which led to a higher thermal-to-acoustic efficiency as shown in Figure 5.10. Increasing the load resistance will decrease the extracted acoustic power by the alternator which will increase the acoustic power circulating in the loop and hence the thermal-to-acoustic efficiency increases. The effect of the load resistance on the volumetric flow rate could be measured at a single point on the engine loop which is at the linear alternator as we have measured the piston displacement. In this research, the change of piston peak displacement will be used as an indicator of the change in the volumetric flow rate along the engine. The measured piston peak displacement was found to be increased by increasing the load resistance, as shown in Figure 5.11, the solid line shows the predicted results using the DeltaEC model. The increase of the volumetric flow rate was coupled with an increase in the pressure amplitude across the engine loop. The pressure amplitude was presented by means of the drive ratio which is the ratio of the pressure amplitude to the mean pressure. Figure 5.12 shows the drive ratio at the linear alternator versus the load resistance.

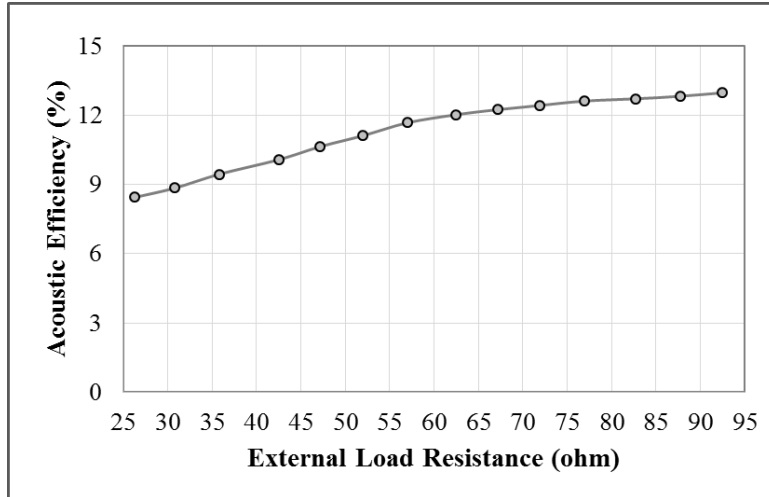


**Figure 5-10:** The relation between load resistance and measured acoustic efficiency at 28 bar mean pressure and 1800 W heating power

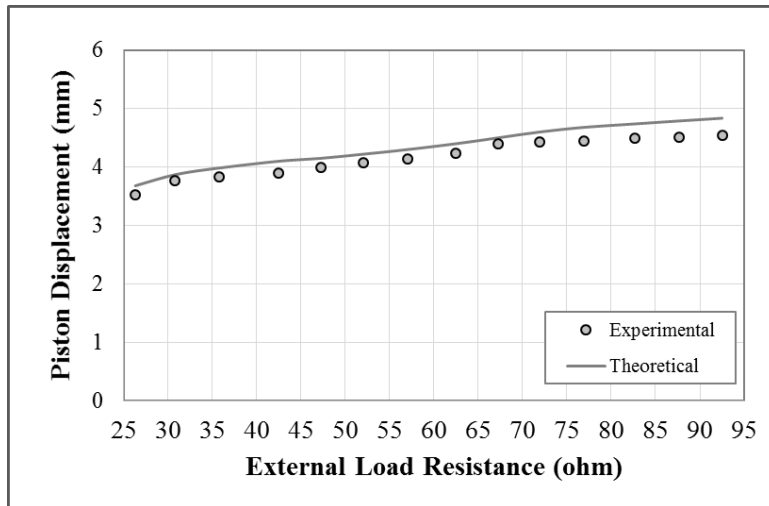


**Figure 5-11:** The alternator piston displacement versus load resistance at 28 bar mean pressure and 1800 W heating power

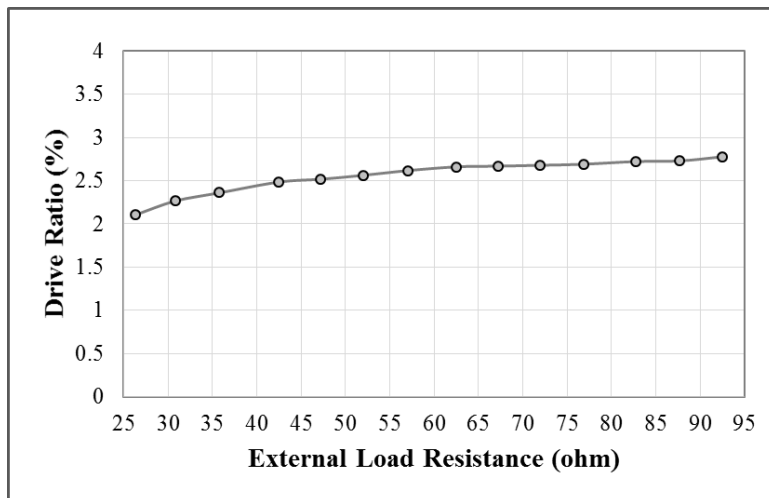


**Figure 5-12:** Measured drive ratio versus load resistance at 28 bar mean pressure and 1800 W heating power

The intense oscillation at higher load resistance affected the regenerator temperature difference, as shown in Figure 5.13. The higher volumetric velocity of the intense oscillation at higher load resistance decreased the regenerator temperature difference. The temperature distribution along the thermodynamic section at various load resistances, shown in Figure 5.14, shows that all temperatures reduced at the hot heat exchanger, hot side and at the centre of the regenerator at higher load resistance. The non-linear temperature distribution graph confirms that there is Gedeon streaming, compared to the linear distribution at no oscillation run. The experiments showed that the Gedeon streaming was lower at lower acoustic intensity when lower load resistance was applied, as the regenerator temperature distribution is closer to linear at lower load resistance.

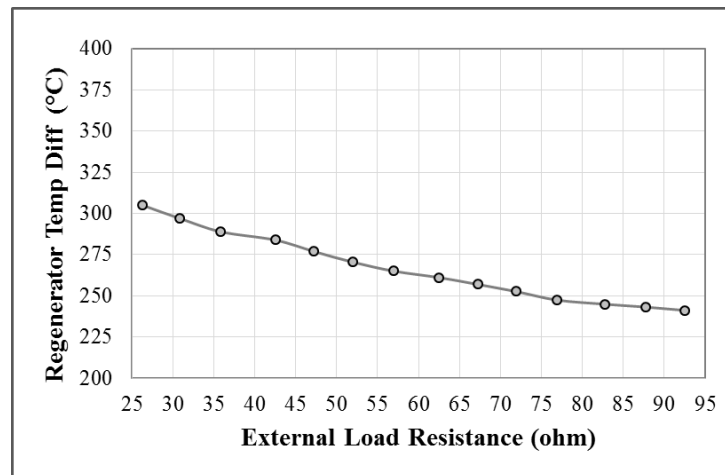


**Figure 5-13:** The effect of load resistance on the measured regenerator temperature difference at 28 bar mean pressure and 1800 W heating power

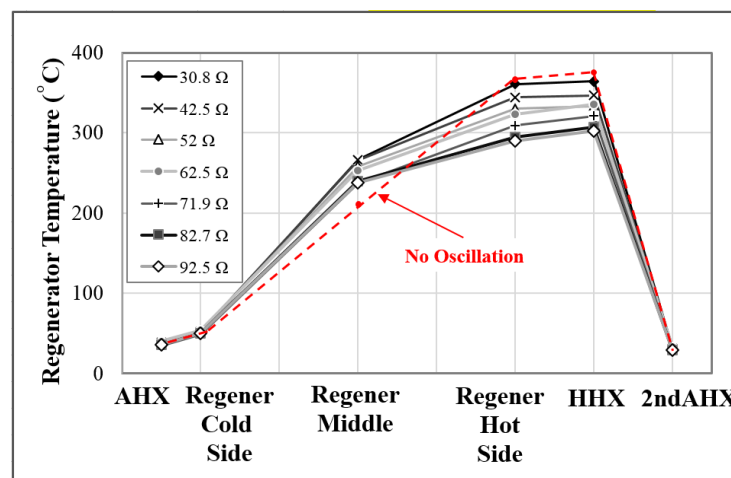


**Figure 5-14:** Core temperature distribution of different load resistance at 28 bar mean pressure and 1800 W heating power

The fraction of the acoustic efficiency to the Carnot efficiency is a very popular measure to evaluate the efficiency of a thermal application with reference to an efficient standard cycle. As the heat generates acoustic power in this application, the fraction to Carnot will be considered as the ratio of the acoustic efficiency to the Carnot efficiency. The Carnot efficiency is the fraction of the temperature difference across the regenerator to the hot side temperature in Kelvin, ( $\eta_{carnot} = \frac{T_H - T_A}{T_H} * 100\%$ ). At the optimum load resistance of 30.8  $\Omega$ , the fraction to Carnot efficiency is 16.8%. The maximum fraction to Carnot efficiency of 27.9% achieved at 92.5  $\Omega$  where the alternator extracts the minimum acoustic power and leave the rest to circulate in the loop, is shown in Figure 5.15. The fraction to Carnot ratio data retain the same trend as the acoustic efficiency but with a steeper trend. The reason for the steeper slope is that the Carnot efficiency, which is the denominator of the fraction, reduces at higher load resistance with the decrease in the regenerator temperature difference as shown in Figure 5.13.

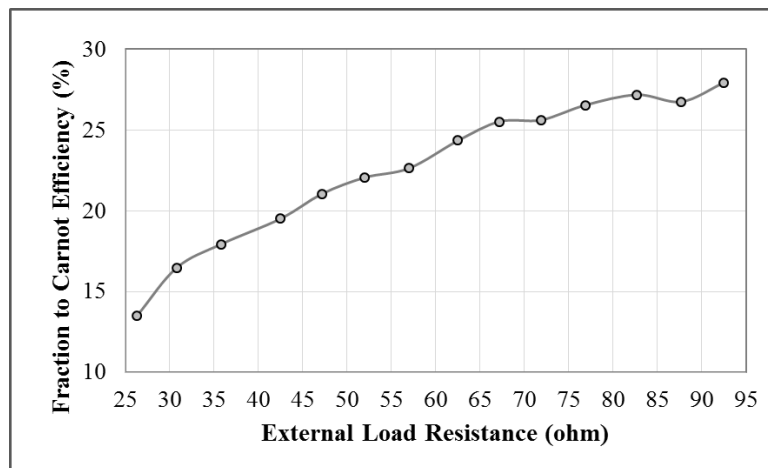


**Figure 5-15:** Fraction to Carnot efficiency for various load resistances at 28 bar mean pressure and 1800 W heating power

As explained in Section 5.2, the local phase difference at the linear alternator obtained in the experiment was different from the model. Figure 5.16 shows the theoretical and experimental local phase difference at the alternator piston at various load resistances. The phase difference is different from the model by 58.3° at 26.3  $\Omega$  and by 61.8° at 92.5  $\Omega$ . Two possible reasons for this effect are the unknown value of inner surface roughness on the pipes and the use of the asymmetric alternator.

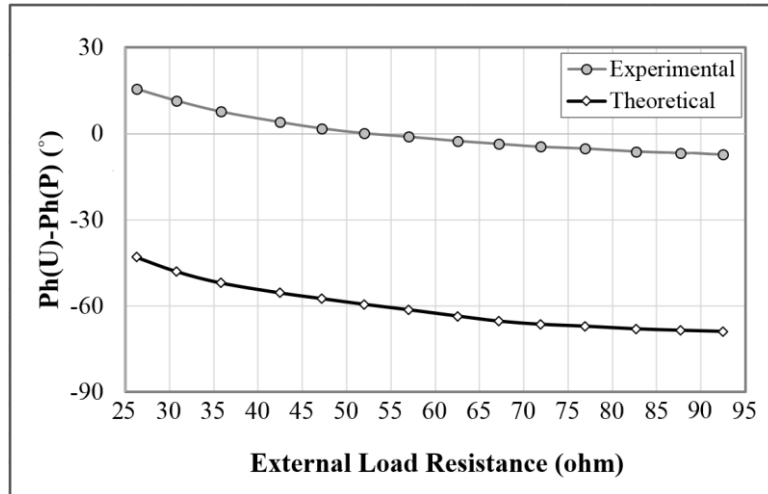


**Figure 5-16:** Experimental and theoretical phase difference versus load resistance at the alternator piston

### 5.2.2 The Effect Of Mean Pressure

In order to investigate the effect of the mean pressure in the system, the pressure of helium is varied in the range between 14 and 28 bar at a heating power of 1800 W. The change in the mean pressure changes the thermodynamic properties of the gas, e.g. density and thermal and viscous penetration depths which influence the energy conversion process of the thermoacoustic system. Swift *et al.* (2002) explained the effect of the mean pressure as being due to changes in the power density factor of  $p_m a A$ . The other very important effect of the mean pressure is that it has a direct effect on the acoustic impedance, therefore, it affects both thermal-to-acoustic and acoustic-to-electrical conversions.

The mean pressure influenced the oscillation frequency. The engine oscillated at 54.7 Hz for a mean pressure range of 28-22 bar and at a frequency of 52.4 Hz for mean pressures between 20 and 14 bar. This inconsistency is due to the effect of the mean pressure on the helium density. Reducing the mean pressure decreases the density which leads to a decrease in the speed of sound as per Equation (2.2). The drop in the speed of sound leads to a decrease in the oscillation frequency as per Equation (2.1). At mean pressure lower than 14 bar, the engine oscillates at a non-harmonic oscillation which failed to maintain itself and quickly damped.

The experiments confirmed that the system generates higher electricity and run at a higher thermal-to-electrical efficiency at elevated mean pressure. Figure 5.17 shows

the experimental and theoretical values of electricity generated at various mean pressures. The error bar represents the repeatability of the experiments and the point is the average of the repeated experiments. The solid line of Figure 5.17 shows the predicted results using the DeltaEC model after applying three measured boundary conditions: load resistance, pressure amplitude at the linear alternator and the temperature difference across the regenerator. There is a clear trend of increasing the generated electricity with increasing the mean pressure from 16 to 28 bar. Surprisingly, the electricity generated also increased when the mean pressure went below 16 bar. The main reason is that at 14 bar mean pressure, the thermal-to-acoustic efficiency goes higher at an approximately stable acoustic-to-electrical conversion as will be shown in the following paragraphs. It is clear that difference between the theoretical and experimental values of generated electricity is lower at lower mean pressure. This may be explained by the fact that the rig presents an acoustic conditions closer to the model at lower mean pressure, as the phase difference across the alternator obtained in experiment is closer to the theoretical value at lower mean pressure than the elevated mean pressure. In fact the reduction of alternator phase difference between 28 and 14 bar is  $3.2^\circ$  only.

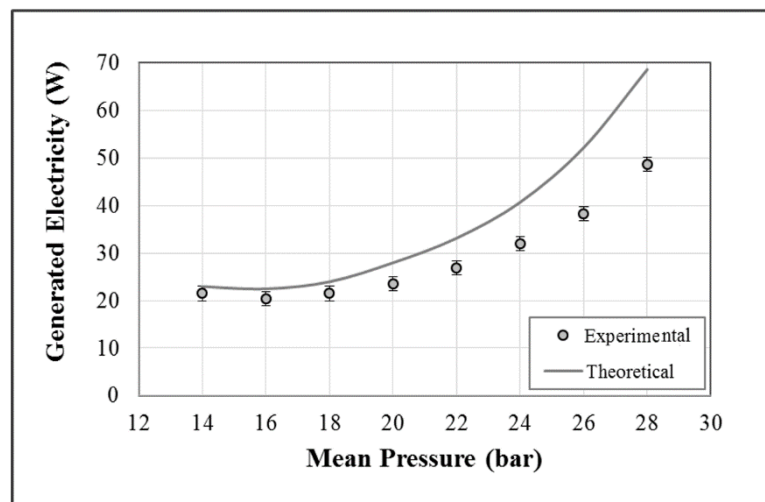


**Figure 5-17:** Theoretical and experimental performance of the engine as a function of the load resistance at 1800 W heating power and  $30\Omega$  load resistance

The study of the effect of the mean pressure was widened to various load resistances. Figure 5.18 shows the effect of mean pressure on the generated electricity at various load resistances. The mean pressure had the same effect on the power generation at all the studied load resistances. Dividing the generated electricity by the heating power, 1800 W, resulting in the total efficiency which is presented in Figure 5.19. The

generated electricity and the total efficiency reduced by dropping the mean pressure to 16 bar, then they increased again. A maximum of 48.6 W of electricity was generated at a total/thermal-to-electric efficiency of 2.7%.

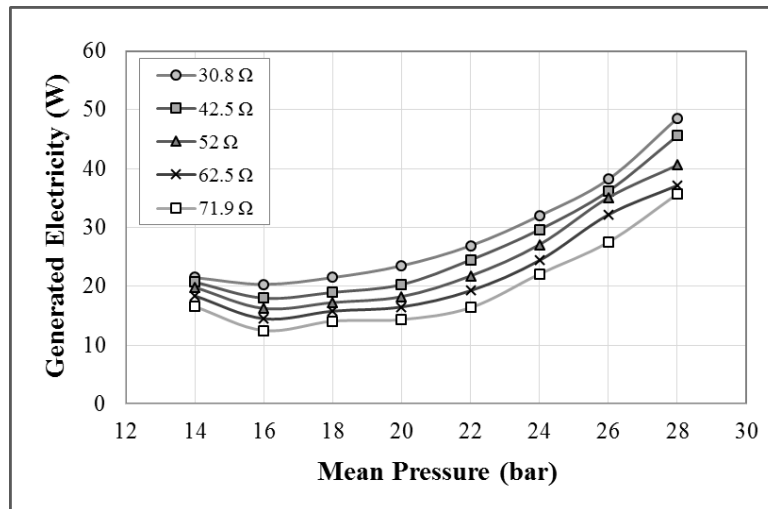


**Figure 5-18:** The performance of the engine versus mean pressure for various load resistances at 1800 W heating power

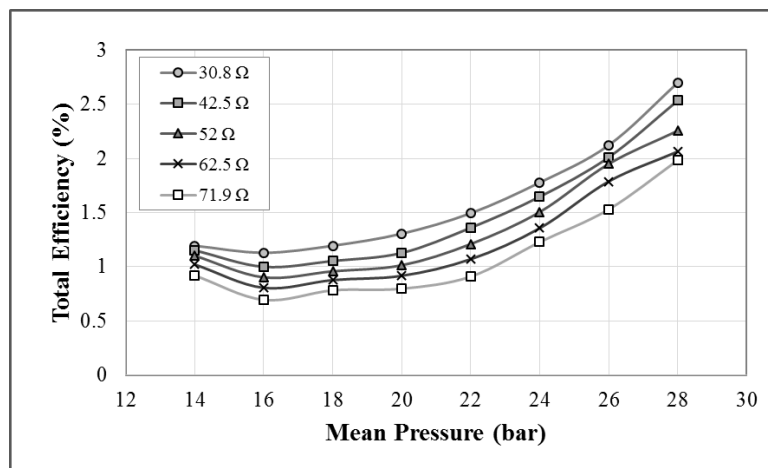


**Figure 5-19:** Total efficiency versus mean pressure for various load resistances at 1800 W heating power

The acoustic efficiency and the fraction to Carnot efficiency showed the same trend in the generated electricity, decreasing with decreasing the mean pressure from 28 to 16 bar and increasing to 14 bar as shown in Figures 5.20 and 5.21. As explained before, the engine ran at a higher acoustic efficiency and fraction to Carnot at higher load resistances. At the optimum load resistance, the thermal-to-acoustic efficiency is 8.85% and fraction to Carnot is 19.24%. While the tests recorded a higher maximum of fraction to Carnot of 28.72% and heat-to-acoustic efficiency of 12.43% at 28 bar mean pressure and 71.9 Ω load resistance. As explained before, the alternator extracts

less acoustic power at higher load resistance which leaves the acoustic power to circulate along the engine loop. The decrease of the heat-to-acoustic and fraction to Carnot efficiency at lower mean pressure can be explained, since reducing the mean pressure decreases the power density factor which reduces the acoustic power generation at a specific heat input. The alternator efficiency showed a different trend at various mean pressures, as shown in Figure 5.22. The mean pressure does not show a significant effect on the alternator efficiency in all the five load resistances studied. This trend is likely to be related to the acoustic conditions since the alternator phase difference does not change with pressure. As mentioned before the reduction of phase difference between the 28 and 14 bar is  $3.2^\circ$  only.

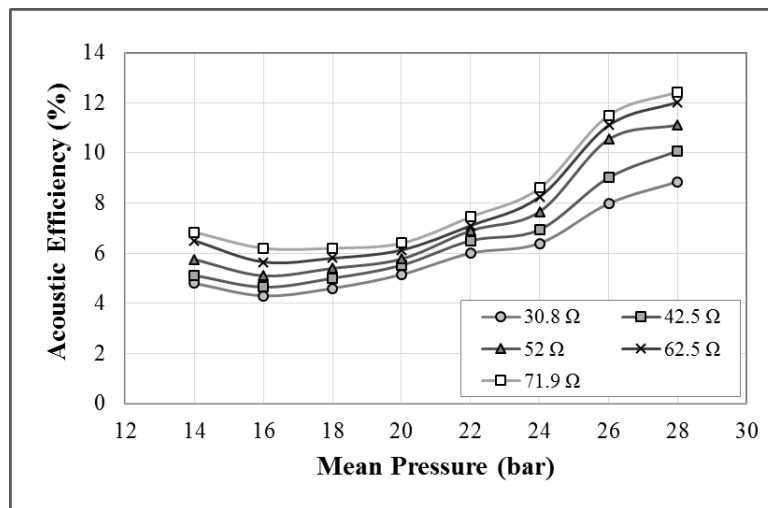


**Figure 5-20:** The relation between mean pressure and acoustic efficiency for various load resistances at 1800 W heating power

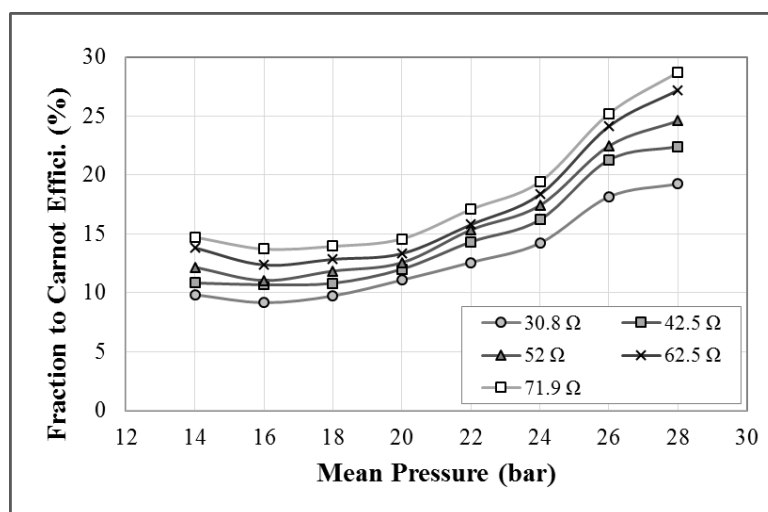


**Figure 5-21:** Fraction to Carnot efficiency versus mean pressure for various load resistances at 1800 W heating power

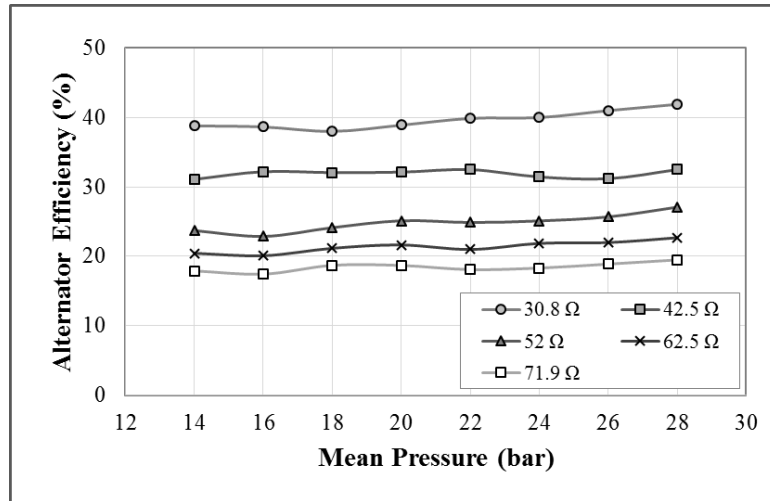


**Figure 5-22:** The effect of mean pressure on the linear alternator efficiency for various load resistance at 1800 W heating power

The drive ratio was increasing by decreasing the mean pressure, as shown in Figure 5.23. The fact is that the pressure amplitude was decreasing with the mean pressure, however, at a lower fraction and hence the ratio increased. A significant increase in drive ratio occurred at 14 bar as the pressure amplitude increased in spite of decreasing the mean pressure, which led to a higher ratio. The highest drive ratio recorded was 4.5% at 14 bar mean pressure and 71.9 Ω load resistance.

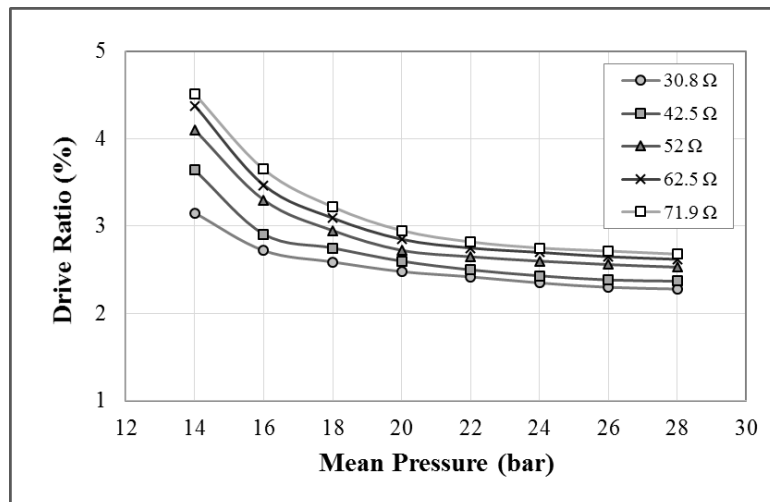


**Figure 5-23:** Measured drive ratio versus mean pressure for various load resistances at 1800 W heating power

The measured piston displacement decreased with decreasing mean pressure until 16 bar when it started to increase, as shown in Figure 5.24. The piston displacement is an indicator of the volume flow rate along the engine including the regenerator, and explains the effect of mean pressure on the regenerator temperature difference shown in Figure 5.25. At lower mean pressure, there was a lower oscillation volumetric flow

rate which lead to lower heat transfer and, hence, the temperature difference across the regenerator increased. Except at 14 bar, the piston displacement increase indicated a higher oscillation volumetric flow rate which lead to lower temperature difference. Figure 5.26 shows a detailed temperature distribution across the thermodynamic section at 1800 W heating power and 30.8  $\Omega$  load resistance. Clearly, the temperature across all the three hot locations of the thermodynamic section was higher at lower mean pressure. The highest hot heat exchanger temperature was recorded at 16 bar.

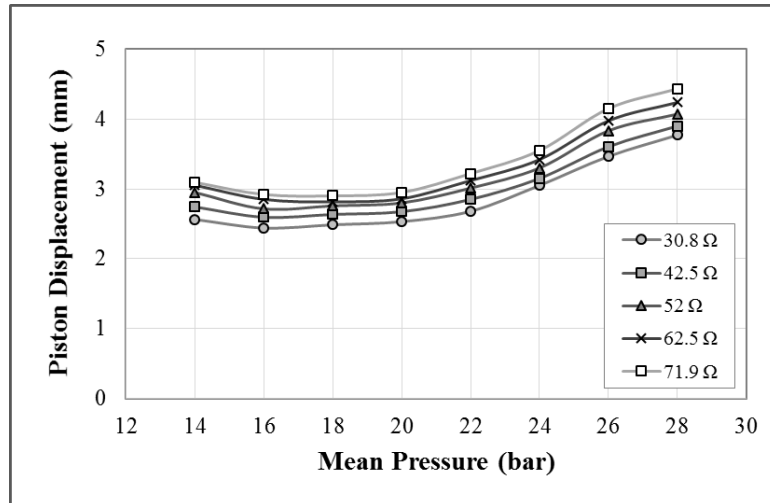


**Figure 5-24:** The effect of mean pressure on the piston displacement for various load resistances at 1800 W heating power

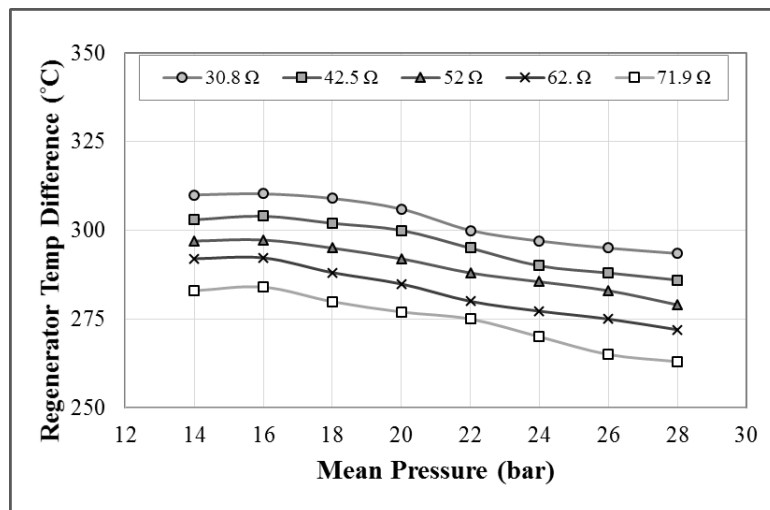


**Figure 5-25:** The effect of mean pressure on the regenerator temperature difference for various load resistances at 1800 W heating power

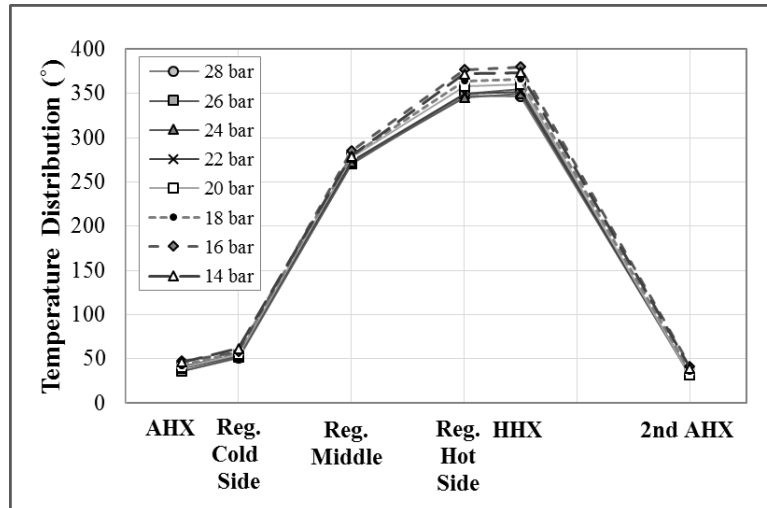


**Figure 5-26:** Core temperature distribution of different mean pressure at 1800 W heating power and 30.8  $\Omega$  load resistance

### 5.2.3 The Effect of Heating Power

The heating power is one of the two main parameters affecting the regenerator hot side temperature besides the amplitude displacement. However, it is the only dominant parameter with the ability to maintain high temperature difference regardless of the peak displacement value. The regenerator temperature difference is one of the main operational parameters defining the acoustic power generation. The heating power in the following graphs represents the summation of the heating power of the two stages. The heating power was always kept equal in the two stages, therefore, the heating power of each stage is half of the summation value. The heating power was varied from the minimum power that is able to maintain the oscillation of 700 W, to a maximum of 900 W, which is the maximum electrical power of the variable transformer. Figure 5.27 shows the effect of the heating power on the generated electricity for both experimental and simulation results. The error bar of the experimental is the repeatability of the test, while the solid line is the predicted results from the DeltaEC model after applying the experimental boundary conditions of load resistance, pressure amplitude at the linear alternator and the temperature difference across the regenerator. The simulation results showed a linear trend while the experimental was a curve. This inconsistent trend in the results may be due to the heat leakage which is happening in practice and cannot be considered at the simulation. The curved behaviour of the practical results of Figure 5.27 illustrates that the heat

leak at 1800 W heating power is higher than at 1600 W, and hence there is not a great reduction in the performance.

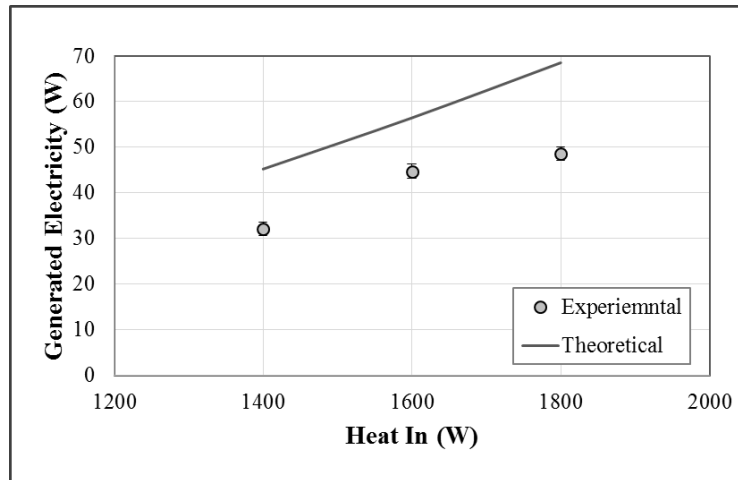


**Figure 5-27:** Theoretical vs experimental generated electricity at 28 bar mean pressure and 30.8  $\Omega$  external load resistance

The effect of the heating power on the electricity generated at various load resistances is shown in Figure 5.28. It shows that reducing the heating power from 1600 W to 1400 W has a greater effect on decreasing the electricity generated compared with reducing the heating power from 1800 W to 1600 W for most of the load resistances studied. The trend of the electricity generated is more linear at higher load resistance than the lower resistance. A possible explanation is that the heat is transferred through the thermoacoustic effect more than by heat leaking at higher load resistance. The total efficiency or the thermal-to-electrical efficiency recorded a new maximum of 2.8% at 28 bar mean pressure, 30.8  $\Omega$  load resistance and 1600 W heating power, as shown in Figure 5.29. The total efficiency is decreased with reduction of the heating power as the electricity generated reduced. Reducing the heating power from 1800 W to 1600 W does not have a significant effect on the total efficiency (except at 71.9  $\Omega$ ), and both the electricity generated and the heating power decreased almost equally.

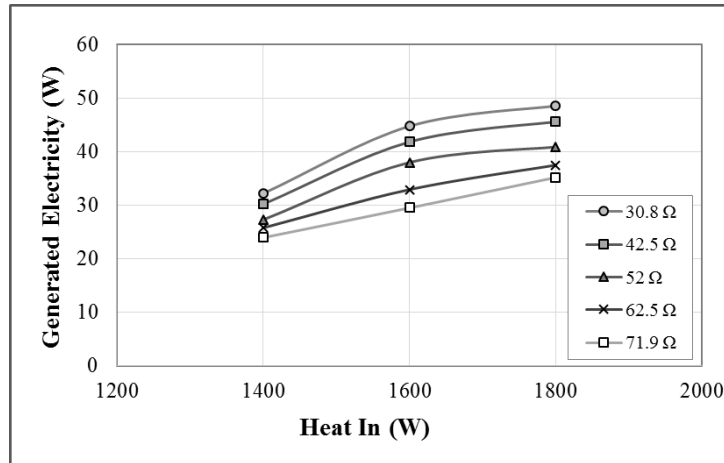


**Figure 5-28:** The performance of the engine as a function of heating power for various load resistances at 28 bar mean pressure

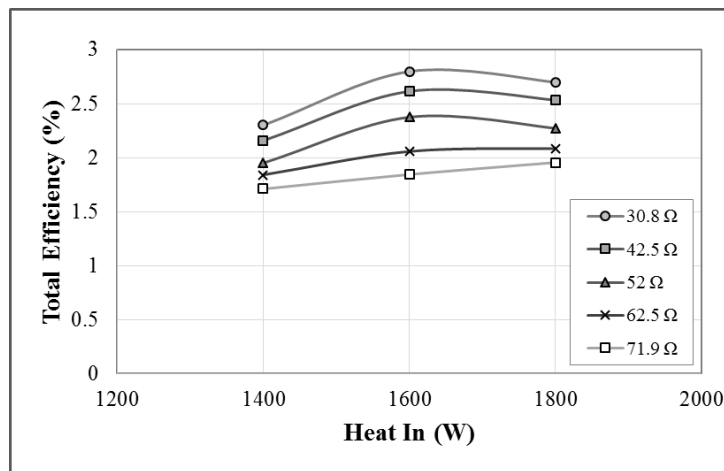


**Figure 5-29:** Total efficiency of different heating power for various load resistances at 28 bar mean pressure

The acoustic efficiency was found to have a linear relation with the heating power, as shown in Figure 5.30. The reduction in heating power reduced the conversion of heat to sound. Dividing this efficiency by Carnot efficiency led to the fraction to Carnot efficiency shown in Figure 5.31. The effect of the heating power on the acoustic and fraction to Carnot efficiencies could be explained as following: reducing the heating power reduces the temperature difference across the regenerator which reduces the acoustic power generation. Similar to the effect of the mean pressure, the heating power does not have a significant effect on the alternator efficiency, as the heating power does not affect the acoustic conditions of the network, as shown in Figure 5.32. At optimum load of  $30.8\Omega$ , the acoustic and fraction to Carnot efficiencies are 6.85% and 14.5%, respectively. The highest acoustic and fraction to Carnot efficiencies are 12.4% and 28.7%, respectively at  $71.9\Omega$  load resistance.

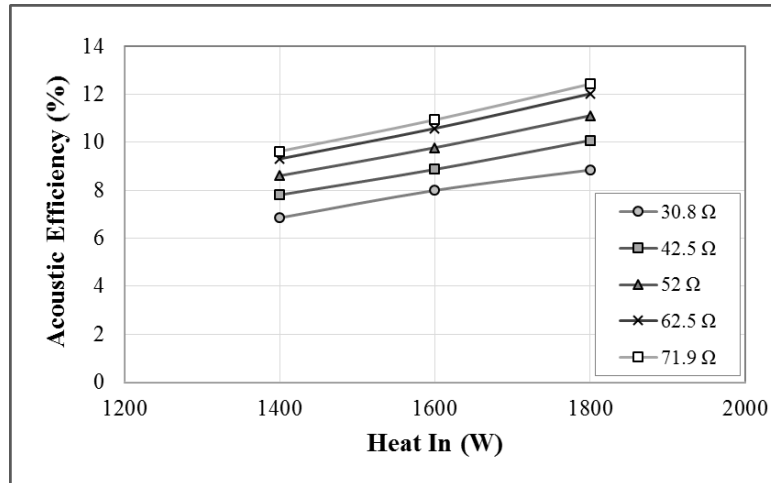


**Figure 5-30:** The relation between heating power and acoustic efficiency for various load resistances at 28 bar mean pressure

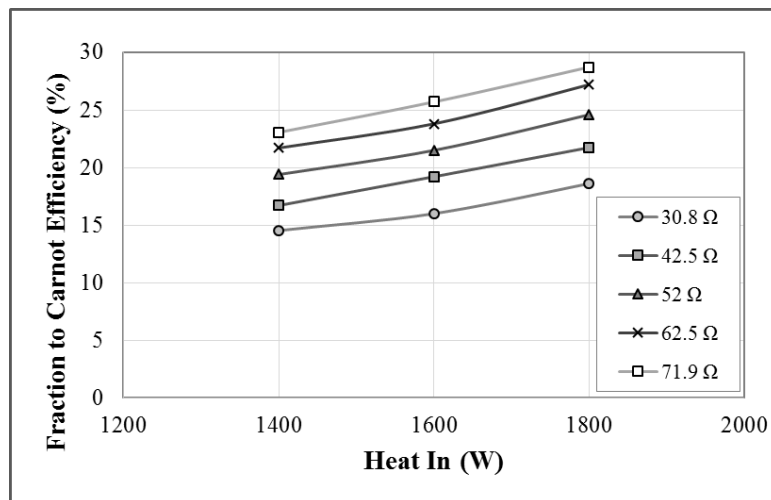


**Figure 5-31:** Fraction to Carnot efficiency versus heating powers for various load resistances at 28 bar mean pressure

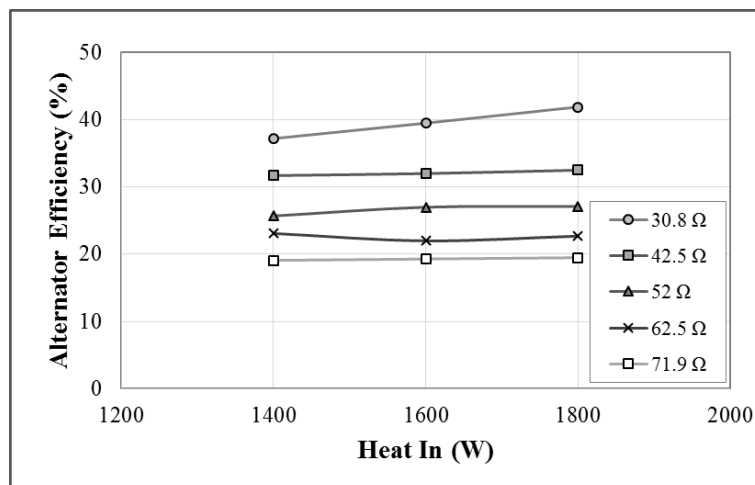


**Figure 5-32:** The effect of heating power on the alternator efficiency for various load resistances at 28 bar mean pressure

The reduction in the heating power decreased the alternator peak displacement, as shown in Figure 5.33. Taking this reduction as an indicator to a reduction in the oscillation displacement along the engine loop and especially the regenerator, this explains the insignificant reduction of the regenerator temperature difference shown in Figure 5.34. The effect is insignificant as the peak displacement is reduced with the reduction of the heating power. A detailed temperature distribution across the thermodynamic section is shown in Figure 5.35. Apart from the streaming, two points could be explained in this graph as it has less data series in comparison with the two previous parameters of Sections 5.2.1 and 5.2.2. First, the regenerator cold side and the ambient heat exchanger temperature rises with higher oscillation peak displacement. Second, the temperature of the regenerator hot side approaches the hot heat exchanger temperature at higher oscillation peak displacement.

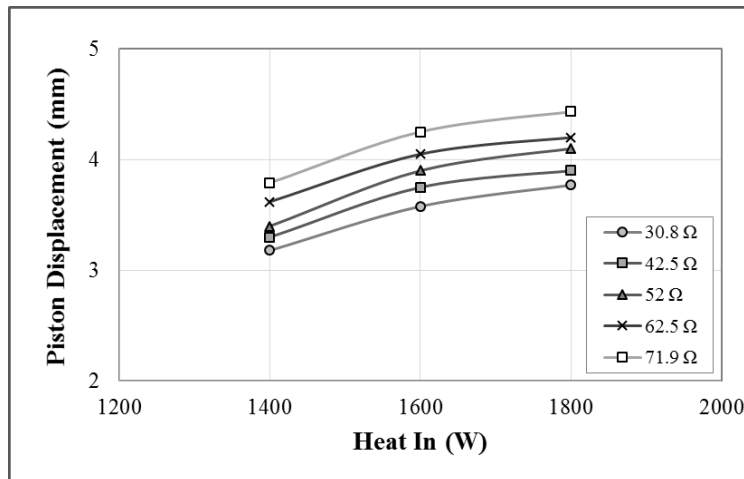


**Figure 5-33:** The effect of heating power on the alternator piston displacement for various load resistances at 28 bar mean pressure

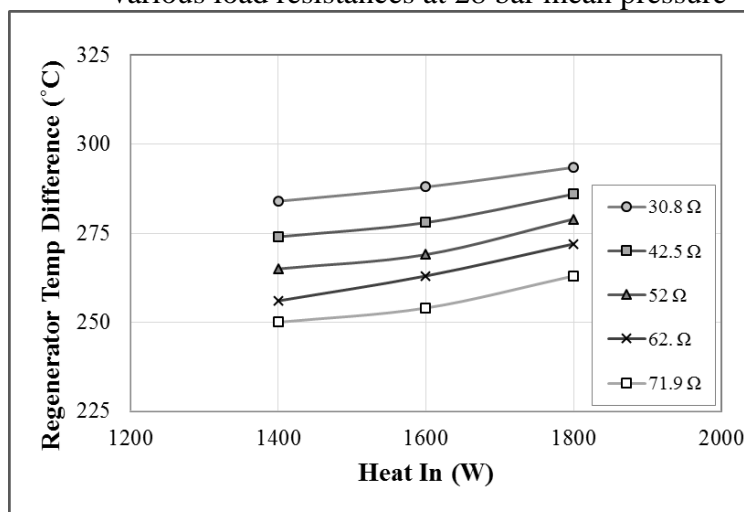


**Figure 5-34:** The effect of heating power on the temperature difference across the regenerator for various load resistances at 28 bar mean pressure

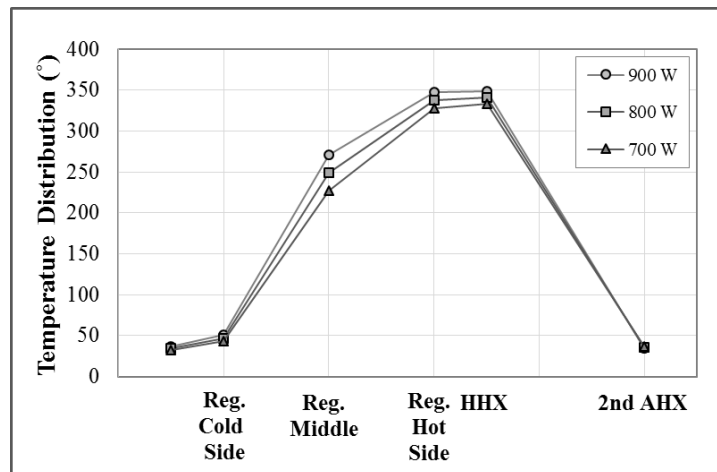


**Figure 5-35:** Core temperature distribution of different heating powers at 28 bar mean pressure

The effect of the mean pressure and heating power could be combined to be presented at a specific load resistance. The performance graphs will be presented at 30.8  $\Omega$  which was proven to be the optimum load resistance. The reduction of 200 W of heating power from 1800 W to 1600 W and 1600 W to 1400 W at various mean pressures reduces the electricity generated by 20-25%, as shown in Figure 5.36. Obviously, the electricity generation increases by increasing the heating power at any mean, increasing the mean pressure leads to generating more electricity at any heating power (except increasing from 14-16 bar). Figure 5.37 shows the effect of the mean pressure on the total efficiency for various heating powers. Clearly, the heating power has less effect on the total efficiency as compared with the generated electricity, as an increase of 200 W in the heating power cannot increase the electricity generated by more than 10 W. The mean pressure clearly has a greater effect at any heating power.

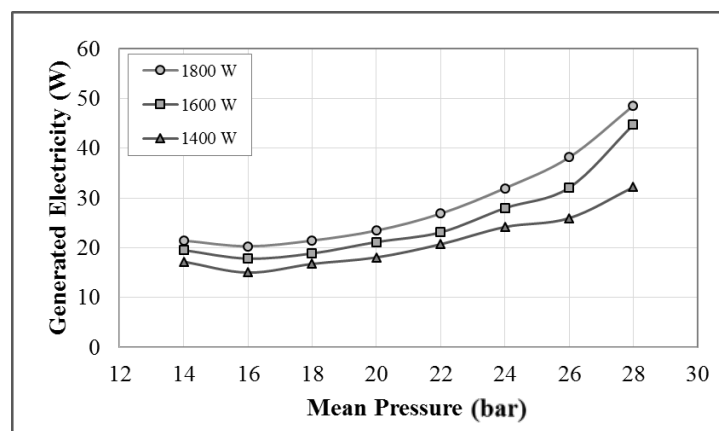


**Figure 5-36:** The performance of the engine as a function of mean pressure and heating power at 30.8  $\Omega$  load resistance

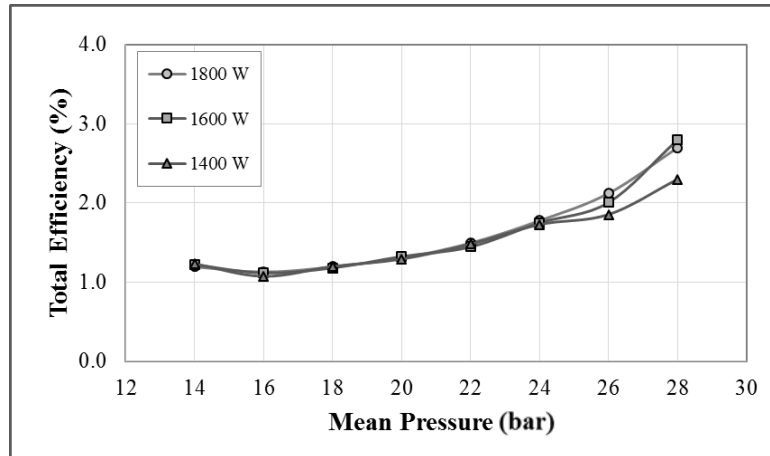


**Figure 5-37:** Total efficiency of different mean pressure for various heating powers at 30.8 Ω load resistance

The effects of the mean pressure and heating power on the acoustic efficiency, shown in Figure 5.38, and the fraction to Carnot, shown in Figure 5.39, are smaller than for the previous results presented as this was at a low load resistance of 30.8 Ω. The engine ran at higher acoustic and fraction to Carnot efficiency at higher mean pressure and heating power. Figure 5.40 shows the experimental data of the alternator efficiency at various mean pressures and heating power. It is apparent from the graph that mean pressure and heating power do not affect the alternator efficiency. The effect of the heating power on the alternator efficiency is more significant at 28 bar, as it has changed the acoustic impedance and phase difference.

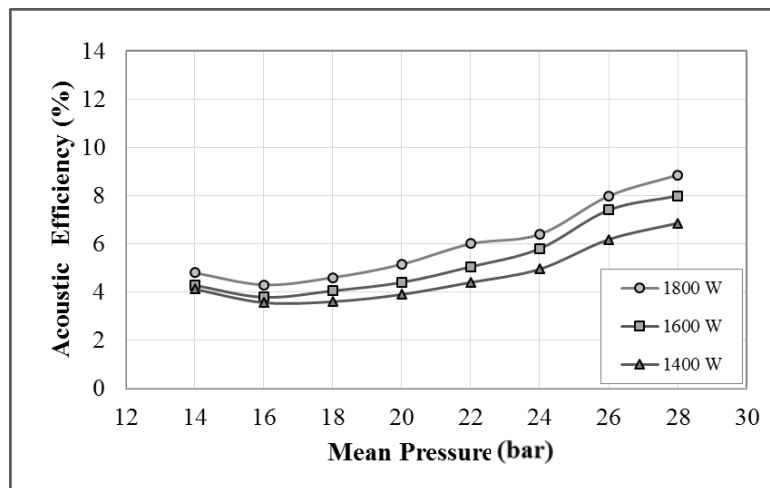


**Figure 5-38:** The effect of mean pressure on the acoustic efficiency for various heating powers at 30.8Ω load resistance

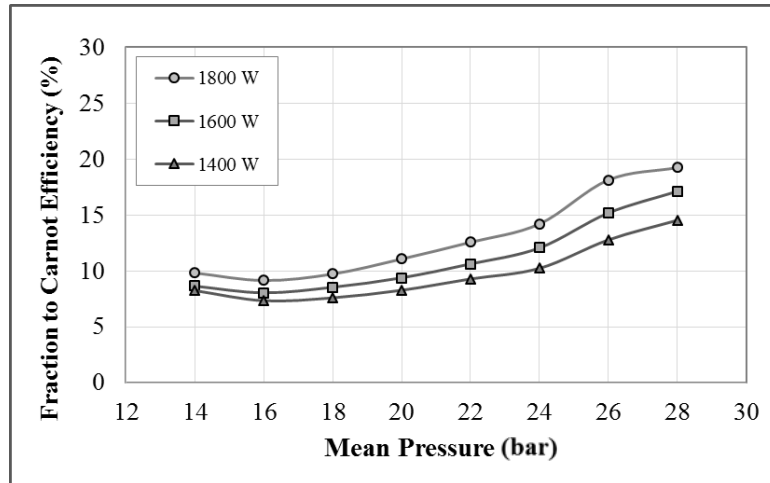


**Figure 5-39:** The effect of mean pressure on the fraction to Carnot efficiency for various heating powers at  $30.8\Omega$  load resistance

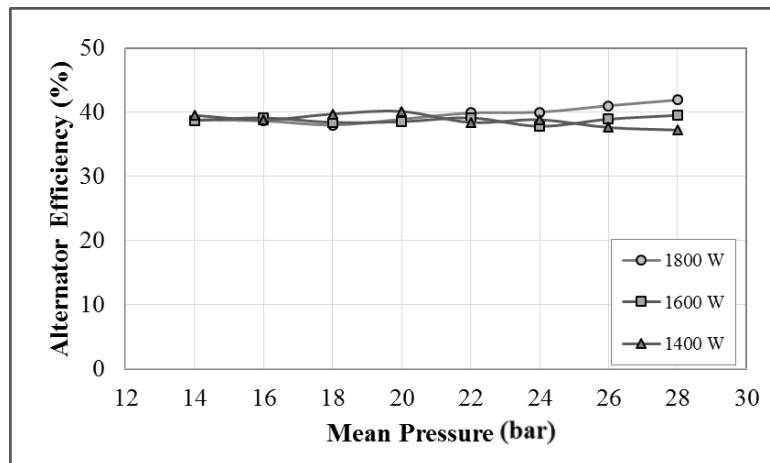


**Figure 5-40:** The effect of mean pressure on the alternator efficiency for various heating powers at  $30.8\Omega$  load resistance

Figure 5.41 shows the effect of the mean pressure on the alternator piston peak displacement at various heating powers. At higher heating power, the piston peak displacement is higher. There is a clear trend of decreasing the piston displacement when decreasing the mean pressure from 28 to 20 bar at any heating power, and an insignificant effect when decreasing the mean pressure from 20 to 14 bar. The trend of the piston displacement behaviour, as an indicator to the oscillation peak displacement along the rig, explains the effect of the mean pressure on the temperature difference shown in Figure 5.42. It also shows that a greater temperature difference was noticed at higher heating power at a specific mean pressure.

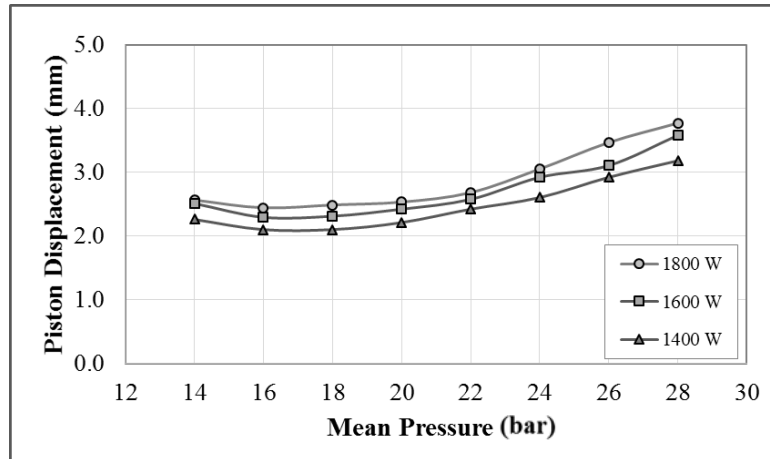


**Figure 5-41:** The effect of mean pressure on the alternator piston displacement for various heating powers at 30Ω load resistance

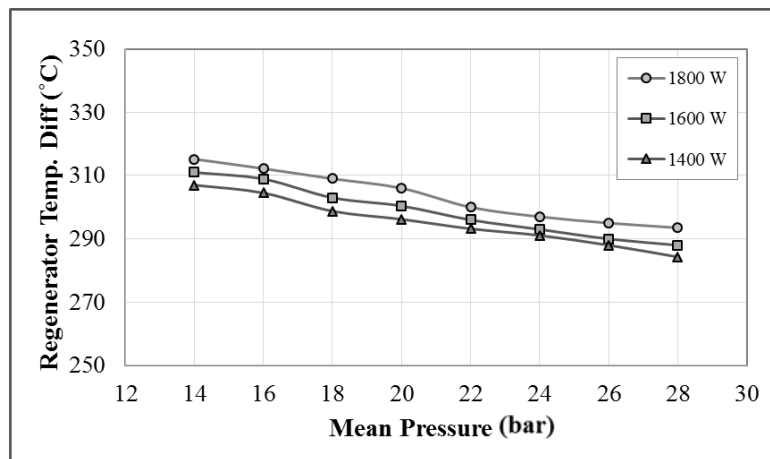


**Figure 5-42:** The effect of mean pressure on the regenerator temperature difference for various heating powers at 30Ω load resistance

### 5.2.4 Mixed Variable Studies

The study was widened aiming to investigate the full performance behaviour of the thermoacoustic engine at various load resistances, mean pressure and heating power. The effect of mean pressure was presented in Section 5.2.2 at 1800 W heating power for various load resistances. More tests were carried out to study the effect at 1600 W and 1400 W. In Section 5.2.3, the effect of heating power was presented at 28 bar mean pressure for various load resistances. More results graphs were also been made at 26, 24, 22, 20, 18, 16 and 14 bar. Selective data will be presented in this Section and the full results can be found in Appendix Four, from Figure A4.1 to A4.82. Table 5.1 provides a summary of the experimental data of the performance behaviour of the engine at mixed variables.

Firstly, some results of the mean pressure parameter at various heating powers will be discussed. The effect of the mean pressure on the frequency was similar for all the three heating powers studied, as it oscillated at 54.7 Hz for a mean pressure range of 28-22 bar and at a frequency of 52.4 Hz between 20 and 14 bar. Also, the minimum mean pressure that maintained the oscillation at a resonance was 14 bar regardless of the heating power.

The effect of mean pressure on the electricity generated for various load resistances at different heating powers is shown in Figures 5.18, A4.1 and A4.10. All the three curves showed that the electricity generated decreased by reducing the mean pressure from 28 to 16 bar and increased a small fraction when reducing the mean pressure from 16 to 14 bar. Reducing the heating power from 1800 W to 1600 W showed a greater influence on the generated electricity series compared to reducing the heating power from 1600 W to 1400 W. At a heating power of 1400 W shown in Figure A4.10, there is no significant difference in the electricity generated for mean pressures between 14 and 20 bar.

Similarly, the effect of mean pressure on the acoustic efficiency was influenced by reducing the heating power from 1800 to 1600 W and higher than 1600 to 1400 W, and the same trend was maintained. In contrast, no significant differences were found for the effect of the mean pressure on the alternator efficiency at various heating powers, as shown in Figures 5.22, A4.5 and A4.16.

The drive ratio behaviour changed when reducing the heating power to 1600 W and 1400 W, as shown in Figures 5.23, A4.7 and A4.15. Increasing the mean pressure from 26 to 28 bar showed an insignificant decrease in the drive ratio at a heating power of 1800 W, while it noticeably decreased at a lower heating power. The main reason is that the high heating power of 1800 W was able to maintain the regenerator temperature difference from a significant decrease when increasing the mean pressure from 26 to 28 bar, while the lower heating power failed to do this, as shown in Figures 5.25, A4.9 and A4.18.

Secondly, some results of the heating power at various mean pressures will be presented. Decreasing the heating power reduces the electricity generated, however, it has mainly an insignificant or no effect on the total efficiency at mean pressures

between 24 and 14 bar as shown in Figures 5.29, A4.19, A4.28, A4.37, A4.46 and A4.55. As the mean pressure reduced from 28 to 18 bar the acoustic efficiency reduced and the influence of the load resistance receded at a specific mean pressure and heating power. When it increased the influence of the load resistance became more intense as the mean pressure reduced from 18 to 14 bar, as shown in Figures 5.30, A4.19, A4.30, A4.39, A4.48, A4.57, A4.66 and A4.75. There is a similar effect on the fraction to Carnot efficiency.

The heating power has shown an insignificant influence on the drive ratio at a specific load resistance at 28 bar mean pressure, as shown Figure A4.85. The flat trend changed to an incline gradually from 28 to 14 bar, as shown in Figures A4.82, A4.24, A4.33, A4.42, A4.51, A4.60, A4.69 and A4.78.

**Table 5.1:** Summary of the main five selected parameters at various heating power and mean pressure

Heating Power	Mean Pressure	Total Efficiency (%), at					Acoustic Efficiency (%),					Fraction to Carnot					Regenerator temperature Difference (°C), at				
		30.8Ω	52Ω	71.9Ω	30.8Ω	52Ω	71.9Ω	at 30.8Ω	at 52Ω	at 71.9Ω	at 30.8Ω	at 52Ω	at 71.9Ω	at 30.8Ω	at 52Ω	at 71.9Ω	at 30.8Ω	at 52Ω	at 71.9Ω		
1800	28	48.6	40.6	35.7	2.7	2.3	2.0	8.9	11.1	12.4	19.2	24.6	28.7	293.5	279.0	263.0					
1800	26	38.2	35.1	27.5	2.1	1.9	1.5	8.0	10.5	11.5	18.1	22.5	25.2	295.0	283.0	265.0					
1800	24	32.0	27.1	22.1	1.8	1.5	1.2	6.4	7.7	8.6	14.2	17.4	19.4	297.0	285.5	270.0					
1800	22	26.9	21.8	16.4	1.5	1.2	0.9	6.0	6.9	7.5	12.6	15.3	17.1	300.0	288.0	275.0					
1800	20	23.5	18.3	14.4	1.3	1.0	0.8	5.2	5.8	6.4	11.1	12.5	14.6	306.0	292.0	277.0					
1800	18	21.5	17.3	14.1	1.2	1.0	0.8	4.6	5.4	6.2	9.7	11.8	13.9	309.0	295.0	279.9					
1800	16	20.3	16.3	12.5	1.1	0.9	0.7	4.3	5.1	6.2	9.2	11.0	13.7	310.3	297.3	284.0					
1800	14	21.5	19.8	16.6	1.2	1.1	0.9	4.8	5.8	6.8	9.8	12.2	14.7	310.0	297.0	283.0					
1600	28	44.8	38.9	29.5	2.8	2.4	1.8	8.0	9.8	10.9	17.1	23.1	27.6	288.0	269.0	254.0					
1600	26	32.1	28.2	23.0	2.0	1.8	1.4	7.6	9.1	10.2	15.2	19.1	22.1	290.0	271.0	258.0					
1600	24	28.0	25.1	19.6	1.8	1.6	1.2	5.8	6.8	7.9	12.1	14.9	17.7	293.0	276.0	262.0					
1600	22	23.1	19.4	15.7	1.4	1.2	1.0	5.1	6.0	6.7	10.6	13.5	15.3	296.0	279.0	264.2					
1600	20	21.2	16.6	12.7	1.3	1.0	0.8	4.4	5.0	5.8	9.4	11.1	13.1	300.4	284.3	270.6					
1600	18	18.9	15.0	12.3	1.2	0.9	0.8	4.1	4.8	5.5	8.5	10.5	12.4	303.0	289.6	274.9					
1600	16	17.9	14.6	12.0	1.1	0.9	0.7	3.8	4.9	5.8	7.9	10.6	12.8	308.9	293.5	279.1					
1600	14	19.6	16.8	14.9	1.2	1.0	0.9	4.2	5.7	6.6	8.6	12.2	14.2	308.5	295.0	278.4					

**Table 5.1:** Continued

Heating Power	Mean Pressure	Generated Electricity (W), at 30.8Ω	Generated Electricity (W), at 52Ω	Generated Electricity (W), at 71.9Ω	Total Efficiency (%), at 30.8Ω	Total Efficiency (%), at 52Ω	Total Efficiency (%), at 71.9Ω	Acoustic Efficiency (%), at 30.8Ω	Acoustic Efficiency (%), at 52Ω	Acoustic Efficiency (%), at 71.9Ω	Fraction to Carnot Efficiency (%), at 30.8Ω	Fraction to Carnot Efficiency (%), at 52Ω	Fraction to Carnot Efficiency (%), at 71.9Ω	Regenerator temperature Difference (°C), at 30.8Ω	Regenerator temperature Difference (°C), at 52Ω	Regenerator temperature Difference (°C), at 71.9Ω
1400	28	32.2	27.3	23.9	2.3	2.0	1.7	6.9	8.6	9.6	14.5	19.5	22.4	284.3	265.0	250.0
1400	26	26.0	22.4	19.4	1.9	1.6	1.4	6.2	8.0	9.0	12.8	16.7	19.4	288.0	268.0	256.2
1400	24	24.2	21.1	17.2	1.7	1.5	1.2	5.0	5.9	6.9	10.2	13.1	15.5	292.2	273.0	257.8
1400	22	20.8	18.0	13.9	1.5	1.3	1.0	4.4	5.3	5.9	9.3	12.0	13.7	294.3	277.4	260.2
1400	20	18.1	15.6	11.5	1.3	1.1	0.8	3.9	4.5	5.1	8.3	9.9	11.5	296.2	282.3	267.1
1400	18	16.8	13.6	10.0	1.2	1.0	0.7	3.6	4.2	5.0	7.6	9.3	11.3	298.8	284.6	271.2
1400	16	15.1	12.3	9.7	1.1	0.9	0.7	3.6	4.2	5.2	7.5	9.2	11.7	304.5	286.9	275.2
1400	14	17.3	14.3	11.8	1.2	1.0	0.8	4.1	5.4	6.2	8.6	11.8	13.7	303.5	285.4	274.0

### 5.3 Concluding Remarks

- In the experiments, the maximum electric power of 48.6 W with a thermal-to-electric efficiency of 2.7% and the maximum thermal-to-electric efficiency of 2.8% with electric power of 44.8 W was achieved. For which the thermal-to-acoustic efficiency and fraction to Carnot efficiency were 8.85% and 18.6%, respectively.
- The effect of load resistance was studied. In practice, the optimum load resistance was 30.8  $\Omega$ . Any load resistance will damp the oscillation. Increasing the load resistance to more than 30.8  $\Omega$  lead to a decrease in the generated electricity and an increase in the acoustic and fraction to Carnot efficiencies.
- Reducing the mean pressure from 28 to 16 bar decreases the generated electricity, acoustic and fraction to Carnot efficiencies. Surprisingly, reducing the mean pressure from 16 to 14 bar generates more electricity and a higher efficiency.
- The heating power was found to have a direct relationship with the electricity generation and performance efficiencies. It was studied at 1400, 1600 and 1800 W.
- The experiments showed a list of problematic issues:
  - The engine failed to self-start.
  - High heat leak.
  - Phase difference shifted about 60°.
  - The alternator extracts acoustic power from one side more than the other.
  - Presence of Gedeon streaming in all the cases studied.

## Chapter 6

### Optimization and Experimental Debugging

In this chapter, the optimization targets are discussed in Section 6.1. The effect of reducing the heat leak is presented and discussed in Section 6.2. The findings of Section 6.3 lead to investigate the effect of increasing the heating power, as presented in Section 6.4. The solution of the engine self-starting is discussed in Section 6.4. Section 6.5, explains the efforts done towards eliminating the streaming. Section 6.6, concludes the results and findings of the previous sections.

#### 6.1 Optimization Target

The optimization process was targeted to delivering measurable performance improvements to the engine. A list of five obstacles was mentioned in Section 5.3. The optimization procedure was designed to solve or eliminate three of them; self-starting, heat leak and streaming. The solutions for the other two is suggested in the future work for serious limitations.

#### 6.2 Heat Leak Reduction: Effect of Installing an Insulating Gasket

The heat leak is understood to happen due to conduction from the hot heat exchanger to the adjacent pieces. There isn't a lot that could be done without manufacturing new pieces that thermally insulate the hot heat exchanger. The time and resource limitations made it difficult to manufacture new pieces in the current research. The calculations of the heat transferred to the main and secondary ambient heat exchangers showed that 400 to 550 W is transferred to the main ambient heat, while only 25 to 75 W is transferred to the secondary ambient heat exchanger. A possible solution is to place a gasket having low thermal conductivity at the metal-to-metal contact between the regenerator holder and the ambient heat exchanger, as shown in figure 6.1. The gasket can reduce the conductive heat transfer, as well as, it can maintain a pressure seal. A gasket made out of thermiculite 715, Flexitallic model number SCRC04003T71515, was used. This gasket material has a low thermal conductivity of 0.3 W/m.K. The minimum available gasket thickness of 1.5 mm was selected. At this thickness, the gasket can seal up to 140 bar at a temperature of up to 540°C.

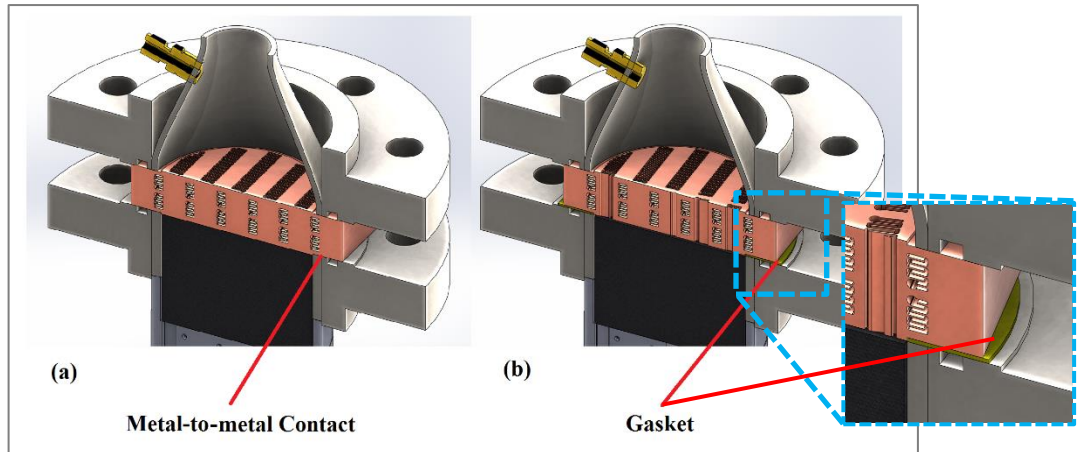


**Figure 6-1:** A cross section of the thermodynamic section showing (a) metal-to-metal contact between the regenerator holder and the ambient heat exchanger, (b) gasket, in yellow, installed in position.

The experiments showed that the insulating gasket improved the performance of the engine. Figure 6.2 compares the performance of the engine with and without an insulating gasket at 30.8  $\Omega$  load resistance, 28 bar mean pressure and 1800 W heating power. The gasket improved the performance by increasing the electricity generated. The main trend of the data was maintained and the maximum was increased from 48.6 to 62.2 W. This improvement is reflected in the total efficiency as shown in Figure 6.3. The maximum thermal-to-electrical efficiency was increased from 2.7% to 3.4%.

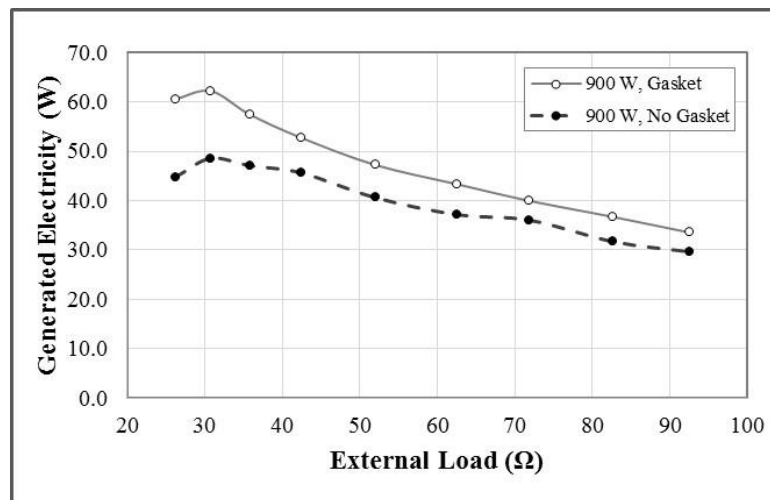


**Figure 6-2:** Performance of the engine with and without an insulating gasket at 28 bar mean pressure and 1800 W heating power

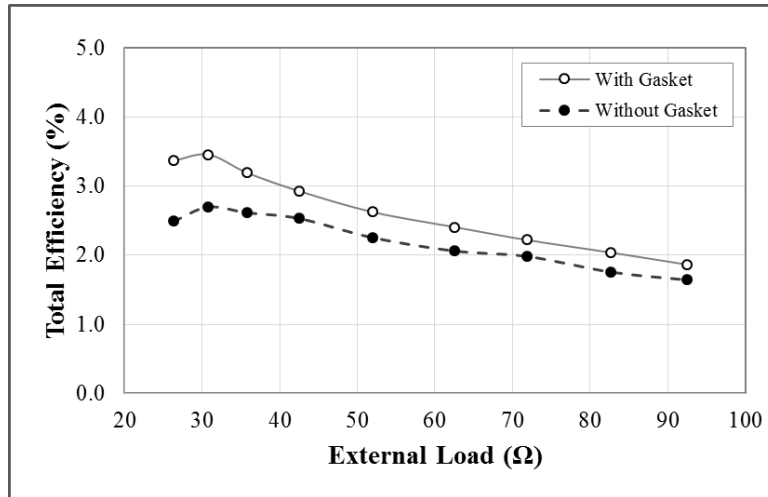


**Figure 6-3:** Total efficiency for both with and without insulating gasket at 28 bar mean pressure and 1800 W heating power

This improvement in performance is as a result of the enhancement of both thermal and acoustical fields. Figure 6.4 compares the regenerator temperature difference before and after installing the insulating gasket, at a similar heating power, load resistance and mean pressure for various values of load resistance. Clearly, installing the gasket increased the temperature difference for all load resistance values. A higher temperature difference generated higher acoustic power. Figure 6.5 shows the improvement of the acoustic efficiency caused by installing the insulating gasket. The new highest acoustic efficiency is 16.8%.

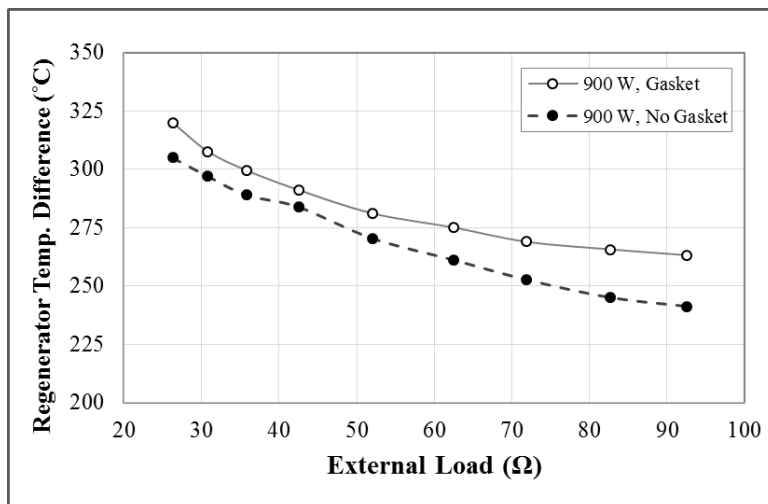


**Figure 6-4:** Regenerator temperature difference with and without an installing insulating gasket at 28 bar mean pressure and 1800 W heating power

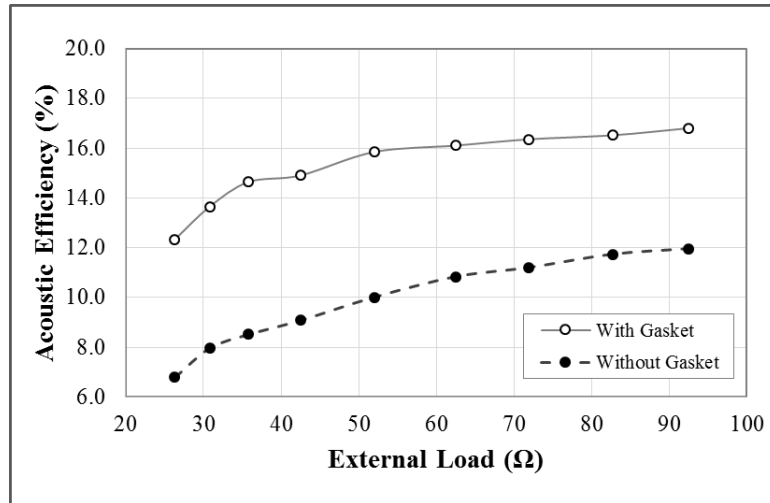


**Figure 6-5:** A comparison of the engine’s acoustic efficiency with and without an insulating gasket at 28 bar mean pressure and 1800 W heating power

The improvement in the acoustic field could be presented in more detail by expressing the drive ratio and linear alternator efficiency. At the same mean pressure of 28 bar, the drive ratio at the linear alternator was improved by at least 35% as shown in Figure 6.6. The new maximum drive ratio is 3.18%. The rise in the drive ratio produced a growth in the acoustic impedance value. As has been discussed previously in Section 3.2, the alternator ran at a higher efficiency and at a higher acoustic impedance. Figure 6.7 shows the increment of the linear alternator efficiency by installing the insulating gasket at various load resistances and almost the same phase difference.

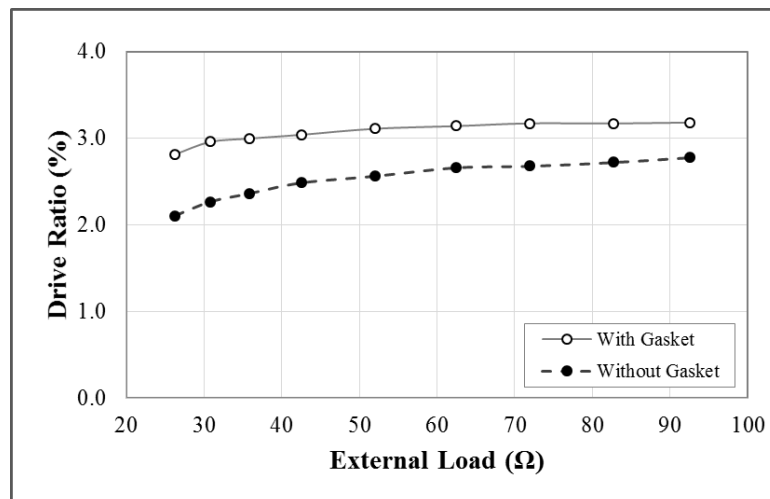


**Figure 6-6:** Drive ratio before and after installing the insulating gasket at 28 bar mean pressure and 1800 W heating power

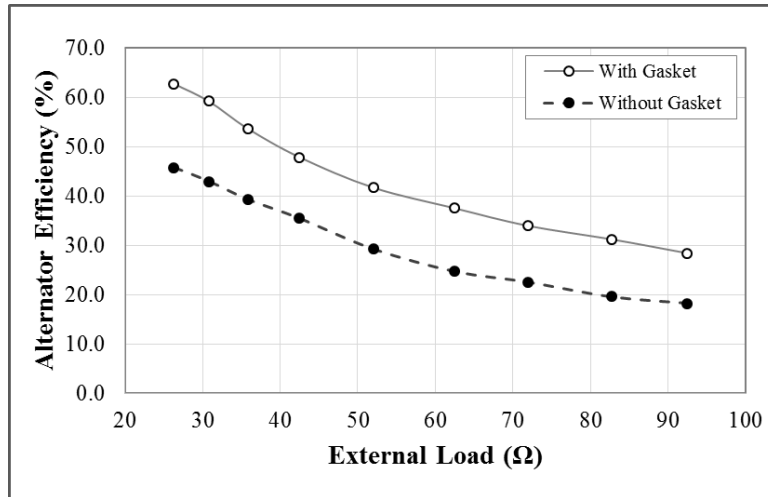


**Figure 6-7:** The effect of using an insulating gasket on the alternator efficiency at 28 bar mean pressure and 1800 W heating power

The enhancement of the performance encouraged a repeat of the full performance behaviour. The scale of the three parameters will be different in this section as compared to Section 5.2.4. The highest load resistance will be increased from 71.2 Ω to 92.5 Ω in order to investigate higher acoustics and fractions to Carnot efficiency. The mean pressure will be reduced in two steps, to only have a trend of data development similar to the steps of the heating power.

Figure 6.8 shows the experimental performance data of the engine at different heating powers for various load resistances with an insulating gasket. The graph compares the results for the case without an insulating gasket, presented in Figure 5.28. The current data series are steeper than Figure 5.28 and the spacing between the data series has increased. The increased spacing could be explained by comparing the alternator efficiency at that load resistance which showed the higher increase, as seen in Figure 6.9, with the previous results shown in Figure 5.32. Similar to the data before installing the gasket, the alternator efficiency did not affect the heating power.

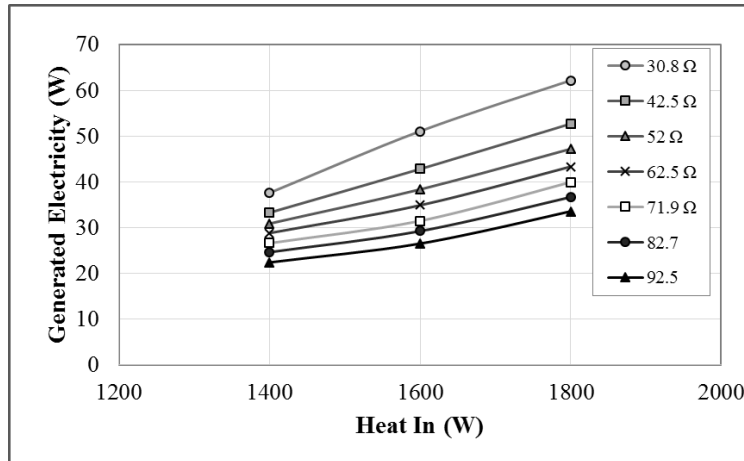


**Figure 6-8:** Performance of the engine with insulating gasket at different heating power for various load resistance at 28 bar mean pressure

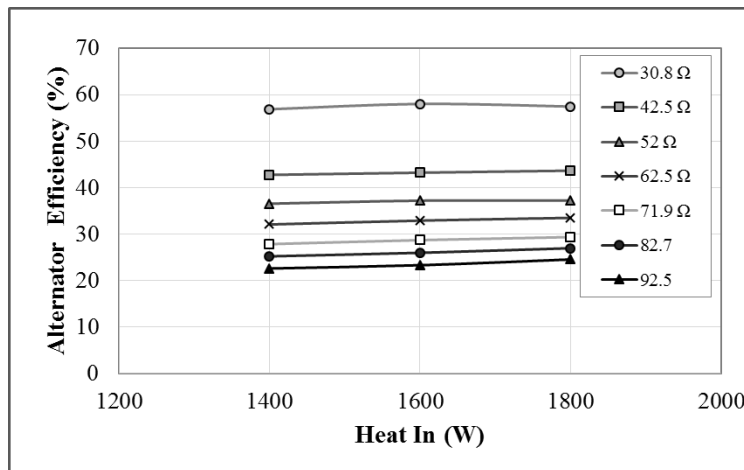


**Figure 6-9:** Alternator efficiency of the engine with insulating gasket at different heating power for various load resistance at 28 bar mean pressure

An interesting finding of this new performance behaviour is that the trend of the thermal-to-electric efficiency was changed by installing the insulating gasket. Previously, as shown in Figure 5.29 of the thermal-to-electric efficiency without an insulating gasket, the maximum efficiency was attained at 1600 W. The conclusion of the previous results is that increasing the heating power to more than 1800 W may decrease the thermal-to-electric efficiency, based on the trend of the data. However, the trend changed after installing the insulating gasket. Figure 6.10 shows the thermal-to-electric efficiency for various heating powers, with insulating gasket installed. The trend show that increasing the heating power from 1400 W to 1600 W and from 1600 W to 1800 W increases the thermal-to-electric efficiency. Based on that new trend, more heaters were installed to increase the heating power and the results will be presented in the next section.

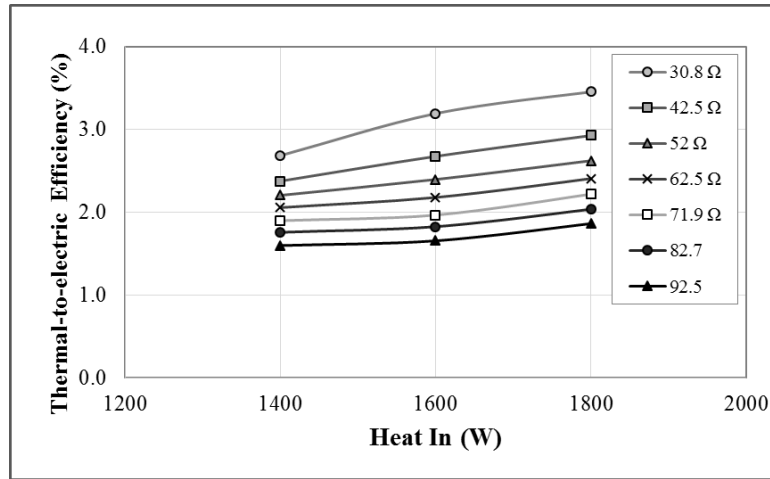


**Figure 6-10:** Thermal-to-electric efficiency at different heating power for various load resistances for an engine with an insulating gasket at 28 bar

The load resistance was limited in this study to 92.5 Ω, because the experiments showed that acoustic efficiency, fraction to Carnot efficiency and drive ratio are very close for resistances higher than 92.5 Ω, however, with less electricity generated. Installing an insulating gasket increased both acoustic efficiency and fraction to Carnot efficiency and reduced the inclination of data series. Figure 6.11 shows the acoustic efficiency versus the heating power and Figure 6.12 shows the fraction to Carnot efficiency versus the heating power, both at 28 bar mean pressure. At optimum load of 30.8Ω, the acoustic efficiency and fraction to Carnot efficiency are 13.65% and 27.68%, respectively. The maximum values of acoustic and fraction to Carnot efficiency are 16.8% and 37.8% at 92.5Ω load resistance, respectively.

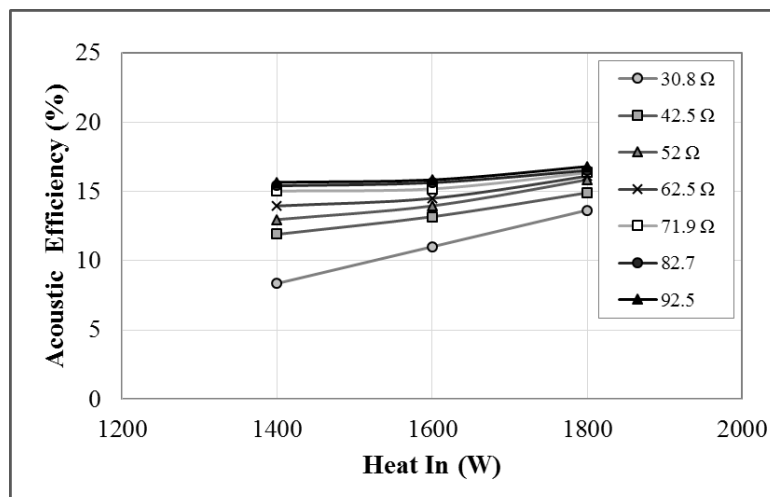


**Figure 6-11:** Acoustic efficiency versus heating power for an engine with an insulating gasket for various load resistances at 28 bar

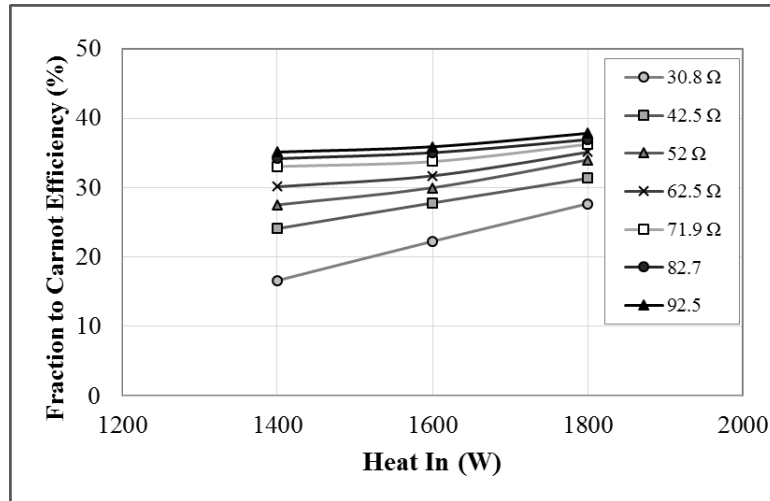


**Figure 6-12:** Fraction to Carnot efficiency versus heating power for the engine with an insulating gasket for various load resistances at 28 bar

Installing the insulating gasket changed the behaviour of the regenerator temperature difference across the regenerator, as shown in Figure 6.13. Comparing this figure to Figure 5.34, Figure 6.13 has higher values and interestingly the minimum was changed from 1400 W to 1600 W. A possible explanation may be the reduction of heat leak combined with the reduction of acoustic oscillations at the 1400 W leading to higher temperature difference.

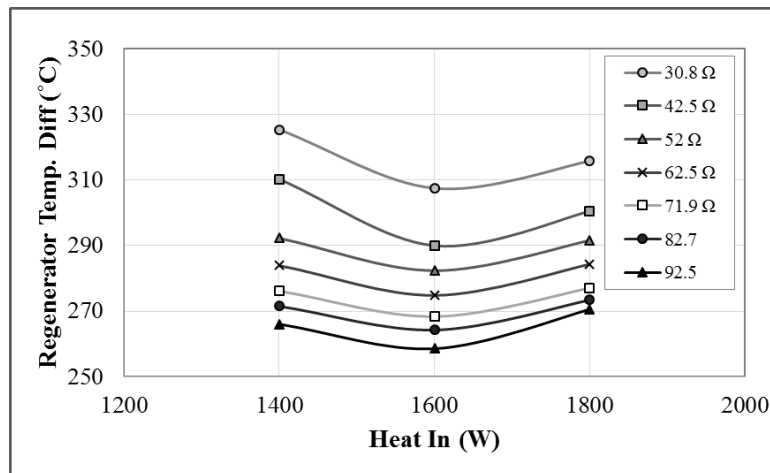


**Figure 6-13:** The effect of heating power on the temperature difference across the regenerator for the engine with an insulating gasket for various load resistances at 28 bar mean pressure

At different mean pressure, the performance after installing the insulating gasket has maintained its trend, however, at higher values. Figure 6.14 shows the performance of the engine, with an insulating gasket installed, versus the mean pressure for various load resistance. Comparing to the performance without gasket of figure 5.18, the performance increased with higher rate at higher mean pressure.

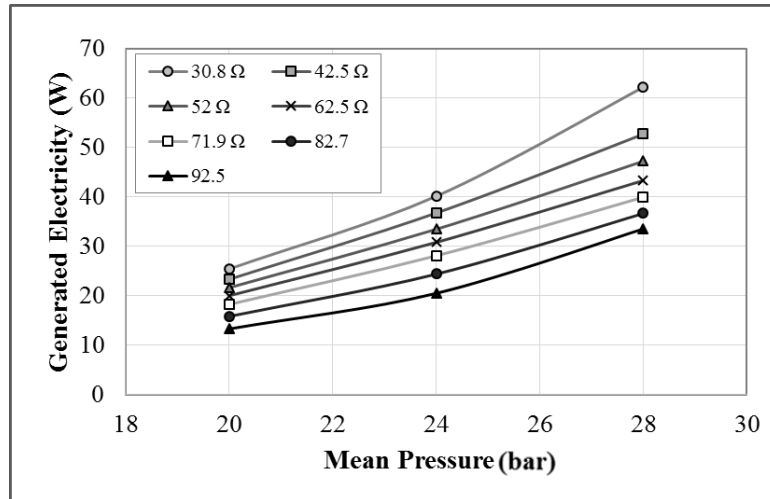


**Figure 6-14:** Performance of the engine with an insulating gasket at different mean pressure for various load resistance at 28 bar mean pressure

The trend of the thermal-to-electric, acoustic efficiency, fraction to Carnot efficiency and peak piston displacement was maintained however, at higher values. It is somewhat surprising that the trend of the drive ratio was changed after installing the insulating gasket. Figure 6.15 shows the experimental drive ratio at different mean pressures for various load resistances. Compared to the drive ratio before installing the insulation gasket shown in Figure 5.23, the current trend is that the drive ratio decreased with decreasing the mean pressure while it was increasing with decreasing the mean pressure previously. This change is understood to be related to the other changes in the regenerator temperature difference trend. The temperature difference after installing the gasket has shown an insignificant increase when reducing the mean pressure, as shown in Figure 6.16, compared with the trend without the gasket shown in Figure 5.25. The difference in trend between the regenerator temperature with and without the gasket is more significant when it is compared at various heating powers instead of various load resistances. Before installing the insulating gasket, the regenerator temperature difference of the lower heating power was lower than that of the higher heating power at the same mean pressure. In contrast, after installing the gasket that was true at 28 bar mean pressure only. Figure 6.17 shows the regenerator temperature difference versus different mean pressures at various heating powers. The 1400 W had the higher temperature difference followed by 1800 W, and the 1600 W was the lowest for both 20 and 24 mean pressure.

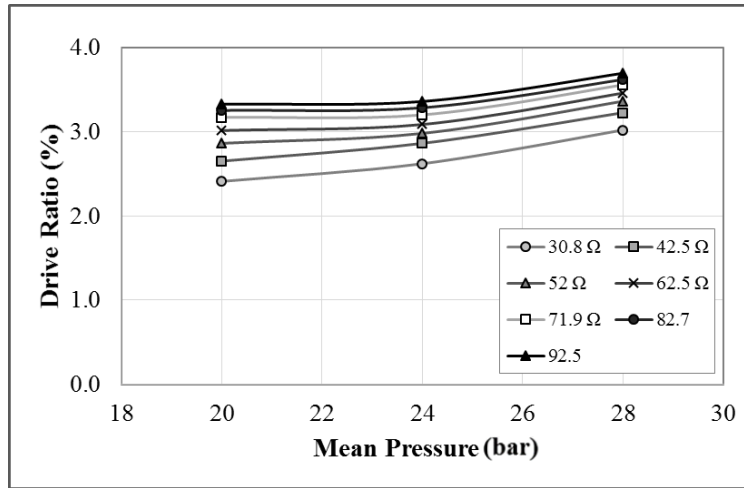


**Figure 6-15:** Drive ratio at different mean pressures for various load resistances with the insulating gasket at 1800 W heating power

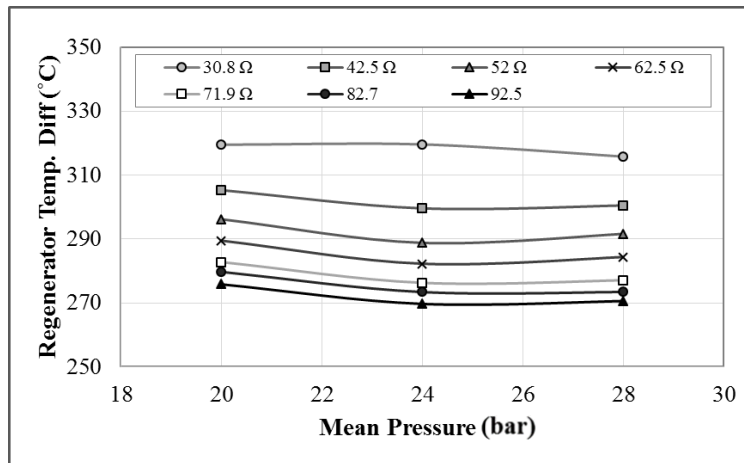


**Figure 6-16:** Regenerator temperature difference after installing the insulating gasket for various load resistances at 1800 W heating power

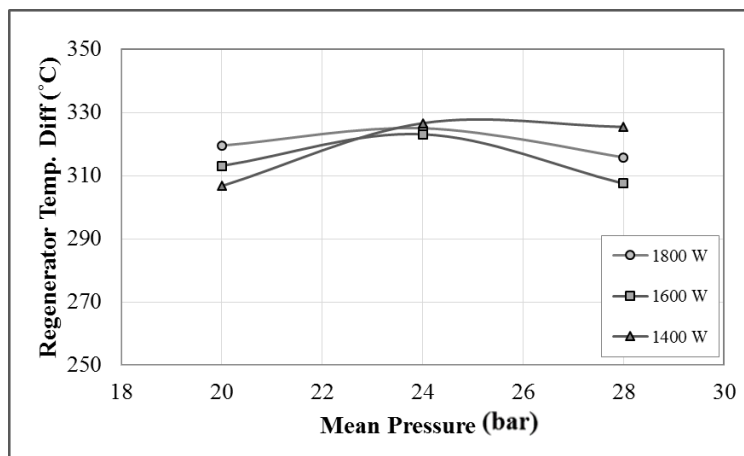


**Figure 6-17:** Regenerator temperature difference after installing the insulating gasket for various heating powers at 30.8 Ω load resistance

In the experiments, installing the insulating gasket enhanced the performance of the engine. The maximum electric power of 62.5 W with a thermal-to-electric efficiency

of 3.5% was achieved. The maximum thermal-to-acoustic efficiency and fraction to Carnot efficiency were 16.8% and 37.8%, respectively. A summary of the results is shown in Table 6.1 and the full detailed results are shown in Appendix 5 in Figures A5.1 to A5.43.

### 6.3 Increase of Heating Power

The increase of the thermal-to-acoustic efficiency with increasing the heating power encouraged investigation of the maximum efficiency by installing more heaters. The effect of heating power was continued at a mean pressure of 28 bar, targeting the maximum electricity generation and efficiencies. All the performance parameters recorded new maxima values. Starting with the electricity generation, the maximum generated electricity of 72.5 W was achieved at a heating power of 2200 W. Figure 6.18 shows the generated electricity at higher heating power for various load resistances. In spite of increasing the heating power increases the regenerator temperature difference across the regenerator, as shown in Figure A5.42, and the generated acoustic power, as shown in Figure 6.21, the generated electricity went down. This could be linked to the alternator efficiency which started to reduce at higher heating power as shown in Figure 6.19. The main reason is that the phase difference increased at higher heating power which reduced the alternator efficiency, as per Figure 3.3. For example, the phase difference for the case of load resistance 30.8  $\Omega$  increased from 15.5° to 17.8° by increasing the heating power from 1800 W to 2600 W.

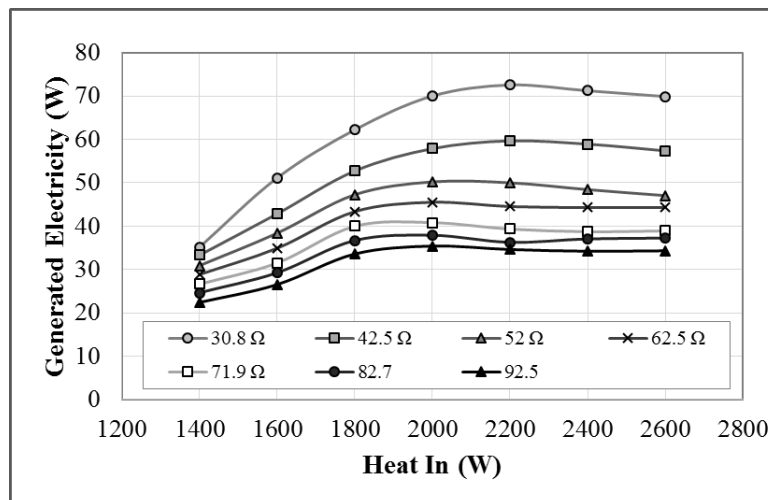


**Figure 6-18:** Performance of the engine with an insulating gasket at extra heating power for various load resistances at 28 bar mean pressure

**Table 6.1:** Summary of the main five selected parameters at various heating power and mean pressure, after installing the insulating gasket

Heating Power	Mean Pressure	Generated Electricity (W), at 30.8Ω	Generated Electricity (W), at 62.5Ω	Generated Electricity (W), at 92.5Ω	Total Efficiency (%), at 30.8Ω	Total Efficiency (%), at 62.5Ω	Total Efficiency (%), at 92.5Ω	Acoustic Efficiency (%), at 30.8Ω	Acoustic Efficiency (%), at 62.5Ω	Acoustic Efficiency (%), at 92.5Ω	Fraction to Carnot Efficiency (%), at 30.8Ω	Fraction to Carnot Efficiency (%), at 62.5Ω	Fraction to Carnot Efficiency (%), at 92.5Ω	Regenerator Temperature difference (°C), at 30.8Ω	Regenerator Temperature Difference (°C), at 62.5Ω	Regenerator Temperature Difference (°C), at 92.5Ω
1800	28	62.2	43.34	33.56	3.5	2.408	1.864	13.7	16.11	16.8	27.7	35.11	37.83	315.8	284.4	270.6
1800	24	40.2	30.85	20.53	2.2	1.714	1.14	6.8	9.238	9.913	13.9	20.38	22.58	325.0	282.3	269.7
1800	20	25.5	20.05	13.34	1.4	1.114	0.741	4.5	6.466	7.085	9.3	14.27	16.12	319.5	289.5	275.8
1600	28	51.1	34.9	26.51	3.2	2.2	1.657	11.0	14.5	15.84	22.3	31.7	35.89	307.5	274.9	258.6
1600	24	33.0	27.8	18.43	2.1	1.7	1.152	6.4	9.5	10.34	13.0	20.8	23.49	323.1	283.7	270
1600	20	22.9	18.9	13.58	1.4	1.181	0.849	4.7	6.7	7.282	9.8	14.9	16.76	313.1	279.1	265.3
1400	28	35.1	28.82	22.4	2.5	2.058	1.6	8.4	13.95	15.67	16.6	30.13	35.12	325.4	284	266.1
1400	24	27.3	24.78	16.33	2.0	1.77	1.166	6.0	9.699	10.77	12.1	21.25	24.4	326.6	285.2	270.4
1400	20	21.4	17.72	13.82	1.5	1.266	0.987	4.9	6.904	7.48	10.2	15.55	17.4	306.7	268.6	254.8

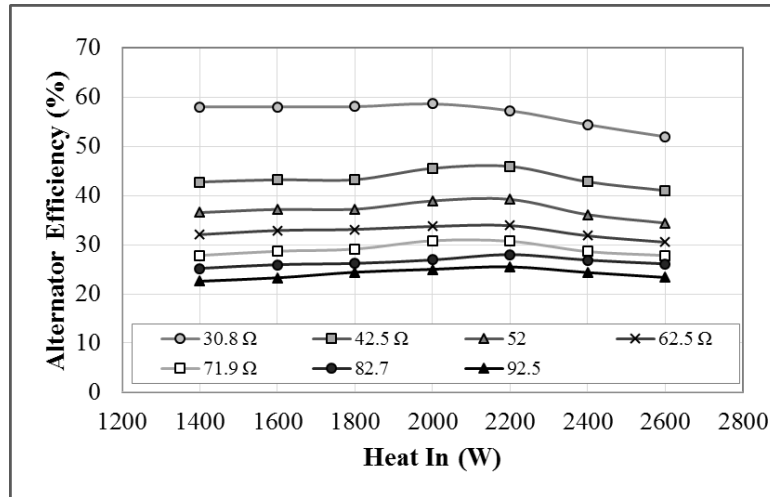


**Figure 6-19:** Alternator efficiency of the engine with an insulating gasket at extra heating power for various load resistances at 28 bar mean pressure

Figure 6.20 shows the thermal-to-electric efficiency with the extra heating power. At the highest generated electricity of 72.5 W, the thermal-to-electric efficiency is 3.3%. The new maximum thermal-to-electric efficiency is 3.5% when generating electricity of 70 W. Both these results are at a heating power of 2000 W and 30.8 Ω load resistance. As the thermal to acoustic efficiency is the ratio between the generated electricity to the heating power, the same explanation of the generated electricity could be drawn here from the last paragraph.

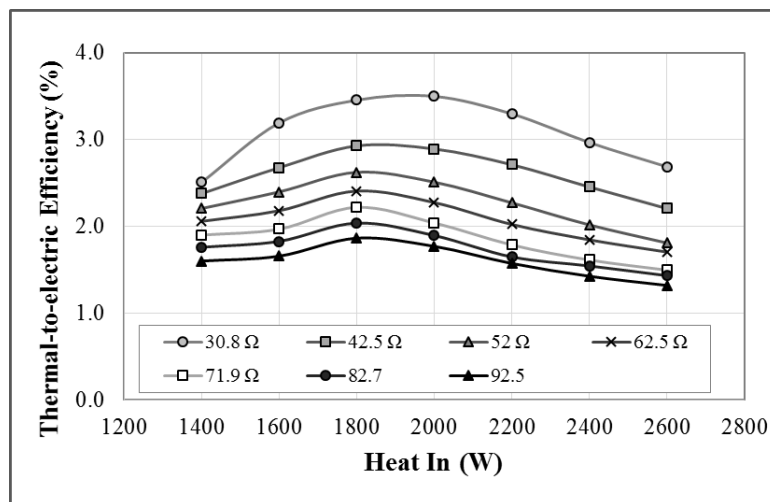


**Figure 6-20:** Thermal-to-electric efficiency at extra heating power for various load resistance for engine with insulating gasket at 28 bar mean pressure

The acoustic efficiency recorded a new maximum of 20% at 2600 W heating power and 92.5 Ω load resistance. This is a promising value for a further optimization and improvement of this engine. At the most productive heating power and load resistance, the acoustic efficiency is 16.87%. Figure 6.21 shows the experimental data

of the acoustic efficiency for various heating powers and load resistances. The increase of the acoustic efficiency values led to an escalation in the fraction to Carnot efficiency. Figure 6.22 is the experimental fraction to Carnot versus heating power. At the most productive heating power and load resistance, the fraction to Carnot efficiency is 34.1%. The maximum fraction to Carnot efficiency of 34.1% is a competitive value. The extra heating power showed that the drive ratio increases with increasing the heating power, as shown in Figure 6.23. The change in the drive ratio values was found to be insignificant when the heating power increased beyond 2200 W. At the most productive heating power and load resistance, the drive ratio is 3.31%. The maximum drive ratio was 3.95% at 2600 W heating power and 92.5  $\Omega$  load resistance. The effect of increasing the heating power on the regenerator temperature difference and piston displacement are shown in Appendix 5, Figures A5.42 and A5.43.

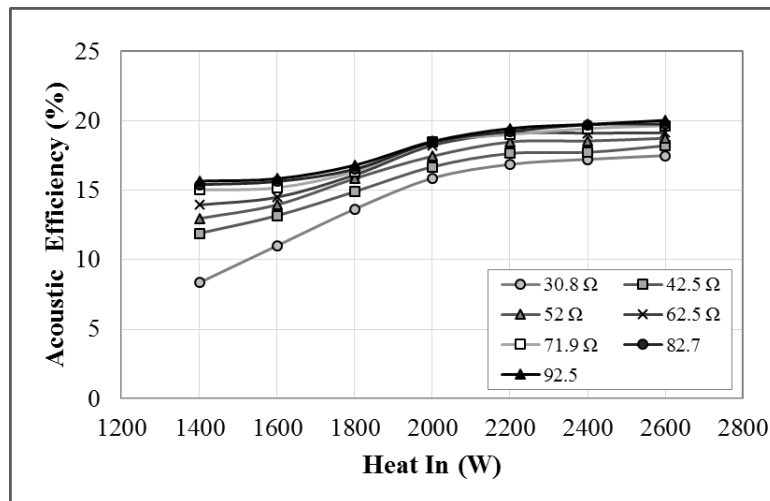


**Figure 6-21:** Acoustic efficiency versus extra heating power for the engine with an insulating gasket for various load resistances at 28 bar mean pressure

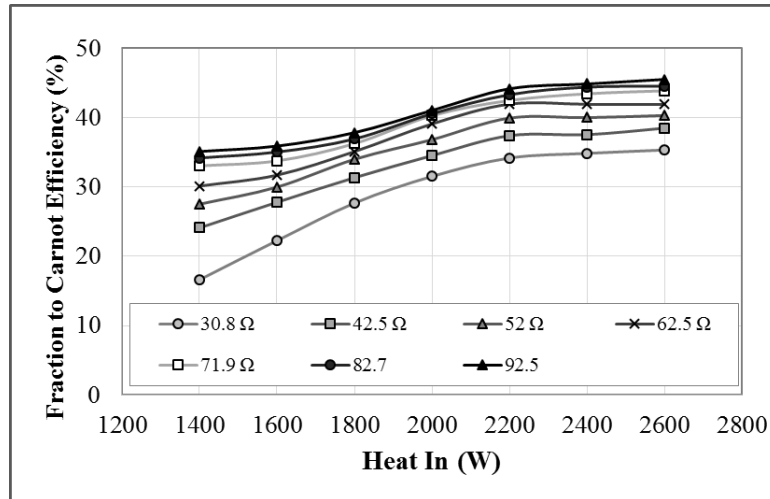


**Figure 6-22:** Fraction to Carnot efficiency versus extra heating power for the engine with an insulating gasket for various load resistances at 28 bar mean pressure

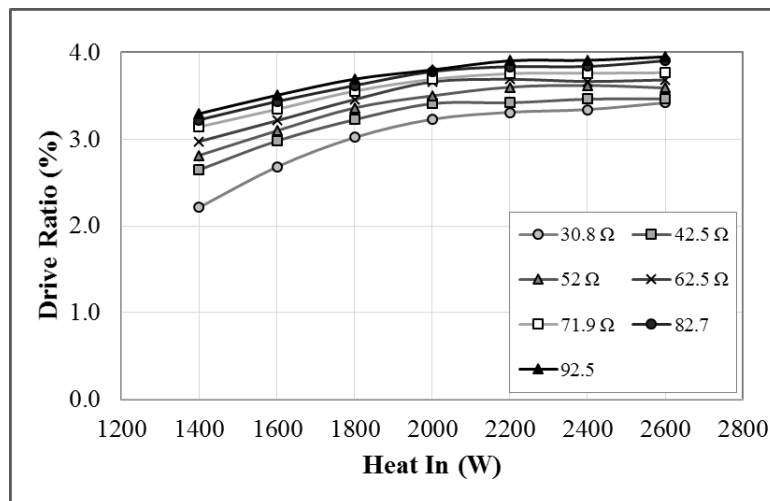


**Figure 6-23:** Drive ratio at extra heating power for various load resistances with the insulating gasket at 28 bar mean pressure

## 6.4 Self-Start-Up Improvement

Many scenarios were considered to improve the starting of the engine. The best one is to change the regenerator impedance. Yu and Jaworski (2010,c) explained the relation between the flow resistance and local acoustic impedance and their effect on the net acoustic power and acoustic power input. It was concluded that the flow resistance plays a key role in determining the regenerator impedance as it determines the volumetric flow rate at a specific pressure amplitude. The acoustic impedance determines the net acoustic power (acoustic power at the end of the regenerator minus acoustic power at the beginning of the regenerator), because it determines the amount of required power to be fed into the regenerator. The flow resistance could be reduced

by decreasing the thickness of the regenerator or increasing the cross-sectional area. At a given pressure amplitude, the higher flow resistance increases the acoustic impedance by decreasing the volumetric flow rate.

In the current research, the regenerator holder was welded to the hot heat exchanger and a heavy flange, therefore its thickness is fixed. The only way to change the regenerator thickness is to replace the coarse mesh separator by a regenerator mesh screen, and vice versa. The coarse mesh screens were accumulated on the cold side of the regenerator, for ease of replacement.

The effect of the regenerator thickness on the self-start and performance was investigated experimentally. The regenerator thickness was increased once and reduced twice by a 1.2 mm step, which is the thickness of a single coarse mesh. The load resistance was changed in three steps 30.8, 62.5 and 92.5  $\Omega$  and the heating power was changed four times to 1800, 2000, 2200 and 2600 W. These steps cover the maximum electrical and acoustical performance of the engine.

The most striking observation is that the engine self-starts at a regenerator thickness of 71.8 mm and 70.6 mm. The engine self-started at a regenerator temperature difference of 280°C. Add to that benefit that reducing the regenerator thickness to 71.8 mm enhanced the performance a very small fraction. The performance behaviour was repeated in a targeted way to check the peak performance values.

The effect of the regenerator thickness was studied at 1800 W heating power and 28 bar. The effect of the regenerator thickness on the generated electricity is shown in Figure 6.24. The reduction of the regenerator thickness from 73 mm to 71.8 mm increased the generated electricity from 62.2 W to 63.4 W. The effect of the load resistance remained the same. Thermally, the reduction of the regenerator thickness reduced the regenerator temperature difference at the same heating power, as shown in Figure 6.25. Increasing the regenerator thickness to 74.2 mm damped the oscillations which lead to an increase in the temperature difference and a decrease in the electricity generated. While decreasing to 70.6 mm reduced the acoustic efficiency, as shown in the next pages, there was a reduction in the electricity generated as well.

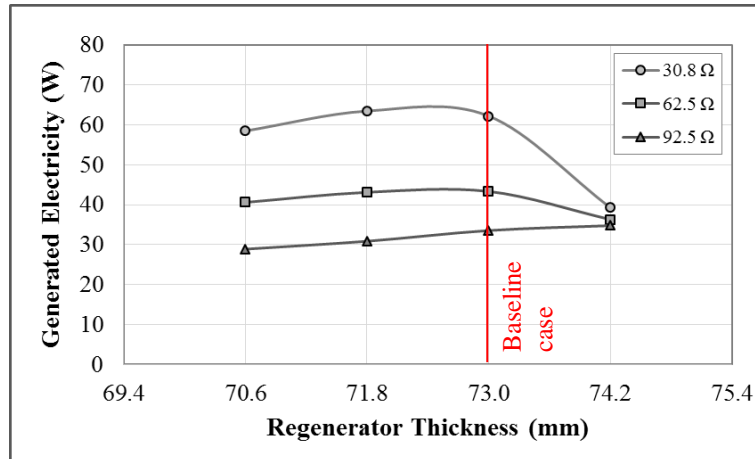


**Figure 6-24:** Performance of the engine with an insulating gasket versus regenerator thickness for various load resistances at 1800 W heating power

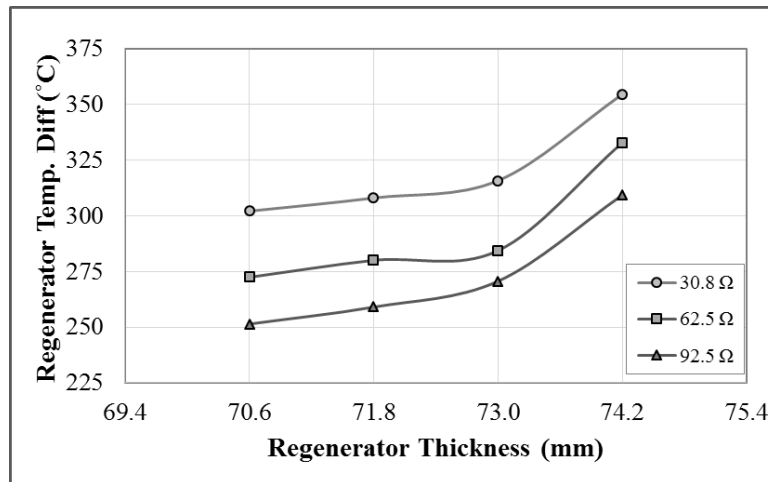


**Figure 6-25:** The effect of regenerator thickness on the temperature difference across the regenerator for the engine with an insulating gasket for various load resistances at 28 bar mean pressure and 1800 W heating power

To investigate the maximum generated electricity and thermal-to-electric efficiency, the experiments were repeated at heating powers of 1800, 2000 and 2200 W. The performance of the 71.8 mm regenerator thickness overtook that previously recorded at 73 mm. Figures 6.26 and 6.27 show the effect on the generated electricity and thermal-to-electric efficiency, respectively. The maximum generated electric power was 73.3 W, 3.33% thermal-to-electric efficiency at heating power of 2200 W, and a maximum efficiency of 3.6% was at 71.9 W electric power at a heating power of 2000 W.

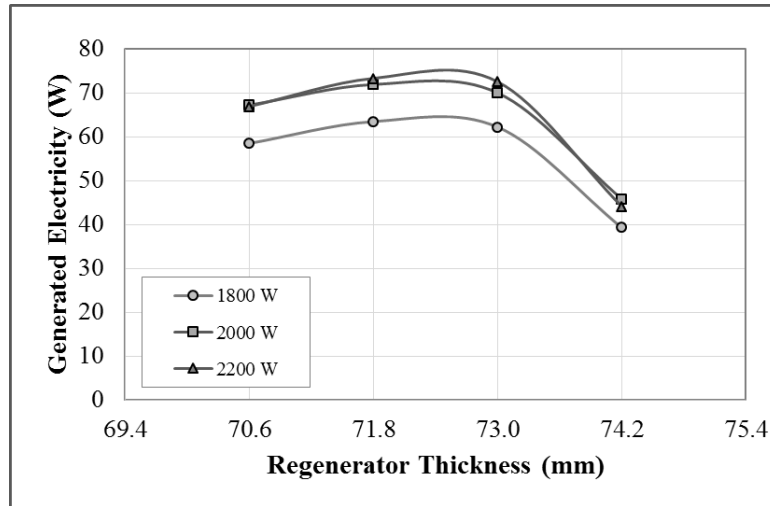


**Figure 6-26:** Performance of the engine with an insulating gasket versus regenerator thickness for various heating powers at  $30.8 \Omega$  load resistance and 28 bar mean pressure

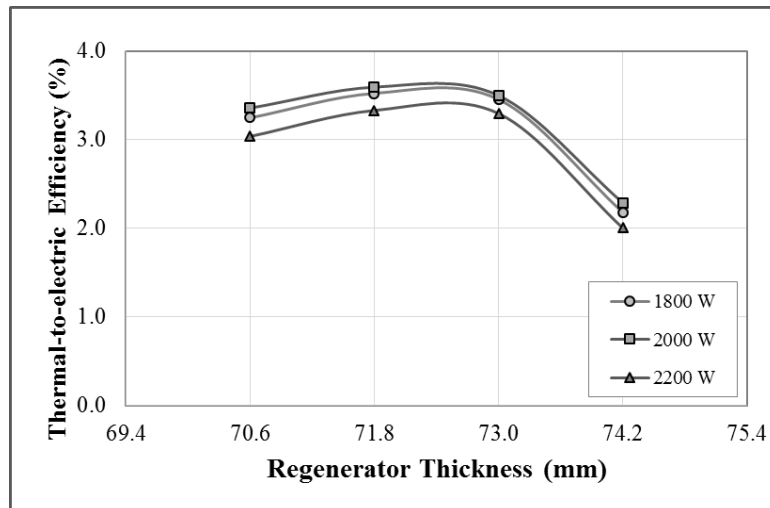


**Figure 6-27:** Thermal-to-electric efficiency at different heating powers for the engine with an insulating gasket at  $30.8 \Omega$  load resistance and 28 bar mean pressure

The effect of regenerator thickness on the acoustic efficiency and the fraction to Carnot efficiency is presented in Figures 6.28 and 6.29. Figure 6.30 shows the drive ratio at various regenerator thicknesses and heating powers. At the most productive heating power of 2200 W and load resistance  $30.8 \Omega$  at 71.8 mm regenerator thickness, the acoustic efficiency and fraction to Carnot efficiency are 17.2% and 39.17%, respectively. At these conditions, the drive ratio is 3.42%. At the most efficient heating power of 2000 W and load resistance  $30.8 \Omega$  at 71.8 mm regenerator thickness, the acoustic efficiency and fraction to Carnot efficiency are 16.0% and 35.32%, respectively. At these conditions, the drive ratio is 3.36%.

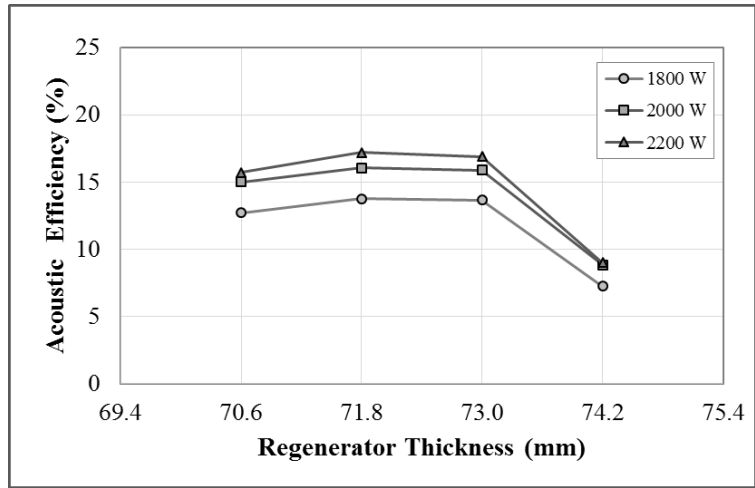


**Figure 6-28:** Acoustic efficiency versus regenerator thickness for the engine with an insulating gasket for various heating powers at 30.8  $\Omega$  load resistance and 28 bar mean pressure

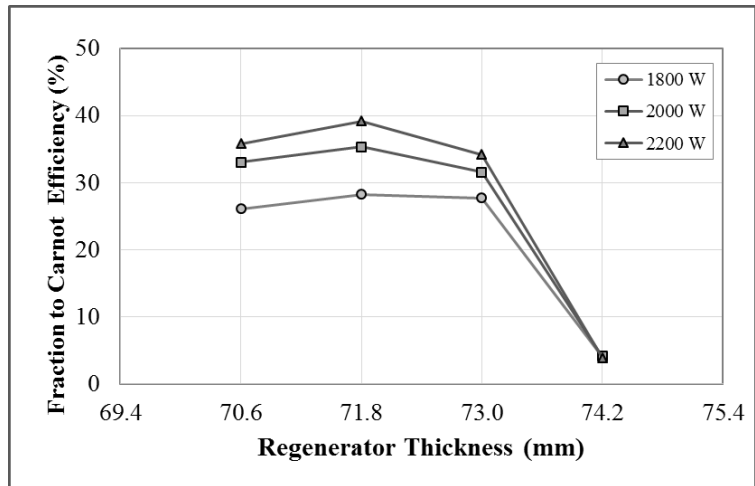


**Figure 6-29:** Fraction to Carnot efficiency versus regenerator thickness for the engine with an insulating gasket for various load resistance at 30.8  $\Omega$  load resistance and 28 bar mean pressure

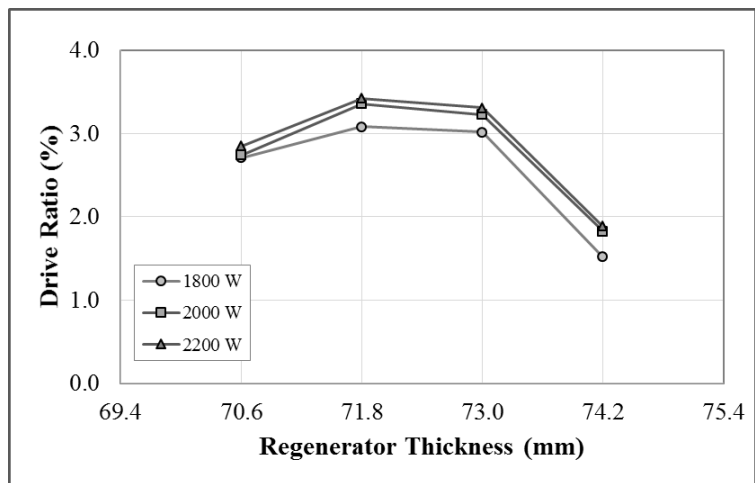


**Figure 6-30:** Drive ratio at different regenerator thickness for various heating power with the insulating gasket at 30.8  $\Omega$  load resistance and 28 bar mean pressure

Comparing the research results to the previous results from the literature clearly shows the current engine overtook all of the looped tube engines by the means of thermal-to-electric efficiency. Only Kang *et al.* (2015) using a looped tube engine was able to generate higher electricity of 204 W and a maximum efficiency of 3.43% at 183 W electric power, using two acoustic loud speakers. Comparing the current engine to the torus engine with standing wave resonator, generally, it generated less electricity and ran at a lower thermal-to-electric efficiency. However, the fraction to Carnot efficiency is competitive. The thermal-to-electrical efficiency of the Backhaus *et al.* (2004) engine was 18% and Tijani *et al.* (2008) was 22.5%, these two engines had been pressurised to a higher mean pressure and run at a higher temperature difference. In contrast, the relatively low temperature difference led to a decrease in the Carnot efficiency, and hence, increased the fraction to Carnot efficiency. In the current research, the fraction to Carnot efficiency is 39.17% at acoustic efficiency of 17.2%. This is less than the highest recorded relative to Carnot of 49% at acoustic efficiency of 32% achieved by Tijani and Spoelstra (2011). Bearing in mind that the Tijani and Spoelstra (2011) engine did not include any electricity generating mechanism, and used acoustic load to dissipate the acoustic power.

## **6.5 Efforts Towards Suppressing Streaming**

The non-linear temperature regenerator distribution along the thermal section shown in Figure 5.14 in Section 5.2.1, concluded that there is Gedeon streaming occurring along the engine loop. It is important to suppress the streaming as it causes heat leaks which significantly reduce the efficiency of the engine. As discussed in Section 2.6.1, the streaming could be suppressed by placing an elastic membrane in an appropriate location in the loop. The location should be close to the minimum volumetric flow rate, to decrease the power loss in the membrane. The ideal membrane will be “transparent” to the oscillatory flow. However, it blocks the streaming. In the literature, the best location is close to the main ambient heat exchanger. Unfortunately, this location on the experimental rig was used to feed through the thermocouples, and hence, the membrane could not be placed there. Potential locations are between two flanges at three locations, as shown in Figure 6.31a. Figure 6.31b shows the locations of the membrane with reference to the theoretical volumetric flow rate.

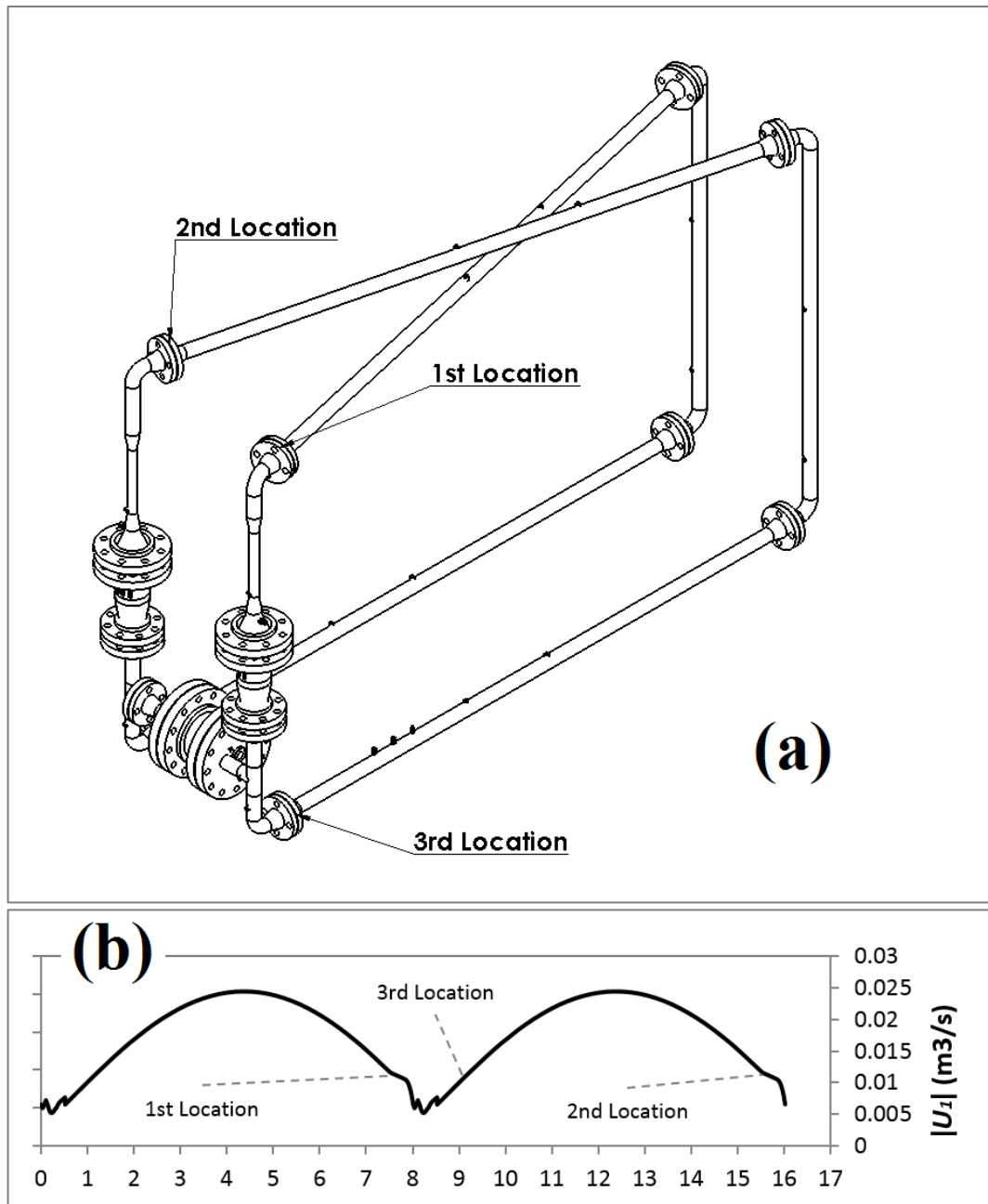


**Figure 6-31:** (a) Locations of the membrane along the engine loop (b) locations of the membrane on the volumetric flow rate graph

The membrane material was selected based on the elastic properties and thickness. A sheet of 100% genuine latex of 0.25 mm thickness, was used. Three profiles of the membrane were tested; flat, concave and loose. Figure 6.32 shows photographs of the three profiles and an example of an assembled membrane. All these three profiles were used in single and double locations. They were used singularly at the 1<sup>st</sup> and 3<sup>rd</sup> locations, shown in Figure 6.31a, and double at the 1<sup>st</sup> and 2<sup>nd</sup> locations. The concave profile was made by continuous stretching and heat treatment.

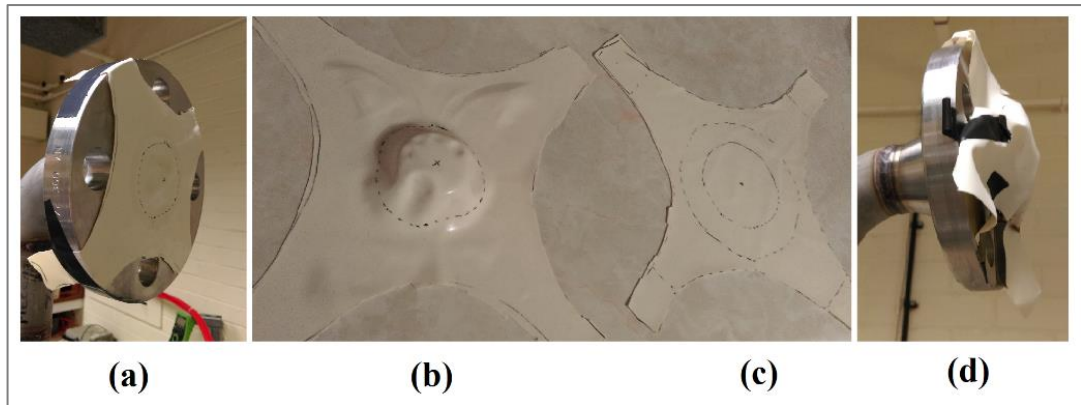


**Figure 6-32:** (a) A membrane assembled on a flange, (b) concave membrane, (c) flat membrane, (d) loose membrane.

The experimental results were encouraging as a means of suppressing the streaming, however disappointing by means of performance. Figure 6.33 compares the temperature distributions along the regenerator obtained for cases “with membrane” and “without membrane” at 1400 W heating power and 28 bar mean pressure. Clearly, the temperature profiles became more linear after installing the membrane. Among all the tested profiles and locations, the highest performance was achieved by using one concave membrane at the 1<sup>st</sup> location when generating 4.2 W of electricity. Table 6.2 shows selected performance values of the experimental tests. The results may be explained by the fact that the membrane acts as a flow resistance damping the oscillations. Figure 6.34 shows the results of the pressure amplitude “with” and “without” a concave membrane at the 1<sup>st</sup> location.

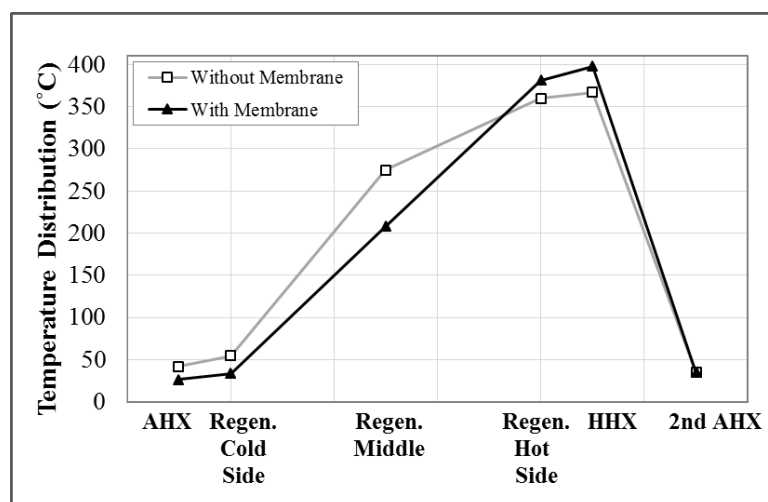


**Figure 6-33:** The effect of the presence of a concave membrane on the temperature profiles in the regenerator at 1400 W heating power and 28 bar mean pressure

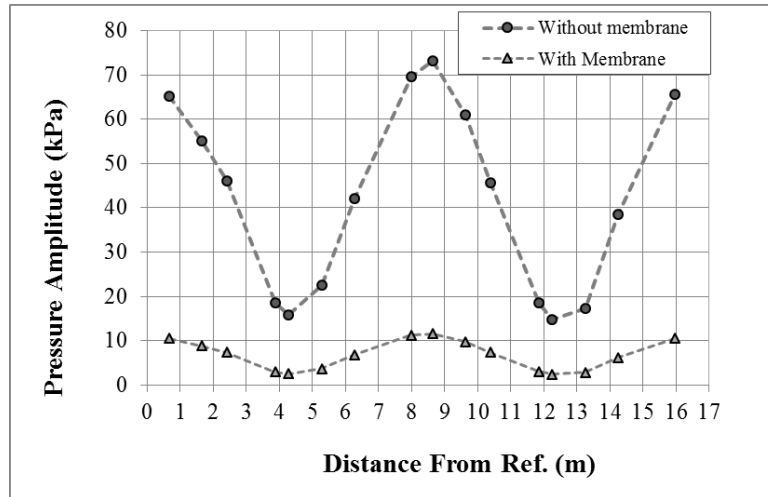


**Figure 6-34:** pressure amplitude distribution along the engine both with and without a concave membrane at 1400 W heating power and 28 bar mean pressure

Obviously, there is a lot still to do towards suppressing the streaming and maintaining a good performance of the engine. Unfortunately, the limited time of this research project did not allow more experimental investigation.

**Table 6.2** Performance of the engine at various membrane profile and locations

	Generated Electricity (W)	Piston displacement (mm)
One flat membrane at 1 <sup>st</sup> location	1.1	0.69
One flat membrane at 3 <sup>rd</sup> location	0.9	0.62
Double flat membrane at 1 <sup>st</sup> and 2 <sup>nd</sup> locations	0.6	0.42
One concave membrane at 1 <sup>st</sup> location	4.2	1.21
One concave membrane at 3 <sup>rd</sup> location	3.7	1.03
Double concave membrane at 1 <sup>st</sup> and 2 <sup>nd</sup> locations	3.4	0.95
One loose membrane at 1 <sup>st</sup> location	0.9	0.61
One loose membrane at 3 <sup>rd</sup> location	0.8	0.56
Double loose membrane at 1 <sup>st</sup> and 2 <sup>nd</sup> locations	0.5	0.51

## 6.6 Concluding Remarks

- The use of an insulating gasket between the regenerator holder and ambient heat exchanger reduced the heat leaks and improved the engine performance. It has increased the generated electricity by 22% to be 62.2 W at 30.8 Ω load resistance, 1800 W heating power and 28 bar mean pressure.
- The insulating gasket changed the trend of the thermal-to-electric efficiency versus heating power, ranging from 700 to 900 W, from curved with a

maximum at 800 W to increase with increasing the heating power. More heaters were installed to investigate the maximum thermal-to-electric efficiency. The highest generated electricity was 72.5 W at 3.3 % thermal-to-electric efficiency, and the maximum thermal-to-electric efficiency is 3.5% generating electricity at 70 W, both at heating powers of 2000 W and 30.8  $\Omega$  load resistance.

- The engine became self-starting when the regenerator thickness was reduced to 71.8 mm. This also improved the performance of the engine a small fraction. The maximum generated electric power was 73.3 W, 3.33% thermal-to-electric efficiency at heating power of 2200 W and a maximum efficiency of 3.6% was at 71.9 W electric power at heating power of 2000 W. At the most productive condition, the acoustic efficiency and fraction to Carnot efficiency are 17.2% and 39.17%, respectively. At the most efficient condition, the acoustic efficiency and fraction to Carnot efficiency are 16.0% and 35.32%, respectively.
- The use of an elastic membrane suppressed the Gedeon streaming along the engine loop. However, it has damped the oscillation and decreased the engine performance.

## Chapter 7

### Development of Two-stage to Four-stage Engine

In this chapter configuration, modelling and design of a four stage engine is proposed. This four-stage engine retains the two-stage thermodynamic section pieces.

#### 7.1 Four-stage Engine

Basically, the development of the two-stage engine to a four-stage engine involves changing the acoustic section only. All the parts of the thermodynamic section will be kept the same, so that the parts of the current two-stage engine could be used in the next research.

The configuration consists of four identical stages each having a power extraction points, and the linear alternators connecting these four points is shown in Figure 7.1. Clearly, there is a power extraction at each stage followed by a feedback loop which leads to the next stage. Theoretically, the flow pressure amplitude and volumetric flow rate of each stage is identical in all the stages.

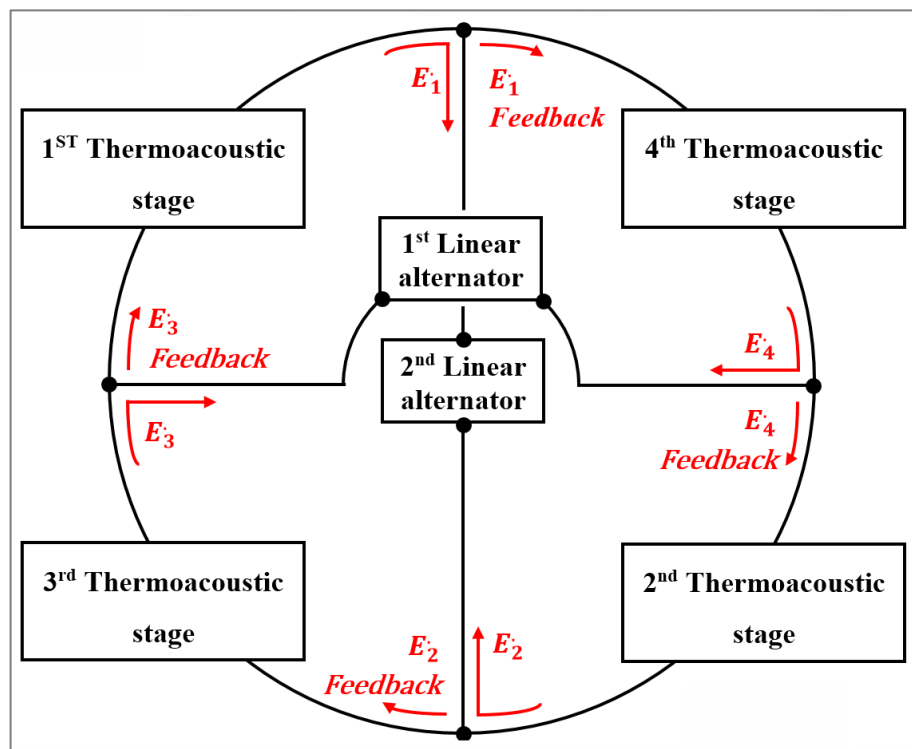


**Figure 7-1:** Conceptual drawing of the proposed four-stage engine.

As explained in Section 3.2, the DeltaEC shooting method cannot run multi-identical stages. The modelling has been done as a quarter of the engine which is one stage and the other three stages were represented as a self-excited hypothetical flow.

There are two self-excited hypothetical flows in this engine, each has a specific flow characterisation based on the understanding of the identical stages and push-pull connection. The first self-excited hypothetical flow is the flow entering the first stage which represents the flow at the end of the fourth stage. The characterisation of this flow was suggested based on the wave behaviour at four identical stages. To apply this behaviour the following boundary conditions were made. The pressure amplitude, volumetric flow rate and total power was set to be equal at the beginning and the end of the simulated stages, as they are expected to repeat themselves in four identical stages. In contrast, the pressure and velocity phase was set to be shifted  $90^\circ$  at the end on the stage with reference to the beginning. The six boundary conditions shown in equations 7.1-7.6, were set as targets at  $x=\lambda/4$  shown in the block diagram Figure 7.2, relating  $x=\lambda/4$  to  $x=0$ .

$$\frac{T_{x=\lambda/4}}{T_{x=0}} = 1 \quad 7.1$$

$$\frac{P_{x=\lambda/4}}{P_{x=0}} = 1 \quad 7.2$$

$$\frac{Ph(P)_{x=\lambda/4+90^\circ}}{Ph(P)_{x=0}} = 1 \quad 7.3$$

$$\frac{U_{x=\lambda/2}}{U_{x=0}} = 1 \quad 7.4$$

$$\frac{Ph(U)_{x=\lambda/4+90^\circ}}{Ph(U)_{x=0}} = 1 \quad 7.5$$

$$\frac{H_{x=\lambda/4}}{H_{x=0}} = 1 \quad 7.6$$

Where  $T$  is temperature,  $P$  is pressure amplitude,  $Ph(P)$  is pressure phase,  $U$  is volumetric flow,  $Ph(U)$  volumetric flow phase and  $H$  is the total power.

The second self-excited hypothetical flow is applied to the other side of the linear alternator. Based on the push-pull run characterization, the pressure amplitude,

volumetric flow and velocity phase was set to be equal on both sides of the alternator piston. Only the pressure phase was set to be out of phase (phase difference of  $180^\circ$ ), and this will push the other three to act in a push-pull manner. The three boundary conditions shown in equations 7.7-7.9, were set as targets at locations 1 and 2 shown in figure 7.2.

$$\frac{P_2}{P_1} = 1 \quad 7.7$$

$$\frac{Ph(P)_2 + 180^\circ}{Ph(P)_1} = 1 \quad 7.8$$

$$\frac{H_2}{H_1} = 1 \quad 7.9$$

A block diagram of the segments in the DeltaEC simulation showing the main layout and parts is shown in Figure 7.2. It is very similar to the two-stage block diagram as it was targeted to use the same thermodynamic section parts, while replacing the feedback loop. The stage in the four-stage models ends with  $X=\lambda/4$ .

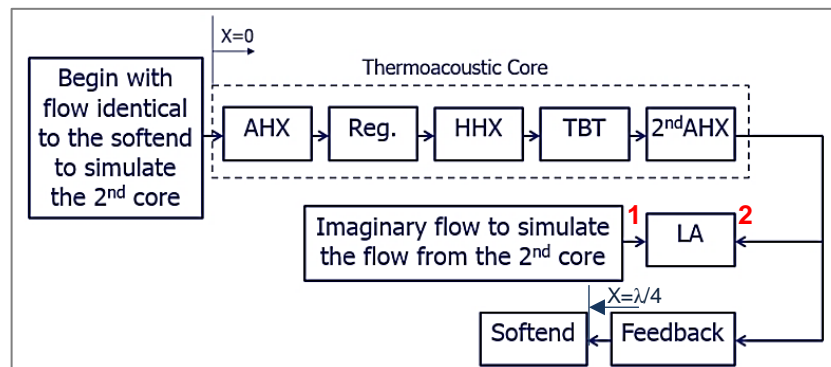


**Figure 7-2:** Block diagram of the segments in the DeltaEC four-stage simulation: ambient heat exchanger (AHX), regenerator (Reg), hot heat exchanger (HHX), thermal buffer tube (TBT), secondary cold heat exchanger (2<sup>nd</sup>AHX), feedback pipe (Feedback), linear alternator (LA).

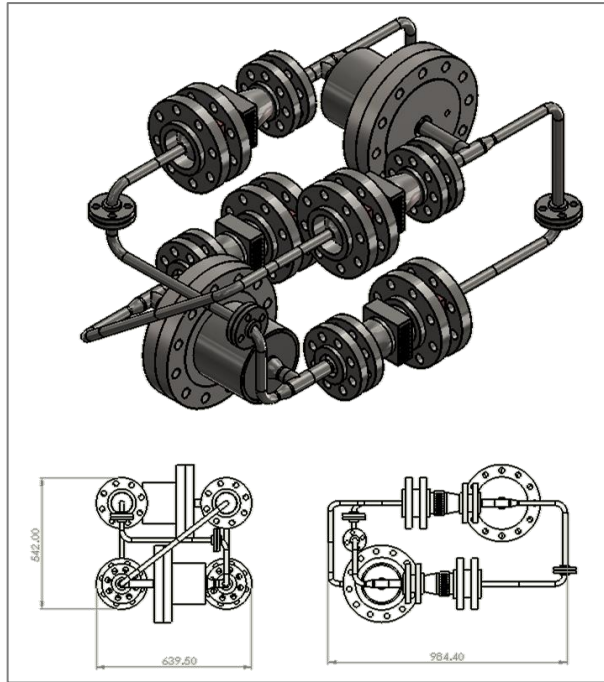
As the required acoustic impedance and thermodynamic section dimension optimization have already been done in Section 3.2, the feedback loop and the alternator holder will be optimised in this section. The feedback loop tube diameter was reduced from 1.5 inch to 10 mm to achieve the acoustic impedance at a lower length. As explained before in Section 3.2, the main role of the feedback loop is to transport acoustic power from the end of a stage to the beginning of another at a specific phasing. The phasing of the quarter wavelength stages needs to be shifted at  $90^\circ$  only, and hence it needs a shorter feedback loop. A feedback loop of 840 mm was

found to be sufficient. The engine configuration is similar to the engines of de Blok (2010, 2012) and Li *et al.* (2016), however, with two linear alternators only.

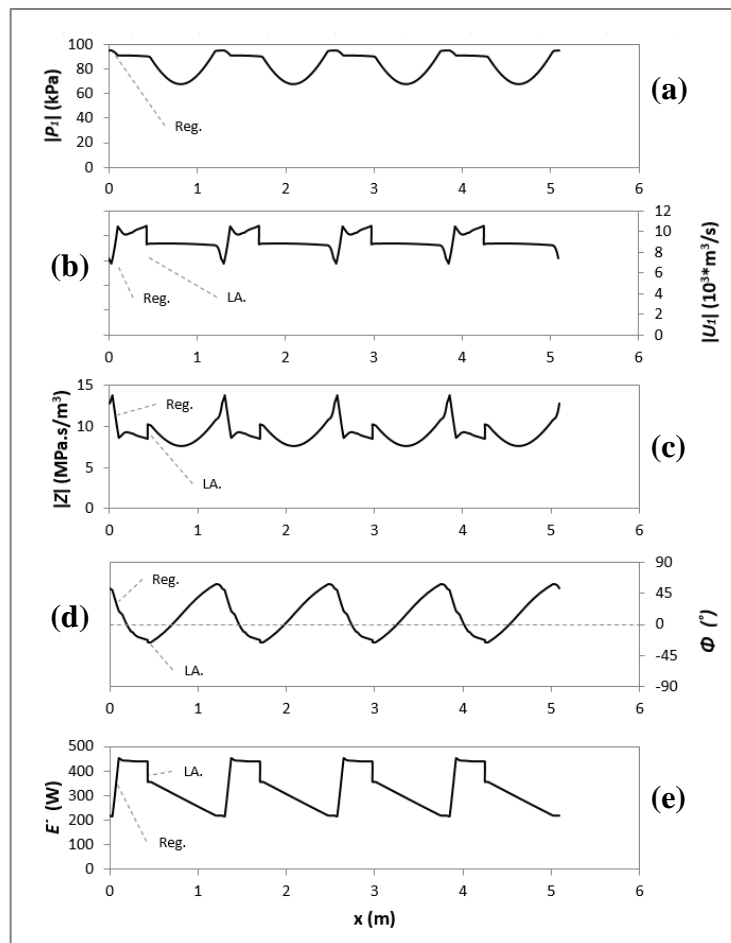
The simulation optimization introduced the dimensions of the physical parts. Figure 7.3 shows a proposed layout of the four-stage engine. The simulation results showed that the engine ran at 54.79 Hz and the total engine length was 5.09 m. Each alternator generated 134.5 W of electricity, and hence, the engine generated 269 W at the thermal to electric efficiency of 14%. Figure 7.2 shows the performance curves of this simulation. Clearly, the four-stage model is inefficient comparing to the two-stage model. This is because the small diameter feedback tube dissipate a lot of acoustic power.

Figure 7.4a shows the calculated pressure amplitude distribution along the engine loop. Clearly, the regenerator is correctly positioned at the pressure amplitude maximum. Figure 7.4b shows the distribution of volumetric velocity along the thermoacoustic engine. The engine was designed to have the lowest volumetric flow rate at the regenerator to reduce the viscous dissipation. Clearly, the regenerator dumps acoustic power by means of increasing the volumetric flow rate and the alternator extracts power by means of reducing the volumetric flow rate. Figure 7.4c is the acoustic impedance profile along the engine. It can be seen that the acoustic impedance is nearly maximum at the regenerators which is one of the design strategies. The acoustic impedance dropped within the regenerator limit, caused by the pressure drop and velocity amplification.

Figure 7.4d shows the phase difference between the velocity and pressure oscillation along the engine. This graph illustrates that the engine needs to be developed by adding a phase shifting application to shift the phase difference at the regenerator closer to the travelling-wave phasing. It is clear that the engine needs to be modified to have a mechanism of phase adjustment in the feedback loop. Figure 7.4e shows the acoustic power distribution along the engine. It is shown that the regenerator amplifies the acoustic power by 238.1 W at the hot end and the alternator extracts 67.3 W from each side.



**Figure 7-3:** A proposed layout of the four-stage engine.



**Figure 7-4:** Simulation results (a) pressure amplitude, (b) volumetric velocity, (c) acoustic impedance, (d) phase difference angle and (e) acoustic power flow along the engine.

## Chapter 8

### 8.1 Conclusions

The overarching theme of the current study was to investigate the ability of a thermoacoustic travelling-wave looped tube engine to generate electricity from internal combustion engine waste heat. Due to laboratory limitations, the exhaust gas as a heat source was simulated by electrical heaters, at a similar temperature and heat flux. Add to that, the implementation of a push-pull linear alternator as a solution to the low acoustic impedance of the looped tube engines was investigated. The activities carried out during the course of this PhD programme can be generally regarded as a “demonstration project” outlining the principles of how thermoacoustic technologies could be applied to meet the overall aim described in Section 1.3.

From the particular point of view of investigation, a rig was built. It was built based on modelling, which was done using the DeltaEC programme, and designed to withstand the elevated pressure and temperature. A number of challenges and obstacles were outlined, solutions and improvements are listed in Section 8.2. The detailed objectives of the study, (1) – (6), have been outlined in Section 1.3.

Objective (1) was achieved through the study outlined in Chapter 3:

1. The modelling procedure was started by a simulation study investigating the required acoustic field at the alternator to generate electricity efficiently. A detailed modelling of a thermoacoustic two-stage engine driving a push-pull linear alternator was carried out. The modelling helped in understanding the wave along the engine by means of the pressure and volumetric flow rate which guided and helped to decide the layout by positioning the thermoacoustic cores and linear alternator branches correctly. The acoustic power generation and dissipation confirmed the suitability of the linear alternator to run in a push-pull mode by two identical stages. The numerical results showed that the engine ran at a frequency of 55.1 Hz, and generated 133.2 W of electricity at a thermal-to-electrical efficiency of 23.06%.

Objective (2) was achieved through the study outlined in Chapter 4:

2. The model served as a starting point to construct the rig. The design, materials and parts selection criteria were based on the availability and durability for the working pressure, pressure sealing of the working gas and moderate cost. The tubes and fittings used in this rig are schedule-40 stainless steel welded pipes. A heat transfer calculation was made to ensure that the heat exchangers are able to transfer the required amount of heat to or from the helium. For the purpose of evaluating the performance of the engine at the testing procedure, measurement techniques were followed to evaluate temperatures and oscillating pressure amplitudes at selected locations along the system and linear alternator piston displacement and generated electrical power. The exhaust gases as a heating source were simulated by electrical heaters.

Objectives (3) and (4) were achieved through the study outlined in Chapter 5:

3. Experiments were executed in order to evaluate the engine performance. Apart from the high heat leak, the biggest obstacle faced was that the engine failed to self-start. A control box was designed and connected to excite the engine to start. In practice, the engine ran at a frequency of 54.7 Hz. The tests showed that the maximum electricity of 48.6 W was generated at a thermal-to-electric efficiency of 2.7% and the maximum thermal-to-electric efficiency of 2.8% with electric power of 44.8 W was achieved.
4. The optimum load resistance is 30.8  $\Omega$  among the studied range from 26.1  $\Omega$  to 92.5  $\Omega$ . The engine was hard to run at 26.1  $\Omega$  as it damped the oscillation and turned the engine off when reducing the load resistance from a higher value. Increasing the load to a value higher than 30.8  $\Omega$  led to a reduction in the electricity generated and encouraged more intense oscillation. The mean pressure has a significant effect on the electricity generation. Reducing the mean pressure from 28 to 16 bar significantly reduced the generated electricity and acoustic efficiency. Surprisingly, decreasing the mean pressure from 16 to 14 bar increased the generated electricity and acoustic efficiency. Reducing the mean pressure reduced the helium density and hence the speed of sound will be lower which leads to a reduction in the oscillation frequency. The engine oscillated at 54.7 Hz for a mean pressure range of 28-22 bar and at a frequency of 52.4 Hz for mean pressure between 20 and 14 bar. The effect of

mean pressure in the frequency is due to the effect of the mean pressure on the helium density. Reducing the mean pressure decreases the density which leads to a decrease in the speed of sound. The reduction of speed of sound decreases the frequency as the length of the rig is constant. The effect of the heating power was studied at 700, 800 and 900 W. Increasing the heating power led to an increase in the acoustic power amplification as well as electricity generation.

Objective (5) was achieved through the study outlined in Chapter 6:

5. The system improvements were targeted at delivering measurable performance improvements to the engine. The optimization procedure was designed to minimize the obstacles of self-starting, heat leak and streaming. The heat leak was reduced by installing an insulating gasket between the regenerator holder and the ambient heat exchanger. It has increased the generated electricity by 22% to be 62.2 W at 30.8  $\Omega$  load resistance, 1800 W heating power and 28 bar mean pressure. The insulating gasket changed the trend of the thermal-to-electric efficiency versus heating power which ranged from 700 to 900 W, from a curve with a maximum at 800 W to increase with increasing the heating power. More heaters were installed to investigate the maximum thermal-to-electric efficiency. The highest generated electricity was 72.5 W at 3.3% thermal-to-electric efficiency, and the maximum thermal-to-electric efficiency was 3.5% generating electricity of 70 W. The engine became self-starting when reducing the regenerator thickness to 71.8 mm. This also improved the performance of the engine a small fraction. The maximum generated electric power was 73.3 W, 3.33% thermal-to-electric efficiency at a heating power of 2200 W, and a maximum efficiency of 3.6% was at 71.9 W electric power at heating power of 2000 W. At the most productive condition, the acoustic efficiency and fraction to Carnot efficiency are 17.2% and 39.17%, respectively, and the drive ratio is 3.42%. At the most efficient condition, the acoustic efficiency and fraction to Carnot efficiency are 16.0% and 35.32%, respectively, and the drive ratio is 3.36%. The use of an elastic membrane has suppressed the Gedeon streaming along the engine loop. However, it damped the oscillation and decreased the engine performance.

Objective (6) was achieved through the study outlined in Chapter 7:

6. The simulation showed that the engine could be developed from two-stages with one linear alternator to four-stages with two linear alternators. The results illustrated that it ran at 54.79 Hz and the total engine length was 5.09 m. Each alternator generated 134.5 W of electricity, and hence, the engine generated 269 W at the thermal to electric efficiency of 14%.

## 8.2 Future Work

Research activities undertaken during this project could be considered as a step towards the implementation of a push-pull linear alternator and design of a thermoacoustic engine for internal combustion engine waste heat recovery. Many steps could be guided by the research findings to improve and develop the engine. Some of this further research will be surveyed and will be categorized as numerical and experimental.

### 8.2.1 Further Simulation

- A phase adjuster mechanism needs to be placed to shift the phase difference at the linear alternator. An optimum mechanism and location could be optimised using DeltaEC. As explained in Section 3.2, the linear alternator can generate more than 230 W of electricity, however, it was limited to 133 W in this research. The reason is that the feedback loop diameter could not be decreased to less than 40 mm to increase the local acoustic impedance because it reduced the local phase difference ( $Ph(U)-Ph(P)$ ) at the linear alternator to less than  $-70^\circ$  which reduced the alternator efficiency dramatically. The phase adjuster will allow the acoustic impedance to increase without harming the local phase difference at the linear alternator.
- The current long feedback loop (around 7.5 m) could be reduced by using a compliance-inertance as suggested in Section 3.2. This could be implemented by a combination of a thin loop followed by a wide diameter tube. This can reduce the total length of the feedback loop and deliver acoustic power at the required phasing.

## 8.2.2 Experimental improvements

- Use a linear alternator that has two pistons which can extract equal amounts of acoustic power from each side.
- Reduce the heat leak. The major step is to re-design and manufacture the hot heat exchanger assembly. The hot heat exchanger needs to be thermally insulated from the surrounding pieces to eliminate the heat lost by conduction. This could be done by manufacturing a cylindrical hot heat exchanger accommodated by a housing cylinder with a thermal insulation between them, as shown in Figure 8.1. The thermal insulation could be manufactured out of low thermal conductivity epoxy.

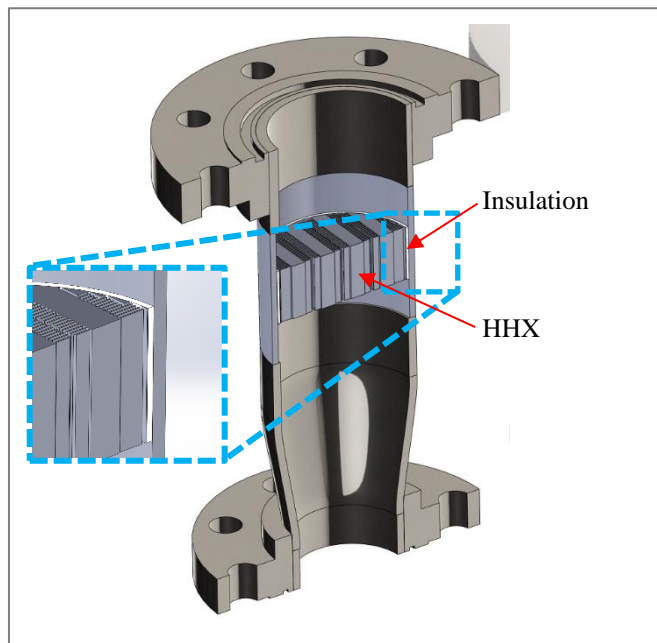


**Figure 8-1:** Proposed hot heat exchanger with insulation jacket

- Separating the hot heat exchanger from the heat exchanger and housing is expected to reduce the thermal section assembly which will allow the engine to charge to a higher mean pressure. This is expected to improve the performance of the engine.
- Remanufacture the feedback piece above the main ambient heat exchanger to provide a membrane housing, to place the membrane close to the velocity node to eliminate the Gedeon streaming.
- Manufacture the gas-to-gas hot heat exchanger proposed in Figure A3.4. The rig needs to be placed in a laboratory having hot air extractor and then it could

be tested to evaluate the performance at a realistic heat source using hot air gun.

## List of References

- Abdoulla, K., Yu, Z. and Jaworski, A.J., 2012. Design of a low-cost two-stage thermoacoustic electricity generator for rural communities in developing countries. In: *19th International Congress on Sound and Vibration*, Vilnius, Lithuania, 8-12 July 2012.
- Abdoulla, K., Kang, H. and Jaworski, A.J., 2013. Travelling wave thermoacoustic electricity generator for rural areas using a side-branch alternator arrangement. In *Proceedings of the World Congress on Engineering 2013. Lecture Notes in Engineering and Computer Science* (Vol. 3, pp. 1835-1840). Newswood Limited.
- Abduljalil, A.S., Yu, Z., Jaworski, A.J. and Shi, L., 2009a. Construction and Performance Characterization of the Looped-Tube Travelling-Wave Thermoacoustic Engine with Ceramic Regenerator. *World Academy of Science, Engineering and Technology, International Journal of Mechanical, Aerospace, Industrial, Mechatronic and Manufacturing Engineering*, 3(1), pp.19-22.
- Abduljalil, A.S., Yu, Z. and Jaworski, A.J., 2009b. Performance studies of travelling-wave thermoacoustic engine for selected low-cost regenerators. In: 2009 SEM Annual Conference & Exposition on Experimental and Applied Mechanics, Albuquerque, NM, USA, 1-4 Jun 2009.
- Abduljalil, A.S., Yu, Z. and Jaworski, A.J., 2009c, August. Experimental characterisation of low-cost regenerators for travelling-wave thermoacoustic devices. In *Proceedings of 7th Annual International Energy Conversion Engineering Conference, Denver* (pp. 2-5).
- Abduljalil, A.S., Yu, Z. and Jaworski, A.J., 2011b. Selection and experimental evaluation of low-cost porous materials for regenerator applications in thermoacoustic engines. *Materials & Design*, 32(1), pp.217-228.
- Abduljalil, A.S., Yu, Z. and Jaworski, A.J., 2011a. Design and experimental validation of looped-tube thermoacoustic engine. *Journal of Thermal Science*, 20(5), pp.423-429.

- Arnott, W.P., Bass, H.E. and Raspet, R., 1991. General formulation of thermoacoustics for stacks having arbitrarily shaped pore cross sections. *The Journal of the Acoustical Society of America*, 90(6), pp.3228-3237.
- Backhaus, S. and Swift, G.W., 1999. A thermoacoustic Stirling heat engine. *Nature*, 399(6734), pp.335-338.
- Backhaus, S. and Swift, G.W., 2000. A thermoacoustic-Stirling heat engine: Detailed study. *The Journal of the Acoustical Society of America*, 107(6), pp.3148-3166.
- Backhaus, S., Tward, E. and Petach, M., 2004. Traveling-wave thermoacoustic electric generator. *Applied Physics Letters*, 85(6), pp.1085-1087.
- Bhansali, P.S., Patunkar, P.P., Gorade, S.V., Adhav, S.S. and Botre, S.S., 2009, AN OVERVIEW OF STACK DESIGN FOR A THERMOACOUSTIC REFRIGERATOR. *IJRET: International Journal of Research in Engineering and Technology* eISSN: 2319-1163 | pISSN: 2321-7308
- Bao, R., Chen, G.B., Tang, K., Jia, Z.Z. and Cao, W.H., 2006. Effect of RC load on performance of thermoacoustic engine. *Cryogenics*, 46(9), pp.666-671.
- Bi, T., Wu, Z., Zhang, L., Yu, G., Luo, E. and Dai, W., 2015. Development of a 5kW traveling-wave thermoacoustic electric generator. *Applied Energy*.
- Biwa, T., Ueda, Y., Yazaki, T. and Mizutani, U., 2002. Thermodynamical mode selection rule observed in thermoacoustic oscillations. *EPL (Europhysics Letters)*, 60(3), p.363.
- Biwa, T., Hasegawa, D. and Yazaki, T., 2010. Low temperature differential thermoacoustic Stirling engine. *Applied physics letters*, 97(3), p.034102.
- de Blok, K., 2008. Low operating temperature integral thermo acoustic devices for solar cooling and waste heat recovery. *Journal of the Acoustical Society of America*, 123(5), pp.3541-3541.
- de Blok, K., 2010, January. Novel 4-stage traveling wave thermoacoustic power generator. In *ASME 2010 3rd Joint US-European Fluids Engineering Summer Meeting collocated with 8th International Conference on Nanochannels, Microchannels, and Minichannels* (pp. 73-79). American Society of Mechanical Engineers.

- de Blok, K. and Systemen, A.T., 2012, July. Multi-stage traveling wave thermoacoustics in practice. In *19th International Congress on Sound and Vibration, Vilnius*.
- Carter, R.L., White, M. and Steele, A.M., 1962. Private communication of atomics international division of North American aviation. *Inc., September, 24*.
- Ceperley, P.H., 1979. A pistonless Stirling engine—The traveling wave heat engine. *The Journal of the Acoustical Society of America*, 66(5), pp.1508-1513.
- Ceperley, P.H., 1985. Gain and efficiency of a short traveling wave heat engine. *The Journal of the Acoustical Society of America*, 77(3), pp.1239-1244.
- *Document by Allis Chalmers. Engine Horse Power and Exhaust Flow. Available: <http://www.asia.donaldson.com/en/exhaust/support/datalibrary/1053747.pdf>.*
- Chen, B., Yousif, A.A., Riley, P.H. and Hann, D.B., 2012. Development and assessment of thermoacoustic generators operating by waste heat from cooking stove. *Engineering Vol.4 No.12(2012)*, Article ID:25859, 4 pages
- Chen, B.M., Riley, P.H., Abakr, Y.A., Pullen, K., Hann, D.B. and Johnson, C.M., 2013. Design and development of a low-cost, electricity-generating cooking Score-Stove™. *Proceedings of the institution of mechanical engineers, Part A: Journal of Power and Energy*, p.0957650913498733.
- Ehsan, M., Sarker, M., Mahmud, R. and Riley, P.H., 2015a. Performance of an Electricity-Generating Cooking Stove with Pressurized Kerosene Burner. *Procedia Engineering*, 105, pp.619-627.
- Ehsan, M., Sarker, M., Mahmud, R. and Riley, P.H., 2015b. Performance of a Score-Stove with a Kerosene Burner and the Effect of Pressurization of the Working Fluid. *Journal of Power and Energy Engineering*, 3(04), p.458.
- Feldman, K.T., 1968a. Review of the literature on Rijke thermoacoustic phenomena. *Journal of Sound and Vibration*, 7(1), pp.83-89.
- Feldman, K.T., 1968b. Review of the literature on Sondhauss thermoacoustic phenomena. *Journal of Sound and Vibration*, 7(1), pp.71-82.

- Fusco, A.M., Ward, W.C. and Swift, G.W., 1992. Two-sensor power measurements in lossy ducts. *The Journal of the Acoustical Society of America*, 91(4), pp.2229-2235.
- Gedeon, D., 1997. DC gas flows in Stirling and pulse tube cryocoolers. In *Cryocoolers 9* (pp. 385-392). Springer US.
- Hasegawa, S., Yamaguchi, T. and Oshinoya, Y., 2013. A thermoacoustic refrigerator driven by a low temperature-differential, high-efficiency multistage thermoacoustic engine. *Applied Thermal Engineering*, 58(1), pp.394-399.
- Higgins, B., 1802. cited by W. Nicholson, On the sound produced by a current of hydrogen gas passing through a tube. With a letter from Dr. Higgins, respecting the time of its discovery. *J. Nat. Phil., Chem., and the Arts*, 1, pp.129-131.
- Hossain, M.M., Malek, M.I., Ehsan, M. and Riley, P.H., 2016, July. Score-stove™ Performance with modified resonating tube shape and layouts. In *INTERNATIONAL CONFERENCE ON MECHANICAL ENGINEERING: Proceedings of the 11th International Conference on Mechanical Engineering (ICME 2015)* (Vol. 1754, No. 1, p. 030013). AIP Publishing.
- Jadhao, J.S. and Thombare, D.G., 2013. Review on exhaust gas heat recovery for IC engine. *International Journal of Engineering and Innovative Technology (IJEIT)*, 2(12).
- Johnson, V.H., 2002. *Heat-generated cooling opportunities in vehicles* (No. 2002-01-1969). SAE Technical Paper.
- Kang, H., Cheng, P., Yu, Z. and Zheng, H., 2015. A two-stage traveling-wave thermoacoustic electric generator with loudspeakers as alternators. *Applied Energy*, 137, pp.9-17.
- Kitadani, Y., Sakamoto, S.I., Sahashi, K. and Watanabe, Y., 2010. Basic study for practical use of thermoacoustic electric generation system. *system*, 1, p.5.
- Li, D., Wu, Z., Luo, E. and Zhang, L., 2014. Experimental Investigation on the Conversion between Heat and Power of the kW-class Thermoacoustic Engine. *Energy Procedia*, 61, pp.1058-1062.

- Li, L., Wu, Z., Hu, J., Yu, G., Luo, E. and Dai, W., 2016. A novel heat-driven thermoacoustic natural gas liquefaction system. Part I: Coupling between refrigerator and linear motor. *Energy*.
- Lord, R., 1945. The theory of sound.
- Luo, E., Ling, H., Dai, W. and Zhnag, Y., 2005. A high pressure-ratio, energy-focused thermoacoustic heat engine with a tapered resonator. *Chinese Science Bulletin*, 50(3), pp.284-286.
- Luo, E.C., Ling, H., Dai, W. and Yu, G.Y., 2006. Experimental study of the influence of different resonators on thermoacoustic conversion performance of a thermoacoustic-Stirling heat engine. *Ultrasonics*, 44, pp.e1507-e1509.
- Luo, E., Dai, W., Zhang, Y. and Ling, H., 2006. Thermoacoustically driven refrigerator with double thermoacoustic-Stirling cycles. *Applied physics letters*, 88(7), p.074102.
- Luo, E., Wu, Z., Dai, W., Li, S. and Zhou, Y., 2008. A 100 W-class traveling-wave thermoacoustic electricity generator. *Chinese Science Bulletin*, 53(9), pp.1453-1456.
- Putnam, A.A. and Dennis, W.R., 1956. Survey of Organ-Pipe Oscillations in Combustion Systems. *The Journal of the Acoustical Society of America*, 28 (2), pp.246-259.
- Qiu, L.M., Sun, D.M., Zhang, W., Chen, G.B., Gan, Z.H. and Yan, W.L., 2003, April. Experimental study of a large-scale multifunction thermoacoustic engine. In *International Conference on Cryogenics and Refrigeration* (pp. 157-160).
- Rayleigh, J.W.S., 1878. The explanation of certain acoustical phenomena. *Nature*, 18(455), pp.319-321.
- Rijke, P.L., 1859. LXXI. Notice of a new method of causing a vibration of the air contained in a tube open at both ends. *The London, Edinburgh, and Dublin Philosophical Magazine and Journal of Science*, 17(116), pp.419-422.
- Rott, N., 1969. Damped and thermally driven acoustic oscillations in wide and narrow tubes. *Zeitschrift für angewandte Mathematik und Physik ZAMP*, 20(2), pp.230-243.

- Rott, N., 1973. Thermally driven acoustic oscillations. Part II: Stability limit for helium. *Zeitschrift für angewandte Mathematik und Physik ZAMP*, 24(1), pp.54-72.
- Rott, N., 1975. Thermally driven acoustic oscillations, Part III: Second-order heat flux. *Zeitschrift für angewandte Mathematik und Physik ZAMP*, 26(1), pp.43-49.
- Rott, N. and Zouzoulas, G., 1976. Thermally driven acoustic oscillations, part IV: tubes with variable cross-section. *Zeitschrift für angewandte Mathematik und Physik ZAMP*, 27(2), pp.197-224.
- Müller, U.A. and Rott, N., 1983. Thermally driven acoustic oscillations, Part VI: Excitation and power. *Zeitschrift für angewandte Mathematik und Physik ZAMP*, 34(5), pp.609-626.
- Saechan, P., Kang, H., Mao, X. and Jaworski, A.J., 2013. Thermoacoustic refrigerator driven by a combustion-powered thermoacoustic engine-Demonstrator of device for rural areas of developing countries. *Lecture Notes in Engineering and Computer Science*, 3, pp.2097-2102.
- Sakamoto, Shin-ichi, Toshiyuki Tsujimoto, and Yoshiaki Watanabe. "Experimental study on the start-up profile of the thermoacoustic cooling system." *ICA 2004 Proc 1* (2004): 693-696.
- Sakamoto, S.I. and Watanabe, Y., 2004. The experimental studies of thermoacoustic cooler. *Ultrasonics*, 42(1), pp.53-56.
- Sakamoto, S.I. and Watanabe, Y., 2006. Experimental study on resonance frequency of loop-tube-type thermoacoustic cooling system. *Acoustical science and technology*, 27(6), pp.361-365.
- Sakamoto, Shin-ichi, et al. "Effect of inner diameter change of phase adjuster on heat-to-sound energy conversion efficiency in loop-tube-type thermoacoustic prime mover." *Japanese Journal of Applied Physics* 47.5S (2008): 4223.
- Sakamoto, S.I., Yoshida, H., Sakaguchi, A. and Watanabe, Y., 2009. Heat Pump Placed in the Resonance Tube Connected to the Loop-Tube-Type Thermoacoustic Cooling System Improves the Cooling Effect. *Japanese Journal of Applied Physics*, 48(7S), p.07GM01.

- Sakamoto S., and Watanabe Y., 2011. Fundamental study of a loop-tube-type thermoacoustic heater. In Proceedings of Symposium on Ultrasonic Electronics. pp. 377–378.
- Sakamoto, S., Sahashi, K. & Watanabe, Y., 2012. Improving Thermoacoustic System Efficiency, Measurement of a Sound Field in the Phase Adjuster. *Proceedings of Symposium on Ultrasonic Electronics*, 33, pp.215–216.
- Sakamoto, S.I. and Watanabe, Y., 2013. Fundamental Study of a Loop-Tube-Type Thermoacoustic Heating System. *Journal of Energy and Power Engineering*, 7(11), p.2096.
- Senga, M. and Hasegawa, S., 2016. Four-stage loop-type cascade traveling-wave thermoacoustic engine. *Applied Thermal Engineering*, 104, pp.258-262.
- So, J.H., Swift, G.W. and Backhaus, S., 2006. An internal streaming instability in regenerators. *The Journal of the Acoustical Society of America*, 120(4), pp.1898-1909.
- Sondhauss, C., 1850. Ueber die Schallschwingungen der Luft in erhitzten Glasröhren und in gedeckten Pfeifen von ungleicher Weite. *Annalen der Physik*, 155(1), pp.1-34.
- Sun, D., Qiu, L., Zhang, W., Yan, W. and Chen, G., 2005. Investigation on traveling wave thermoacoustic heat engine with high pressure amplitude. *Energy conversion and management*, 46(2), pp.281-291.
- Sun, D.M., Wang, K., Zhang, X.J., Guo, Y.N., Xu, Y. and Qiu, L.M., 2013. A traveling-wave thermoacoustic electric generator with a variable electric RC load. *Applied energy*, 106, pp.377-382.
- Swift, G.W., 1988. Thermoacoustic engines. *The Journal of the Acoustical Society of America*, 84(4), pp.1145-1180.
- Swift, G.W., 2000, July. Streaming in thermoacoustic engines and refrigerators. In *NONLINEAR ACOUSTICS AT THE TURN OF THE MILLENNIUM: ISNA 15, 15th International Symposium* (Vol. 524, No. 1, pp. 105-114). AIP Publishing.
- Swift, G.W., 2002. *Thermoacoustics*. Acoustical society of America.
- Taymaz, I., 2006. An experimental study of energy balance in low heat rejection diesel engine. *Energy*, 31(2), pp.364-371.

- Tijani, H., Spoelstra, S. and Poignand, G., 2008. Study of a thermoacoustic-Stirling engine. *Journal of the Acoustical Society of America*, 123(5), p.3541.
- Tijani, M.E.H. and Spoelstra, S., 2011. A high performance thermoacoustic engine. *Journal of Applied Physics*, 110(9), p.093519.
- Tijani, M.E.H. and Spoelstra, S., 2012. High temperature thermoacoustic heat pump. In *The 19th Intl. Congress of Sound and Vibration* (pp. 8-12).
- Tijani, M.E.H. and Spoelstra, S., 2013. A hot air driven thermoacoustic-Stirling engine. *Applied Thermal Engineering*, 61(2), pp.866-870.
- Ueda, Y., Biwa, T., Mizutani, U. and Yazaki, T., 2002. Acoustic field in a thermoacoustic Stirling engine having a looped tube and resonator. *Applied physics letters*, 81(27), pp.5252-5254.
- Ueda, Y., Biwa, T., Mizutani, U. and Yazaki, T., 2004. Experimental studies of a thermoacoustic Stirling prime mover and its application to a cooler. *The Journal of the Acoustical Society of America*, 115(3), pp.1134-1141.
- Wang, K., Sun, D., Zhang, J., Xu, Y., Zou, J., Wu, K., Qiu, L. and Huang, Z., 2015. Operating characteristics and performance improvements of a 500W traveling-wave thermoacoustic electric generator. *Applied Energy*, 160, pp.853-862.
- Wang, K., Sun, D., Zhang, J., Xu, Y., Luo, K., Zhang, N., Zou, J. and Qiu, L., 2016a. An acoustically matched traveling-wave thermoacoustic generator achieving 750 W electric power. *Energy*, 103, pp.313-321.
- Wang, K., Zhang, J., Zhang, N., Sun, D., Luo, K., Zou, J. and Qiu, L., 2016b. Acoustic matching of a traveling-wave thermoacoustic electric generator. *Applied Thermal Engineering*, 102, pp.272-282.
- Ward B, Clark J and Swift G. Design Environment for Low (amplitude) Thermoacoustic Energy Conversion DeltaEC Version 6.3 b11 Users Guide. Los Alamos national laboratory. 2012.
- Wilcox, D. and Spoor, P., 2014. Gedeon streaming suppression in a small scale thermoacoustic-Stirling engine-generator. *The Journal of the Acoustical Society of America*, 135(4), pp.2408-2408.

- Wu, Z., Man, M., Luo, E., Dai, W. and Zhou, Y., 2011. Experimental investigation of a 500 W traveling-wave thermoacoustic electricity generator. *Chinese Science Bulletin*, 56(19), pp.1975-1977.
- Wu, Z., Dai, W., Man, M. and Luo, E., 2012. A solar-powered traveling-wave thermoacoustic electricity generator. *Solar Energy*, 86(9), pp.2376-2382.
- Wu, Z., Zhang, L., Dai, W. and Luo, E., 2014a. Investigation on a 1kW traveling-wave thermoacoustic electrical generator. *Applied Energy*, 124, pp.140-147.
- Wu, Z., Yu, G., Zhang, L., Dai, W. and Luo, E., 2014b. Development of a 3kW double-acting thermoacoustic Stirling electric generator. *Applied Energy*, 136, pp.866-872.
- Xu, J., Hu, J., Zhang, L., Dai, W. and Luo, E., 2015a. Effect of coupling position on a looped three-stage thermoacoustically-driven pulse tube cryocooler. *Energy*, 93, pp.994-998.
- Xu, J., Yu, G., Zhang, L., Dai, W., Wu, Z. and Luo, E., 2015b. Numerical investigation on a 300Hz pulse tube cryocooler driven by a three-stage traveling-wave thermoacoustic heat engine. *Cryogenics*, 71, pp.68-75.
- Xu, J., Zhang, L., Hu, J., Wu, Z., Bi, T., Dai, W. and Luo, E., 2016. An efficient looped multiple-stage thermoacoustically-driven cryocooler for liquefaction and recondensation of natural gas. *Energy*, 101, pp.427-433.
- Yang, Z., Zhuo, Y., Ercang, L. and Yuan, Z., 2014. Travelling-wave thermoacoustic high-temperature heat pump for industrial waste heat recovery. *Energy*, 77, pp.397-402.
- Yazaki, T., Iwata, A., Maekawa, T. and Tominaga, A., 1998. Traveling wave thermoacoustic engine in a looped tube. *Physical Review Letters*, 81(15), p.3128.
- Yazaki, T., T. Biwa, and A. Tominaga. "A pistonless Stirling cooler." *Applied Physics Letters* 80.1 (2002): 157-159.
- Yu, Z.B., Li, Q., Chen, X., Guo, F.Z. and Xie, X.J., 2005. Experimental investigation on a thermoacoustic engine having a looped tube and resonator. *Cryogenics*, 45(8), pp.566-571.

- Yu, B., Luo, E.C., Li, S.F., Dai, W. and Wu, Z.H., 2011. Experimental study of a thermoacoustically-driven traveling wave thermoacoustic refrigerator. *Cryogenics*, 51(1), pp.49-54.
- Yu, Z., Backhaus, S. and Jaworski, A.J., 2009. Design and testing of a travelling-wave looped-tube engine for low-cost electricity generators in remote and rural areas. *American Institute of Aeronautics and Astronautics*.
- Yu, Z., Jaworski, A.J. and Backhaus, S., 2010(a). A low-cost electricity generator for rural areas using a travelling-wave looped-tube thermoacoustic engine. *Proceedings of the Institution of Mechanical Engineers, Part A: Journal of Power and Energy*, 224(6), pp.787-795.
- Yu, Z., Jaworski, A.J. and Backhaus, S., 2010(b), January. Design of a Low-Cost Thermoacoustic Electricity Generator and Its Experimental Verification. In *ASME 2010 10th Biennial Conference on Engineering Systems Design and Analysis* (pp. 191-199). American Society of Mechanical Engineers.
- Yu, Z. and Jaworski, A.J., 2010(c). Impact of acoustic impedance and flow resistance on the power output capacity of the regenerators in travelling-wave thermoacoustic engines. *Energy conversion and management*, 51(2), pp.350-359.
- Yu, Z., Saechan, P. and Jaworski, A.J., 2011. A method of characterising performance of audio loudspeakers for linear alternator applications in low-cost thermoacoustic electricity generators. *Applied acoustics*, 72(5), pp.260-267.
- Yu, Z., Jaworski, A.J. and Backhaus, S., 2012. Travelling-wave thermoacoustic electricity generator using an ultra-compliant alternator for utilization of low-grade thermal energy. *Applied Energy*, 99, pp.135-145.
- Yu, Z. and Jaworski, A.J., 2012. Demonstrator of a combustion driven thermoacoustic electricity generator for remote and rural areas of developing countries. In: 19th International Congress on Sound and Vibration, Vilnius, Lithuania, 8-12 Jul 2012.
- Zhang, L.M., Hu, J.Y., Wu, Z.H., Luo, E.C., Xu, J.Y. and Bi, T.J., 2015. A 1 kW-class multi-stage heat-driven thermoacoustic cryocooler system operating at liquefied natural gas temperature range. *Applied Physics Letters*, 107(3), p.033905.

- Zhang, X. and Chang, J., 2015. Onset and steady-operation features of low temperature differential multi-stage travelling wave thermoacoustic engines for low grade energy utilization. *Energy Conversion and Management*, 105, pp.810-816.
- Zhang, X., Chang, J., Cai, S. and Hu, J., 2016. A multi-stage travelling wave thermoacoustic engine driven refrigerator and operation features for utilizing low grade energy. *Energy Conversion and Management*, 114, pp.224-233.

## **Appendix 1**

### **List of publications**

- Hamood, A., Mao, X. and Jaworski, A.J., 2015. Design of two-stage thermoacoustic Stirling engine coupled with push-pull linear alternator for waste heat recovery. *Proceedings of ICR2015*.
- Hamood, A., Mao, X. and Jaworski, A.J., 2016, April. Two-Stage Thermoacoustic Electricity Generator for Waste Heat Recovery. In *Proceedings of World Congress on Engineering 2016*. IAENG.

## Appendix 2

In this appendix, the DeltaEC model of two-stage thermoacoustic electricity generator with push-pull linear alternator is presented. The model gives a detailed segment by segment dimensions and calculations along the engine loop. It also shows the assumptions made in modelling half of the engine and connect it to a self-excited imaginary flow.

```

1  QDrv Sch40 28bar
2  0 BEGIN
3      2.8000E+06 a Mean P Pa
4  Gues      55.190 b Freq Hz
5  Gues      297.00 c TBeg K
6  Gues      8.7180E+04 d |p| Pa
7      20.000 e Ph(p) deg
8  Gues      6.6099E-03 f |U| m^3/s
9  Gues      86.947 g Ph(U) deg
10 Gues      69.325 h Htot W
11 Optional Parameters
12 helium Gas type
13 1 DUCT 102mm Dia Core
14      8.2130E-03 a Area m^2 Mstr      8.7180E+04 A |p| Pa
15      0.32131 b Perim m 1a      20.000 B Ph(p) deg
16      0.0000 c Length m      6.6099E-03 C |U| m^3/s
17      5.0000E-04 d Srough      86.947 D Ph(U) deg
18 Master-Slave Links      69.325 E Htot W
19 Optional Parameters      112.82 F Edot W
20 ideal Solid type
21 2 HX 1mm plate spacing
22 Same 1a 8.2130E-03 a Area m^2      8.7301E+04 A |p| Pa
23      0.2920 b GasA/A      19.946 B Ph(p) deg
24      3.0000E-02 c Length m      6.1047E-03 C |U| m^3/s
25      5.0000E-04 d y0 m      85.538 D Ph(U) deg
26 Gues      -123.89 e HeatIn W      -54.568 E Htot W
27 Master-Slave Links      110.12 F Edot W
28 Possible targets      297.00 G GasT K
29 ideal Solid type      294.85 H SolidT K
30 3 RPN ChangeMe
31 Targ      297.00 a G or T      297.00 A ChngeMe
32 2G
33 4 DUCT Cold gap
34 Same 1a 8.2130E-03 a Area m^2 Mstr      8.7302E+04 A |p| Pa
35      0.32131 b Perim m 4a      19.945 B Ph(p) deg
36      1.3000E-03 c Length m      6.0415E-03 C |U| m^3/s
37      1.0000E-04 d Srough      85.267 D Ph(U) deg
38 Master-Slave Links      -54.568 E Htot W
39 Optional Parameters      110.11 F Edot W
40 ideal Solid type
41 5 STKSCREEN 0.065mm wide diameter, app 0.18mm, 78.9% porosity
42 Same 1a 8.2130E-03 a Area m^2      8.4799E+04 A |p| Pa
43      0.7890 b VolPor      17.767 B Ph(p) deg

```

44		7.3000E-02	c	Length	m		7.1122E-03	C	U	m^3/s
45		6.0200E-05	d	rh	m		56.770	D	Ph(U)	deg
46		0.1000	e	ksFrac			-54.568	E	Htot	W
47	Master-Slave Links						234.34	F	Edot	W
48							297.00	G	TBeg	K
49	stainless			Solid type			673.00	H	TEnd	K
50	6 RPN			Displacement						
51		0.0000	a	G or T			6.3302	A	Displ.	
52	5C 5a / w / 1000 * 2 * 5b /									
53	7 RPN			Net Power						
54		0.0000	a	G or T			124.24	A	Net Pow	
55	5F 4F -									
56	8 DUCT			Hot gap						
57	Same 1a	8.2130E-03	a	Area	m^2	Mstr	8.4800E+04	A	p	Pa
58		0.32131	b	Perim	m	8a	17.767	B	Ph(p)	deg
59		1.3000E-03	c	Length	m		7.0696E-03	C	U	m^3/s
60		1.0000E-04	d	Srough			56.346	D	Ph(U)	deg
61	Master-Slave Links						-54.568	E	Htot	W
62	Optional Parameters						234.33	F	Edot	W
63	ideal			Solid type						
64	9 HX			HHX						
65	Same 1a	8.2130E-03	a	Area	m^2		8.4813E+04	A	p	Pa
66		0.3440	b	GasA/A			17.708	B	Ph(p)	deg
67		4.0000E-02	c	Length	m		6.3639E-03	C	U	m^3/s
68	Same 2d	5.0000E-04	d	y0	m		50.814	D	Ph(U)	deg
69	Gues	288.79	e	HeatIn	W		234.22	E	Htot	W
70	Master-Slave Links						226.06	F	Edot	W
71	Possible targets						673.00	G	GasT	K
72	ideal			Solid type			678.32	H	SolidT	K
73	10 RPN			ChangeMe						
74	Targ	673.00	a	G or T			673.00	A	ChngMe	
75	9G									
76	11 STKDUCT			TBT-1 4" Pipe						
77	Same 1a	8.2130E-03	a	Area	m^2	Mstr	8.4819E+04	A	p	Pa
78		0.32131	b	Perim	m	11a	17.698	B	Ph(p)	deg
79		3.0000E-02	c	Length	m		5.6565E-03	C	U	m^3/s
80		7.3000E-04	d	WallA	m^2		37.502	D	Ph(U)	deg
81	Master-Slave Links						234.22	E	Htot	W
82							225.70	F	Edot	W
83							673.00	G	TBeg	K
84	stainless			Solid type			659.64	H	TEnd	K
85	12 STKCONE			TBT 2 4" to 3"						
86	Same 1a	8.2130E-03	a	AreaI	m^2	Mstr	8.4809E+04	A	p	Pa
87		0.32131	b	PerimI	m	12a	17.645	B	Ph(p)	deg
88		0.1020	c	Length	m		5.7364E-03	C	U	m^3/s
89	Same 14a	4.7686E-03	d	AreaF	m^2	Mstr	-5.0075	D	Ph(U)	deg
90		0.24482	e	PerimF	m	12d	234.22	E	Htot	W
91		1.0000E-03	f	f_wall			224.48	F	Edot	W
92	Master-Slave Links						659.64	G	TBeg	K
93	stainless			Solid type			393.58	H	TEnd	K
94	13 STKDUCT			TBT-3 3" Pipe						
95	Same 12d	4.7686E-03	a	Area	m^2	Mstr	8.4786E+04	A	p	Pa
96		0.24482	b	Perim	m	13a	17.615	B	Ph(p)	deg
97		3.0000E-02	c	Length	m		6.1334E-03	C	U	m^3/s

98		1.0000E-04	d WallA	m^2		-12.793	D Ph(U)	deg
99	Master-Slave Links					234.22	E Htot	W
100						224.25	F Edot	W
101						393.58	G TBeg	K
102	stainless		Solid type			297.00	H TEnd	K
103	14 HX		Secondary ambient HX					
104		4.7686E-03	a Area	m^2	Mstr	8.4681E+04	A  p	Pa
105		0.3050	b GasA/A		15a	17.536	B Ph(p)	deg
106		2.0000E-02	c Length	m		6.2202E-03	C  U	m^3/s
107	Same	2d	5.0000E-04	d y0		-14.543	D Ph(U)	deg
108	Gues		-98.289	e HeatIn		135.94	E Htot	W
109	TargSame	2H	294.85	f SolidT		223.16	F Edot	W
110	Master-Slave Links					297.00	G GasT	K
111	ideal		Solid type			294.85	H SolidT	K
112	15 CONE		Cone before T-branch					
113		5.4576E-03	a AreaI	m^2	Mstr	8.4450E+04	A  p	Pa
114		0.26191	b PerimI	m	15a	17.357	B Ph(p)	deg
115		8.9000E-02	c Length	m		7.3408E-03	C  U	m^3/s
116	Same	16a	1.4360E-03	d AreaF	Mstr	-26.675	D Ph(U)	deg
117			0.13433	e PerimF	15d	135.94	E Htot	W
118			5.0000E-04	f Srough		222.85	F Edot	W
119	Master-Slave Links							
120	Optional Parameters							
121	ideal		Solid type					
122	16 DUCT		Feedback Pipe before Alternator					
123		1.4360E-03	a Area	m^2	Mstr	8.3834E+04	A  p	Pa
124		0.13444	b Perim	m	16a	16.962	B Ph(p)	deg
125		0.1000	c Length	m		7.9895E-03	C  U	m^3/s
126		5.0000E-04	d Srough			-31.38	D Ph(U)	deg
127	Master-Slave Links					135.94	E Htot	W
128	Optional Parameters					222.60	F Edot	W
129	ideal		Solid type					
130	17 TBRANCH		Change Me					
131	Gues		4.1093E+07	a Re(Zb)		8.3834E+04	A  p	Pa
132	Gues		-1.9819E+06	b Im(Zb)		16.962	B Ph(p)	deg
133	Gues		66.610	c HtotBr		2.0377E-03	C  U	m^3/s
134	Master-Slave Links					19.724	D Ph(U)	deg
135	Optional Parameters					66.610	E HtotBr	W
136						85.317	F EdotBr	W
137						137.28	G EdotTr	W
138	18 DUCT		Change Me					
139		1.4360E-03	a Area	m^2	Mstr	8.3572E+04	A  p	Pa
140		0.13434	b Perim	m	18a	16.596	B Ph(p)	deg
141		0.2400	c Length	m		2.8817E-03	C  U	m^3/s
142		5.0000E-04	d Srough			-28.654	D Ph(U)	deg
143	Master-Slave Links					66.610	E Htot	W
144	Optional Parameters					84.773	F Edot	W
145	ideal		Solid type					
146	19 VESPEAKER		Change Me					
147		1.3850E-03	a Area	m^2		8.3572E+04	A  p	Pa
148		1.9700	b R	ohms		-163.4	B Ph(p)	deg
149		4.4100E-02	c L	H		2.8817E-03	C  U	m^3/s
150		46.720	d BLProd	T-m		-28.654	D Ph(U)	deg
151		0.7895	e M	kg		-66.61	E Htot	W
152		4.1430E+04	f K	N/m		-84.773	F Edot	W
153		7.0700	g Rm	N-s/m		-133.22	G WorkIn	W
154	Gues		57.732	h  V		57.732	H Volts	V
155	Gues		104.77	i Ph(V)		4.6151	I Amps	A

156							180.00	J	Ph(V/I)	deg
157							1.6714E+05	K	Px	Pa
158	ideal	Solid type					-163.4	L	Ph(Px)	deg
159	20 DUCT	Zero length duct								
160	Same 26a	1.4360E-03	a Area	m^2	Mstr		8.3572E+04	A	p	Pa
161		0.13434	b Perim	m	20a		-163.4	B	Ph(p)	deg
162		0.0000	c Length	m			2.8817E-03	C	U	m^3/s
163		5.0000E-04	d Srough				-28.654	D	Ph(U)	deg
164	Master-Slave Links						-66.61	E	Htot	W
165	Optional Parameters						-84.773	F	Edot	W
166	ideal	Solid type								
167	21 RPN	ChangeMe								
168	Targ	6.0000	a G or T				6.0000	A	disp	
169	19C 19a / w / 1000 *									
170	22 RPN	ChangeMe								
171	Targ	180.00	a G or T				180.00	A	ChngeMe	
172	19J									
173	23 RPN	Heat/Electrical Efficiency								
174		0.0000	a G or T				23.065	A	Efficie	
175	19G 9e / 2 / mag 100 *									
176	24 RPN	Heat/Acc Efficiency								
177		0.0000	a G or T				43.019	A	Acc Eff	
178	7A 9e / 100 *									
179	25 RPN	LA Efficiency								
180		0.0000	a G or T				78.575	A	LA Eff	
181	18E 18F / 100 *									
182	26 DUCT	Change Me								
183	Same 18a	1.4360E-03	a Area	m^2	Mstr		8.3834E+04	A	p	Pa
184		0.13434	b Perim	m	26a		-163.04	B	Ph(p)	deg
185	Same 18c	0.2400	c Length	m			2.0377E-03	C	U	m^3/s
186		5.0000E-04	d Srough				19.724	D	Ph(U)	deg
187	Master-Slave Links						-66.61	E	Htot	W
188	Optional Parameters						-85.317	F	Edot	W
189	ideal	Solid type								
190	27 RPN	ChangeMe								
191	Targ	1.0000	a G or T				1.0000	A	ChngeMe	
192	18A 20A /									
193	28 RPN	ChangeMe								
194	Targ	1.0000	a G or T				1.0000	A	ChngeMe	
195	18B 180 - 20B /									
196	29 RPN	ChangeMe								
197	Targ	-1.000	a G or T				-1.000	A	ChngeMe	
198	18E 20E /									
199	30 SOFTEND	Change Me								
200							8.3834E+04	A	p	Pa
201							-163.04	B	Ph(p)	deg
202							2.0377E-03	C	U	m^3/s
203							19.724	D	Ph(U)	deg
204							-66.61	E	Htot	W
205	Possible targets						-85.317	F	Edot	W
206							-12.822	G	Re(z)	
207							0.61842	H	Im(z)	
208							297.00	I	T	K
209	31 CONE	Cone next T-branch								
210		1.3164E-03	a AreaI	m^2	Mstr		8.3834E+04	A	p	Pa
211		0.12861	b PerimI	m	31a		16.962	B	Ph(p)	deg
212		0.0000	c Length	m			6.8948E-03	C	U	m^3/s

213	Same	32a	1.3138E-03	d AreaF	m <sup>2</sup>	Mstr	-44.678	D Ph(U)	deg
214			0.12854	e PerimF	m	31d	69.325	E Htot	W
215			5.0000E-04	f Srough			137.28	F Edot	W
216	Master-Slave Links								
217	Optional Parameters								
218	ideal	Solid type							
219	32 DUCT 1.5" Feedback TUBE								
220			1.3138E-03	a Area	m <sup>2</sup>	Mstr	7.6271E+04	A  p	Pa
221			0.12854	b Perim	m	32a	-157.85	B Ph(p)	deg
222			6.9750	c Length	m		1.1849E-02	C  U	m <sup>3</sup> /s
223			5.0000E-04	d Srough			-82.619	D Ph(U)	deg
224	Master-Slave Links								
225	Optional Parameters								
226	ideal	Solid type							
227	33 CONE Change Me								
228	Same	32a	1.3138E-03	a AreaI	m <sup>2</sup>	Mstr	7.7600E+04	A  p	Pa
229			0.12854	b PerimI	m	33a	-158.13	B Ph(p)	deg
230			6.4000E-02	c Length	m		1.1525E-02	C  U	m <sup>3</sup> /s
231	Same	34a	5.5740E-04	d AreaF	m <sup>2</sup>	Mstr	-83.027	D Ph(U)	deg
232			8.3716E-02	e PerimF	m	33d	69.325	E Htot	W
233			5.0000E-04	f Srough			114.96	F Edot	W
234	Master-Slave Links								
235	Optional Parameters								
236	ideal	Solid type							
237	34 DUCT 1" Tube								
238			5.5740E-04	a Area	m <sup>2</sup>	Mstr	8.5911E+04	A  p	Pa
239			8.3707E-02	b Perim	m	34a	-159.76	B Ph(p)	deg
240			0.2750	c Length	m		1.0607E-02	C  U	m <sup>3</sup> /s
241			5.0000E-04	d Srough			-84.194	D Ph(U)	deg
242	Master-Slave Links								
243	Optional Parameters								
244	ideal	Solid type							
245	35 CONE Change Me								
246	Same	34a	5.5740E-04	a AreaI	m <sup>2</sup>	Mstr	8.7180E+04	A  p	Pa
247			8.3716E-02	b PerimI	m	35a	-160.0	B Ph(p)	deg
248			0.1780	c Length	m		6.6099E-03	C  U	m <sup>3</sup> /s
249	Same	1a	8.2130E-03	d AreaF	m <sup>2</sup>	Mstr	-93.053	D Ph(U)	deg
250			0.32135	e PerimF	m	35d	69.325	E Htot	W
251	Same	33f	5.0000E-04	f Srough			112.82	F Edot	W
252	Master-Slave Links								
253	Optional Parameters								
254	ideal	Solid type							
255	36 RPN Set Tm								
256	Targ		1.0000	a G or T			1.0000	A ChngeMe	
257	Tm 0c /								
258	37 RPN Set p1 mag								
259	Targ		1.0000	a G or T			1.0000	A ChngeMe	
260	p1 mag 0d /								
261	38 RPN Set p1 phase								
262	Targ		1.0000	a G or T			1.0000	A ChngeMe	
263	p1 arg mag 160 /								
264	39 RPN Set mag U1								
265	Targ		1.0000	a G or T			1.0000	A ChngeMe	
266	U1 mag 0f /								
267	40 RPN Set U1 phase								
268	Targ		1.0000	a G or T			1.0000	A ChngeMe	
269	U1 arg 180 + 0g /								
270	41 RPN Set Htot								
271	Targ		1.0000	a G or T			1.0000	A ChngeMe	
272	1E H2k /								

### Appendix 3

In this appendix, the design drawings and pressure test results will be shown.

- Figures A3.1, A3.2 and A3.3 shows the design drawings and pressure test of the main ambient heat exchanger.
- At first, the hot heat exchanger was designed to be cross flow. The drawings shown in Appendix three, figure A3.4 show the proposed design of the hot heat exchanger which is able to transfer more than 800 W of heat from a flow of hot air at 420°C flowing in the long channels at a flow rate of 300 l/m. It was planned to simulate the exhaust gases with hot air using an air gun and electrical heaters. The calculations showed that shorter fins were more efficient for the low carbon steel as it has low thermal conductivity. At a fin length of 3 mm at the helium side and 2.5 mm at the hot air side, the total gas-to-metal contact was 0.12 and 0.128 m<sup>2</sup> for the helium and hot air sides respectively. Figures A3.4 shows the design drawings of the gas-to-gas cross-flow heat exchanger. This heat exchanger was designed based on heat transfer calculations. Theoretically, it can transfer up to 600 W through the fins from the hot gas flowing from the right to the left to the helium oscillating perpendicular to the drawing.
- Figures A3.5, A3.6 and A3.7 shows the design drawings and pressure test of the hot heat exchanger, at 500°C.
- Figures A3.8, A3.9 and A3.10 shows the design drawings and pressure test of the main ambient heat exchanger.

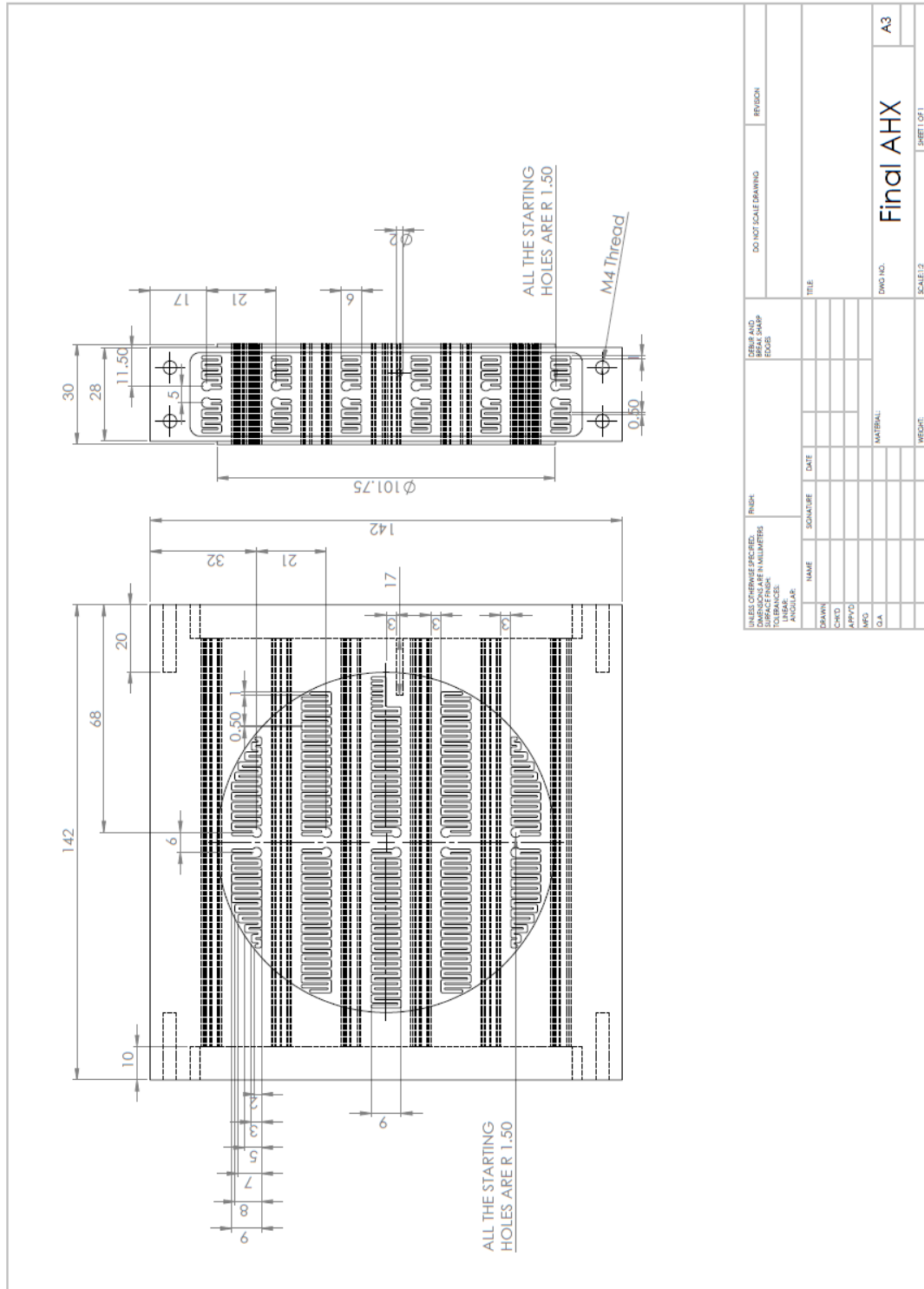


**Figure A3-1:** Ambient heat exchanger detailed drawing

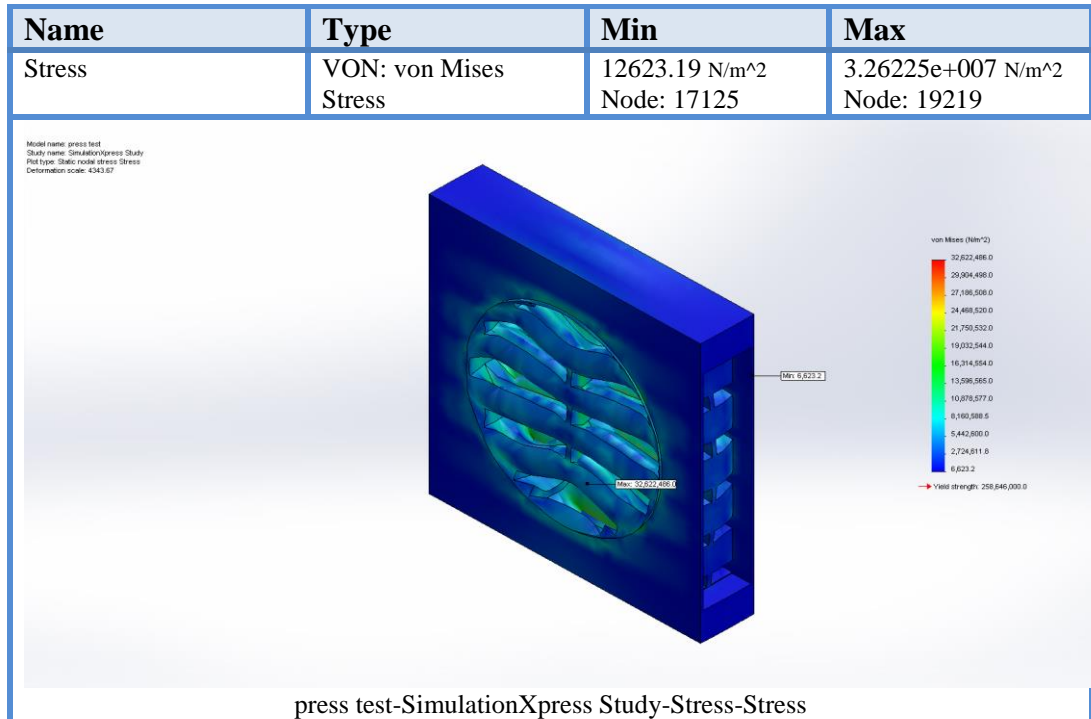


**Figure A3-2:** Simulation of stress of the ambient heat exchanger, done by the SolidWorks

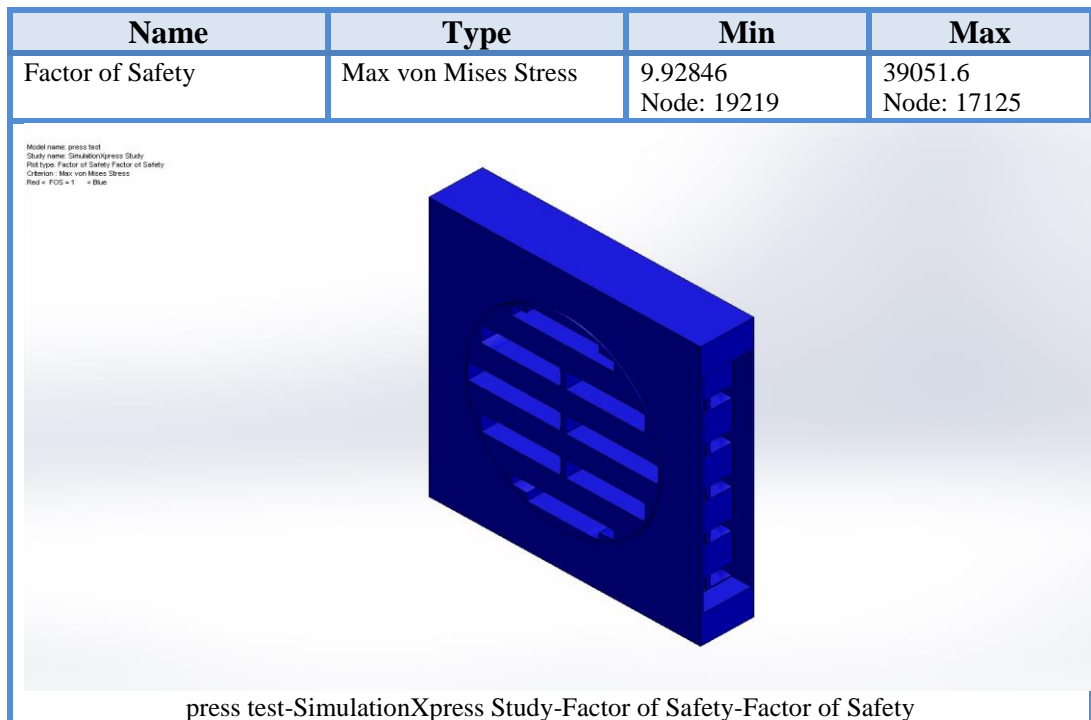


**Figure A3-3:** Simulation of factor of safety of the ambient heat exchanger, done by the SolidWorks



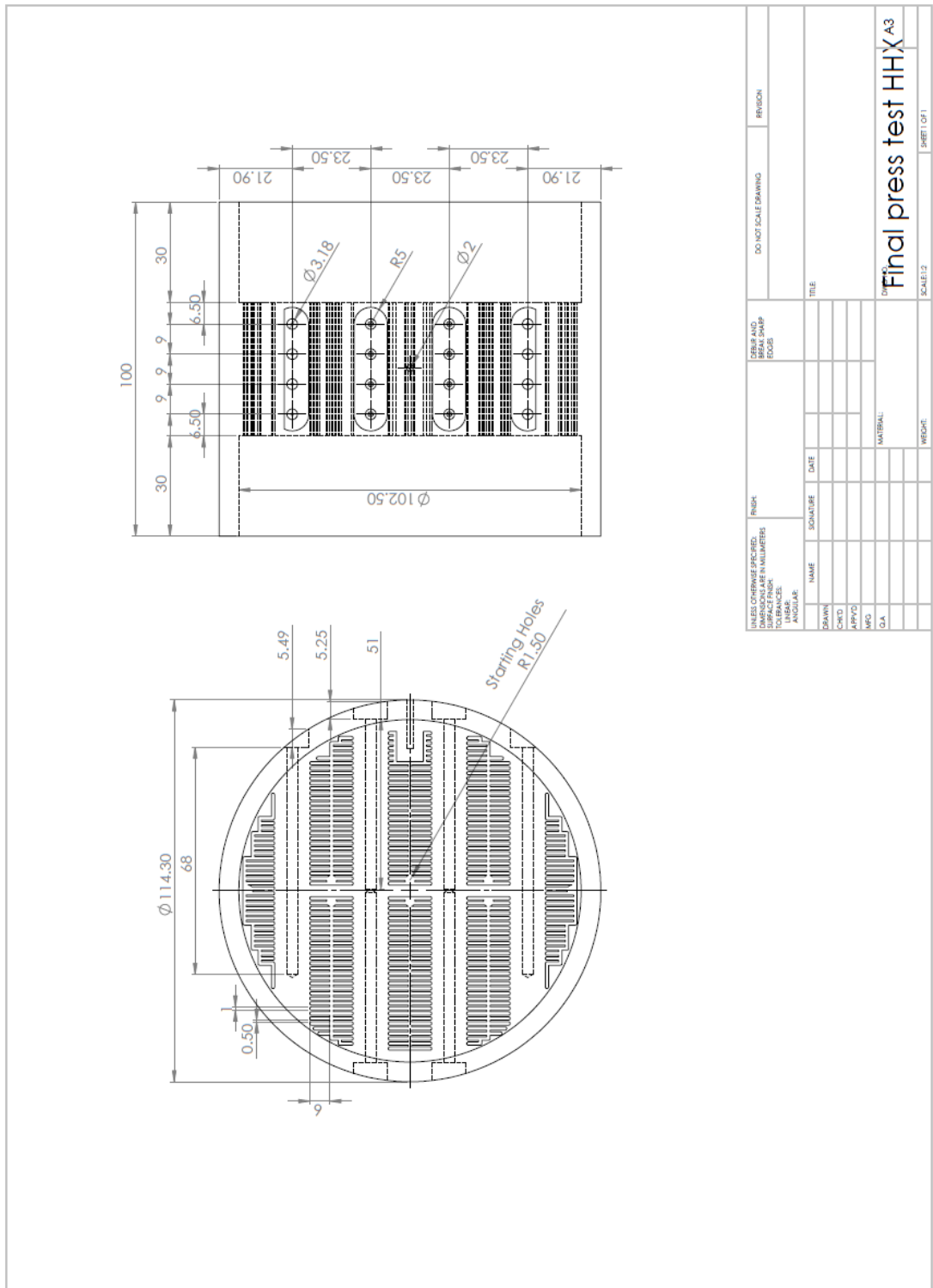


**Figure A3-5:** Detailed drawing of the hot heat exchanger

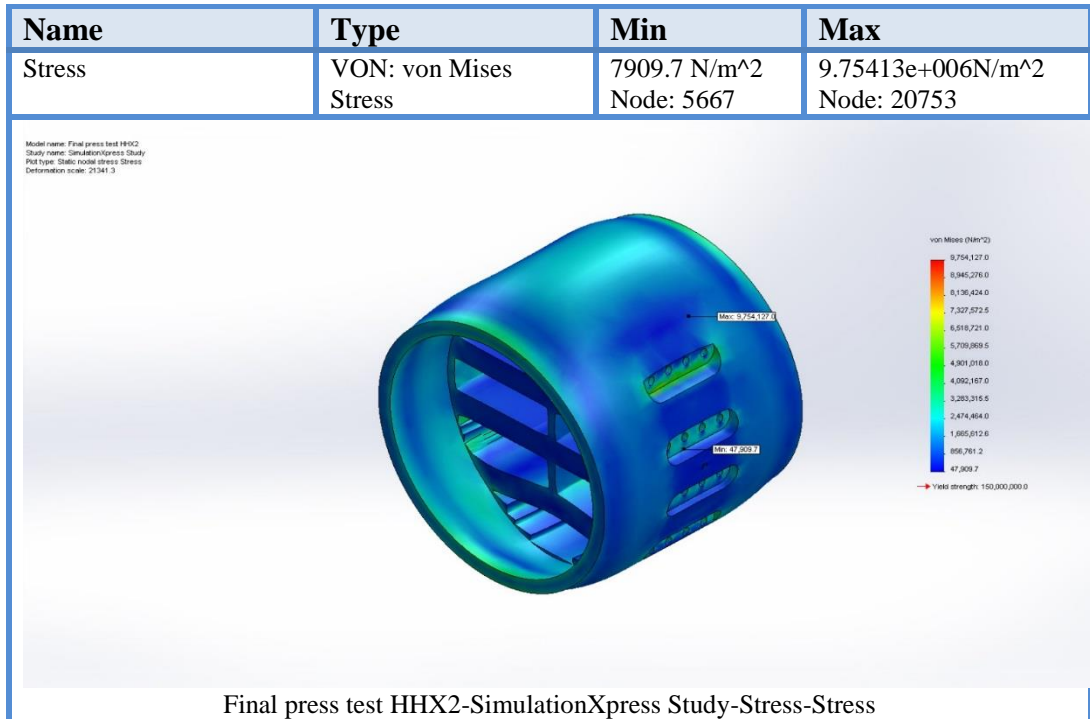


**Figure A3-6:** Simulation of stress of the hot heat exchanger at 400°C, done by the SolidWorks



**Figure A3-7:** Simulation of factor of safety of the hot heat exchanger at 400°C, done by the SolidWorks



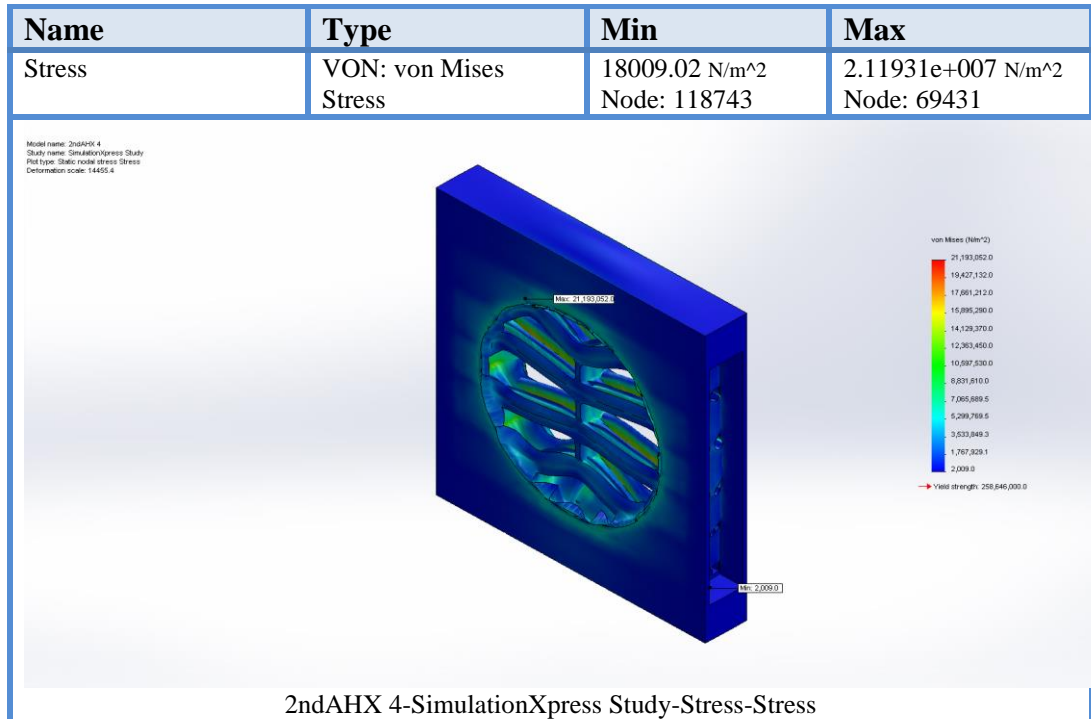


**Figure A3-9:** Simulation of stress of the secondary ambient heat exchanger, done by the SolidWorks

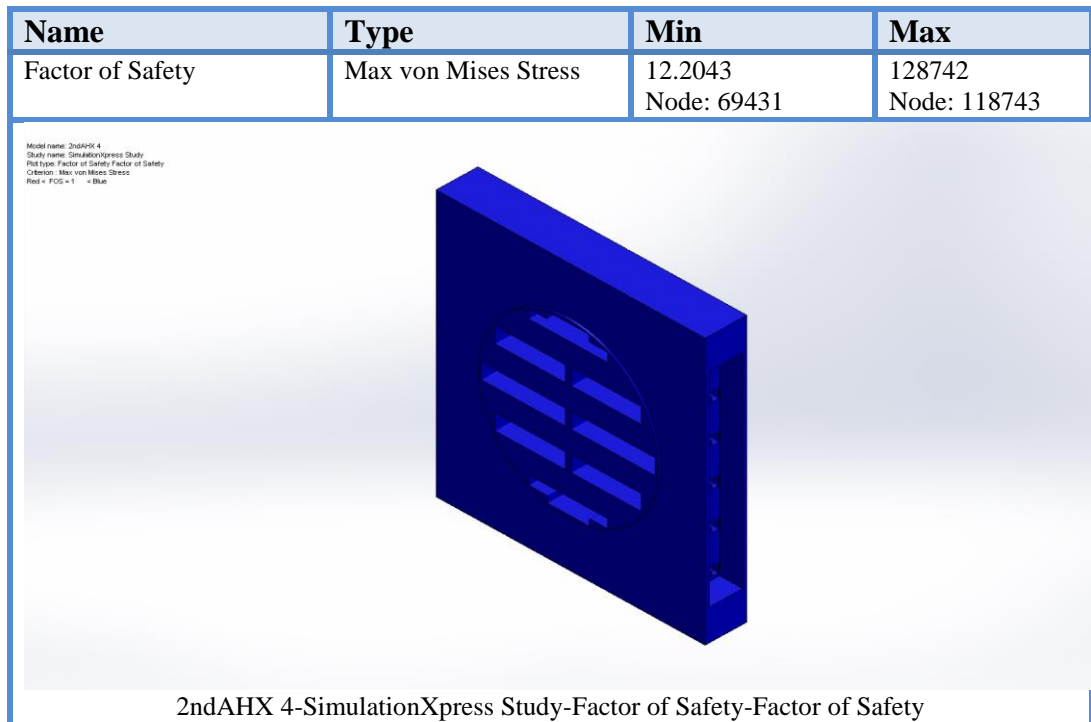


**Figure A3-10:** Simulation of factor of safety of the secondary ambient heat exchanger, done by the SolidWorks

## Appendix 4

In this appendix, performance drawings is presented of the experimental tests. These test, as explained in chapter four, for the rig before the optimization.

- Figures A4.1-A4.9, shows the performance graphs at different mean pressures for various load resistances, at 1600 W heating power.
- Figures A4.10-A4.18, shows the performance graphs at different mean pressures for various load resistances, at 1400 W heating power.
- Figures A4.19-A4.27, shows the performance graphs at different heating powers for various load resistances, at 26 bar mean pressure.
- Figures A4.28-A4.36, shows the performance graphs at different heating powers for various load resistances, at 24 bar mean pressure.
- Figures A4.37-A4.45, shows the performance graphs at different heating powers for various load resistances, at 22 bar mean pressure.
- Figures A4.46-A4.54, shows the performance graphs at different heating powers for various load resistances, at 20 bar mean pressure.
- Figures A4.55-A4.63, shows the performance graphs at different heating powers for various load resistances, at 18 bar mean pressure.
- Figures A4.64-A4.72, shows the performance graphs at different heating powers for various load resistances, at 16 bar mean pressure.
- Figures A4.73-A4.81, shows the performance graphs at different heating powers for various load resistances, at 14 bar mean pressure.
- Figure A4.82 is the measured drive ratio versus heating power for various load resistances at 28 bar mean pressure

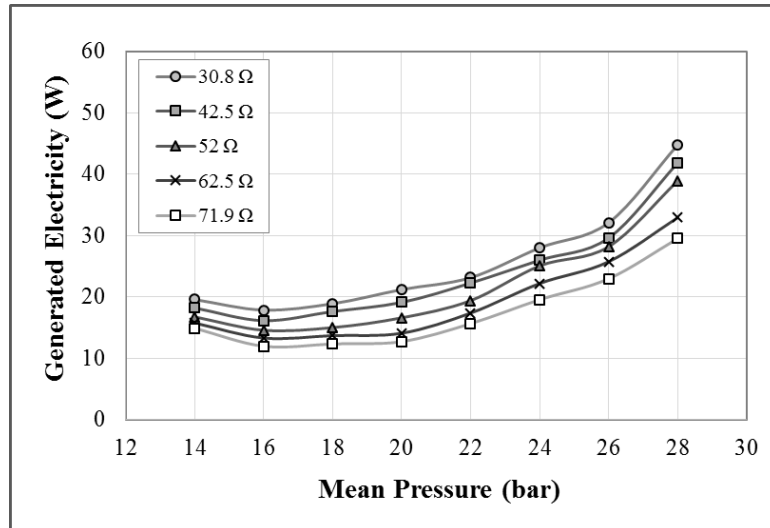


**Figure A4-1:** The performance of the engine versus mean pressure for various load resistances at 1600 W heating power

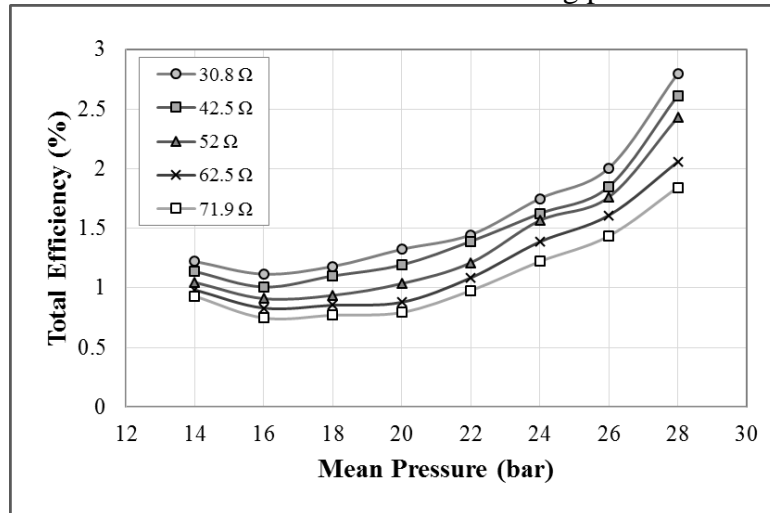


**Figure A4-2:** Total efficiency for different load resistances at 28 bar mean pressure and 1600 W heating power

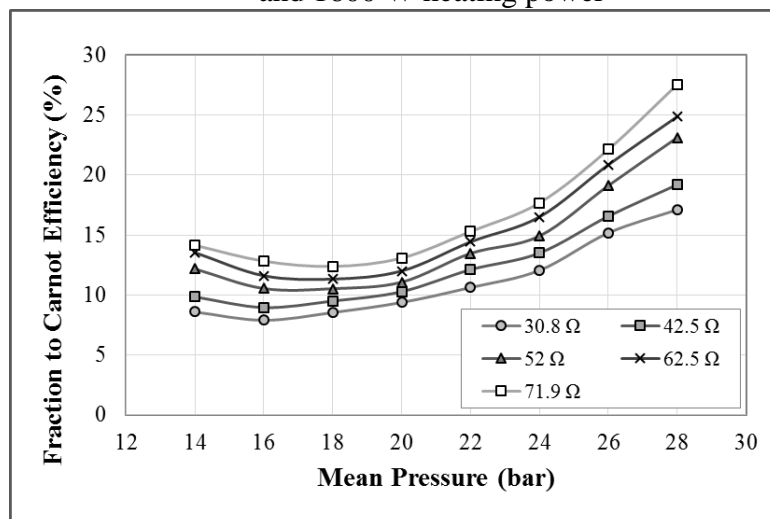


**Figure A4-3:** Fraction to Carnot efficiency versus mean pressure for various load resistances at 1600 W heating power

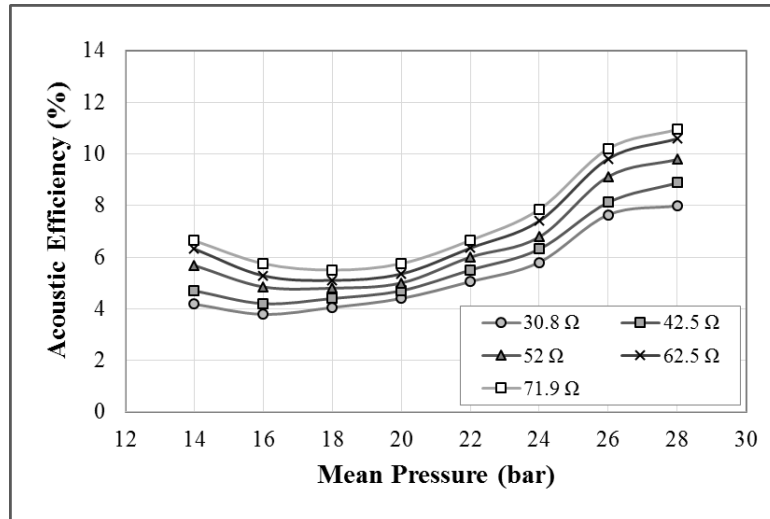


**Figure A4-4:** The relation between mean pressure and acoustic efficiency for various load resistances at 1600 W heating power

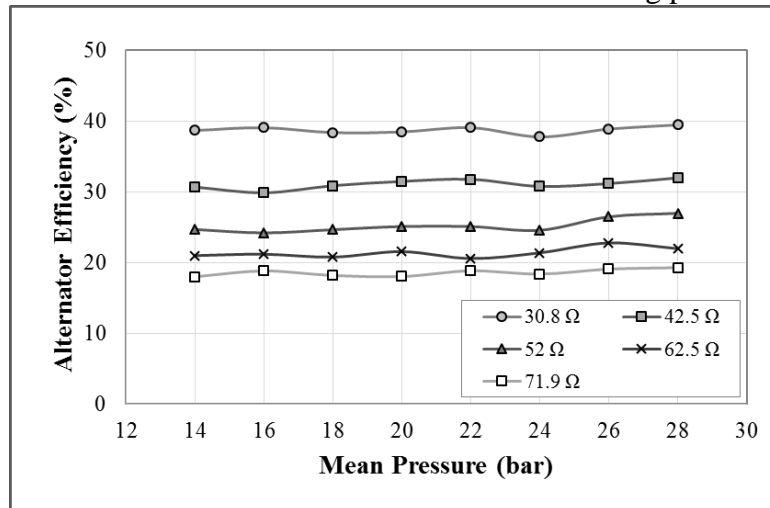


**Figure A4-5:** The effect of mean pressure on the linear alternator efficiency for various load resistance at 1600 W heating power

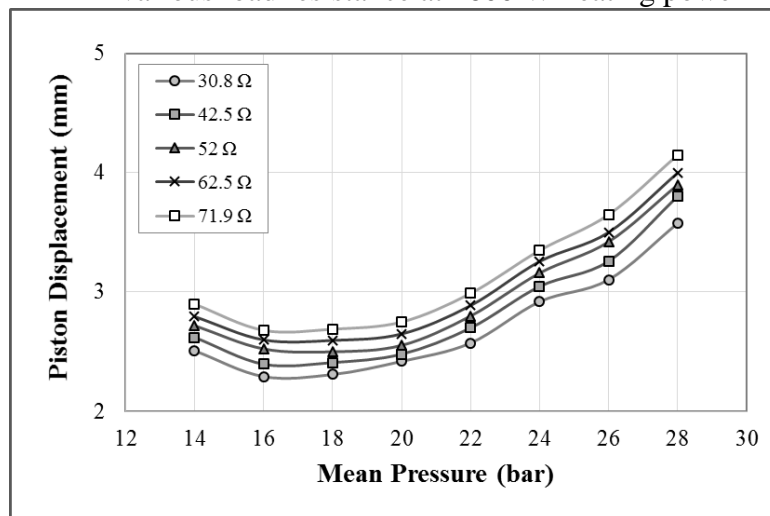


**Figure A4-6:** The effect of mean pressure on the piston displacement for various load resistances at 1600 W heating power

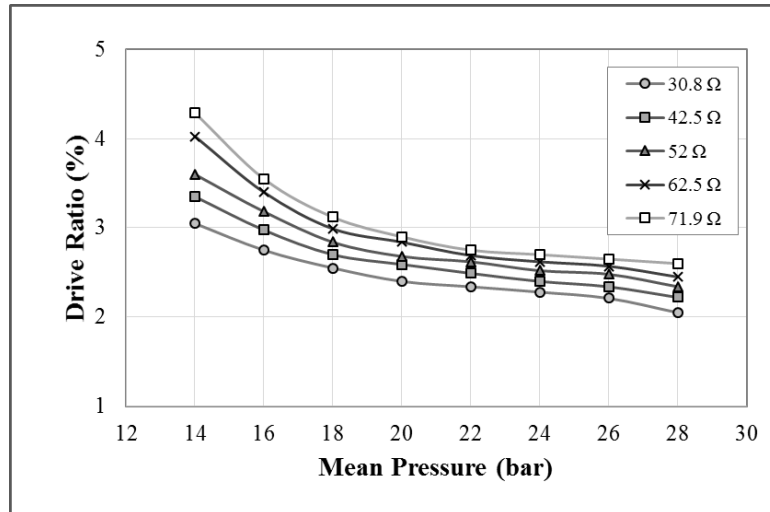


**Figure A4-7:** Measured drive ratio versus mean pressure for various load resistances at 1600 W heating power

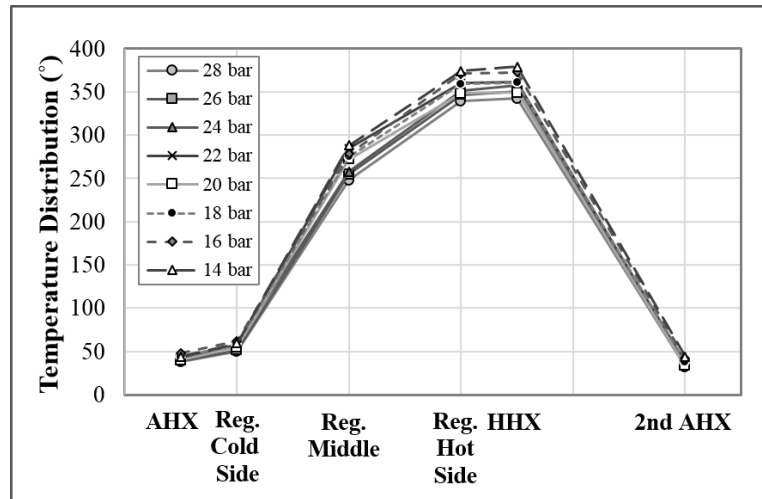


**Figure A4-8:** Core temperature distribution of different mean pressure at 1600 W heating power and 30.8 Ω load resistance

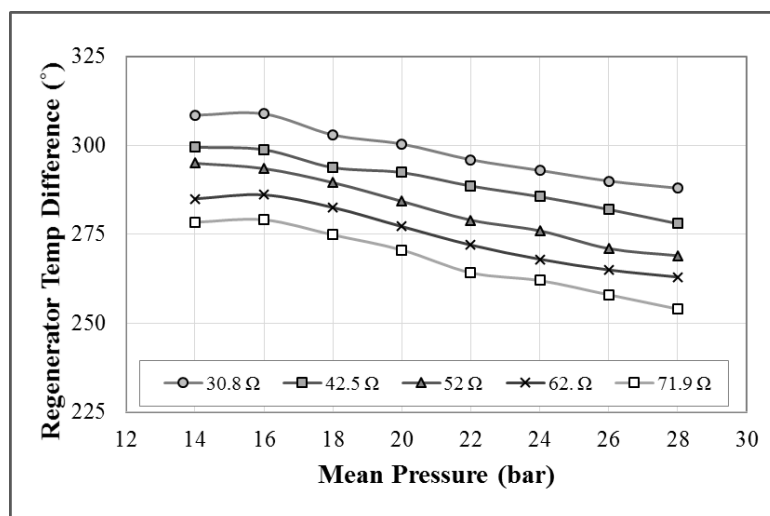


**Figure A4-9:** The effect of mean pressure on the regenerator temperature difference for various load resistances at 1600 W heating power

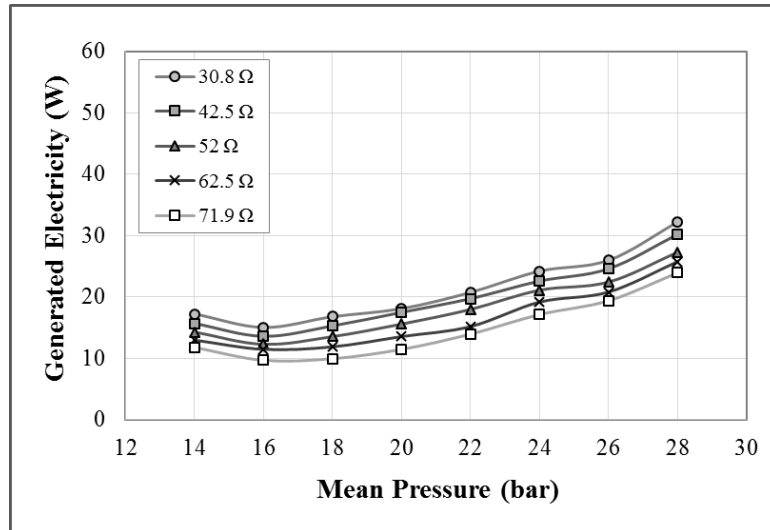


**Figure A4-10:** The performance of the engine versus mean pressure for various load resistances at 1400 W heating power

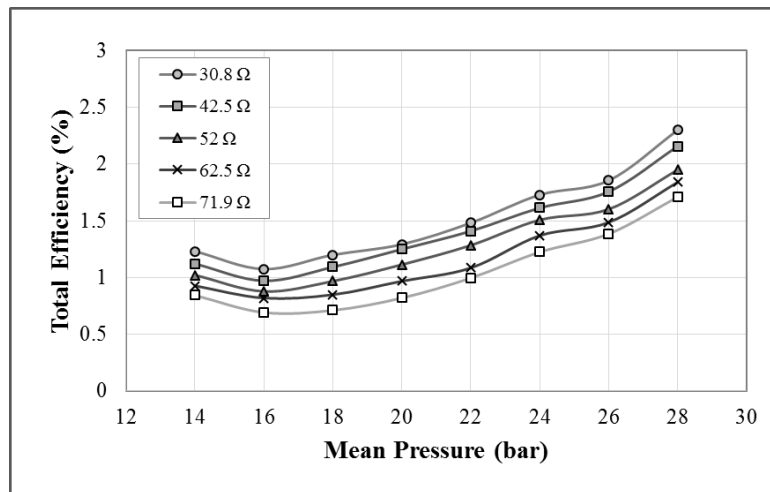


**Figure A4-11:** Total efficiency for different load resistances at 28 bar mean pressure and 1400 W heating power

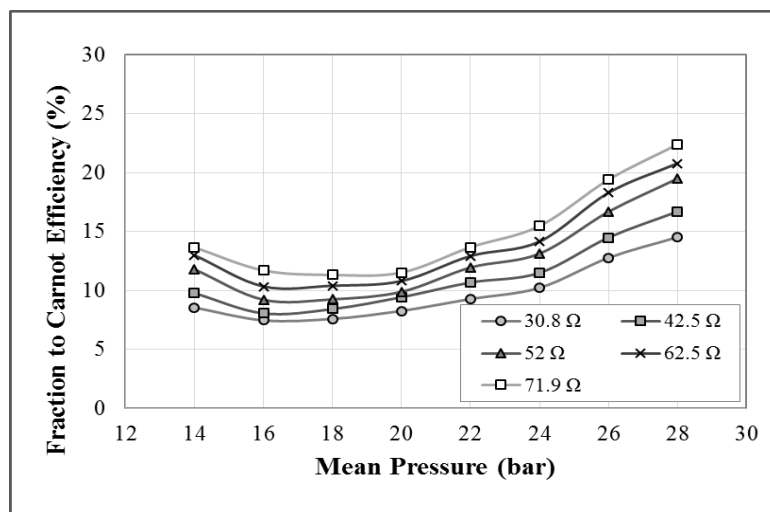


**Figure A4-12:** Fraction to Carnot efficiency versus mean pressure for various load resistances at 1400 W heating power

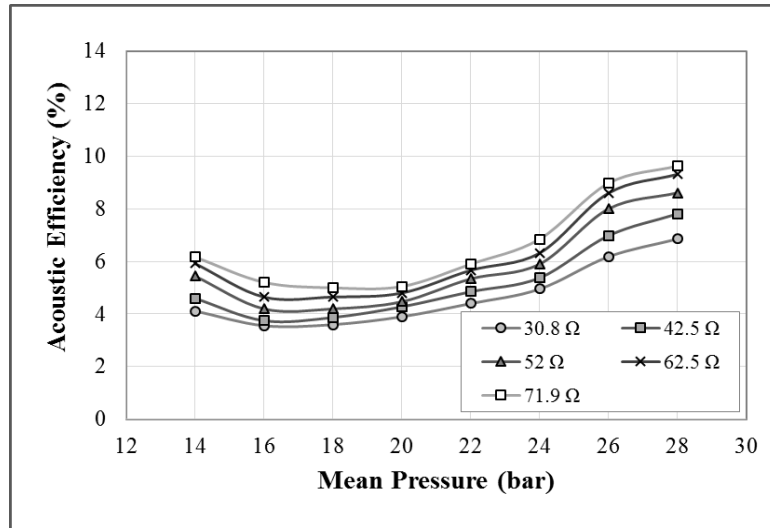


**Figure A4-13:** The relation between mean pressure and acoustic efficiency for various load resistances at 1400 W heating power

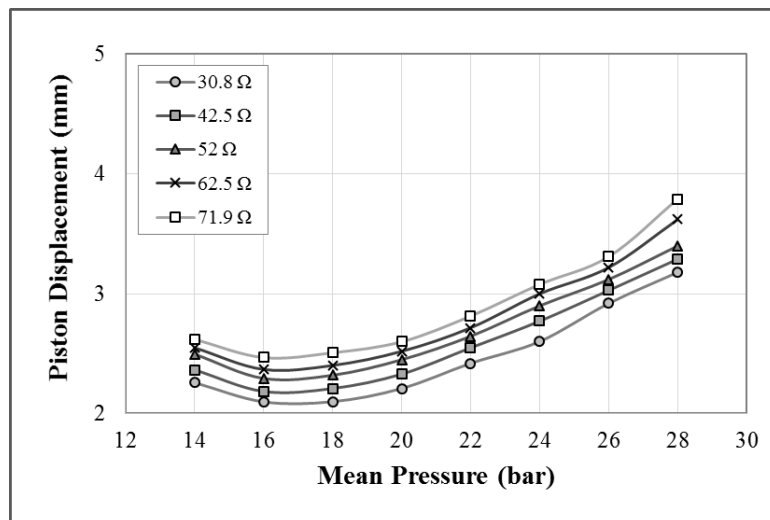


**Figure A4-14:** The effect of mean pressure on the piston displacement for various load resistances at 1400 W heating power

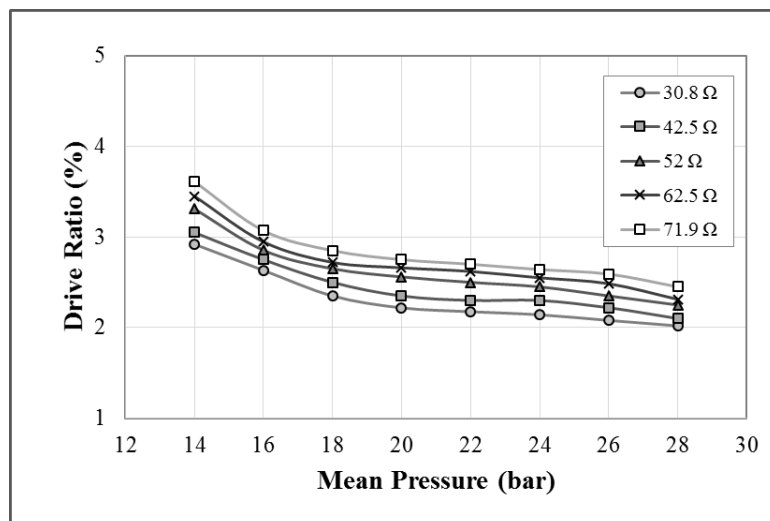


**Figure A4-15:** Measured drive ratio versus mean pressure for various load resistances at 1400 W heating power

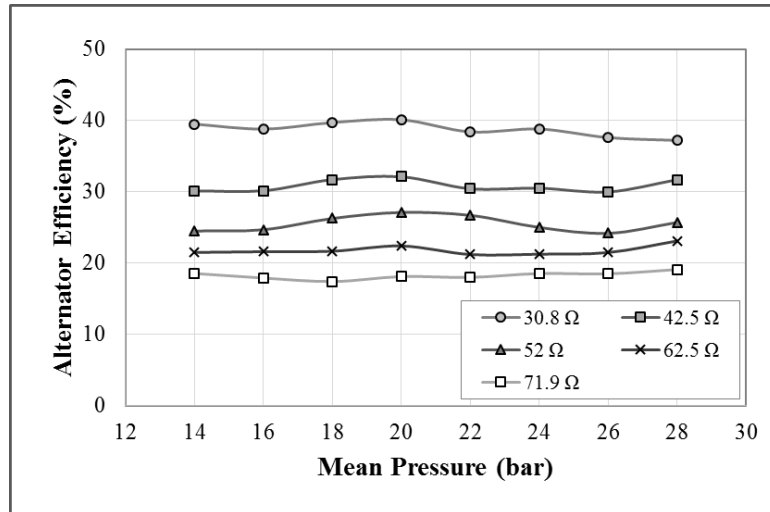


**Figure A4-16:** The effect of mean pressure on the linear alternator efficiency for various load resistance at 1400 W heating power

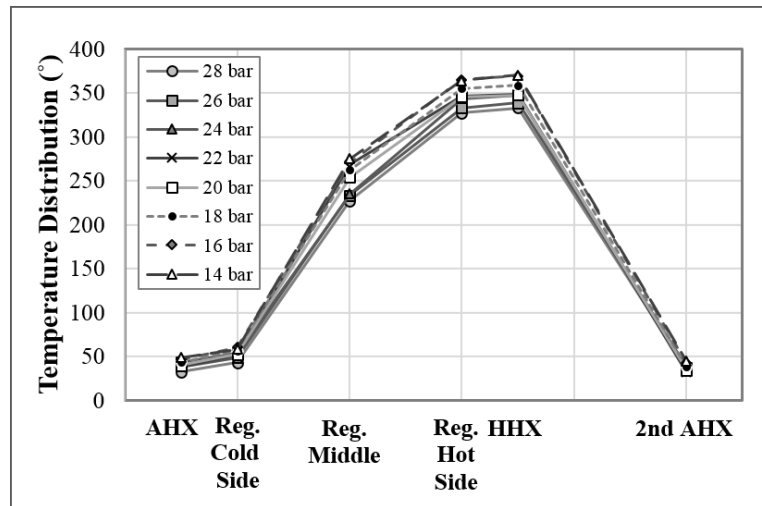


**Figure A4-17:** Core temperature distribution of different mean pressure at 1400 W heating power and 30.8 Ω load resistances

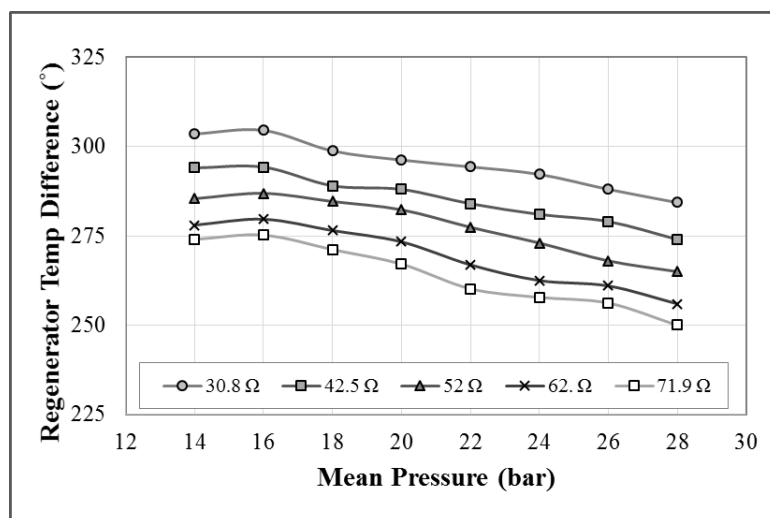


**Figure A4-18:** The effect of mean pressure on the regenerator temperature difference for various load resistance at 1400 W heating power

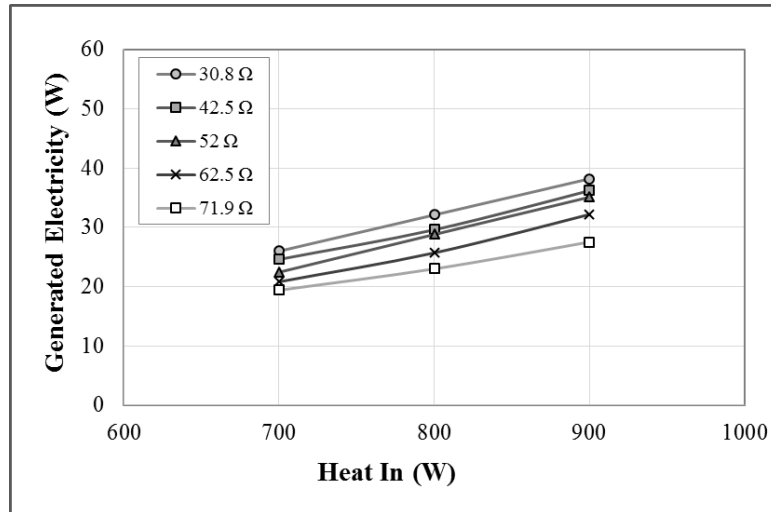


**Figure A4-19:** The performance of the engine as a function of heating power for various load resistances at 26 bar mean pressure

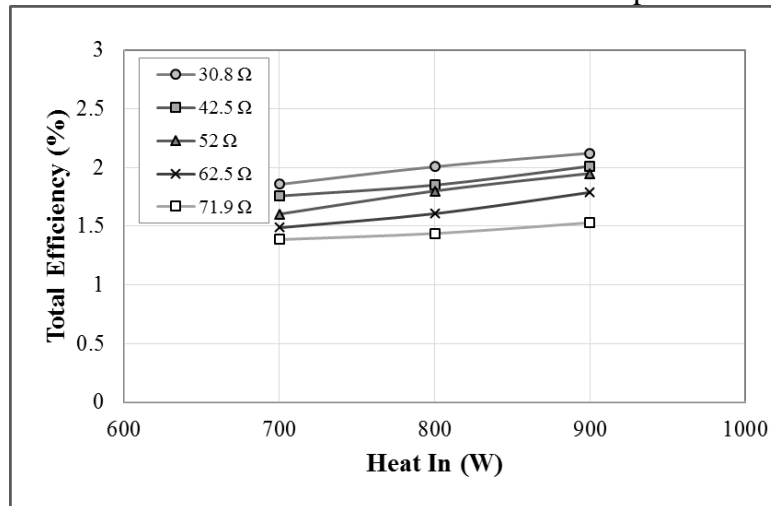


**Figure A4-20:** Total efficiency of different heating power for various load resistances at 26 bar mean pressure

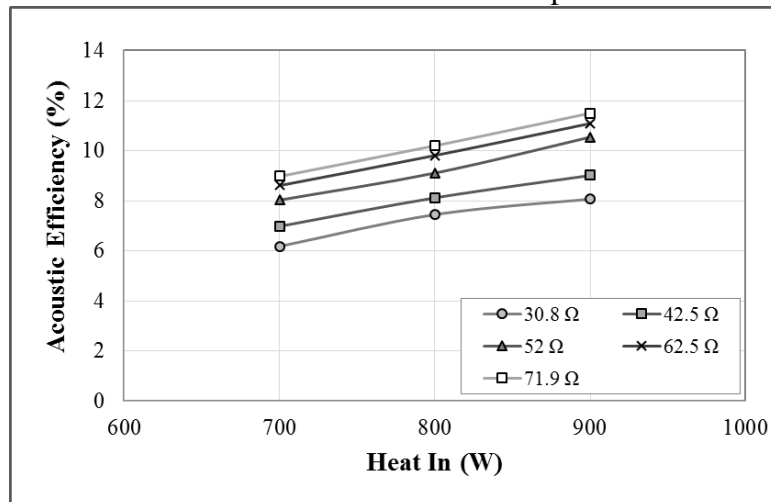


**Figure A4-21:** The relation between heating power and acoustic efficiency for various load resistances at 26 bar mean pressure

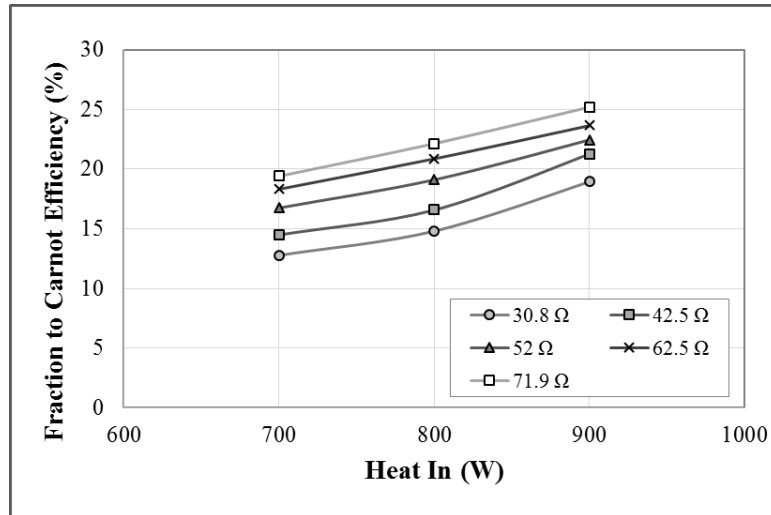


**Figure A4-22:** Fraction to Carnot efficiency versus heating powers for various load resistances at 26 bar mean pressure

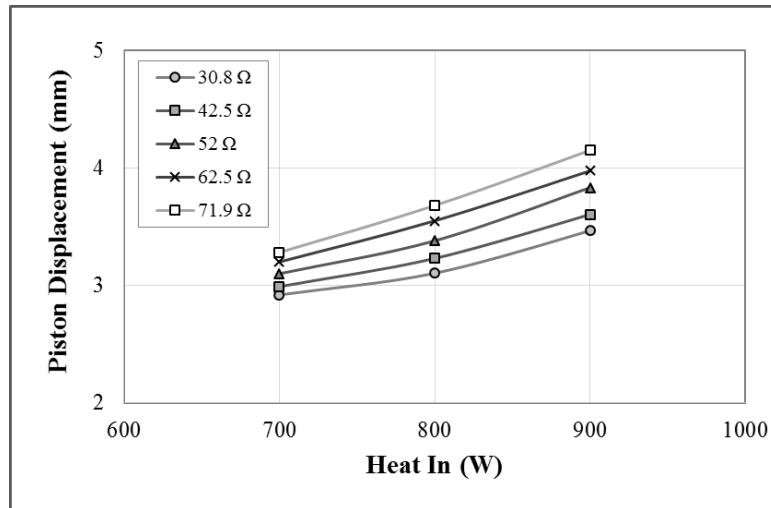


**Figure A4-23:** The effect of heating power on the alternator piston displacement for various load resistances at 26 bar mean pressure

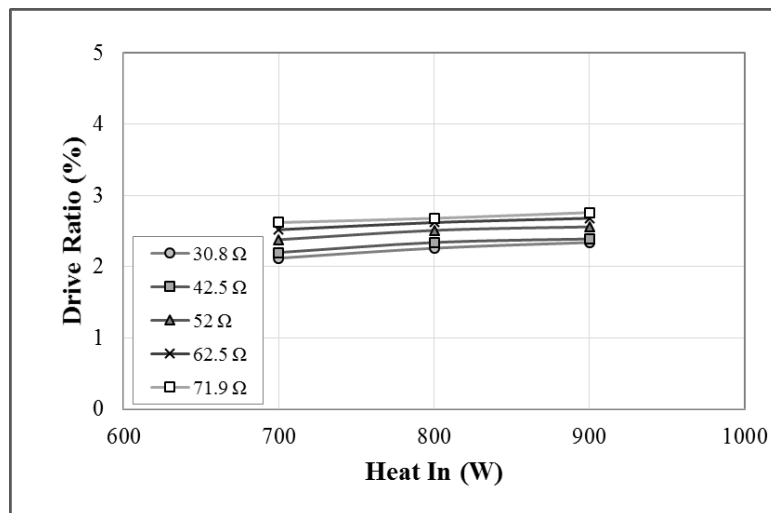


**Figure A4-24:** Measured drive ratio versus heating power for various load resistances at 26 bar mean pressure

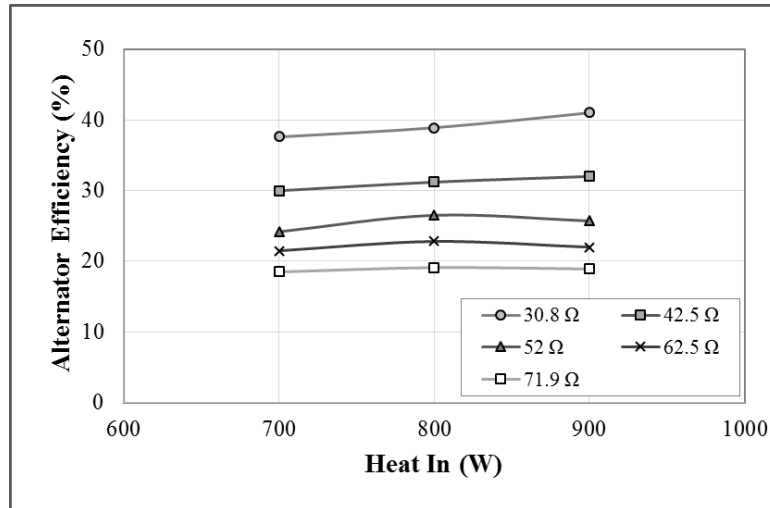


**Figure A4-25:** The effect of heating power on the alternator efficiency for various load resistances at 26 bar mean pressure

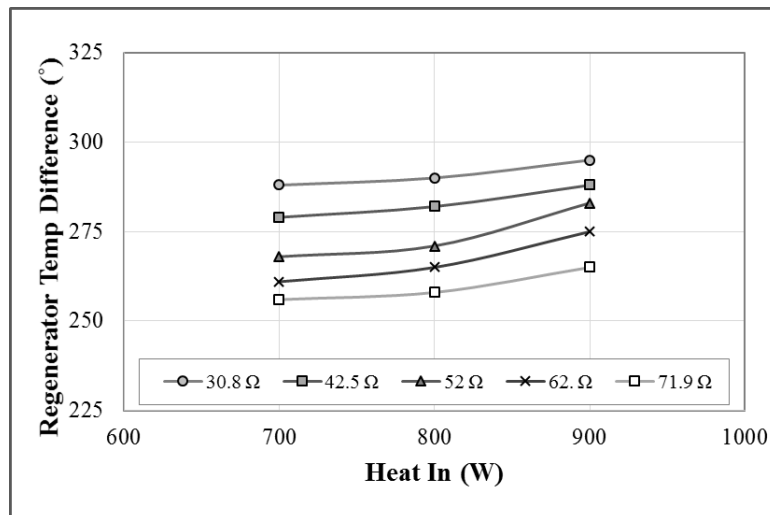


**Figure A4-26:** The effect of heating power on the temperature difference across the regenerator for various load resistances at 26 bar mean pressure

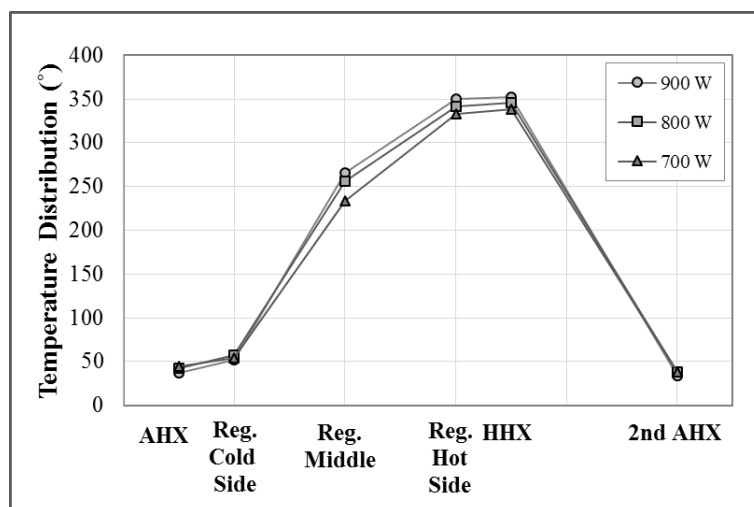


**Figure A4-27:** Core temperature distribution of different heating powers at 26 bar mean pressure

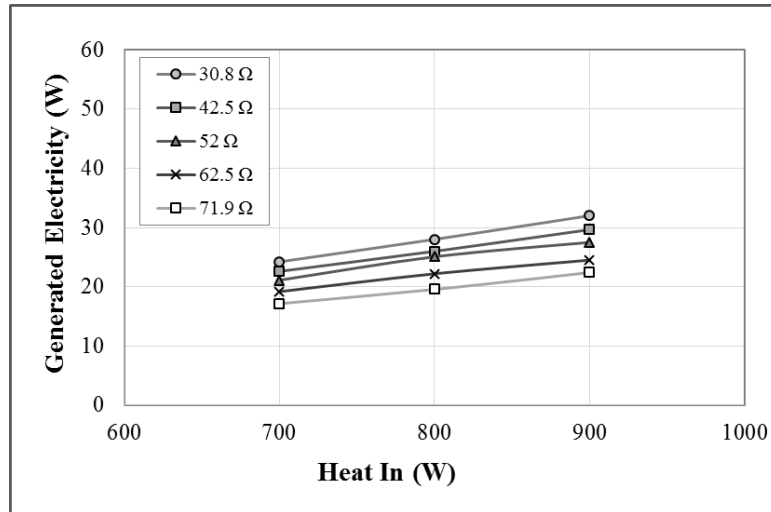


**Figure A4-28:** The performance of the engine as a function of heating power for various load resistances at 24 bar mean pressure

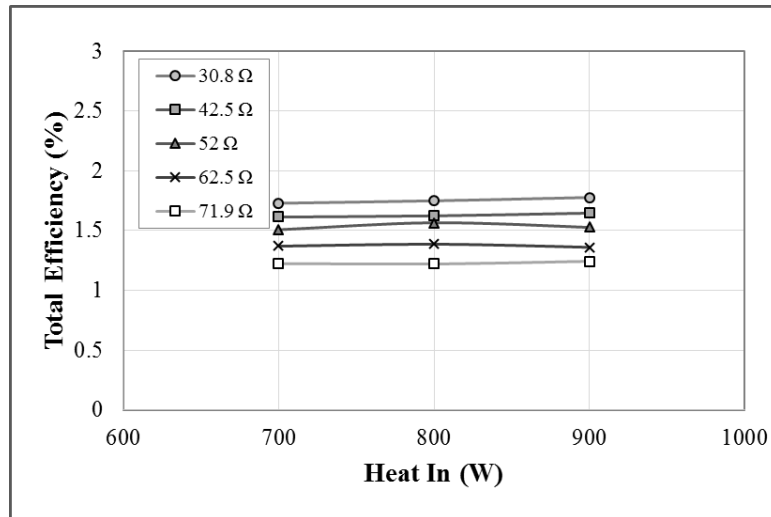


**Figure A4-29:** Total efficiency of different heating power for various load resistances at 24 bar mean pressure

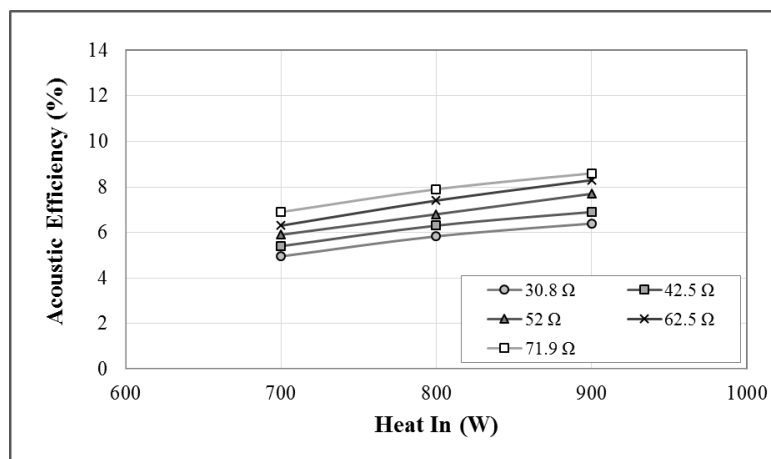


**Figure A4-30:** The relation between heating power and acoustic efficiency for various load resistances at 24 bar mean pressure

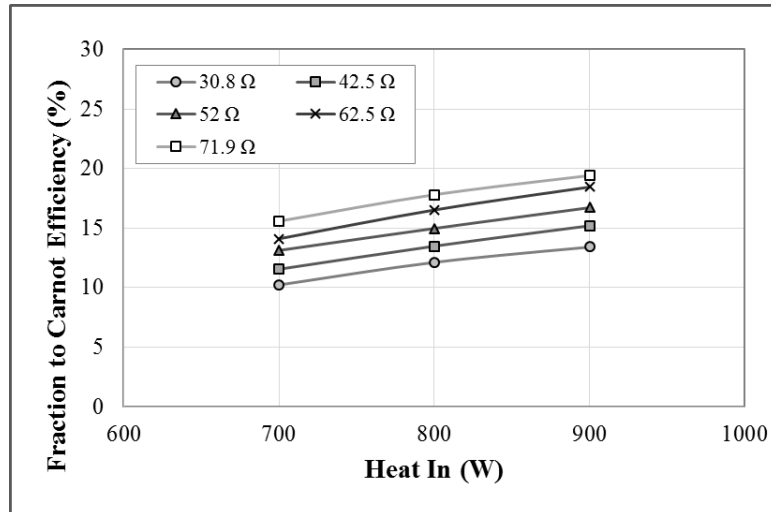


**Figure A4-31:** Fraction to Carnot efficiency versus heating powers for various load resistances at 24 bar mean pressure

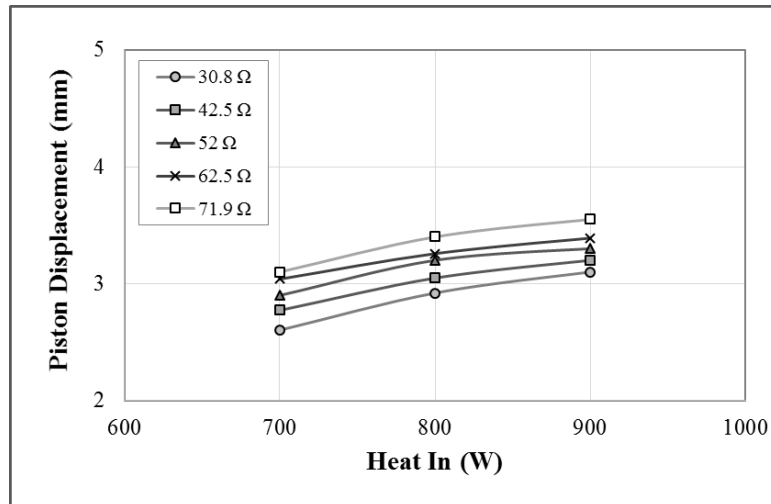


**Figure A4-32:** The effect of heating power on the alternator piston displacement for various load resistances at 24 bar mean pressure

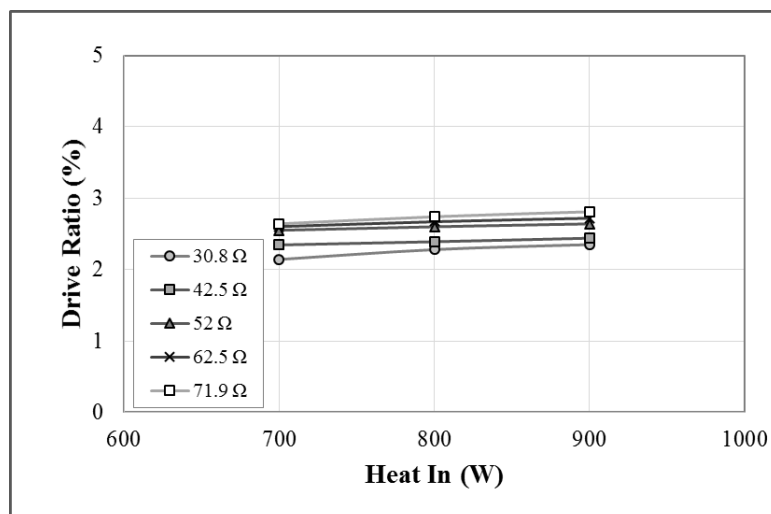


**Figure A4-33:** Measured drive ratio versus heating power for various load resistances at 24 bar mean pressure

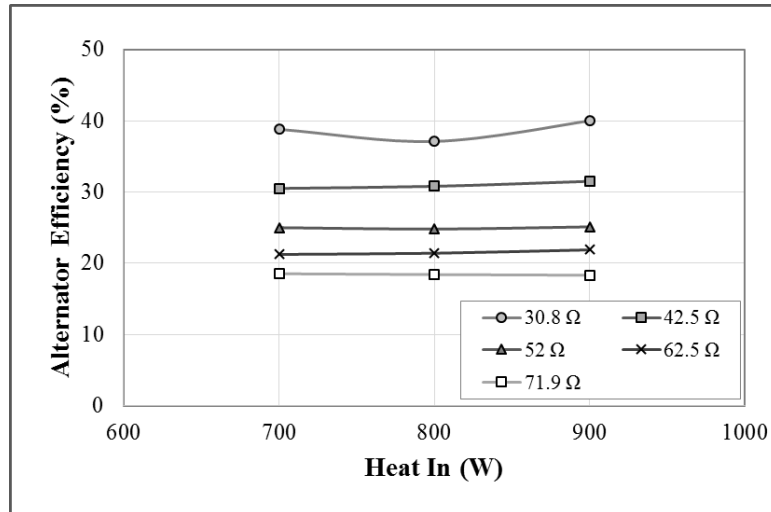


**Figure A4-34:** The effect of heating power on the alternator efficiency for various load resistances at 24 bar mean pressure

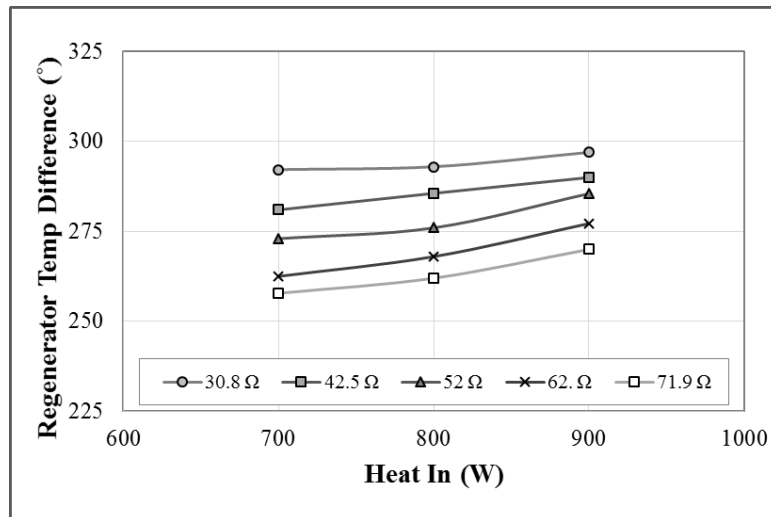


**Figure A4-35:** The effect of heating power on the temperature difference across the regenerator for various load resistances at 24 bar mean pressure

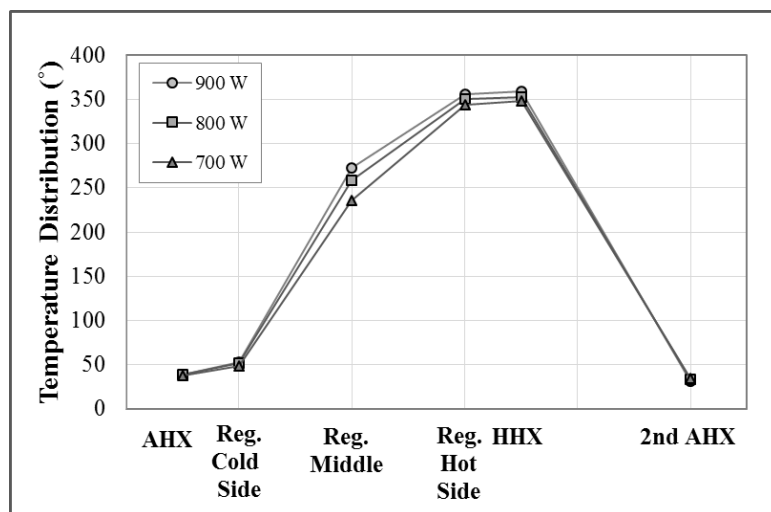


**Figure A4-36:** Core temperature distribution of different heating powers at 24 bar mean pressure

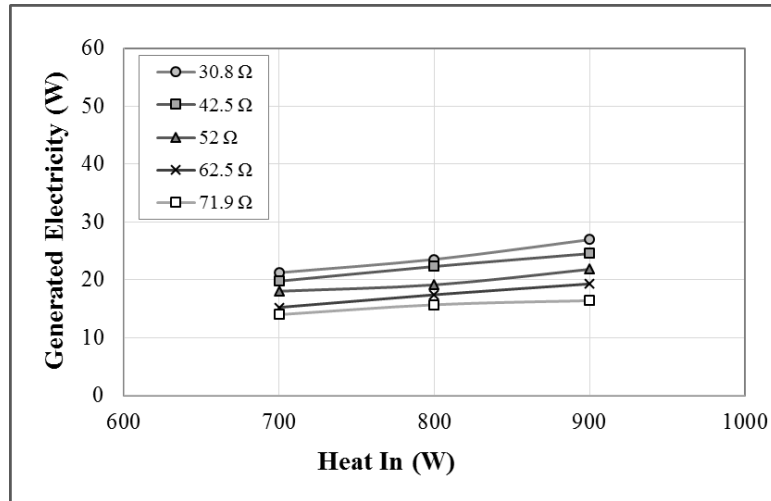


**Figure A4-37:** The performance of the engine as a function of heating power for various load resistances at 22 bar mean pressure

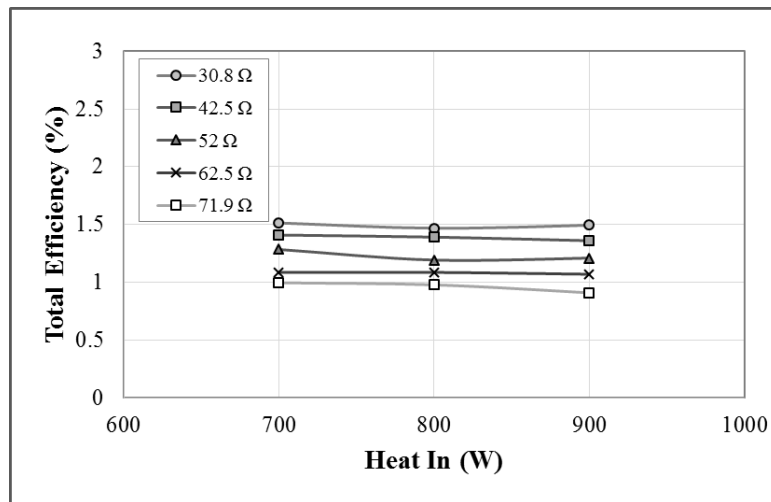


**Figure A4-38** Total efficiency of different heating power for various load resistances at 22 bar mean pressure

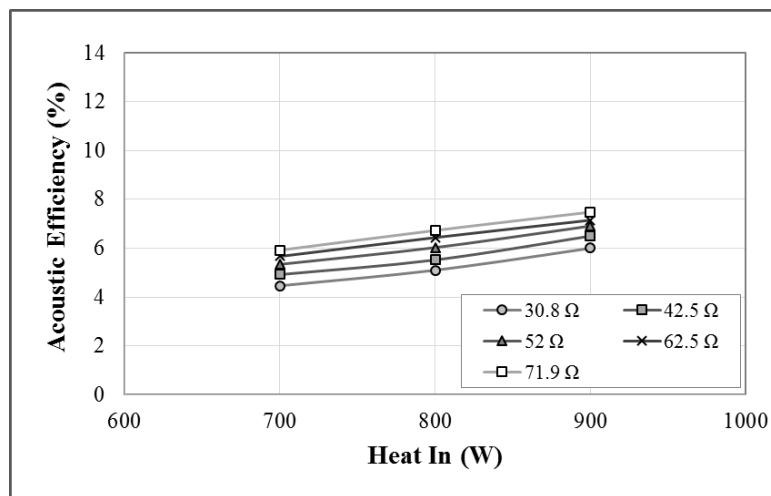


**Figure A4-39:** The relation between heating power and acoustic efficiency for various load resistances at 22 bar mean pressure

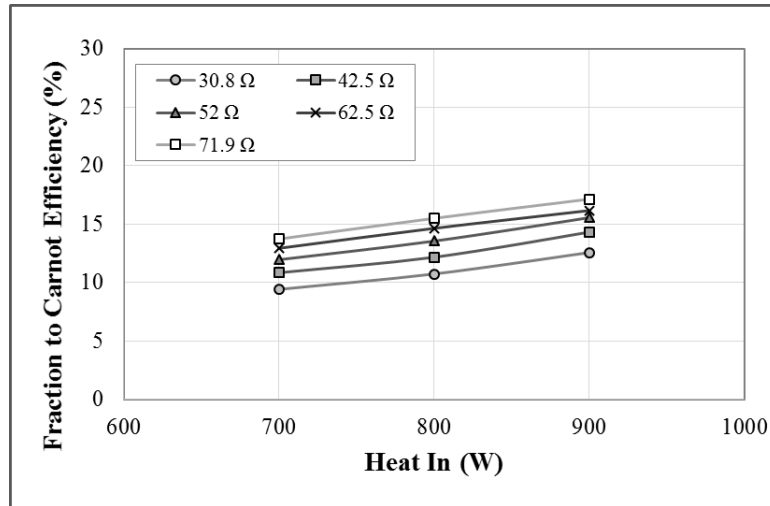


**Figure A4-40:** Fraction to Carnot efficiency versus heating powers for various load resistances at 22 bar mean pressure

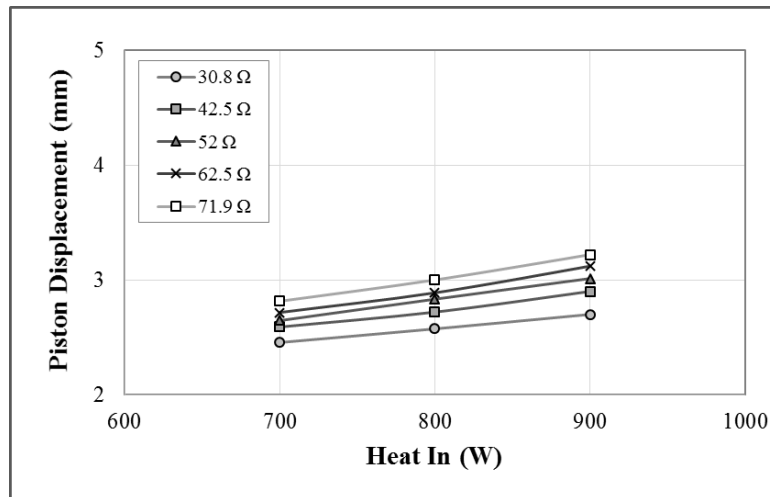


**Figure A4-41:** The effect of heating power on the alternator piston displacement for various load resistances at 22 bar mean pressure

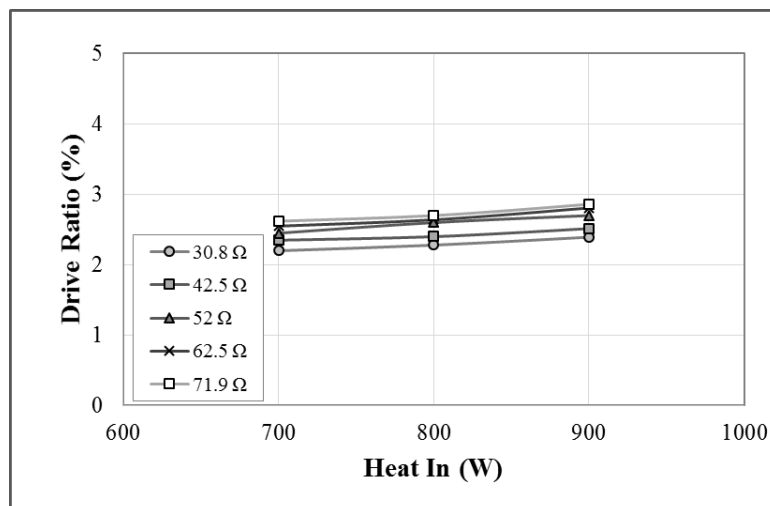


**Figure A4-42:** Measured drive ratio versus heating power for various load resistances at 22 bar mean pressure

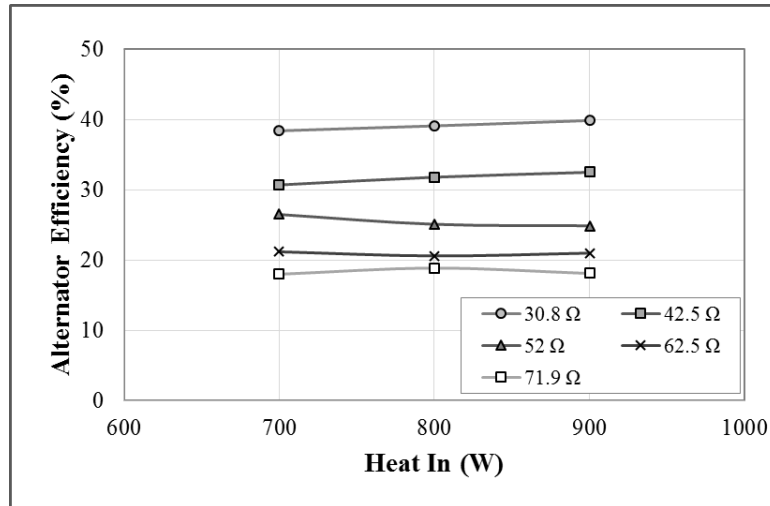


**Figure A4-43:** The effect of heating power on the alternator efficiency for various load resistances at 22 bar mean pressure

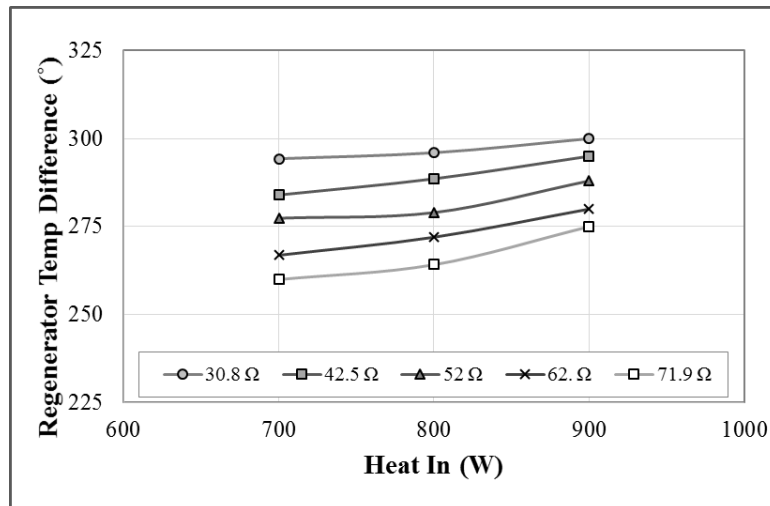


**Figure A4-44:** The effect of heating power on the temperature difference across the regenerator for various load resistances at 22 bar mean pressure

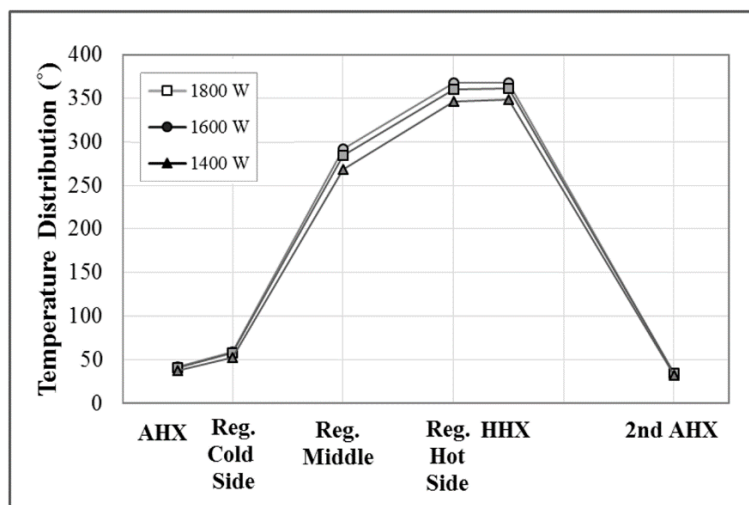


**Figure A4-45:** Core temperature distribution of different heating powers at 22 bar mean pressure

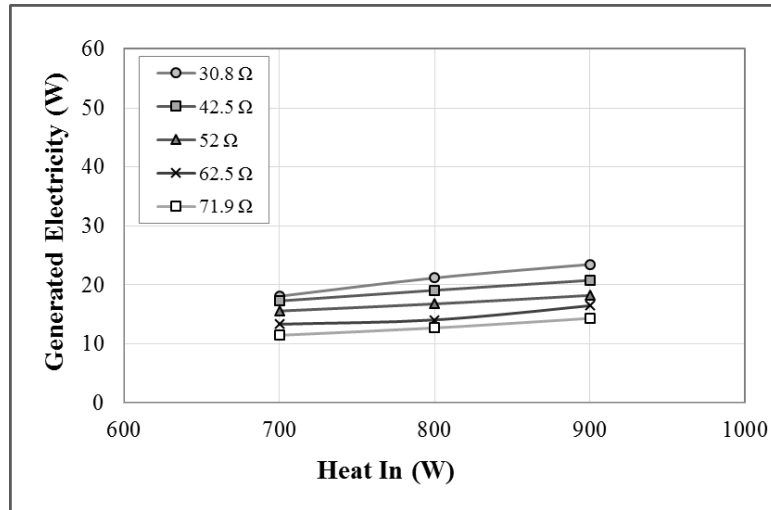


**Figure A4-46:** The performance of the engine as a function of heating power for various load resistances at 20 bar mean pressure

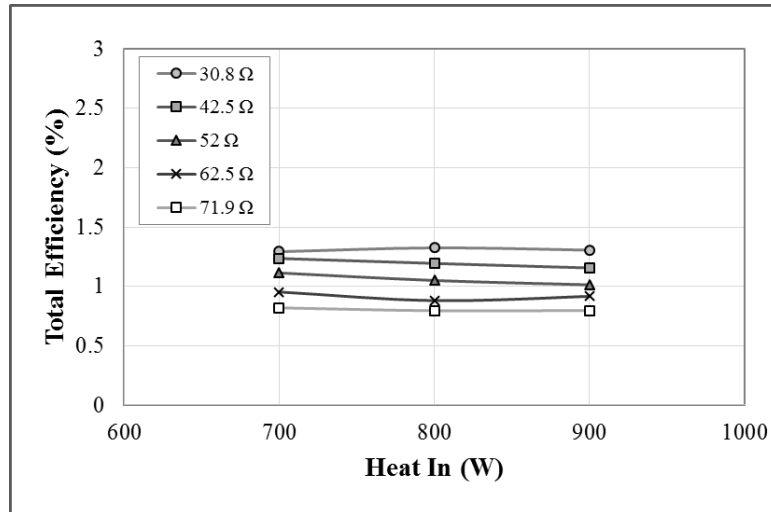


**Figure A4-47:** Total efficiency of different heating power for various load resistances at 20 bar mean pressure

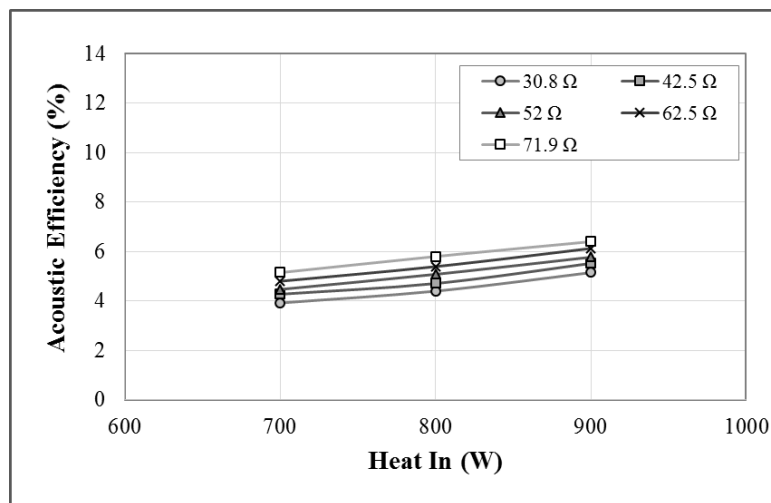


**Figure A4-48:** The relation between heating power and acoustic efficiency for various load resistances at 20 bar mean pressure

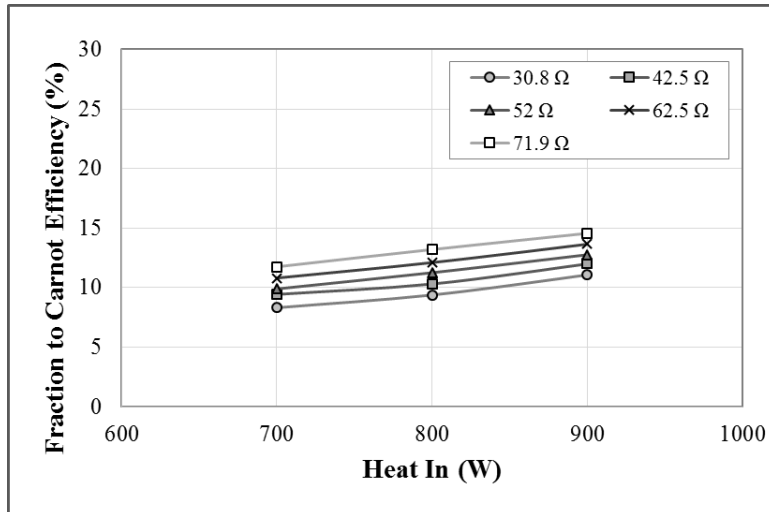


**Figure A4-49:** Fraction to Carnot efficiency versus heating powers for various load resistances at 20 bar mean pressure

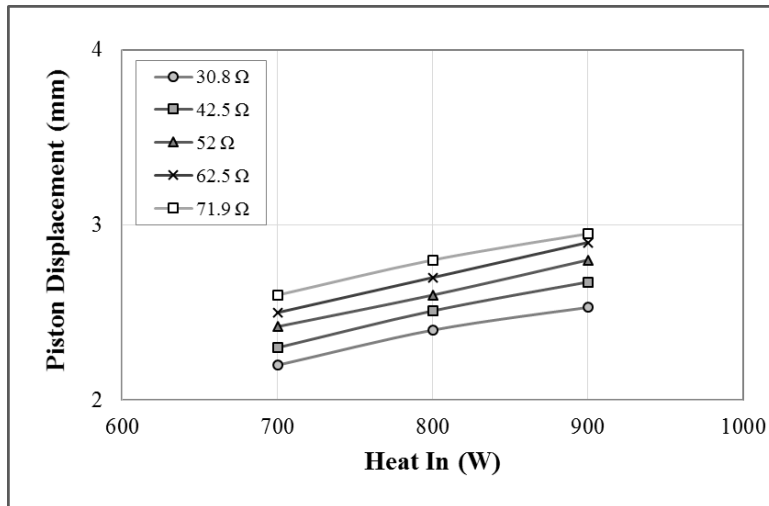


**Figure A4-50:** The effect of heating power on the alternator piston displacement for various load resistances at 20 bar mean pressure

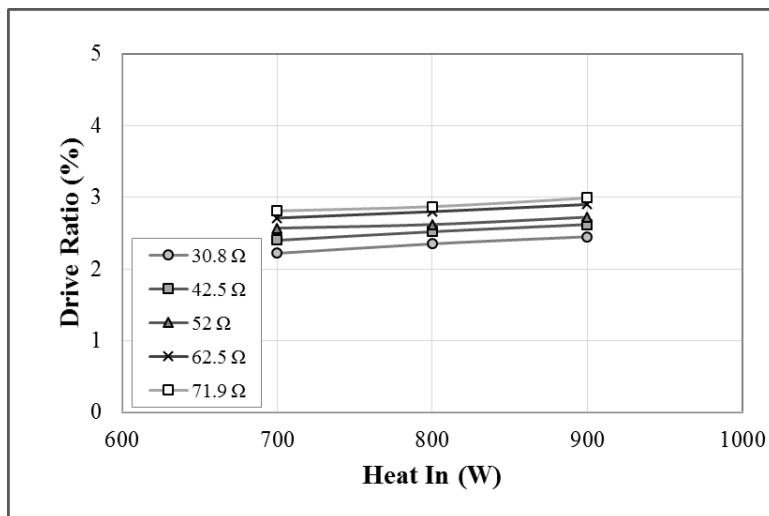


**Figure A4-51:** Measured drive ratio versus heating power for various load resistances at 20 bar mean pressure

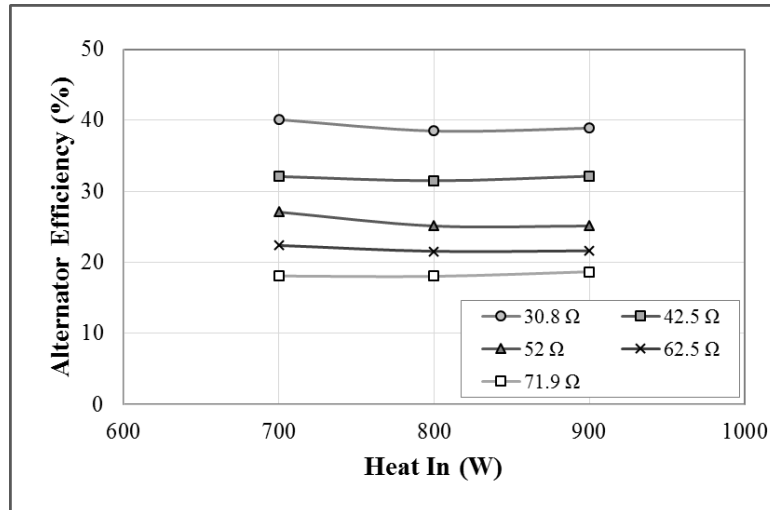


**Figure A4-52:** The effect of heating power on the alternator efficiency for various load resistances at 20 bar mean pressure

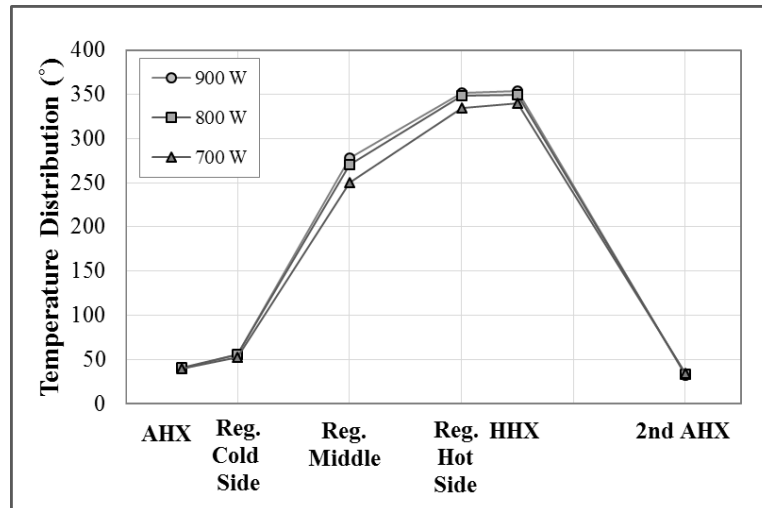


**Figure A4-53:** Core temperature distribution of different heating powers at 20 bar mean pressure

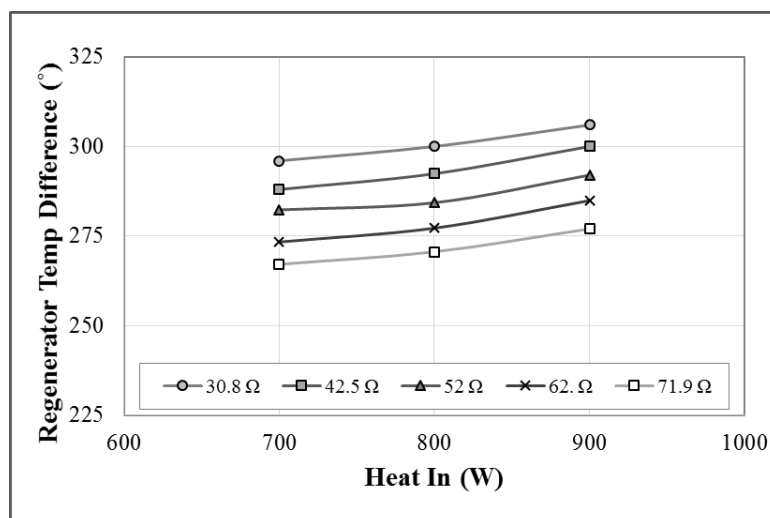


**Figure A4-54:** The effect of heating power on the temperature difference across the regenerator for various load resistances at 20 bar mean pressure

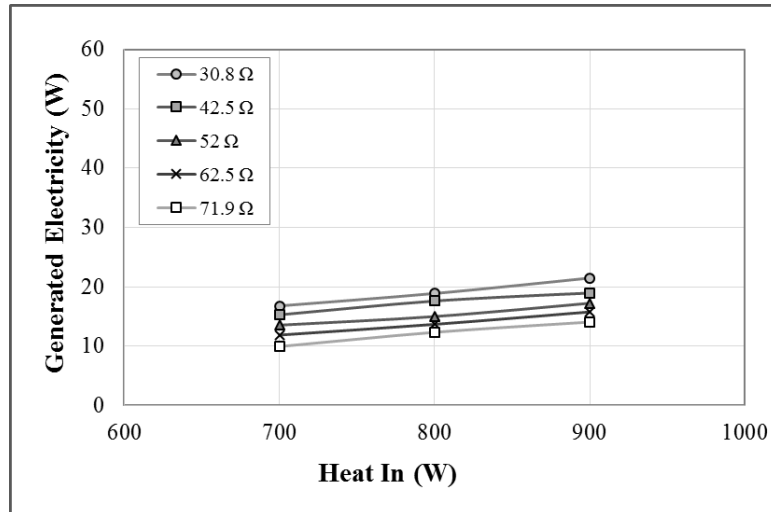


**Figure A4-55:** The performance of the engine as a function of heating power for various load resistances at 18 bar mean pressure

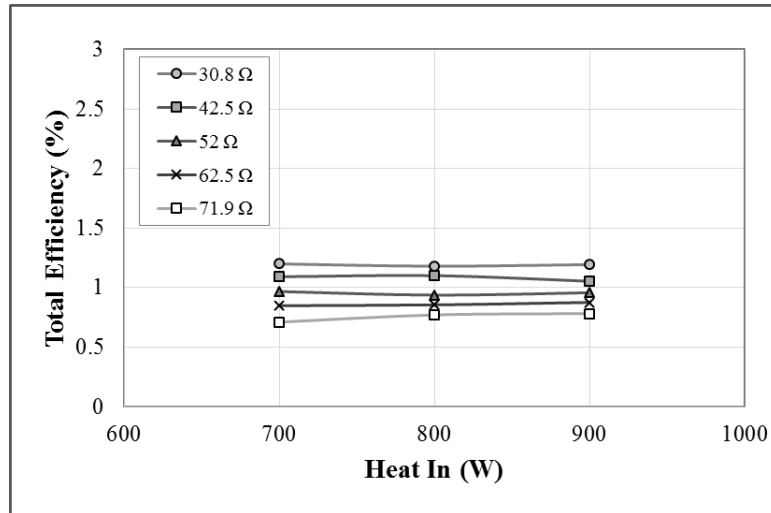


**Figure A4-56:** Total efficiency of different heating power for various load resistances at 18 bar mean pressure

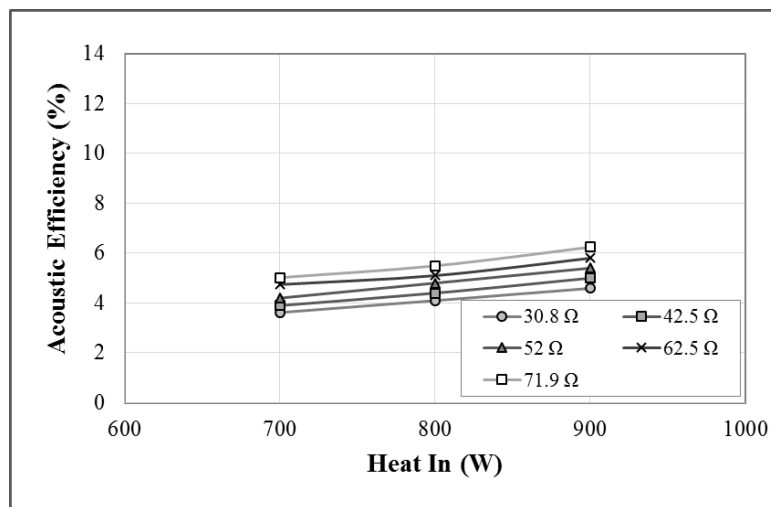


**Figure A4-57:** The relation between heating power and acoustic efficiency for various load resistances at 18 bar mean pressure

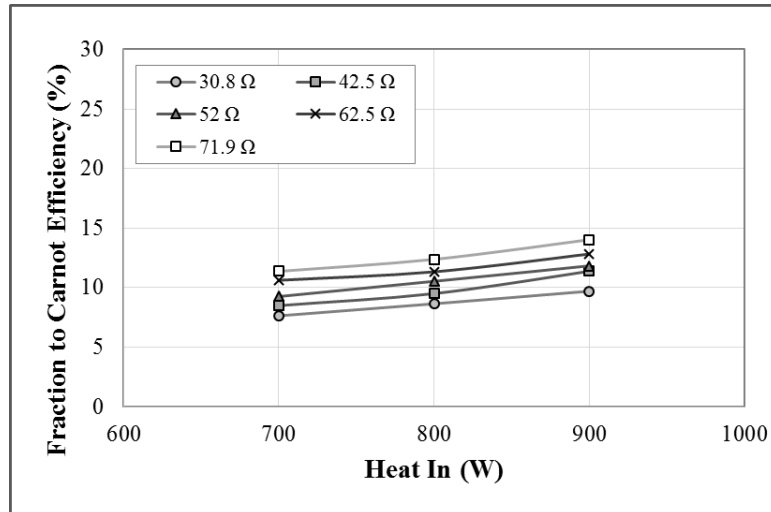


**Figure A4-58:** Fraction to Carnot efficiency versus heating powers for various load resistances at 18 bar mean pressure

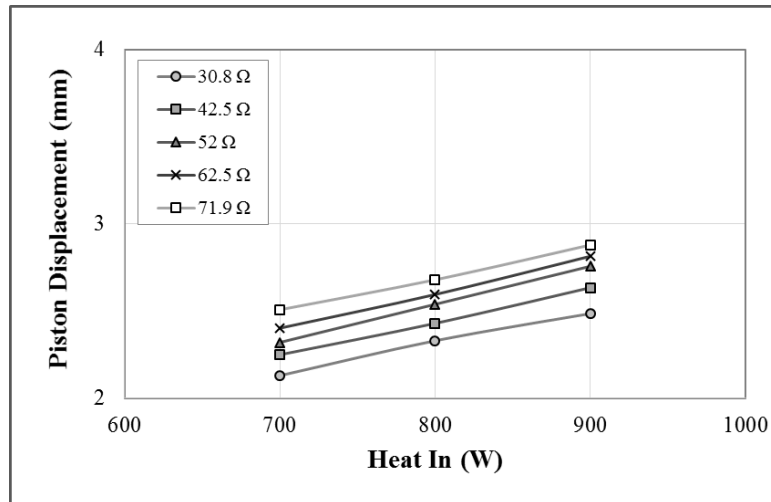


**Figure A4-59:** The effect of heating power on the alternator piston displacement for various load resistances at 18 bar mean pressure

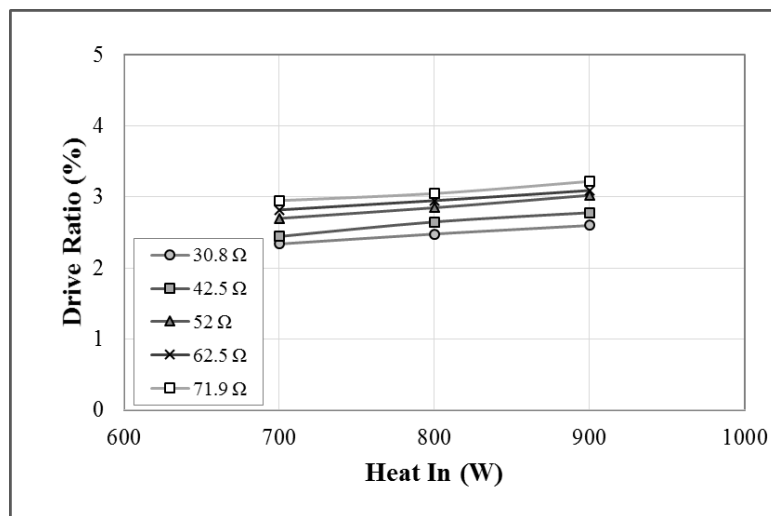


**Figure A4-60:** Measured drive ratio versus heating power for various load resistances at 18 bar mean pressure

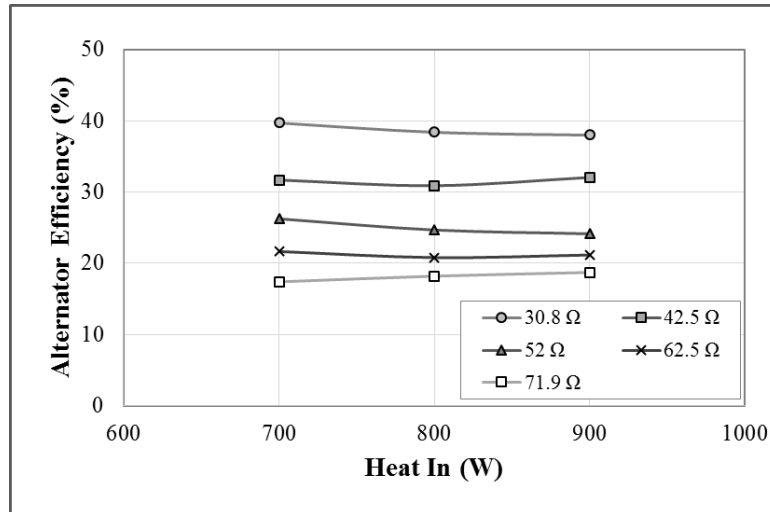


**Figure A4-61:** The effect of heating power on the alternator efficiency for various load resistances at 18 bar pressure

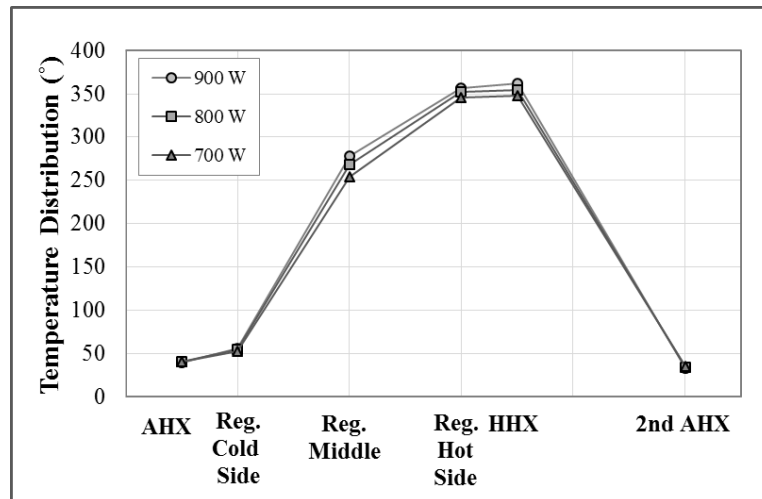


**Figure A4-62:** Core temperature distribution of different heating powers at 18 bar mean pressure

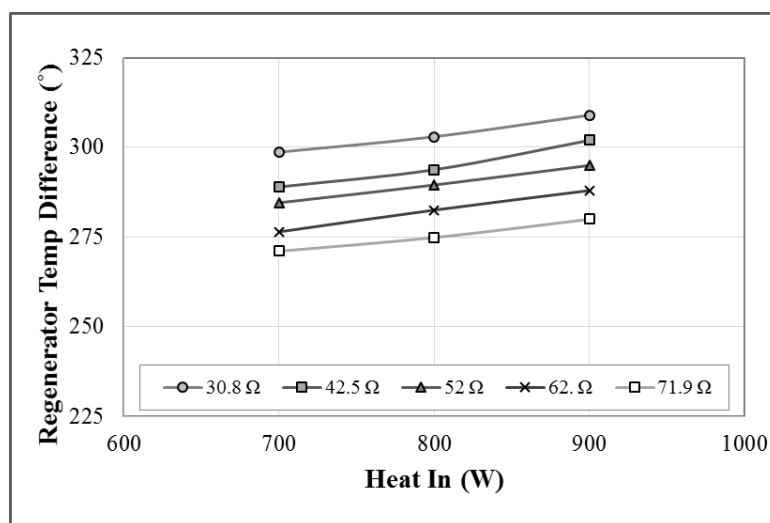


**Figure A4-63:** The effect of heating power on the temperature difference across the regenerator for various load resistances at 18 bar mean pressure

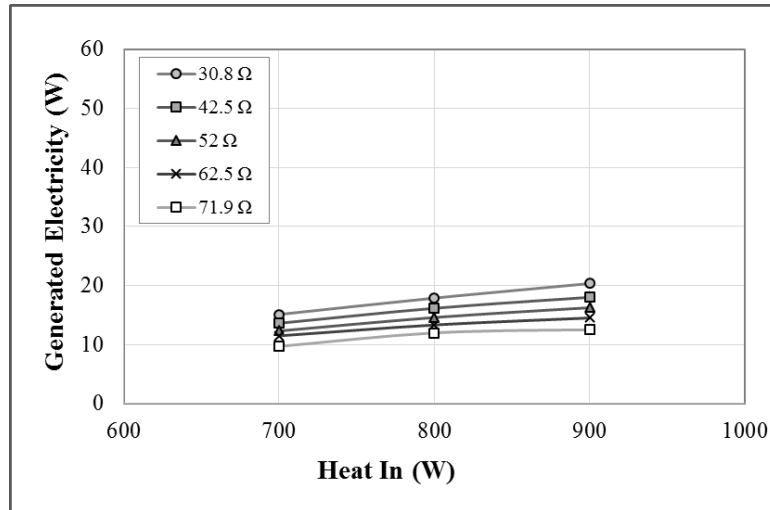


**Figure A4-64:** The performance of the engine as a function of heating power for various load resistances at 16 bar mean pressure

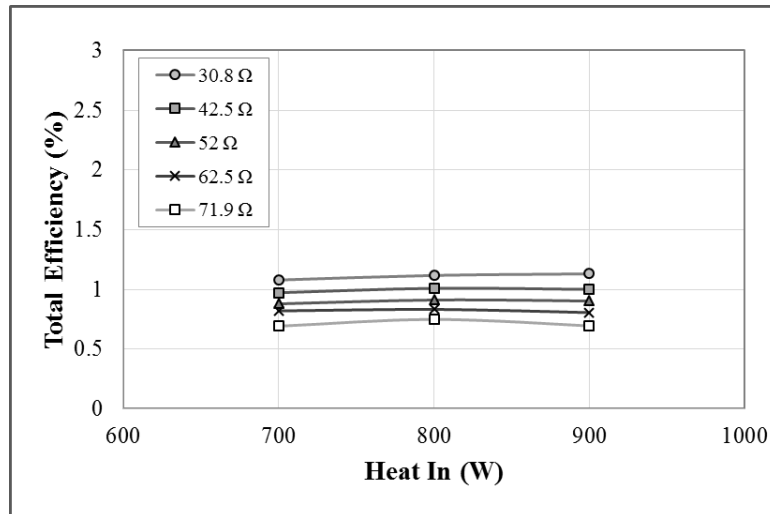


**Figure A4-65:** Total efficiency of different heating power for various load resistances at 16 bar mean pressure

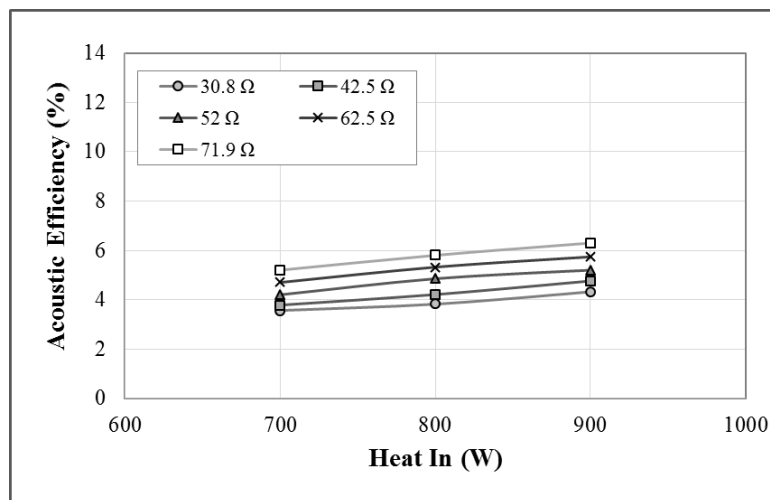


**Figure A4-66:** The relation between heating power and acoustic efficiency for various load resistances at 16 bar mean pressure

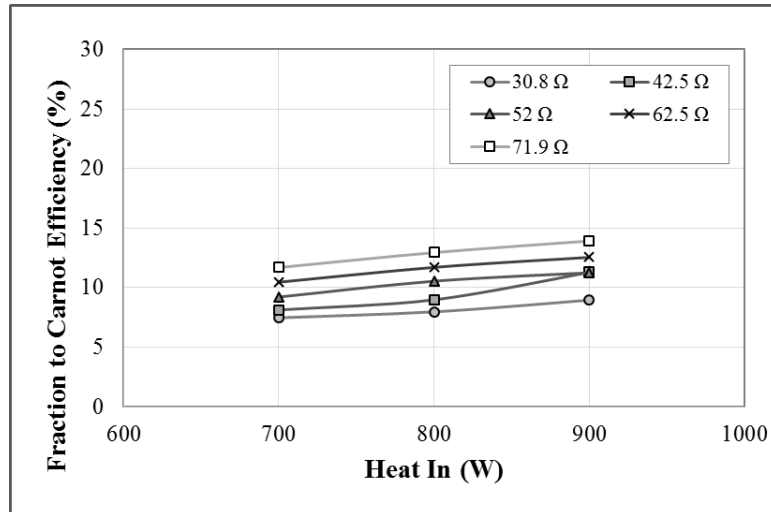


**Figure A4-67:** Fraction to Carnot efficiency versus heating powers for various load resistances at 16 bar mean pressure

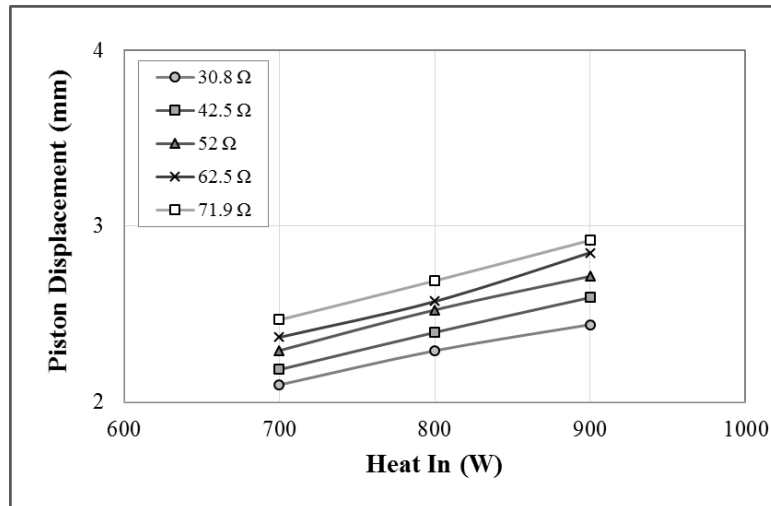


**Figure A4-68:** The effect of heating power on the alternator piston displacement for various load resistances at 16 bar mean pressure

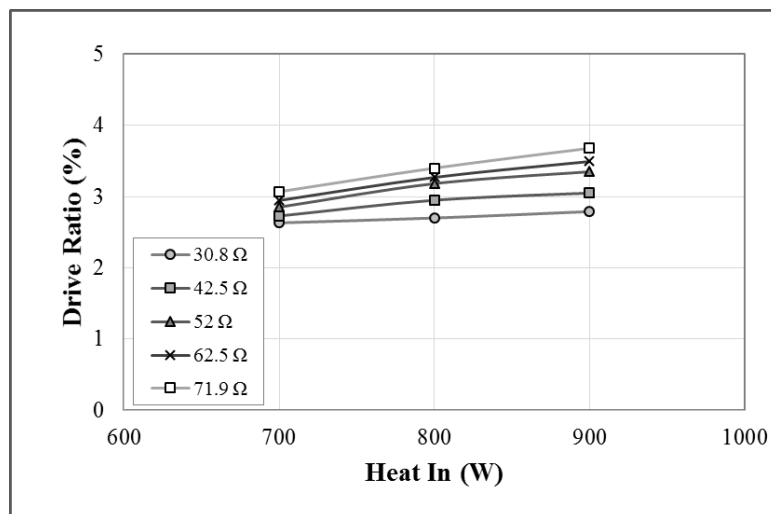


**Figure A4-69:** Measured drive ratio versus heating power for various load resistances at 16 bar mean pressure

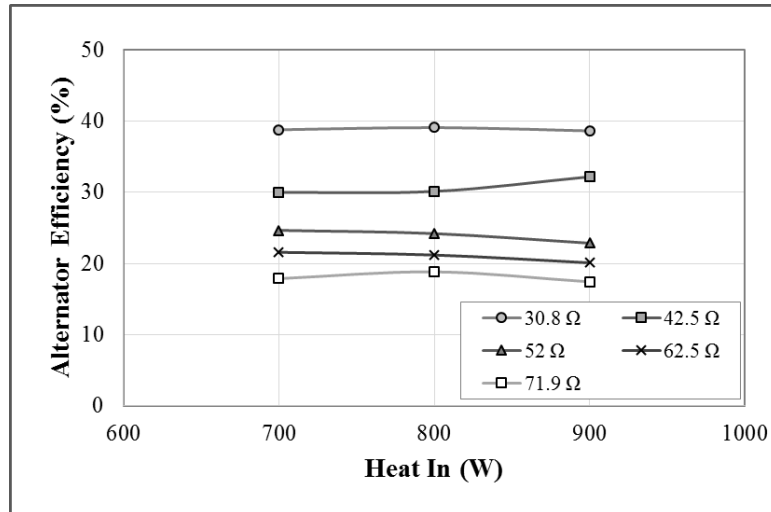


**Figure A4-70:** The effect of heating power on the alternator efficiency for various load resistances at 16 bar mean pressure

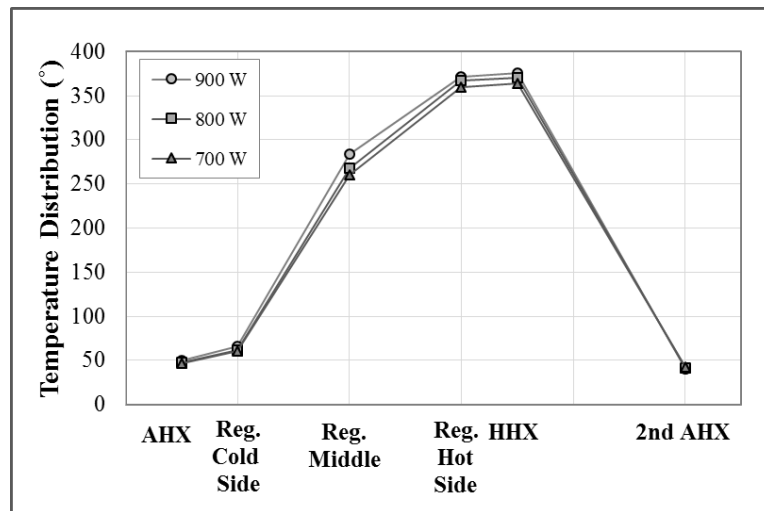


**Figure A4-71:** Core temperature distribution of different heating powers at 16 bar mean pressure

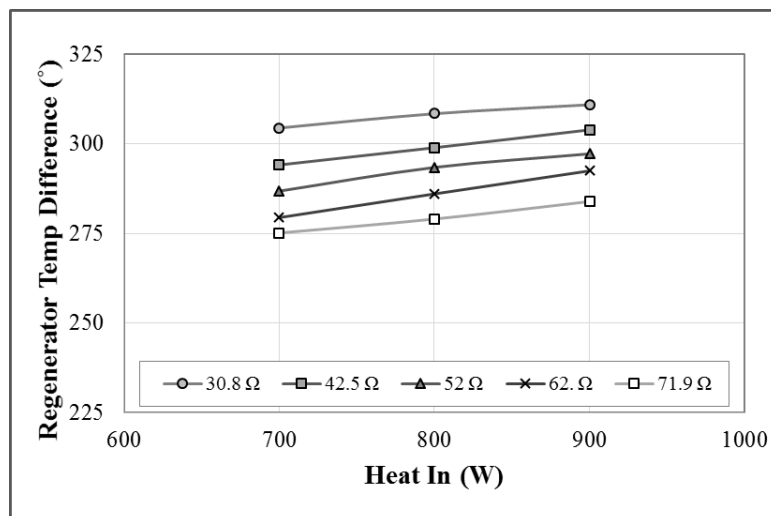


**Figure A4-72:** The effect of heating power on the temperature difference across the regenerator for various load resistances at 16 bar mean pressure

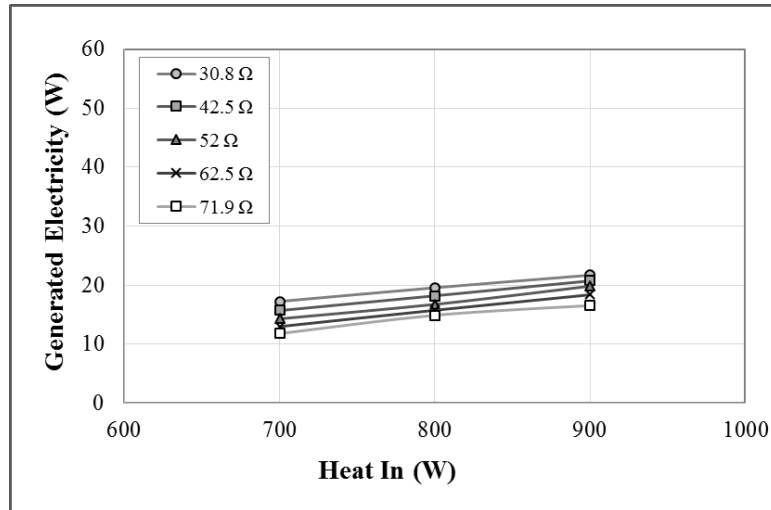


**Figure A4-73:** The performance of the engine as a function of heating power for various load resistances at 14 bar mean pressure

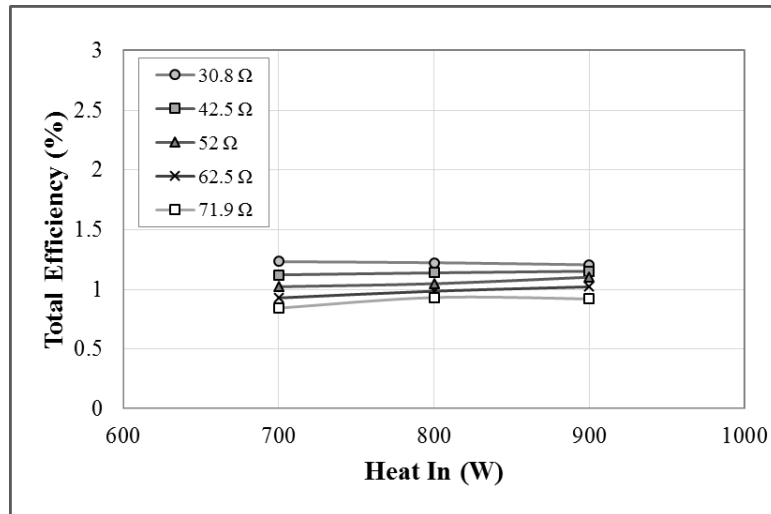


**Figure A4-74:** Total efficiency of different heating power for various load resistances at 14 bar mean pressure

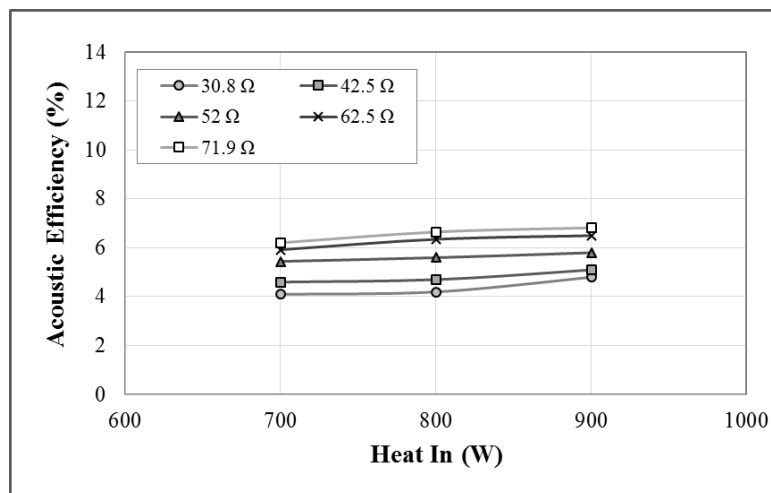


**Figure A4-75:** The relation between heating power and acoustic efficiency for various load resistances at 14 bar mean pressure

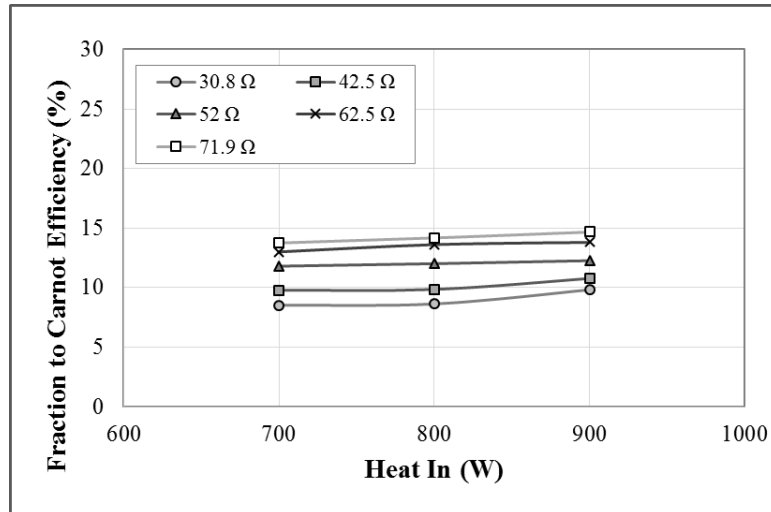


**Figure A4-76:** Fraction to Carnot efficiency versus heating powers for various load resistances at 14 bar mean pressure

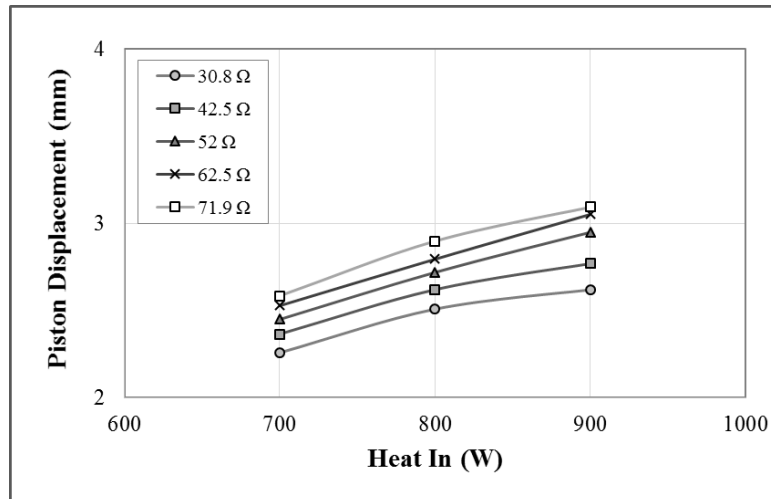


**Figure A4-77:** The effect of heating power on the alternator piston displacement for various load resistances at 14 bar mean pressure

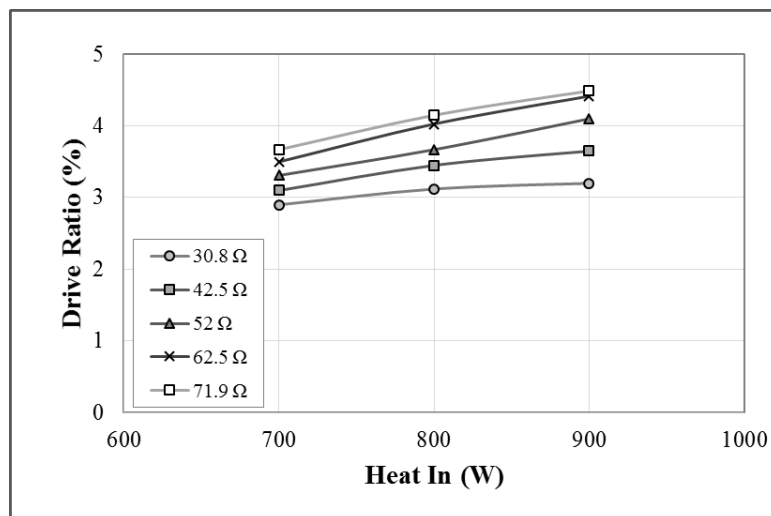


**Figure A4-78:** Measured drive ratio versus heating power for various load resistances at 14 bar mean pressure

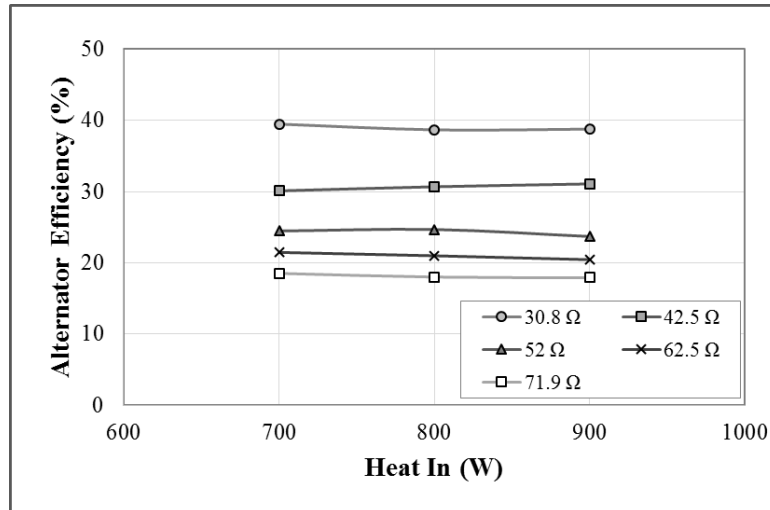


**Figure A4-79:** The effect of heating power on the alternator efficiency for various load resistances at 14 bar mean pressure

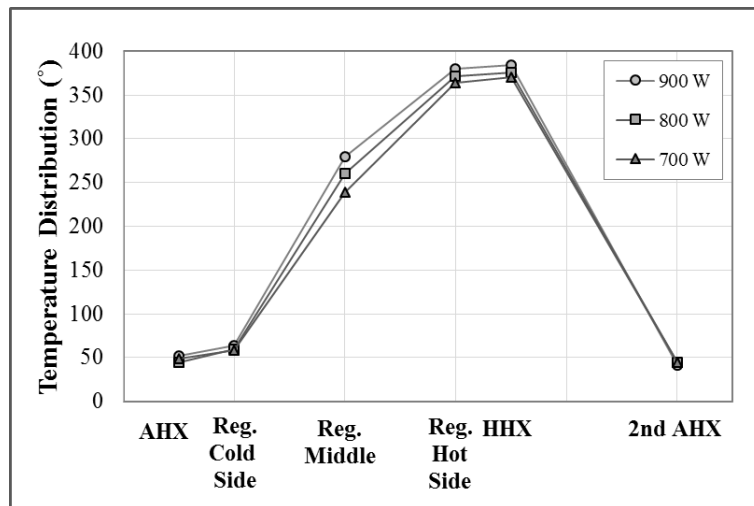


**Figure A4-80:** Core temperature distribution of different heating powers at 14 bar mean pressure

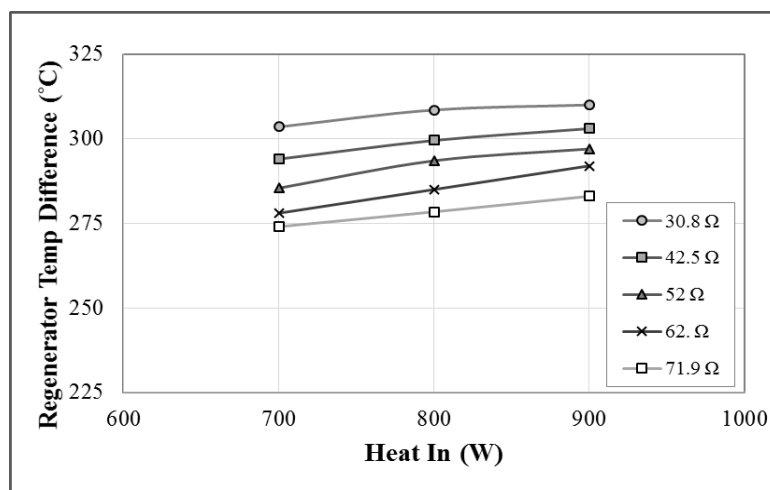


**Figure A4-81:** The effect of heating power on the temperature difference across the regenerator for various load resistances at 14 bar mean pressure

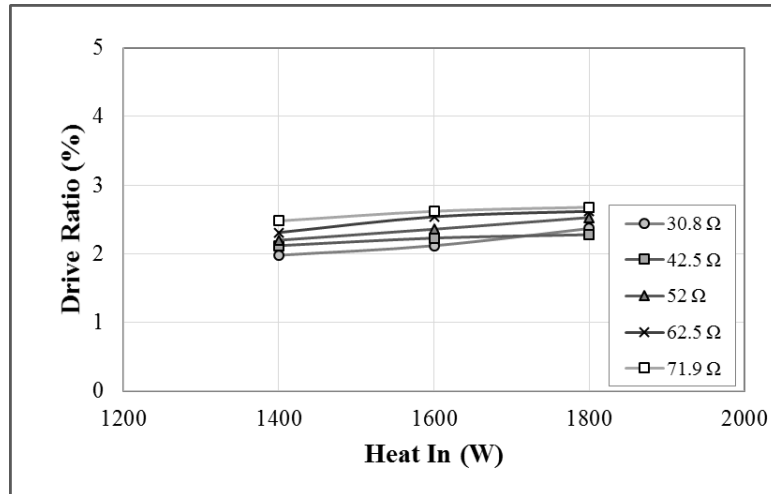


**Figure A4-82:** Measured drive ratio versus heating power for various load resistances at 28 bar mean pressure

## Appendix 5

In this appendix, performance drawings is presented of the experimental tests, after doing some experimental optimization. These test, as explained in chapter four, for the rig before the optimization.

- Figures A5.1-A5.2, shows the drive ratio and peak piston displacement graphs of the engine with an insulating gasket at different heating for various load resistances, at 28 bar mean pressure
- Figures A5.3-A5.10, shows the performance graphs at different heating powers of the engine with an insulating gasket for various load resistances, at 24 bar mean pressure.
- Figures A5.11-A5.18, shows the performance graphs at different heating powers of the engine with an insulating gasket for various load resistances, at 20 bar mean pressure.
- Figures A5.19-A5.25, shows the performance graphs at different mean pressures of the engine with an insulating gasket for various load resistances, at 1800 W heating power.
- Figures A5.26-A5.33, shows the performance graphs at different mean pressures of the engine with an insulating gasket for various load resistances, at 1600 W heating power.
- Figures A5.34-A5.42, shows the performance graphs at different mean pressures of the engine with an insulating gasket for various load resistances, at 1400 W heating power.
- Figures A5.43 is the effect of extra heating power on the temperature difference across the regenerator for engine with insulating gasket for various load resistance at 28 bar mean pressure

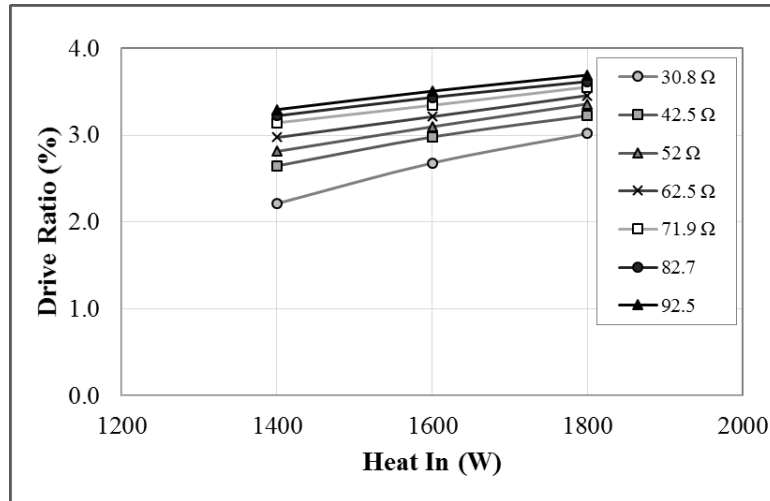


**Figure A5-1:** Measured drive ratio versus heating power for various load resistance at 28 bar mean pressure with insulating gasket

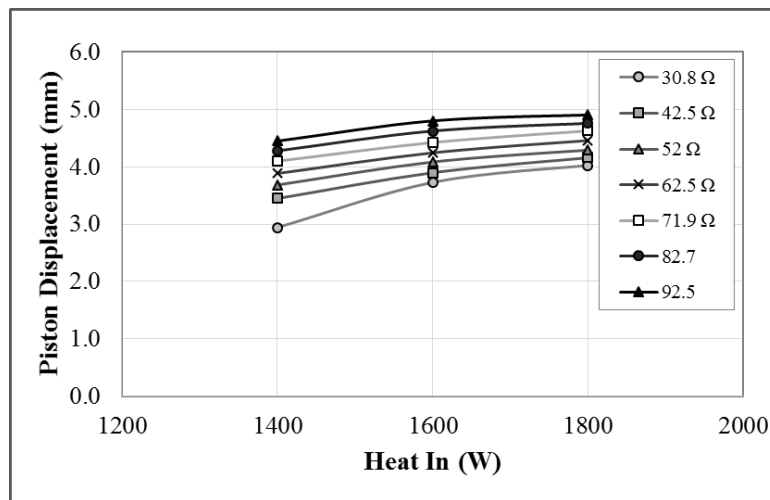


**Figure A5-2:** The effect of mean pressure on the piston displacement with insulating gasket installed for various load resistance at 28 bar mean pressure

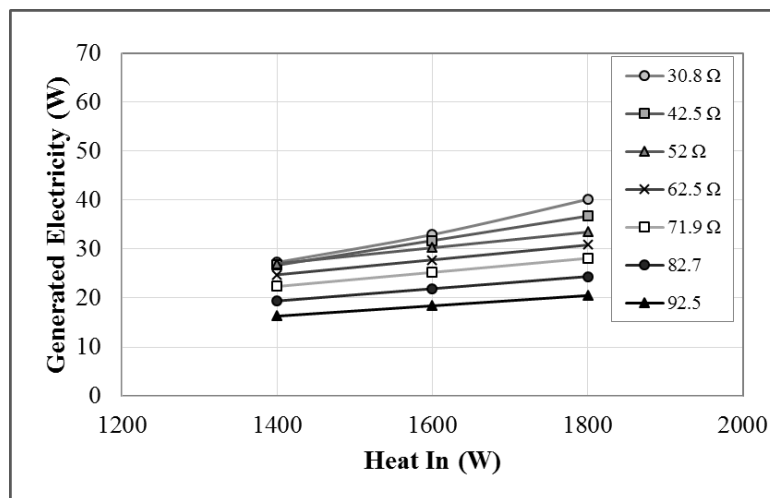


**Figure A5-3:** Performance of the engine with insulating gasket at different heating power for various load resistance at 24 bar mean pressure

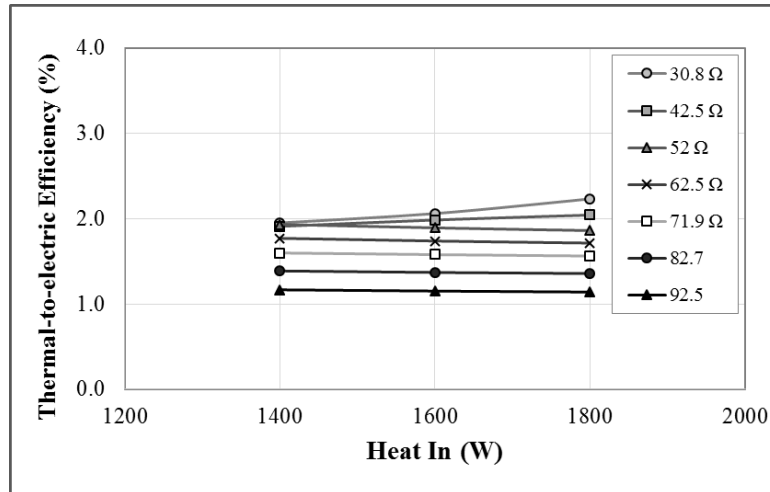


**Figure A5-4:** Thermal-to-electric efficiency at different heating power for various load resistance for engine with insulating gasket at 24 bar

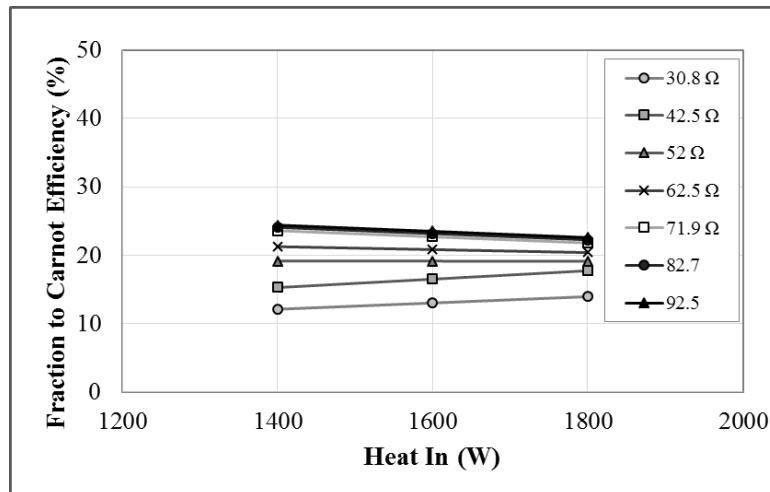


**Figure A5-5:** Fraction to Carnot efficiency versus heating power for engine with insulating gasket for various load resistance at 24 bar

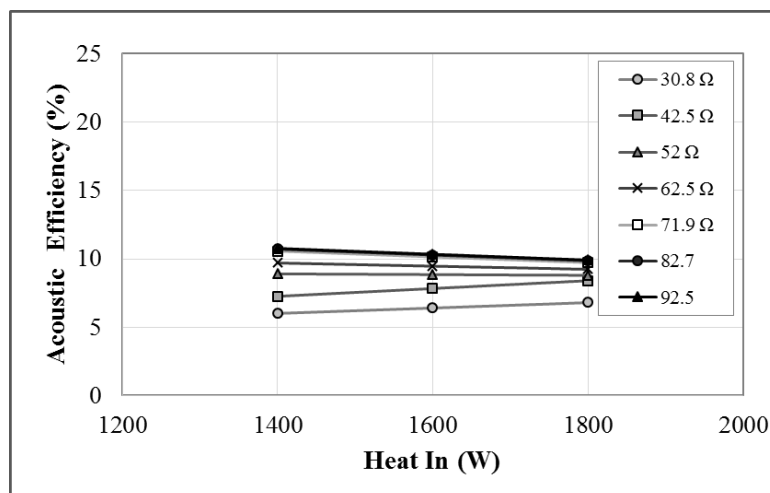


**Figure A5-6:** Acoustic efficiency versus heating power for engine with insulating gasket for various load resistance at 24 bar

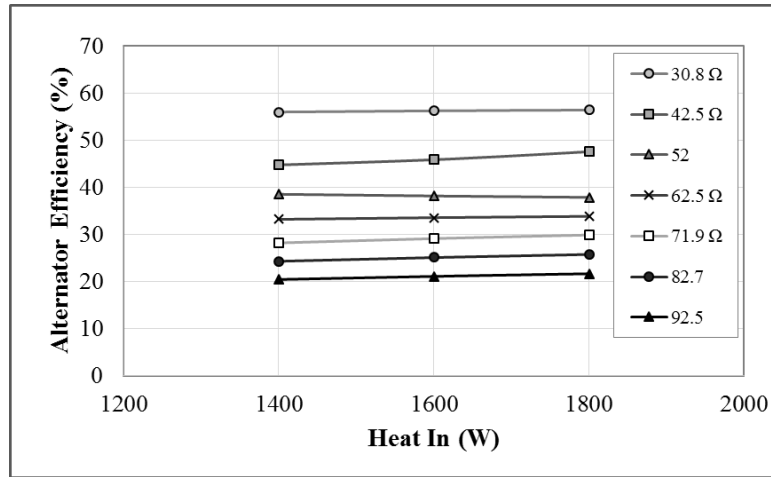


**Figure A5-7:** Alternator efficiency of the engine with insulating gasket at different heating power for various load resistance at 24 bar mean pressure

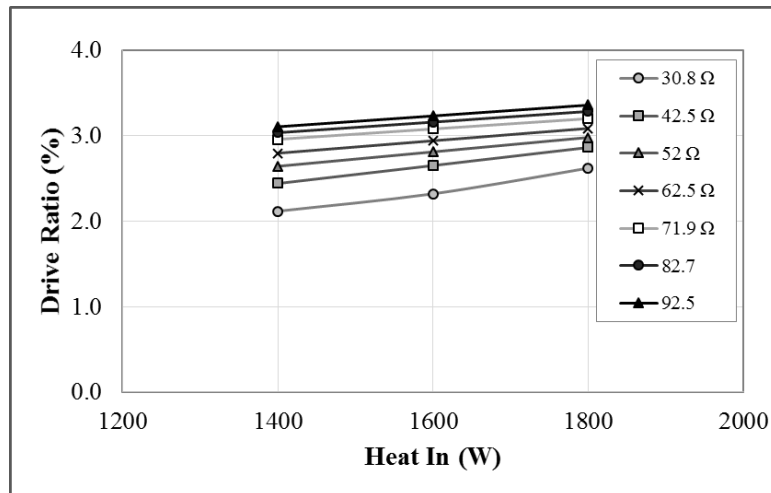


**Figure A5-8:** Drive ratio at different heating power for various load resistance with the insulating gasket at 24 bar mean pressure

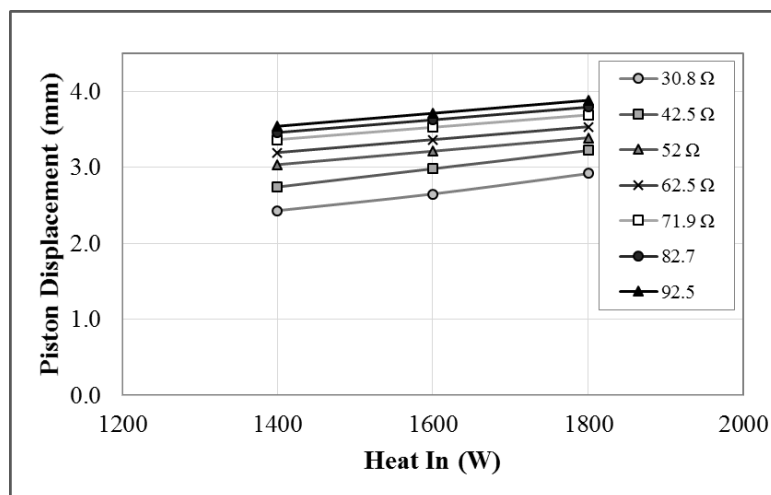


**Figure A5-9:** The effect of heating power on the piston displacement with insulating gasket installed for various load resistance at 24 bar mean pressure

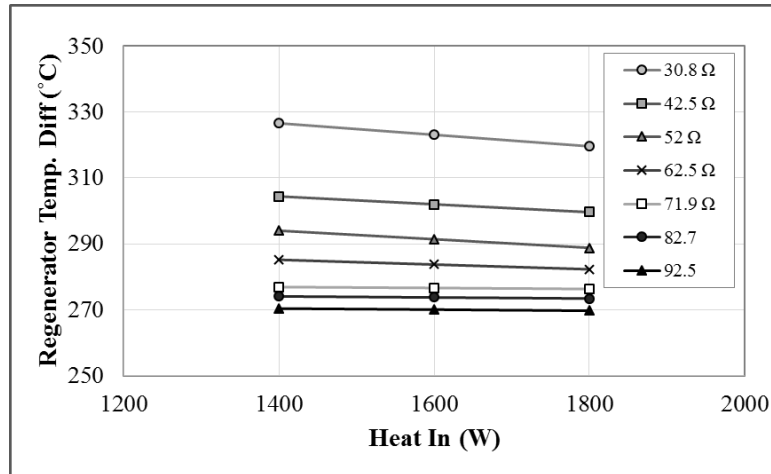


**Figure A5-10:** The effect of heating power on the temperature difference across the regenerator for engine with insulating gasket for various load resistance at 24 bar mean pressure

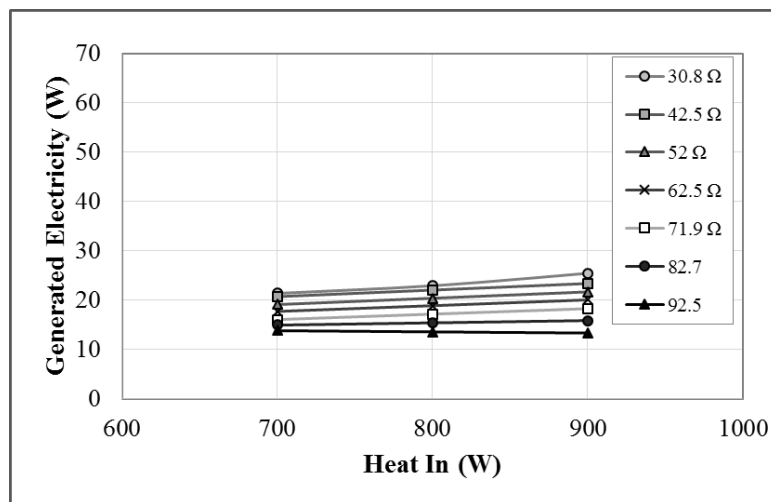


**Figure A5-11:** Performance of the engine with insulating gasket at different heating power for various load resistance at 20 bar mean pressure

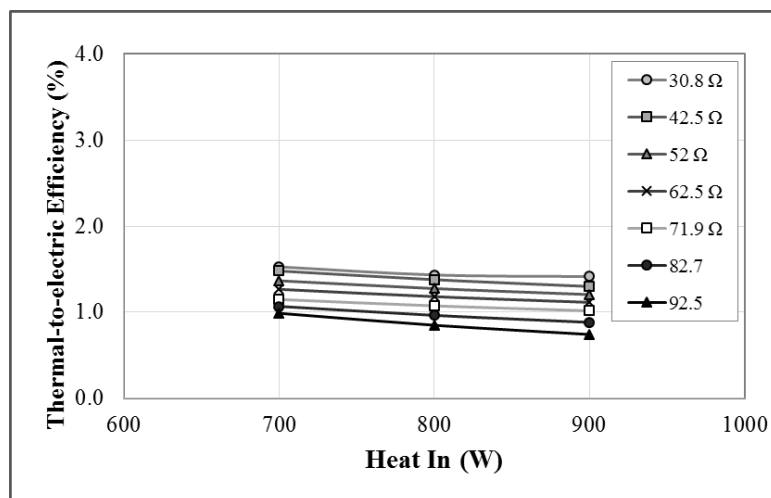


**Figure A5-12:** Thermal-to-electric efficiency at different heating power for various load resistance for engine with insulating gasket at 20 bar mean pressure

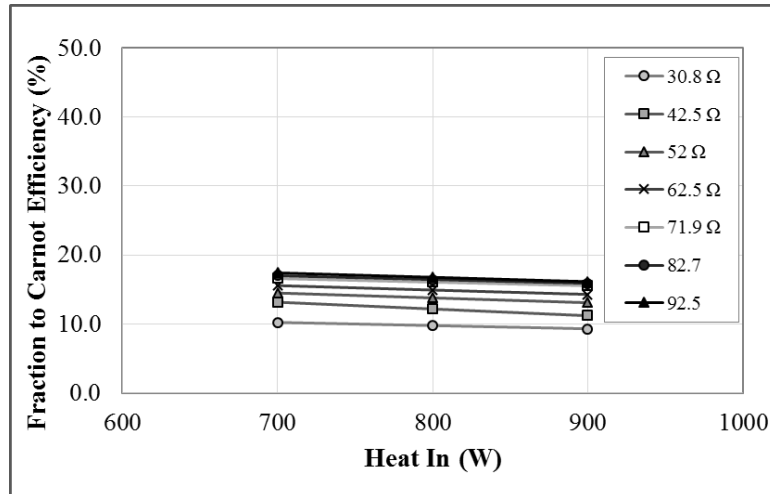


**Figure A5-13:** Fraction to Carnot efficiency versus heating power for engine with insulating gasket for various load resistance at 20 bar mean pressure

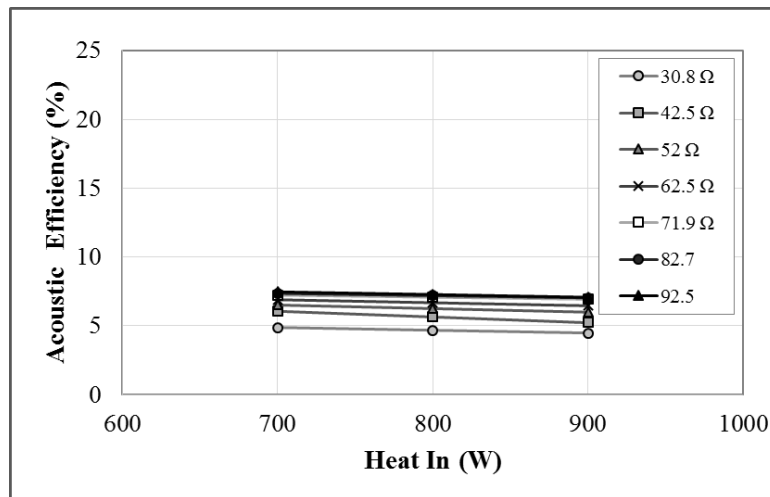


**Figure A5-14:** Fraction to Carnot efficiency versus heating power for engine with insulating gasket for various load resistance at 20 bar mean pressure

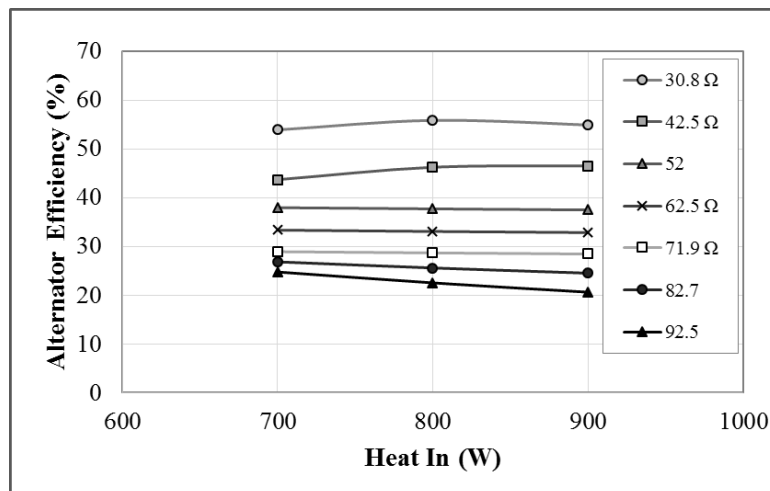


**Figure A5-15:** Alternator efficiency of the engine with insulating gasket at different heating power for various load resistance at 20 bar mean pressure

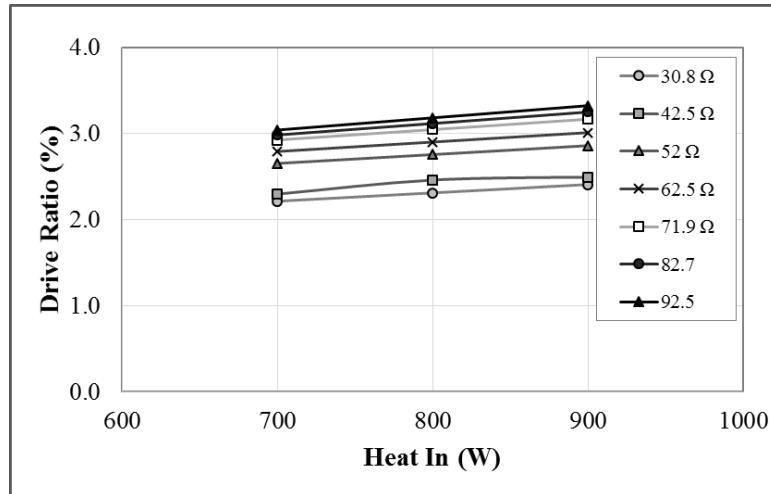


**Figure A5-16:** Drive ratio at different heating power for various load resistance with the insulating gasket at 20 bar mean pressure

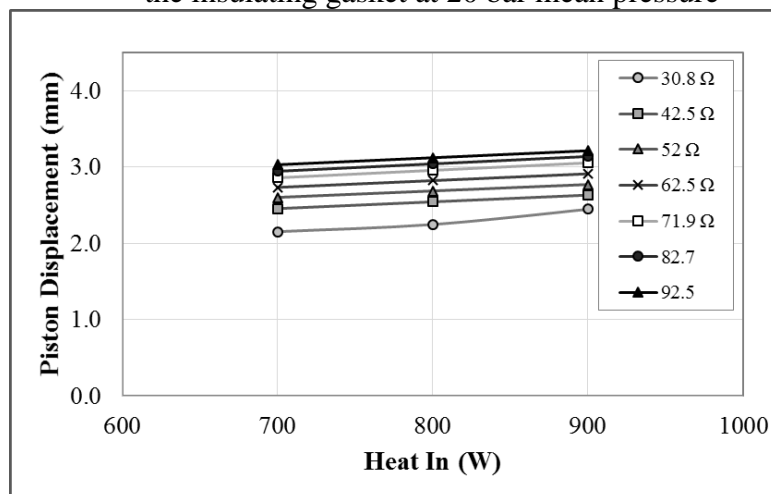


**Figure A5-17:** The effect of heating power on the piston displacement with insulating gasket installed for various load resistance at 20 bar mean pressure

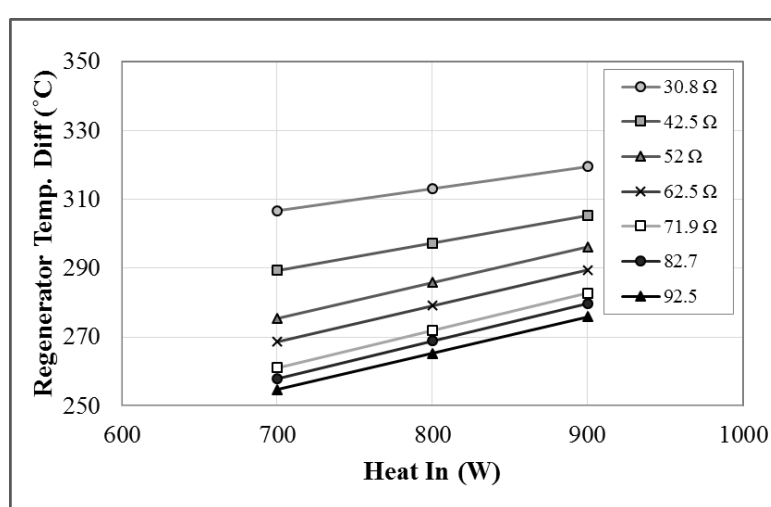


**Figure A5-18:** The effect of mean pressure on the temperature difference across the regenerator for engine with insulating gasket for various load resistance at 20 bar mean pressure

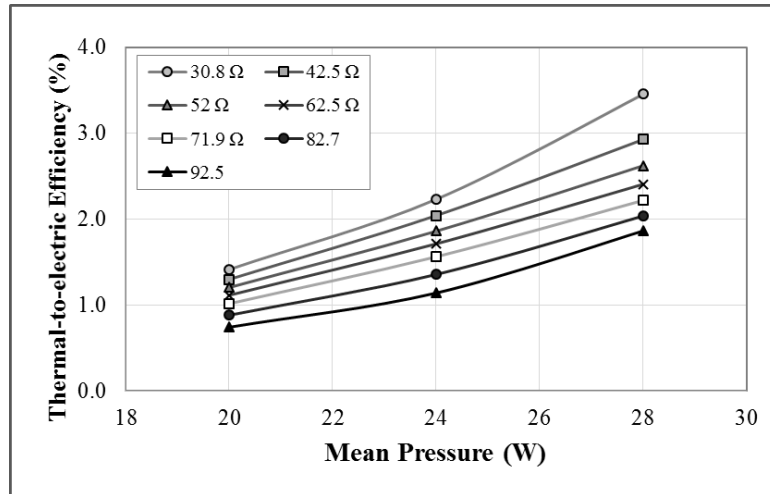


**Figure A5-19:** Performance of the engine with insulating gasket at different mean pressure for various load resistance at 1800 W heating power

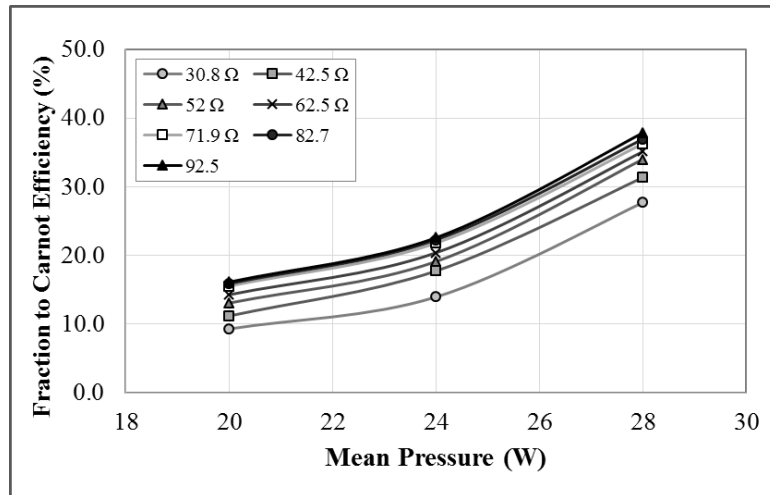


**Figure A5-20:** Fraction to Carnot efficiency versus mean pressure for engine with insulating gasket for various load resistance at 1800 W heating power

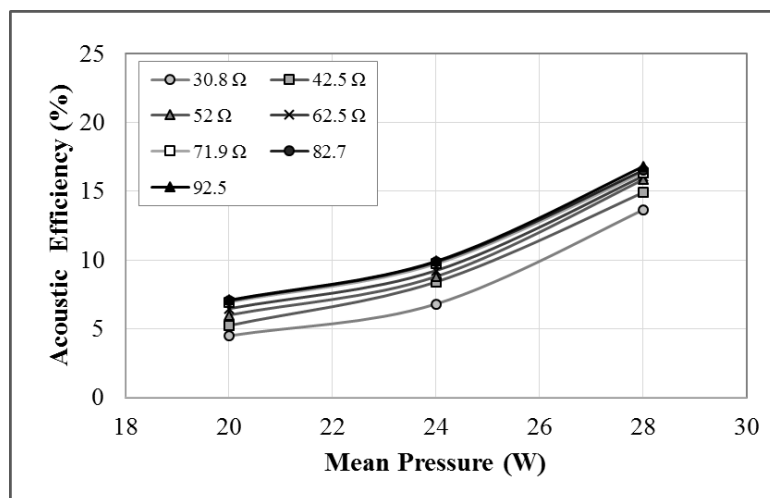


**Figure A5-21:** Acoustic efficiency versus mean pressure for engine with insulating gasket for various load resistance at 1800 W heating power

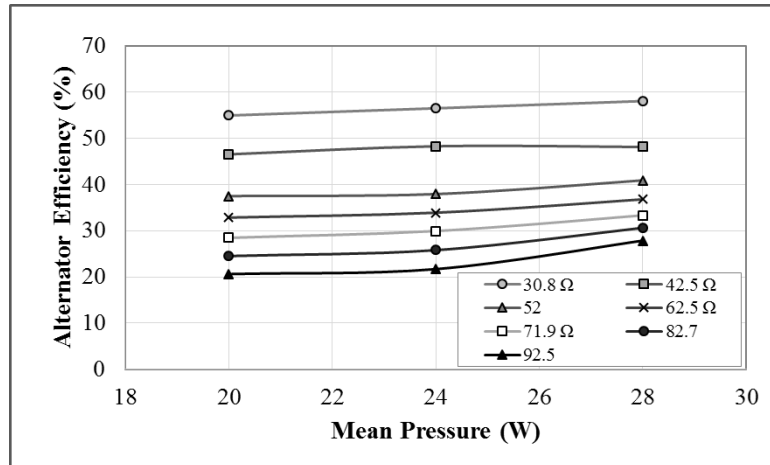


**Figure A5-22:** Alternator efficiency of the engine with insulating gasket at different mean pressure for various load resistance at 1800 W heating power

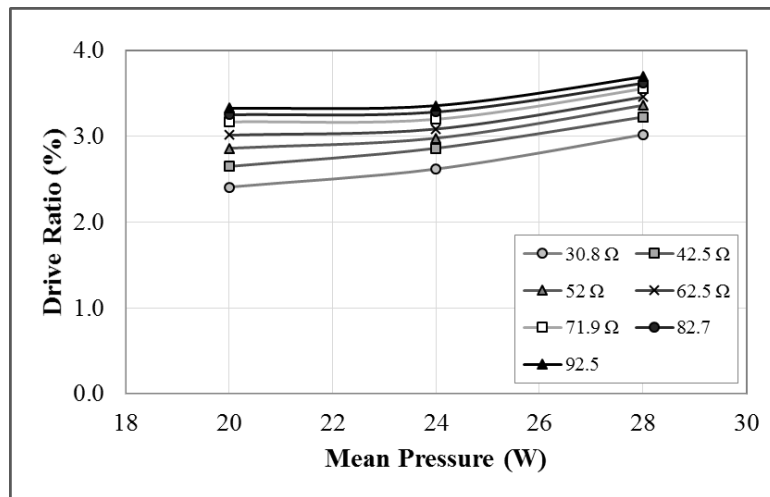


**Figure A5-23:** Drive ratio at different mean pressure for various load resistance with the insulating gasket at 1800 W heating power

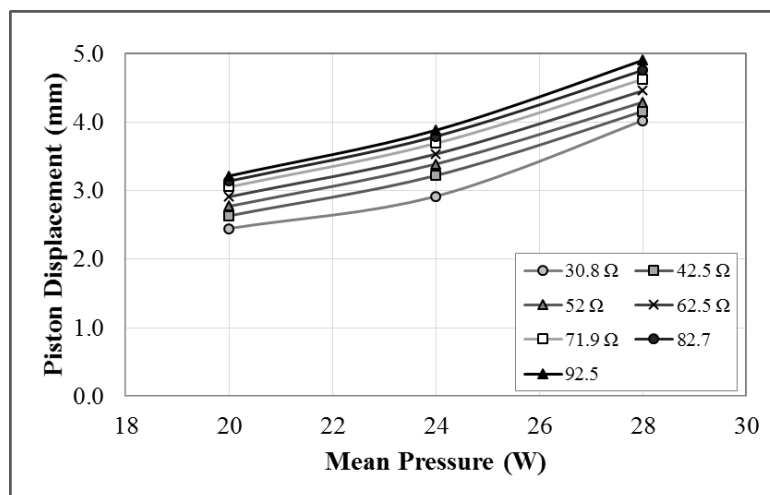


**Figure A5-24:** The effect of mean pressure on the piston displacement with insulating gasket installed for various load resistance at 1800 W heating power

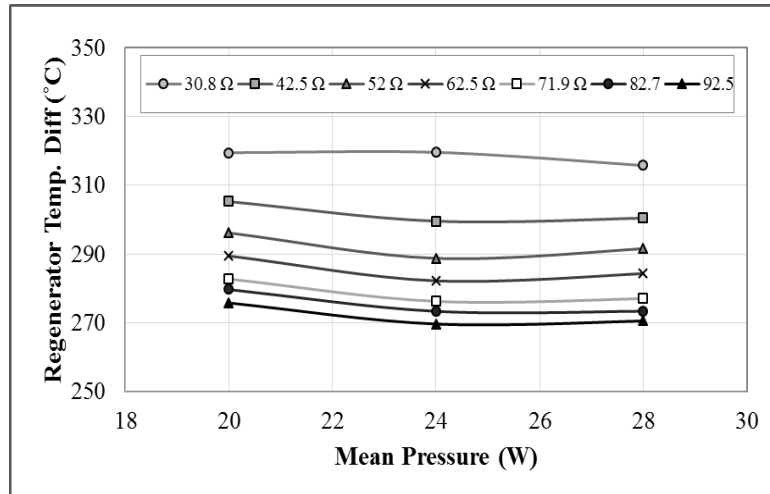


**Figure A5-25:** The effect of mean pressure on the temperature difference across the regenerator for engine with insulating gasket for various load resistance at 1800 W heating power

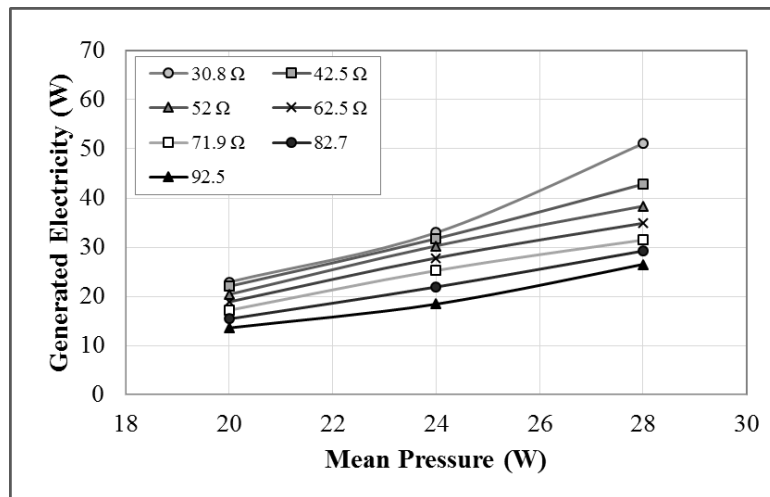


**Figure A5-26:** Performance of the engine with insulating gasket at different mean pressure for various load resistance at 1600 W heating power

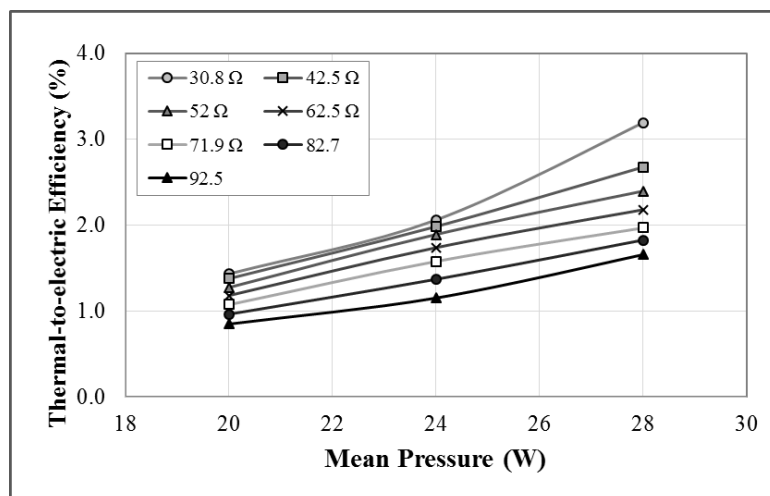


**Figure A5-27:** Thermal-to-electric efficiency at different mean pressure for various load resistance for engine with insulating gasket at 1600 W heating power

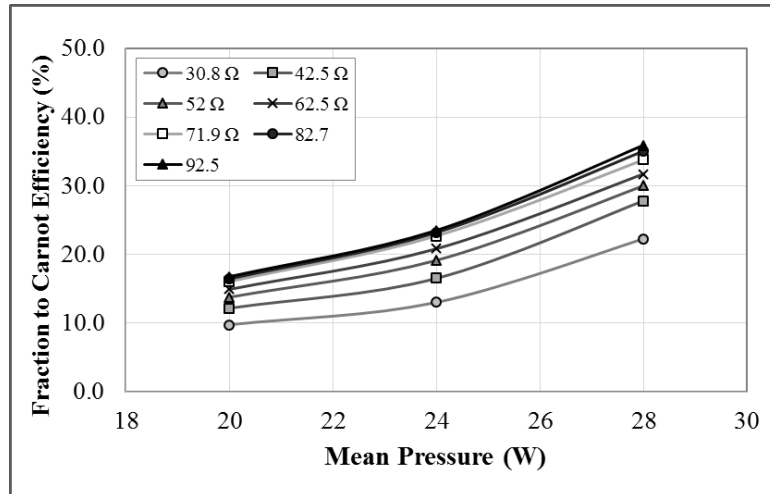


**Figure A5-28:** Fraction to Carnot efficiency versus mean pressure for engine with insulating gasket for various load resistance at 1600 W heating power

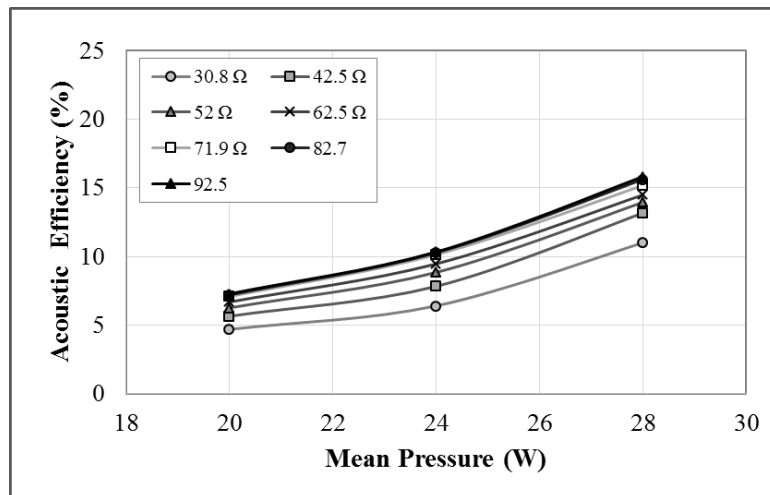


**Figure A5-29:** Acoustic efficiency versus mean pressure for engine with insulating gasket for various load resistance at 1600 W heating power

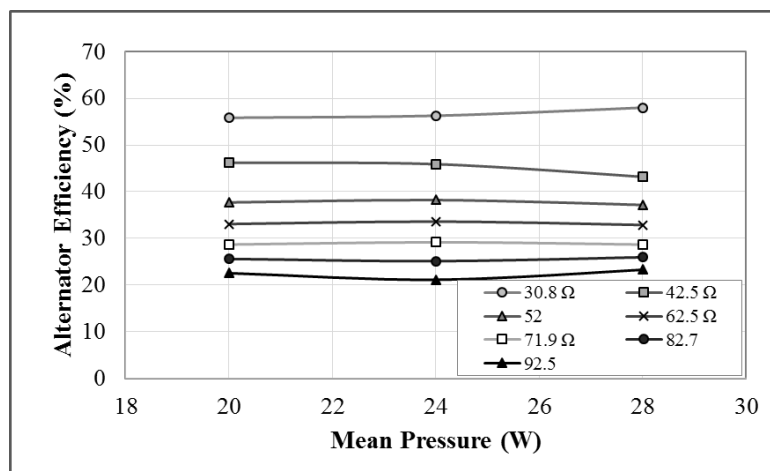


**Figure A5-30:** Alternator efficiency of the engine with insulating gasket at different mean pressure for various load resistance at 1600 W heating power

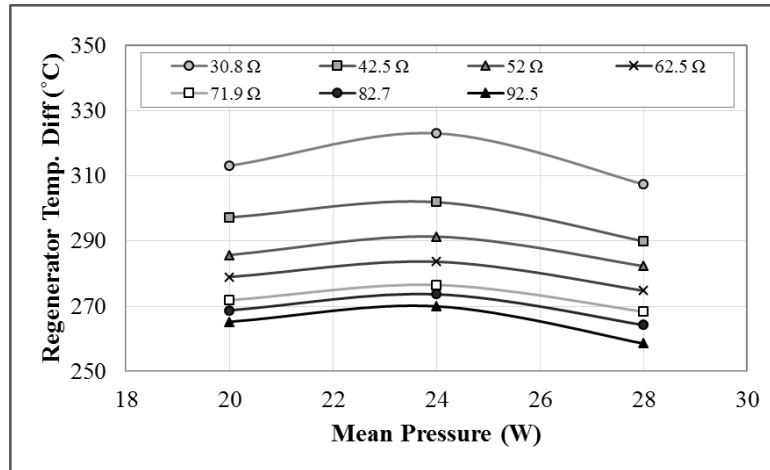


**Figure A5-31:** The effect of mean pressure on the temperature difference across the regenerator for engine with insulating gasket for various load resistance at 1600 W heating power

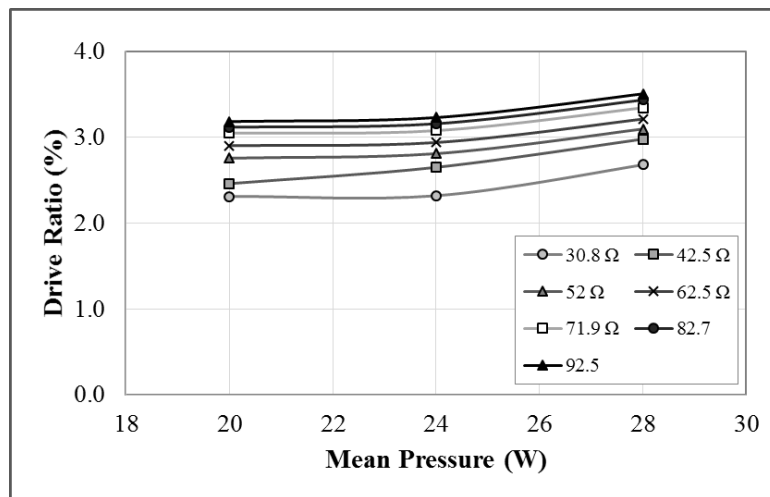


**Figure A5-32:** Drive ratio at different mean pressure for various load resistance with the insulating gasket at 1600 W heating power

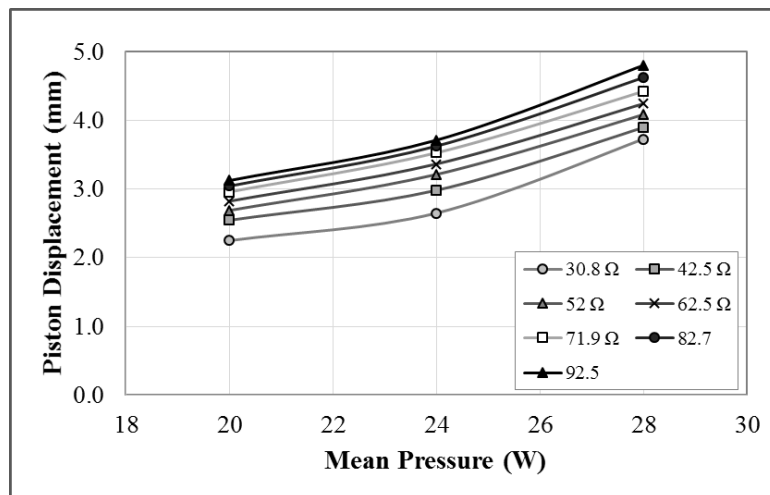


**Figure A5-33:** The effect of mean pressure on the piston displacement with insulating gasket installed for various load resistance at 1600 W heating power

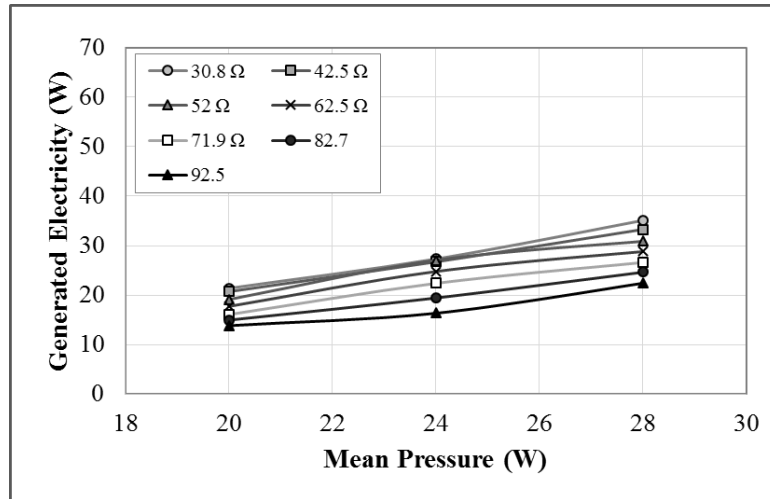


**Figure A5-34:** Performance of the engine with insulating gasket at different mean pressure for various load resistance at 1400 W heating power

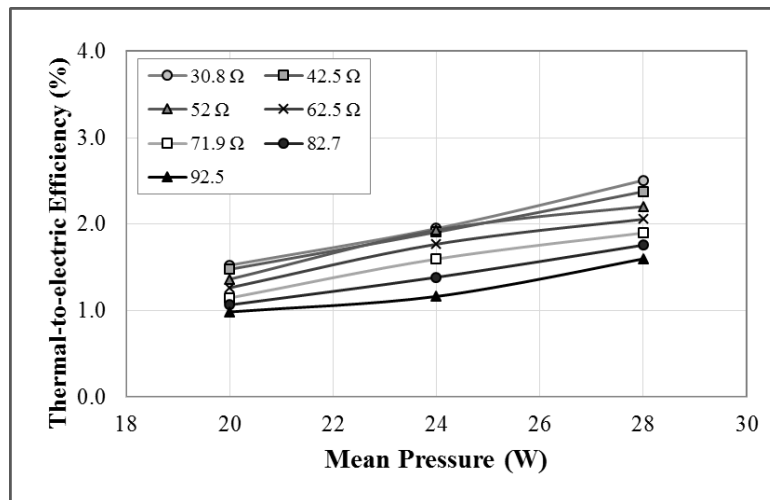


**Figure A5-35:** Thermal-to-electric efficiency at different mean pressure for various load resistance for engine with insulating gasket at 1400 W heating power

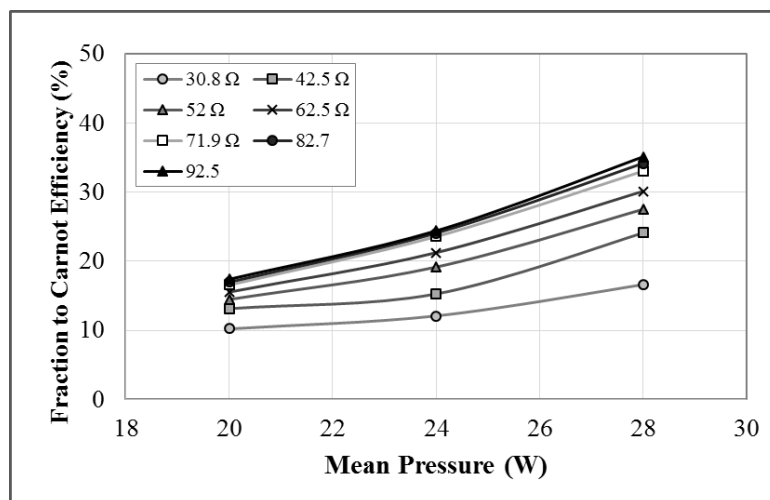


**Figure A5-36:** Fraction to Carnot efficiency versus mean pressure for engine with insulating gasket for various load resistance at 1400 W heating power

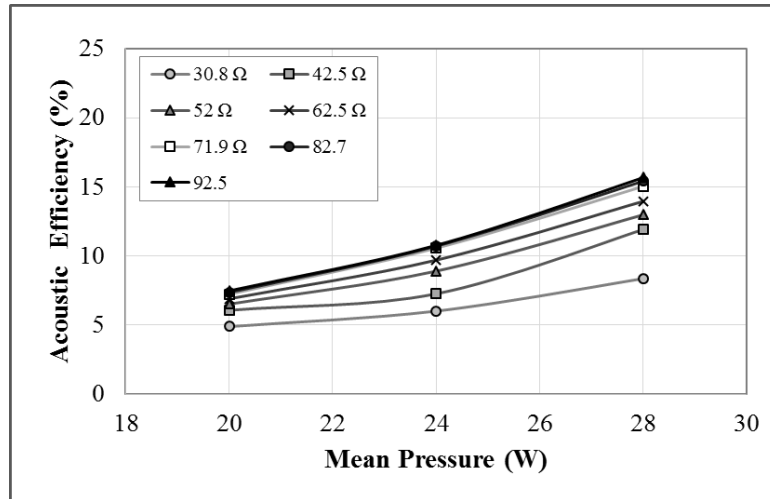


**Figure A5-37:** Acoustic efficiency versus mean pressure for engine with insulating gasket for various load resistance at 1400 W heating power

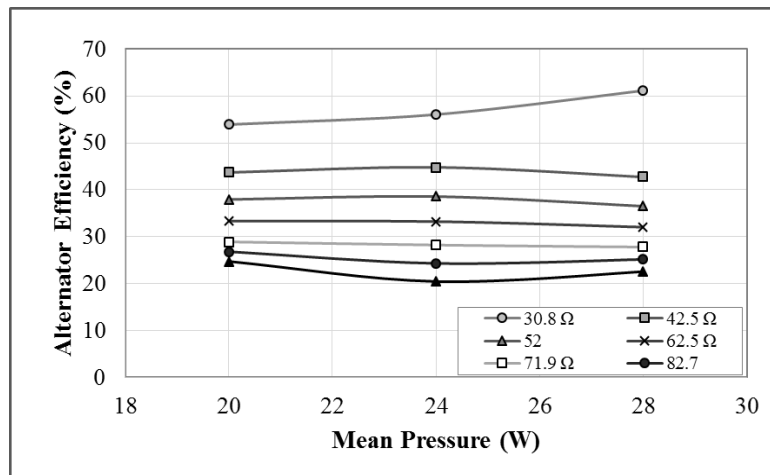


**Figure A5-38:** Alternator efficiency of the engine with insulating gasket at different mean pressure for various load resistance at 1400 W heating power

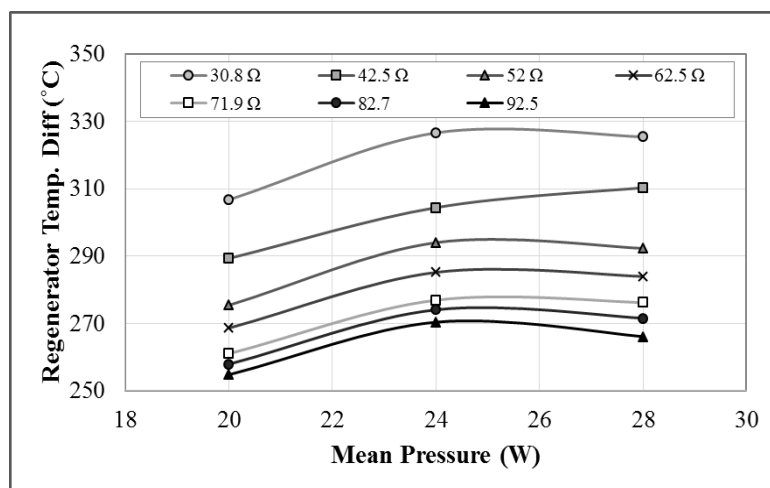


**Figure A5-39:** The effect of mean pressure on the temperature difference across the regenerator for engine with insulating gasket for various load resistance at 1400 W heating power

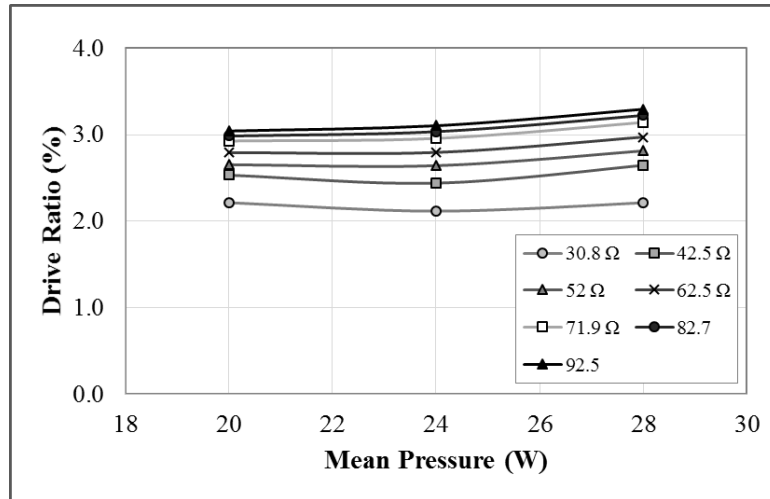


**Figure A5-40:** Drive ratio at different mean pressure for various load resistance with the insulating gasket at 1400 W heating power

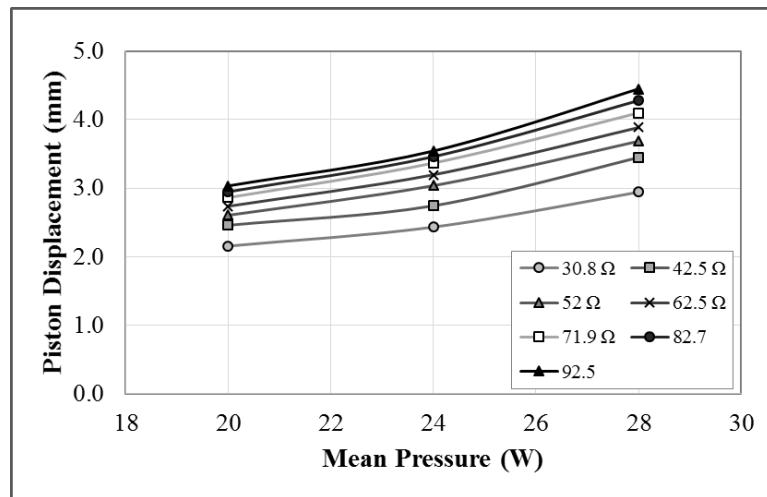


**Figure A5-41:** The effect of mean pressure on the piston displacement with insulating gasket installed for various load resistance at 1400 W heating power

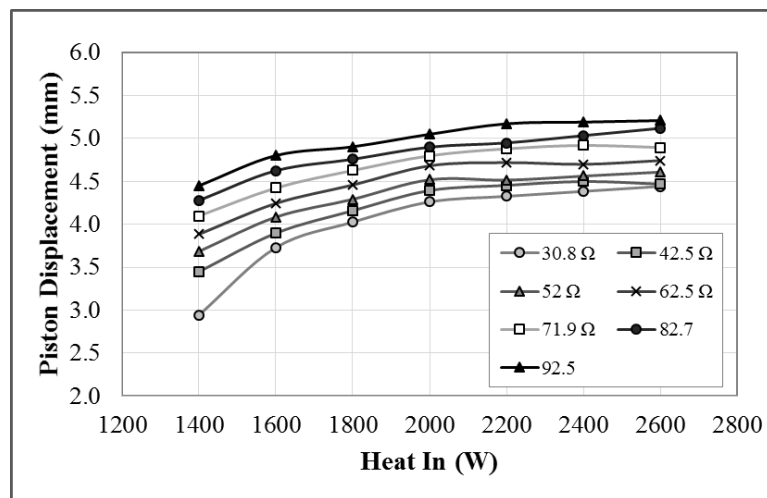


**Figure A5-42:** The effect of extra heating power on the piston displacement with insulating gasket installed for various load resistance at 28 bar mean pressure

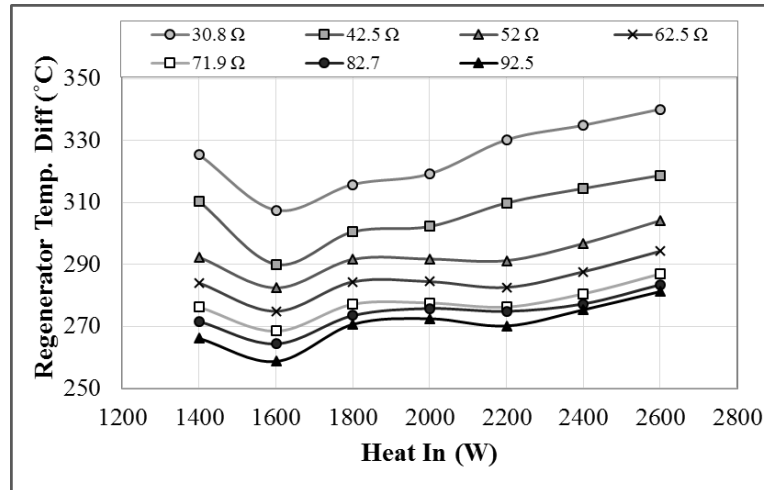


**Figure A5-43:** The effect of extra heating power on the temperature difference across the regenerator for engine with insulating gasket for various load resistance at 28 bar mean pressure

## Appendix 6

In this appendix, the DeltaEC model of four-stage thermoacoustic electricity generator with push-pull linear alternator is presented. The model gives a detailed segment by segment dimensions and calculations along the engine loop. It also shows the assumptions made in modelling half of the engine and connect it to a self-excited imaginary flow.

```

1  Four-stage
2  0 BEGIN
3      2.8000E+06 a Mean P Pa
4  Gues      54.795 b Freq Hz
5  Gues      297.00 c TBeg K
6  Gues      9.4999E+04 d |p| Pa
7      20.000 e Ph(p) deg
8  Gues      7.3927E-03 f |U| m^3/s
9  Gues      71.656 g Ph(U) deg
10 Gues      194.88 h Htot W
11 Optional Parameters
12 helium Gas type
13 1 DUCT 4" Dia Core
14      8.2418E-03 a Area m^2 Mstr      9.4999E+04 A |p| Pa
15      0.32188 b Perim m la      20.000 B Ph(p) deg
16      0.0000 c Length m      7.3927E-03 C |U| m^3/s
17      5.0000E-04 d Srough      71.656 D Ph(U) deg
18 Master-Slave Links      194.88 E Htot W
19 Optional Parameters      217.85 F Edot W
20 ideal Solid type
21 2 HX 1mm plate spacing
22 Same 1a 8.2418E-03 a Area m^2      9.5103E+04 A |p| Pa
23      0.2920 b GasA/A      19.925 B Ph(p) deg
24      3.0000E-02 c Length m      6.9110E-03 C |U| m^3/s
25      5.0000E-04 d y0 m      69.150 D Ph(U) deg
26 Gues      -285.03 e HeatIn W      -90.15 E Htot W
27 Master-Slave Links      214.62 F Edot W
28 Possible targets      297.00 G GasT K
29 ideal Solid type      292.62 H SolidT K
30 3 RPN ChangeMe
31 Targ      297.00 a G or T      297.00 A ChngeMe
32 2G
33 4 DUCT Cold gap
34 Same 1a 8.2418E-03 a Area m^2 Mstr      9.5104E+04 A |p| Pa
35      0.32188 b Perim m 4a      19.924 B Ph(p) deg
36      1.0000E-03 c Length m      6.8671E-03 C |U| m^3/s
37      1.0000E-04 d Srough      68.835 D Ph(U) deg
38 Master-Slave Links      -90.15 E Htot W
39 Optional Parameters      214.62 F Edot W
40 ideal Solid type
41 5 STKSCREEN 0.065mm wide diameter, app 0.18mm, 75.6% porocity
42 Same 1a 8.2418E-03 a Area m^2      9.0978E+04 A |p| Pa
43      0.7565 b VolPor      18.305 B Ph(p) deg
44      7.3000E-02 c Length m      1.0519E-02 C |U| m^3/s
45      6.0241E-05 d rh m      37.183 D Ph(U) deg
46      0.1000 e ksFrac      -90.15 E Htot W
47 Master-Slave Links      452.77 F Edot W
48      297.00 G TBeg K
49 stainless Solid type      673.00 H TEnd K
50 6 DUCT Hot gap
51 Same 1a 8.2418E-03 a Area m^2 Mstr      9.0978E+04 A |p| Pa

```

52		0.32188	b	Perim	m	6a	18.304	B	Ph(p)	deg	
53		1.0000E-03	c	Length	m		1.0501E-02	C	U	m^3/s	
54		1.0000E-04	d	Strough			36.896	D	Ph(U)	deg	
55	Master-Slave Links							-90.15	E	Htot	W
56	Optional Parameters							452.75	F	Edot	W
57	ideal	Solid type									
58	7	HX	HHX								
59	Same	1a	8.2418E-03	a	Area	m^2	9.0951E+04	A	p	Pa	
60			0.3440	b	GasA/A		18.221	B	Ph(p)	deg	
61			4.0000E-02	c	Length	m	1.0025E-02	C	U	m^3/s	
62	Same	2d	5.0000E-04	d	y0	m	31.827	D	Ph(U)	deg	
63	Gues		551.83	e	HeatIn	W	461.68	E	Htot	W	
64	Master-Slave Links							443.10	F	Edot	W
65	Possible targets							673.00	G	GasT	K
66	ideal	Solid type									
67	8	RPN	ChangeMe								
68	Targ		673.00	a	G or T		673.00	A	ChngMe		
69	7G										
70	9	STKDUCT	TBT-1 3" Pipe								
71	Same	1a	8.2418E-03	a	Area	m^2	9.0953E+04	A	p	Pa	
72			0.32188	b	Perim	m	18.216	B	Ph(p)	deg	
73			1.0000E-02	c	Length	m	9.9055E-03	C	U	m^3/s	
74			7.3000E-04	d	WallA	m^2	28.708	D	Ph(U)	deg	
75	Master-Slave Links							461.68	E	Htot	W
76							442.94	F	Edot	W	
77							673.00	G	TBeg	K	
78	stainless	Solid type									
79	10	STKCONE	TBT 2 3" to 2"								
80	Same	1a	8.2418E-03	a	AreaI	m^2	9.0948E+04	A	p	Pa	
81			0.32188	b	PerimI	m	18.142	B	Ph(p)	deg	
82			7.8000E-02	c	Length	m	9.8234E-03	C	U	m^3/s	
83	Same	12a	4.7680E-03	d	AreaF	m^2	9.1337	D	Ph(U)	deg	
84			0.2448	e	PerimF	m	461.68	E	Htot	W	
85			1.0000E-03	f	f_wall		441.20	F	Edot	W	
86	Master-Slave Links							662.76	G	TBeg	K
87	stainless	Solid type									
88	11	STKDUCT	TBT-3 2" Pipe								
89	Same	10d	4.7680E-03	a	Area	m^2	9.0943E+04	A	p	Pa	
90			0.2448	b	Perim	m	18.123	B	Ph(p)	deg	
91			1.0000E-02	c	Length	m	9.8738E-03	C	U	m^3/s	
92			1.0000E-04	d	WallA	m^2	7.3147	D	Ph(U)	deg	
93	Master-Slave Links							461.68	E	Htot	W
94							441.01	F	Edot	W	
95							339.25	G	TBeg	K	
96	stainless	Solid type									
97	12	HX	Secondary ambient HX 2"								
98			4.7680E-03	a	Area	m^2	9.0850E+04	A	p	Pa	
99			0.3050	b	GasA/A		17.978	B	Ph(p)	deg	
100			2.0000E-02	c	Length	m	9.8924E-03	C	U	m^3/s	
101	Same	2d	5.0000E-04	d	y0	m	6.0368	D	Ph(U)	deg	
102	Gues		-199.53	e	HeatIn	W	262.14	E	Htot	W	
103	Targ	Same	2H	292.62	f	SolidT	439.64	F	Edot	W	
104	Master-Slave Links							297.00	G	GasT	K
105	ideal	Solid type									
106	13	CONE	Cone before T-branch								
107	Same	12a	4.7680E-03	a	AreaI	m^2	9.0726E+04	A	p	Pa	
108			0.2448	b	PerimI	m	17.726	B	Ph(p)	deg	
109			6.7431E-02	c	Length	m	1.0240E-02	C	U	m^3/s	
110	Same	14a	1.3800E-03	d	AreaF	m^2	-1.2041	D	Ph(U)	deg	
111			0.13168	e	PerimF	m	262.14	E	Htot	W	

```

112          5.0000E-04 f Srough          439.37 F Edot W
113 Master-Slave Links
114 Optional Parameters
115 ideal      Solid type
116 14 DUCT    Feedback Pipe before Alternator 1"
117          1.3800E-03 a Area m^2      Mstr      9.0292E+04 A |p| Pa
118          0.13179 b Perim m          14a      17.027 B Ph(p) deg
119          0.1000 c Length m          1.0566E-02 C |U| m^3/s
120          5.0000E-04 d Srough      -5.9851 D Ph(U) deg
121 Master-Slave Links          262.14 E Htot W
122 Optional Parameters          439.07 F Edot W
123 ideal      Solid type
124 15 TBRANCH Change Me
125 Gues      4.7524E+07 a Re(Zb) Pa-s/m^3      9.0292E+04 A |p| Pa
126 Gues      7.7427E+06 b Im(Zb) Pa-s/m^3      17.027 B Ph(p) deg
127 Gues      67.269 c HtotBr W          1.8752E-03 C |U| m^3/s
128 Master-Slave Links          7.7737 D Ph(U) deg
129 Optional Parameters          67.269 E HtotBr W
130          83.557 F EdotBr W
131          355.51 G EdotTr W
132 16 DUCT    Change Me
133 Same 14a 1.3800E-03 a Area m^2      Mstr      8.9998E+04 A |p| Pa
134          0.13169 b Perim m          16a      16.754 B Ph(p) deg
135          0.2050 c Length m          2.8610E-03 C |U| m^3/s
136          5.0000E-04 d Srough      -33.085 D Ph(U) deg
137 Master-Slave Links          67.269 E Htot W
138 Optional Parameters          83.030 F Edot W
139 ideal      Solid type
140 17 VESPEAKER Change Me
141          1.3850E-03 a Area m^2      8.9998E+04 A |p| Pa
142          1.9700 b R ohms          -163.25 B Ph(p) deg
143          4.4100E-02 c L H          2.8610E-03 C |U| m^3/s
144          46.720 d BLProd T-m      -33.085 D Ph(U) deg
145          0.7895 e M kg          -67.269 E Htot W
146          4.1430E+04 f K N/m      -83.03 F Edot W
147          7.0700 g Rm N-s/m      -134.54 G WorkIn W
148 Gues      65.963 h |V| V          65.963 H Volts V
149 Gues      106.98 i Ph(V) deg      4.0792 I Amps A
150          180.00 J Ph(V/I) deg
151          1.8000E+05 K |Px| Pa
152 ideal      Solid type          -163.25 L Ph(Px) deg
153 18 CONE    Change Me
154          1.1385E-03 a AreaI m^2      Mstr      8.9998E+04 A |p| Pa
155          0.11961 b PerimI m          18a      -163.25 B Ph(p) deg
156          0.0000 c Length m          2.8610E-03 C |U| m^3/s
157          1.3800E-03 d AreaF m^2      Mstr      -33.085 D Ph(U) deg
158          0.13169 e PerimF m          18d      -67.269 E Htot W
159          5.0000E-04 f Srough      -83.03 F Edot W
160 Master-Slave Links
161 Optional Parameters
162 ideal      Solid type
163 19 DUCT    Zero length duct
164 Same 25a 1.3800E-03 a Area m^2      Mstr      8.9998E+04 A |p| Pa
165          0.13169 b Perim m          19a      -163.25 B Ph(p) deg
166          0.0000 c Length m          2.8610E-03 C |U| m^3/s
167          5.0000E-04 d Srough      -33.085 D Ph(U) deg
168 Master-Slave Links          -67.269 E Htot W
169 Optional Parameters          -83.03 F Edot W
170 ideal      Solid type
171 20 RPN     ChangeMe
172 Targ      6.0000 a G or T          6.0000 A disp

```

```

173 17C 17a / w / 1000 *
174 21 RPN ChangeMe
175 Targ 180.00 a G or T 180.00 A ChngeMe
176 17J
177 22 RPN Heat/Electrical Efficiency
178 0.0000 a G or T 12.190 A Efficie
179 17G 7e / 2 / mag 100 *
180 23 RPN Heat/Acc Efficiency
181 0.0000 a G or T 43.157 A Acc Eff
182 238.150304396 7e / 100 *
183 24 RPN IA Efficiency
184 0.0000 a G or T 81.017 A LA Eff
185 16E 16F / 100 *
186 25 DUCT Change Me
187 Same 16a 1.3800E-03 a Area m^2 Mstr 9.0292E+04 A |p| Pa
188 0.13169 b Perim m 25a -162.97 B Ph(p) deg
189 Same 16c 0.2050 c Length m 1.8752E-03 C |U| m^3/s
190 5.0000E-04 d Srough 7.7737 D Ph(U) deg
191 Master-Slave Links -67.269 E Htot W
192 Optional Parameters -83.557 F Edot W
193 ideal Solid type
194 26 RPN ChangeMe
195 Targ 1.0000 a G or T 1.0000 A ChngeMe
196 16A 19A /
197 27 RPN ChangeMe
198 Targ 1.0000 a G or T 1.0000 A ChngeMe
199 16B 180 - 19B /
200 28 RPN ChangeMe
201 Targ -1.000 a G or T -1.000 A ChngeMe
202 16E 19E /
203 29 SOFTEND Change Me
204 9.0292E+04 A |p| Pa
205 -162.97 B Ph(p) deg
206 1.8752E-03 C |U| m^3/s
207 7.7737 D Ph(U) deg
208 -67.269 E Htot W
209 Possible targets -83.557 F Edot W
210 -14.251 G Re(z)
211 -2.3218 H Im(z)
212 297.00 I T K
213 30 CONE Cone next T-branch
214 Same 14a 1.3800E-03 a AreaI m^2 Mstr 8.9443E+04 A |p| Pa
215 0.13168 b PerimI m 30a 16.130 B Ph(p) deg
216 4.0000E-02 c Length m 8.8259E-03 C |U| m^3/s
217 Same 31a 8.0936E-05 d AreaF m^2 Mstr -9.8546 D Ph(U) deg
218 3.1903E-02 e PerimF m 30d 194.88 E Htot W
219 5.0000E-04 f Srough 354.81 F Edot W
220 Master-Slave Links
221 Optional Parameters
222 ideal Solid type
223 31 DUCT 1cm Dia Tube
224 8.0936E-05 a Area m^2 Mstr 9.4034E+04 A |p| Pa
225 3.1898E-02 b Perim m 31a -69.563 B Ph(p) deg
226 0.7300 c Length m 8.6770E-03 C |U| m^3/s
227 5.0000E-04 d Srough -11.952 D Ph(U) deg
228 Master-Slave Links 194.88 E Htot W
229 Optional Parameters 218.54 F Edot W
230 ideal Solid type
231 32 CONE Change Me
232 Same 31a 8.0936E-05 a AreaI m^2 Mstr 9.4999E+04 A |p| Pa

```

233		3.1901E-02	b PerimI	m	32a	-70.00	B Ph(p)	deg
234		7.3000E-02	c Length	m		7.3927E-03	C  U	m^3/s
235	Same 1a	8.2418E-03	d AreaF	m^2	Mstr	-18.344	D Ph(U)	deg
236		0.32191	e PerimF	m	32d	194.88	E Htot	W
237		5.0000E-04	f Srough			217.85	F Edot	W

238 Master-Slave Links

239 Optional Parameters

240 ideal Solid type

241	33 RPN	Set Tm						
242	Targ	1.0000	a G or T		1.0000	A	ChngeMe	
243	Tm 0c /							
244	34 RPN	Set p1 mag						
245	Targ	1.0000	a G or T		1.0000	A	ChngeMe	
246	p1 mag 0d /							
247	35 RPN	Set p1 phase						
248	Targ	1.0000	a G or T		1.0000	A	ChngeMe	
249	-70 p1 arg /							
250	36 RPN	Set mag U1						
251	Targ	1.0000	a G or T		1.0000	A	ChngeMe	
252	U1 mag 0f /							
253	37 RPN	Set U1 phase						
254	Targ	1.0000	a G or T		1.0000	A	ChngeMe	
255	0g 90 - U1 arg /							
256	38 RPN	Set Htot						
257	Targ	1.0000	a G or T		1.0000	A	ChngeMe	
258	1E H2k /							

## Appendix 7

- This appendix showing the models used to generate Figure 3.3, which is the local acoustic field required by the linear alternator to generate electricity efficiently. Both at an acoustic impedance of  $3.8 \times 10^7$  Pa.s/m<sup>3</sup> and phase difference of -11°.
- Appendix 7.1 is the push-pull configuration model. In this model the linear alternator was placed in between a forced acoustic field from a side of a linear alternator and a self-excited from the other side. The self-excited flow characteristics set by two boundary conditions shown in segments 8 and 9.
- Appendix 7.2 is the compliance housing configuration model. In this model the linear alternator was placed in between a forced acoustic field from a side of a compliance representing the housing from the other side. The compliance volume was assumed based on a 6 inch pipe housing, which is the minimum to accommodate this alternator.

### Appendix 7.1

```

1 Push-pull
2 0 BEGIN
3      2.8000E+06 a Mean P Pa
4      56.000 b Freq Hz
5      297.00 c TBeg K
6 Gues      1.1111E+05 d |p| Pa
7      76.093 e Ph(p) deg
8 Gues      2.9239E-03 f |U| m^3/s
9 Gues      65.093 g Ph(U) deg
10 Gues      115.36 h Htot W
11 Optional Parameters
12 helium Gas type
13 1 DUCT Change Me
14      1.3200E-03 a Area m^2 Mstr      1.1111E+05 A |p| Pa
15      0.1288 b Perim m la      76.093 B Ph(p) deg
16      0.0000 c Length m      2.9239E-03 C |U| m^3/s
17      5.0000E-04 d Srough      65.093 D Ph(U) deg
18 Master-Slave Links      115.36 E Htot W
19 Optional Parameters      159.45 F Edot W
20 ideal Solid type
21 2 RPN ChangeMe
22 Targ      -11.00 a G or T      -11.00 A ChngeMe
23 1D 1B -
24 3 RPN ChangeMe
25 Targ      3.8000E+07 a G or T      3.8000E+07 A ChngeMe
26 1A 1C /
27 4 VESPEAKER Change Me
28      1.3850E-03 a Area m^2      1.1111E+05 A |p| Pa
29      1.9700 b R ohms      -103.91 B Ph(p) deg

```

```

30          4.4100E-02 c L      H          2.9239E-03 C |U|      m^3/s
31          46.720 d BLProd T-m          65.093 D Ph(U)    deg
32          0.7895 e M        kg          -115.36 E Htot     W
33          4.1430E+04 f K      N/m        -159.45 F Edot     W
34          7.0700 g Rm       N-s/m      -230.72 G WorkIn    W
35 Gues      -83.847 h |V|     V          83.847 H Volts     V
36 Gues      -6.9267E+05 i Ph(V) deg          8.5711 I Amps      A
37          129.95 J Ph(V/I) deg          2.2222E+05 K |Px|   Pa
38          2.2222E+05 K |Px|   Pa          -103.91 L Ph(Px)   deg
39 ideal      Solid type
40 5 DUCT      Zero length duct
41          1.3200E-03 a Area   m^2      Mstr      1.1111E+05 A |p|    Pa
42          0.1288 b Perim   m          5a        -103.91 B Ph(p)    deg
43          0.0000 c Length  m          2.9239E-03 C |U|    m^3/s
44          5.0000E-04 d Srough          65.093 D Ph(U)    deg
45 Master-Slave Links          -115.36 E Htot     W
46 Optional Parameters          -159.45 F Edot     W
47 ideal      Solid type
48 6 RPN      ChangeMe
49 Targ      6.0000 a G or T          6.0000 A disp
50 4C 4a / w / 1000 *
51 7 RPN      LA Efficiency
52          0.0000 a G or T          72.346 A LA Eff
53 1E 1F / 100 *
54 8 RPN      ChangeMe
55 Targ      1.0000 a G or T          1.0000 A ChngeMe
56 1A 5A /
57 9 RPN      ChangeMe
58 Targ      1.0000 a G or T          1.0000 A ChngeMe
59 1B 180 - 5B /
60 10 RPN     ChangeMe
61 Targ      -1.000 a G or T          -1.000 A ChngeMe
62 1E 5E /
63 11 HARDEND Change Me
64          1.1111E+05 A |p|    Pa
65          -103.91 B Ph(p)    deg
66          2.9239E-03 C |U|    m^3/s
67          65.093 D Ph(U)    deg
68 Possible targets          -115.36 E Htot     W
69          -159.45 F Edot     W
70          -8.5834E-02 G R(1/z)
71          1.6684E-02 H I(1/z)

```

## Appendix 7.2

```

1 Compliance housing
2 0 BEGIN
3          2.8000E+06 a Mean P Pa
4          56.000 b Freq     Hz
5          297.00 c TBeg     K
6 Gues      1.1114E+05 d |p|   Pa
7          20.000 e Ph(p)   deg
8 Gues      2.9247E-03 f |U|   m^3/s
9 Gues      9.0000 g Ph(U)  deg
10 Gues     105.94 h Htot     W
11 Optional Parameters
12 helium    Gas type

```

```

13      1 DUCT      Change Me
14          1.3850E-03 a Area    m^2      Mstr      1.1114E+05 A |p|    Pa
15          0.13193 b Perim   m        1a        20.000 B Ph(p)   deg
16          0.0000 c Length  m        2.9247E-03 C |U|    m^3/s
17          5.0000E-04 d Srough                9.0000 D Ph(U)   deg
18 Master-Slave Links                105.94 E Htot   W
19 Optional Parameters                159.53 F Edot   W
20 ideal      Solid type
21      2 RPN      ChangeMe
22 Targ      -11.00 a G or T      -11.00      A ChngeMe
23 1D 1B -
24      3 RPN      ChangeMe
25 Targ      3.8000E+07 a G or T      3.8000E+07 A ChngeMe
26 1A 1C /
27      4 VESPEAKER Change Me
28          1.3850E-03 a Area    m^2      3.8780E+04 A |p|    Pa
29          1.9700 b R        ohms      -80.852 B Ph(p)   deg
30          4.4100E-02 c L      H        2.9239E-03 C |U|    m^3/s
31          46.720 d BLProd  T-m        9.0023 D Ph(U)   deg
32          0.7895 e M        kg        0.0000 E Htot   W
33          4.1430E+04 f K      N/m      0.14442 F Edot   W
34          7.0700 g Rm      N-s/m    -105.94 G WorkIn W
35 Gues      35.415 h |V|     V        35.415 H Volts   V
36 Gues      112.51 i Ph(V)  deg      6.1822 I Amps   A
37                165.41 J Ph(V/I) deg
38                1.2441E+05 K |Px|    Pa
39 ideal      Solid type                -142.17 L Ph(Px) deg
40      5 RPN      ChangeMe
41 Targ      6.0000 a G or T      6.0000      A disp
42 4C 4a / w / 1000 *
43      6 RPN      LA Efficiency
44          0.0000 a G or T      66.407      A LA Eff
45 1E 1F / 100 *
46      7 COMPLIANCE Change Me
47          4.0000E-02 a SurfAr  m^2      3.8780E+04 A |p|    Pa
48          1.0000E-03 b Volume  m^3      -80.852 B Ph(p)   deg
49 Master-Slave Links                1.2266E-18 C |U|    m^3/s
50                45.000 D Ph(U)   deg
51                0.0000 E Htot   W
52 ideal      Solid type                -1.3930E-14 F Edot   W
53      8 HARDEND  Change Me
54 Targ      0.0000 a R(1/z)      3.8780E+04 A |p|    Pa
55 Targ      0.0000 b I(1/z)      -80.852 B Ph(p)   deg
56 Targ      0.0000 c Htot    W        1.2266E-18 C |U|    m^3/s
57                45.000 D Ph(U)   deg
58                0.0000 E Htot   W
59                -1.3930E-14 F Edot   W
60                -6.1557E-17 G R(1/z)
61                8.5188E-17 H I(1/z)

```

## Appendix 8

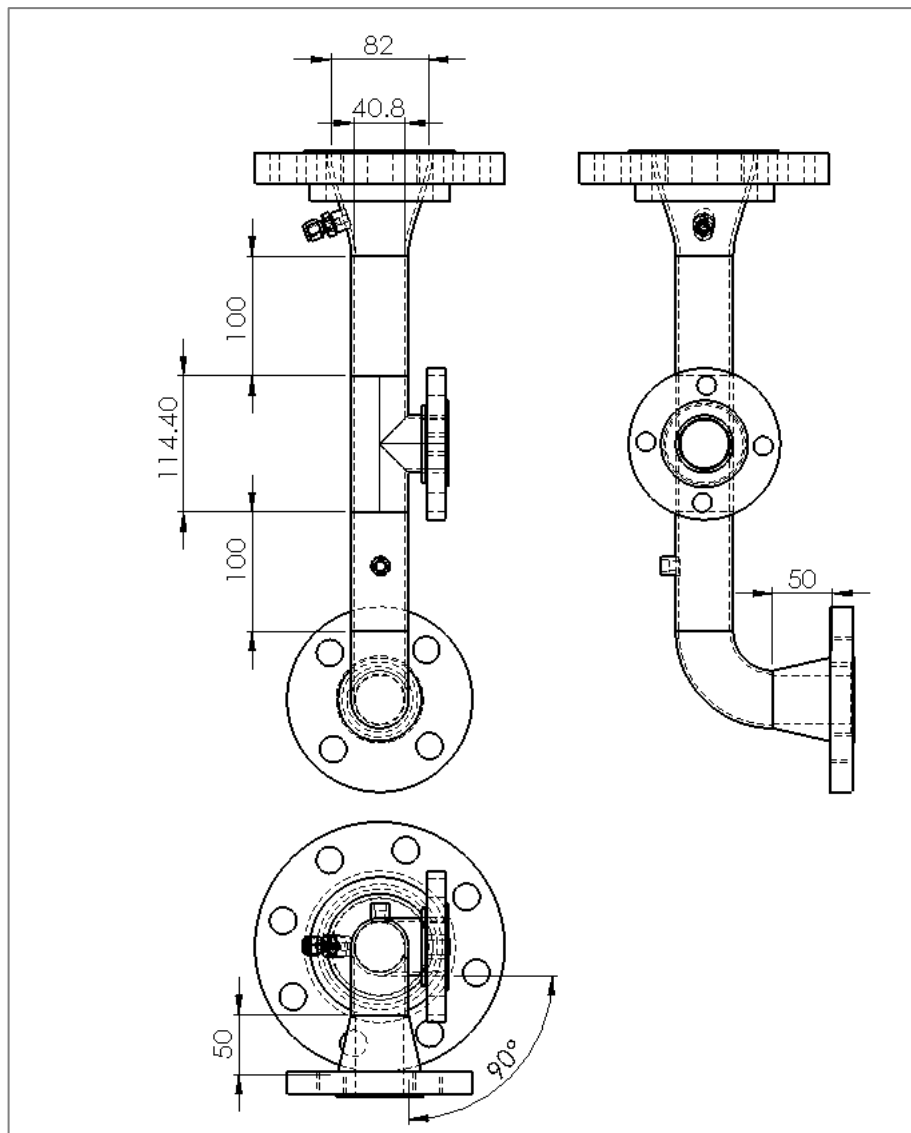


**Figure A8-1:** The first part of the acoustic section, showing the reducer and tee branch

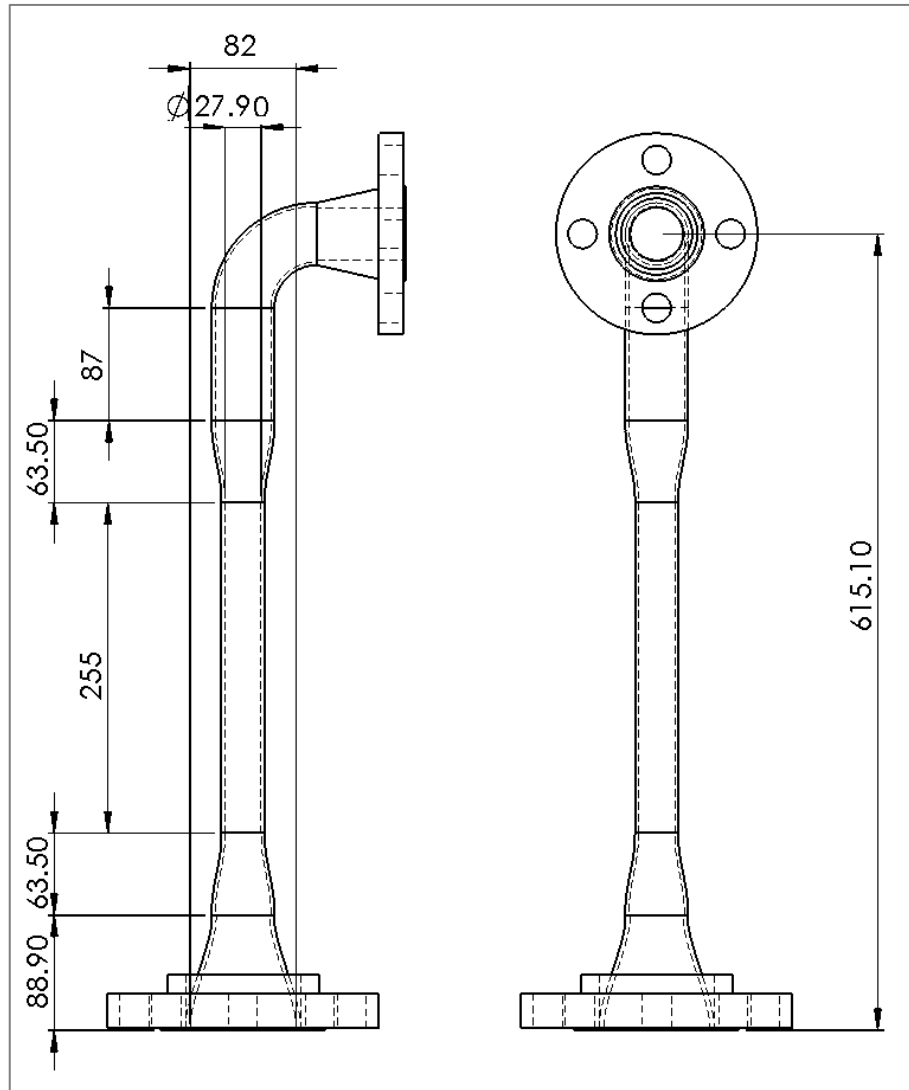


**Figure A8-2:** The last part of the acoustic section, showing the reducers and 1 inch diameter tube